Tracing the evolution of the Galactic halo through asymptotic giant branch stars

Cherie Kate Fishlock

A thesis submitted for the degree of

Doctor of Philosophy

of the Australian National University

Australian National University

Research School of Astronomy & Astrophysics

Submitted March 2015

Accepted October 2015

To Gerad.

Disclaimer

I hereby declare that the work in this thesis is that of the candidate alone, except where indicated below or in the text of the thesis. The work was undertaken between September 2010 and February 2015 at the Australian National University, Canberra. It has not been submitted in whole or in part for any other degree at this or any other university.

David Yong led the Magellan proposal that was successful in receiving two nights to obtain the data required for this research. David Yong and Amanda Karakas assisted with the Magellan observing run in June 2011. Amanda Karakas calculated the evolutionary sequences for the 4.5 and 5.5 $M_{\odot}$ models presented in Chapter 3.

Cherie Kate Fishlock

3 March 2015

Supplementary Research

In addition to the work presented in this thesis, the candidate has contributed to a number of other research projects. Some of these collaborations have resulted in peer-reviewed publications. All papers authored or co-authored by the candidate throughout the graduate program are listed here in reverse chronological order:

1. **Neutron-capture and Sc abundances in Galactic low- and high-α field halo stars**
   Fishlock, C. K.; *et al.*

   To be submitted to the Monthly Notices of the Royal Astronomical Society

2. **Evolution and nucleosynthesis of asymptotic giant branch stellar models of low metallicity**
   Fishlock, C. K.; *Karakas, A. I.; Lugaro, M.; and Yong, D., 2014*

   Published in The Astrophysical Journal, 797, 44

3. **The s-Process Enrichment of the Globular Clusters M4 and M22**
   Shingles, L. J.; Karakas, A. I.; Hirschi, R.; **Fishlock, C. K.**; *Yong, D.; Da Costa, G. S.; and Marino, A. F., 2014*

   Published in The Astrophysical Journal, 795, 34

4. **The Aquarius Co-Moving Group is Not a Disrupted Classical Globular Cluster**
   Casey, A. R.; Keller, S. C.; Alves Brito, A.; Frebel, A.; Da Costa, G. S.; Karakas, A. I.; Yong, D.; Schlaufman, K.; Jacobson, H. R.; Yu, Q.; and **Fishlock, C. K.**, *2014*

   Published in the Monthly Notices of the Royal Astronomical Society, 443, 828

5. **The outer halo globular cluster system of M31 - I. The final PAndAS catalogue**
   Huxor, A. P.; Mackey, A. D.; Ferguson, A. M. N.; Irwin, M. J.; Martin, N. F.; Tanvir, N. R.; Veljanoski, J.; McConnachie, A.; **Fishlock, C. K.**; *Ibata, R.; Lewis, G. F., 2014.*

   Published in the Monthly Notices of the Royal Astronomical Society, 442, 2165

6. **Iron and neutron-capture element abundance variations in the globular cluster M2 (NGC 7089)**
   Yong, D.; Roederer, I. U.; Grundahl, F.; Da Costa, G. S.; Karakas, A. I.; Norris, J. E.; Aoki, W.; **Fishlock, C. K.**; *Marino, A. F.; Milone, A. P.; Shingles, L. J., 2014.*

   Published in the Monthly Notices of the Royal Astronomical Society, 441, 3396

7. **Chemical abundances in bright giants of the globular cluster M62 (NGC 6266)**
Yong, D.; Alves Brito, A.; Da Costa, G. S.; Alonso-García, J.; Karakas, A. I.; Pignatari, M.; Roederer, I. U.; Aoki, W.; **Fishlock, C. K.***; Grundahl, F.; Norris, J. E., 2014.*

Published in the Monthly Notices of the Royal Astronomical Society, 439, 2638

8. **The effect of including molecular opacities of variable composition on the evolution of intermediate-mass AGB stars**
Fishlock, C. K.*; Karakas, A. I.; Stancliffe, R. J., 2014.*

Published in the Monthly Notices of the Royal Astronomical Society, 438, 1741

9. **Newly discovered globular clusters in NGC 147 and NGC 185 from PAndAS**
Veljanoski, J.; Ferguson, A. M. N.; Huxor, A. P.; Mackey, A. D.; **Fishlock, C. K.***; Irwin, M. J.; Tanvir, N.; Chapman, S. C.; Ibata, R. A.; Lewis, G. F.; McConnachie, A., 2013.*

Published in the Monthly Notices of the Royal Astronomical Society, 435, 3654

Acknowledgments

When I first started at ANU little did I know what lay ahead. Without the support and guidance from many people I don't think my time at ANU would have turned out as incredible as it has.

First, and foremost, I thank Amanda Karakas and Dave Yong for being amazing supervisors. With your guidance and honest words I have become a far better researcher and communicator. Thank you for believing in me.

Many thanks goes to Maria Lugaro and Richard Stancliffe who, with their incredible patience, have helped me further understand the intricacies of stellar evolution. I thank Joelene Buntain for all the times spent commiserating together on neutron densities and for being only an email away. I also thank Luke Shingles for being a great PhD 'brother'. Further thanks goes to Dougal Mackey for supervising me on a three month project.

A big thanks goes to Tammy Roderick and Louise Howes for being the best officemates. You guys are awesome. Thanks to Wolfgang Kerzendorf and Melissa Ness for convincing me that ANU is the most awesome place to do a PhD and to Stephan Peters for being a great House 10 friend. Thanks to my family, Mumsie, Heidi, and Dad, for attempting to understand what I've been doing for the past few years and to Gerad's family for making me feel welcome into theirs.

Last, but not least, I thank Gerad Newton. I could not have made it this far without you. Your unwavering support has kept me grounded and there are no words to describe how much you mean to me.

I would like to gratefully acknowledge the many sources of funding that have supported me during my PhD: ANU, RSAA, Joan Duffield Research Scholarship, ANSTO AMRFP, John Norris, Amanda Karakas, Maria Lugaro, the Go8 Germany Joint Research Co-operation Scheme, and Gerad Newton. This research has made use of the Magellan Clay telescope at Las Campanas Observatory, COALA at RSAA, and the National Computational Infrastructure at ANU.

So long and thanks for all the fish.

Abstract

The discovery of the ongoing accretion of the Sagittarius dwarf spheroidal galaxy confirms that mergers with satellite dwarf galaxies are contributing to the formation of the Galactic halo. Additionally, a number of satellite dwarf galaxies show evidence of pollution by asymptotic giant branch (AGB) stars at around [Fe/H] of -1 as a result of a slower star formation rate than the Galactic halo. However, finding stars that were accreted during the earliest times of the formation of the Galactic halo has been difficult. Using the knowledge that the atmospheres of low-mass stars retain information about the chemical composition of the gas cloud in which they formed, we can find signatures of the history of our Galaxy encoded in the stars. The study by Nissen & Schuster (2010) uncovered convincing evidence that the Galactic halo hosts two populations that are separated in [α/Fe]. They argued that the low-α stars have kinematics consistent with accretion from a satellite galaxy with a slower star formation rate than the high-α population which most likely formed in-situ in the Galaxy.

The aim of this thesis is to investigate the role AGB stars have had in the chemical enrichment of halo stars that were either accreted from dwarf galaxies or formed in-situ in the Galaxy. Through an analysis of chemical abundances we seek to determine the extent to which the chemical properties of the surviving galaxies are similar to the satellite galaxies that were accreted long ago. With this analysis, we hope to reveal how environmental differences such as the star formation rate have influenced the observed abundance ratios. The sample compiled by Nissen & Schuster (2010) presents a unique opportunity to further investigate the chemical evolution of neutron-capture elements in dwarf galaxies and the Galactic halo through a comparison of the low- and high-α populations.

Theoretical models play a key role in furthering our understanding of the origin of the elements. In order to understand the influence of AGB stars on the chemical enrichment of the low-α stars, we calculate detailed theoretical models of AGB stars at the mean metallicity of the low- and high-α populations. Stellar models are subject to uncertainties and we analyse the uncertainty related to the treatment of low-temperature molecular opacities in AGB stellar models. Previous detailed intermediate-mass AGB models calculated with the Mt Stromlo evolutionary code used a molecular opacity treatment which did not consider the depletion of C and O due to hot bottom burning. We perform tests on two masses, 5 $M_\odot$ and 6 $M_\odot$, and two metallicities, $Z = 0.001$ and $Z = 0.02$, to quantify the variations between the two opacity treatments: one that accounts for the depletion of carbon and oxygen and one that does not. We find that the treatment of opacity is more crucial in the lower metallicity models.

We present stellar evolutionary tracks and nucleosynthesis predictions for a grid of stellar models of low- and intermediate-mass AGB stars at $Z = 0.001$ ([Fe/H] $= -1.2$). The models have an initial mass range of 1 $M_\odot$ to 7 $M_\odot$. The intermediate-mass models have been calculated with the updated low-temperature opacity treatment. Final surface abundances and stellar yields are calculated for all elements from hydrogen to bismuth as well as isotopes up to the iron group. We present the first study of neutron-capture nucleosynthesis in

intermediate-mass AGB models at [Fe/H] = −1.2. We also present the first full *s*-process predictions and yields for a super-AGB star at any metallicity.

Neutron-capture elemental abundances have been measured, using high-resolution spectra obtained from Magellan, for a sub-sample of the low- and high-α stars compiled by Nissen & Schuster (2010). We find that the low-α stars display the same chemical signature that is observed in present-day dwarf spheroidal galaxies with low [α/Fe] and [Y/Eu] and high [Ba/Y]. This confirms that the Galactic halo contains a population of stars accreted from dwarf galaxies and that AGB stars were able to contribute to the chemical evolution of the earliest dwarf galaxies. However, models of AGB stars are unable explain the lower [*hs*/Eu] ratios observed in the low-α stars compared to the high-α stars.

Contents

List of Figures

List of Tables

CHAPTER 1

Introduction

> A better understanding of the nucleosynthesis of the elements is, however, important in order to learn more about the formation and evolution of the various populations.
>
> – P. E. Nissen [1]

It is advantageous that the atmospheres of low-mass stars retain information, to this day, about the chemical composition of the gas cloud in which they formed. With this knowledge, it is possible to find signatures of the history of our Galaxy encoded in the stars. Through the study of the kinematics and chemical abundances of the surviving stellar populations, we can uncover information about their origin and how they were enriched by previous generations of stars.

The study by Eggen et al. (1962) was the first to use measurements of stellar abundances to help explain the formation of the Galaxy. By studying the motions and abundances of high-velocity stars, Eggen et al. (1962) proposed that the Galaxy formed from the rapid collapse of a protogalactic cloud, starting from the first stars. The study found that the metal abundance and orbital angular momenta of stars decreased with increasing orbital energies and eccentricities. This implies that there exists an abundance gradient with galactocentric distance due to the monolithic collapse of the Galaxy.

Later, Searle & Zinn (1978) observed that globular clusters have a range of metallicities regardless of their distance from the Galactic centre. This is in disagreement with the theory of monolithic collapse which predicts an abundance gradient of Galactic globular cluster metallicity in the outer halo (Eggen et al. 1962). Searle & Zinn (1978) concluded that protogalactic fragments continued to be accreted by the Galaxy long after the formation of its central regions. Numerical simulations also predict that hierarchical structure formation is driven by the Λ cold dark matter (ΛCDM) cosmological model (e.g., White & Rees 1978)

[1] *Chemical abundances as population tracers* (Nissen 2011)

where small-scale fluctuations result in the build-up of cosmological structure. This model of hierarchical formation has since become the leading paradigm in explaining how our Galaxy has evolved.

Throughout this thesis we[2] aim to reveal more about the formation of the Galactic halo as a result of mergers with dwarf galaxies and how the stars of the surviving population of dwarf galaxies compare to the stars of the accreted dwarf galaxies. In particular, we hope to further understand the role of asymptotic giant branch stars in the enrichment of the Galactic halo and the dwarf galaxies that were accreted long ago.

1.1. The formation of the Galactic halo

One of the most important questions in the formation and evolution of the Galaxy is the process that formed the Galactic halo. Despite only comprising approximately 1 per cent of the total stellar mass in the Galaxy (Klement 2010), the Galactic halo is now known to host a number of stellar streams which remain from the accretion of satellite galaxies (e.g., Ibata et al. 1994; Helmi et al. 1999; Belokurov et al. 2007).

The use of theoretical simulations to model the formation of the Galaxy have provided predictions for understanding the accretion history of the halo and the origin of stellar streams. Using a semi-analytic method, Bullock & Johnston (2005) modelled accretion events by a Milky Way type halo and compared the results to observations of the Galactic halo and its orbiting satellite galaxies. They concluded that the bulk of the halo for large galaxies, like the Milky Way, formed through the accretion of disrupted satellites. The more massive of these disrupted satellites contributed to the build up of the inner halo and were accreted more than 9 Gyr ago while the dwarf satellites, being lower in mass, were accreted at a later time.

With the discovery of on-going accretion events, the hierarchical structure formation of the Galactic halo due to mergers as well as in-situ star formation has been well accepted (Freeman & Bland-Hawthorn 2002). However, the relative fraction of stars that have been accreted to stars that have formed in-situ is unknown (e.g., Bell et al. 2008). One approach in determining the fraction of stars that have been accreted by the Galactic halo is to compare chemical abundance patterns between halo stars and stars located in satellite dwarf galaxies. When looking for chemical similarities, it is important to understand the extent to which the chemical properties of the surviving stars have in common with the stars from satellite galaxies that were accreted long ago.

Abundance ratios can be used to trace the chemical evolution of a system. This is because the nucleosynthesis of the elements occurs on different timescales in stars of different masses (Tinsley 1979). Massive stars contribute α elements (for example, O, Mg, Si, and Ca) and some Fe during Type II supernovae, whereas Type Ia supernovae contribute Fe but little of the α elements. The timescales are also different with Type II supernovae exploding after

[2]For stylistic reasons I use the plural form throughout this thesis to refer to work led by myself but naturally done in collaboration with my supervisor and advisory panel. The text however is solely my own.

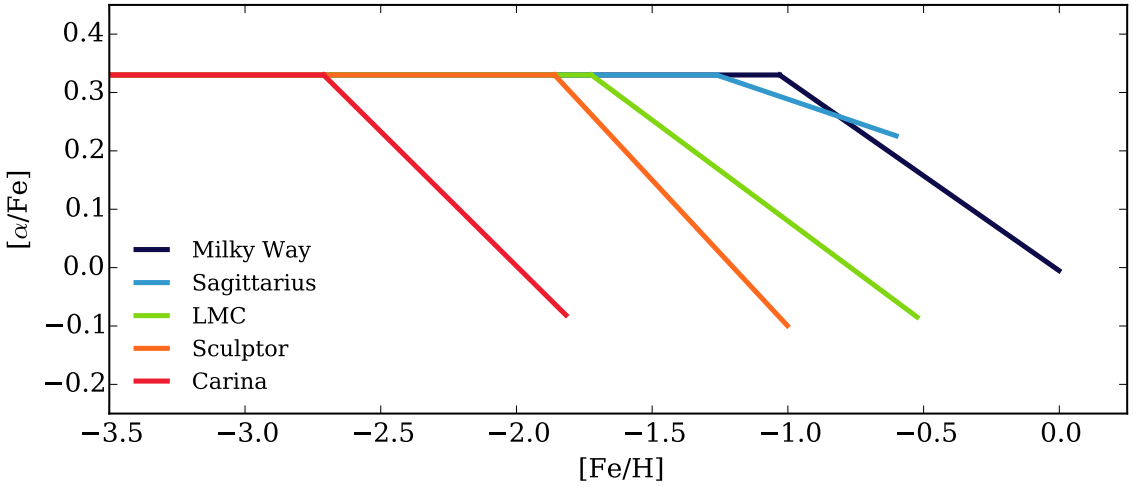

Figure 1.1 Best fits to observations showing the location of the 'knee' of the Milky Way, Large Magellanic Cloud (LMC), and three dSphs. Data taken from de Boer et al. (2014).

a few 10^7 years while Type Ia supernovae start exploding after 10^9 years (Tinsley 1979) or, for prompt Type Ia supernovae, 10^8 years (Bonaparte et al. 2013). Therefore, the relative abundance of α elements to Fe can be used as an indicator of the star formation history of a system.

At [Fe/H][3] less than approximately −2, there exists an overlap in [α/Fe][4] between the dwarf spheroidal galaxies (dSphs) and stars in the Galaxy with both populations showing an almost constant, and high, [α/Fe] of approximately +0.5. However, at higher metallicities, dSph and Galactic stars separate in [α/Fe] with the dSphs stars having a lower abundance of α elements than Galactic stars (Tolstoy et al. 2009). Therefore, the lower [α/Fe] abundances observed in dSph stars imply a slower star formation rate in dSphs than in the Galaxy. A slower star formation rate means that Type Ia supernovae are able to contribute to the chemical enrichment of a system before the next generation of stars form. Therefore, the abundance of [α/Fe] starts to decrease at a lower metallicity (McWilliam 1997; Tolstoy et al. 2009). This turnover point is seen as a 'knee' in Figure 1.1 of [Fe/H] against [α/Fe].

A number of observational studies have concluded that the Galactic halo does not consist entirely of stars similar to those found in surviving dSphs (e.g., Fulbright 2002; Venn et al. 2004; Geisler et al. 2005). Fulbright (2002) concluded, using a sample of Galactic halo stars with low [α/Fe] abundances, that field halo stars in the solar neighbourhood do not show the same [X/Fe] abundance patterns as observed in present-day dSphs. This conclusion was also drawn by Geisler et al. (2005) who compared abundance trends of stars in the Sculptor dSph to stars in the Galactic halo.

Hendricks et al. (2014) demonstrated that the metallicity of the [α/Fe] knee occurs at lower [Fe/H] for lower mass galaxies. For the Sagittarius dwarf galaxy that is currently being accreted by the Galaxy, the metallicity of the knee at [Fe/H] = −1.27 is only slightly more

[3] $[X/Y] = \log_{10}(N_X/N_Y)_\star - \log_{10}(N_X/N_Y)_\odot$ where N_X and N_Y are the abundances (by number) of elements X and Y.

[4] Average of the α-elements which can include, for example, Mg, Ca, Ti.

metal-poor than [Fe/H] = −1.04 which is observed in the Galaxy (de Boer et al. 2014). In comparison, the location of the knee in Sculptor, the next most massive dSph after Sagittarius, is at [Fe/H] = −1.87 (Starkenburg et al. 2013). These values suggest that any possible chemical abundance differences not yet observed in the abundances between the Galactic halo stars and stars accreted from dwarf galaxies during the formation of the Galactic halo could be quite small and difficult to measure.

The stars in dSphs and the Galactic halo are faint due to their large distances and, as such, it is difficult to determine precise chemical abundances, especially for a large number of stars. As more sophisticated and larger telescopes such as the Giant Magellan Telescope[5] are built, the knowledge of the chemical abundances and enrichment histories will increase. However, until the advent of the extremely large telescopes, extensive high-resolution spectroscopic surveys are currently out of reach.

Rather than relying on the prohibitively long exposure times required to obtain high-quality spectra for a large sample of stars in dSphs, Nissen & Schuster (2010) studied a sample of stars with halo kinematics that are currently passing through the solar neighbourhood. Using archived data for 94 stars from the UVES instrument on the Very Large Telescope and the FIES instrument on the Nordic Optical Telescope, Nissen & Schuster (2010) performed a high-precision analysis with a 1σ precision, resulting in abundance measurement errors better than 0.02 dex for [α/Fe]. When a high-precision analysis of [Mg/Fe] was performed, Nissen & Schuster (2010) discovered the sample separated into two populations: one with a high-α abundance and one with a low-α abundance (Figure 1.2(a)). The high-α population has [Mg/Fe] abundances of between +0.25 and +0.4 whereas the low-α population has [Mg/Fe] abundances that decrease from approximately +0.3 to +0.1. Nissen & Schuster (2010) concluded that the low-α population originally formed in dwarf galaxies before being accreted by the Galaxy and that the high-α population formed in-situ in the Galaxy.

Nissen & Schuster (2010) measured seven elements (Na, Mg, Si, Ca, Ti, Cr, and Ni) and of these elements, the low- and high-α populations were able to be separated in Na, Mg, Si, Ca, Ti, and Ni with the low-α population having a lower abundance for each of these elements. There was no observed separation in Cr. These abundance differences provide further evidence that at least two populations exist in the Galactic halo. It is only with the high-resolution spectra and high-precision measurements that these separations become apparent.

Using kinematic information, Nissen & Schuster (2010) also demonstrated that the high-α stars have prograde orbits whereas two-thirds of the low-α stars have retrograde orbits. This further suggests that the high-α stars formed in the Galaxy and were heated to halo kinematics whereas the low-α stars were likely to have been accreted from dwarf galaxies. In addition, Nissen & Schuster (2010) suggested that the retrograde low-α stars could have been stripped from the ω Centauri globular cluster due to the similarity of their average Galactic rotation velocity of $V_{\rm LSR} \simeq -260$ km s^{-1}. However, a number of abundance patterns in the low-α population do not match stars observed in ω Centauri, casting doubt on this theory (Nissen & Schuster 2011).

[5] http://www.gmto.org/

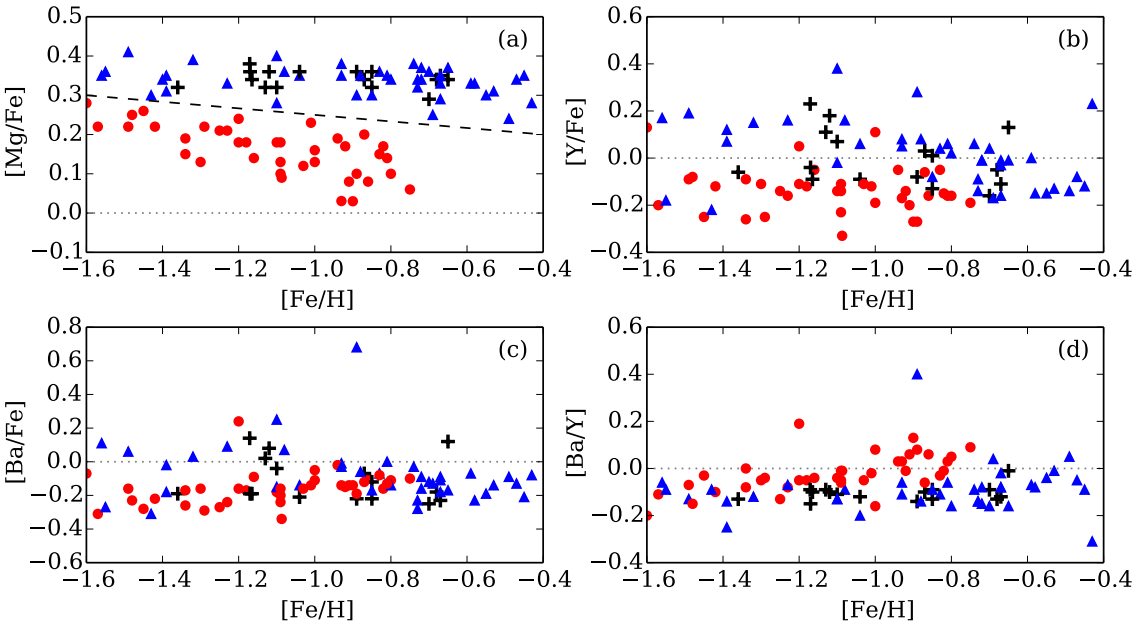

Figure 1.2 [Mg/Fe], [Y/Fe], [Ba/Fe], and [Ba/Y] versus [Fe/H] for the Nissen & Schuster (2010) sample. The blue symbols show the high-α halo stars and the red symbols show the low-α stars, separated by the long-dashed line. The crosses represent thick disc stars. The dashed line shows the separation between the populations as determined by Nissen & Schuster (2010). Data compiled from Nissen & Schuster (2010) and Nissen & Schuster (2011).

In a follow-up study, Nissen & Schuster (2011) measured abundances for five additional elements: Mn, Cu, Zn, Y, and Ba. These elements provide further insight into the connection between the low-α population and their possible origin as dSphs stars that were accreted by the Galaxy. In the low-α population, lower abundances were observed for [Cu/Fe] and [Zn/Fe] but no difference was found for [Mn/Fe] when compared to the high-α population. The observed [Cu/Fe] abundances agrees with the theory that Cu is formed in massive stars via the weak *s*-process. The low-α stars also show a higher scatter in the abundances of [Cu/Fe] and [Zn/Fe] compared to the high-α stars. Figure 1.2 shows that there is minimal separation for [Y/Fe] and no clear separation for [Ba/Fe]. However, for [Ba/Y], a separation starts to show at higher metallicities with the low-α stars having a higher [Ba/Y] ratio than the high-α stars.

Through an abundance comparison between stars in dSphs and the Galaxy, Venn et al. (2004) were able to identify two unique chemical signatures distinct to dSphs. When comparing stars at the same metallicity, most dSph stars showed a higher [Ba/Y] ratio and lower [Y/Eu] ratio. Therefore, the observed enhancement in [Ba/Y] for the low-α population agrees with the theory that these stars formed in an environment with a slower star formation rate, in comparison to the high-α population (Nissen & Schuster 2011). Where there is delayed star formation, low-mass stars of less than approximately 3 $M_\odot$ are able to evolve through the asymptotic giant branch (AGB) phase and eject their enriched envelope before star formation ceases. During the AGB phase, stars undergo rich nucleosynthesis producing heavy elements from Cu to Bi through the capture of neutrons onto seed nuclei (see Section 4.4.3 for further details). The low-mass, low-metallicity stars have a high

neutron-to-seed ratio which results in the production of more Ba than Y (Busso et al. 1999). This increases the abundance of [Ba/Y] in a system.

By determining differential abundance ratios, Nissen & Schuster (2010) and Nissen & Schuster (2011) were able to uncover chemical similarities between the low-α population and present-day dSphs. They suggested that the low-α stars formed in massive dwarf galaxies before being accreted during the formation of the Galactic halo. The dSphs that have survived today have a larger offset in [α/Fe] to Galactic halo stars as they experienced an even slower star formation rate compared to the low-α population. Therefore, it is theorised that, as a result of the slower star formation rate, AGB stars in the galaxies that are the progenitors of the low-α population had less time to contribute to the chemical enrichment than observed in present-day dSphs. By measuring abundances of neutron-capture elements predominantly produced in AGB stars in the low- and high-α populations, it will be possible to quantify the differences between the two populations and the contribution of AGB stars to the chemical enrichment of these stars.

1.2. The origin of the elements

Understanding the origin of the elements is pivotal to understanding how the observed abundance ratios trace a stellar population (Nissen 2011). Indeed, one of the questions from the Decadal Plan for Australian Astronomy[6] is: *How do stars produce and recycle the elemental building-blocks of life?*

Alongside observations of stars and measurements of their elemental abundances, theoretical models have played a key role in furthering our understanding of the origin of the elements. Calculations of theoretical stellar models follow the structure and chemical composition of a star with a given mass and metallicity, providing predictions that can be compared to observations. The study by Haselgrove & Hoyle (1956) first detailed how the evolution of a star could be calculated using a computer and there has since been considerable progress, due to the advent of supercomputers, in the field of theoretical stellar evolution.

Studies of detailed stellar models have established that elemental yields[7] are dependent on the initial mass and, to a lesser extent, the metallicity of a star (e.g., Woosley & Weaver 1995; Karakas 2010). Oxygen, for example, is thought to be predominately produced in massive stars and is less dependent on the initial metallicity as it can be synthesised from only hydrogen(Woosley & Weaver 1995). However, while the origins of the light elements ($Z \leq 30$) are reasonably well understood, the origins of the heavier elements are less certain. The production of neutron-capture elements ($31 \leq Z \leq 83$, see Figure 1.3) is theorised to occur through two main processes: the slow (*s*-) process and the rapid (*r*-) process (Burbidge et al. 1957). Each process produces roughly half of the elements heavier than Fe. The *s*-process occurs when the timescale for the decay of an unstable isotope is generally shorter than the timescale for neutron capture. In contrast, the *r*-process occurs under conditions of

[6] New Horizons: A decadal plan for Australian astronomy (2006-2015)

[7] The total mass of an element ejected through mass loss over the lifetime of a star.

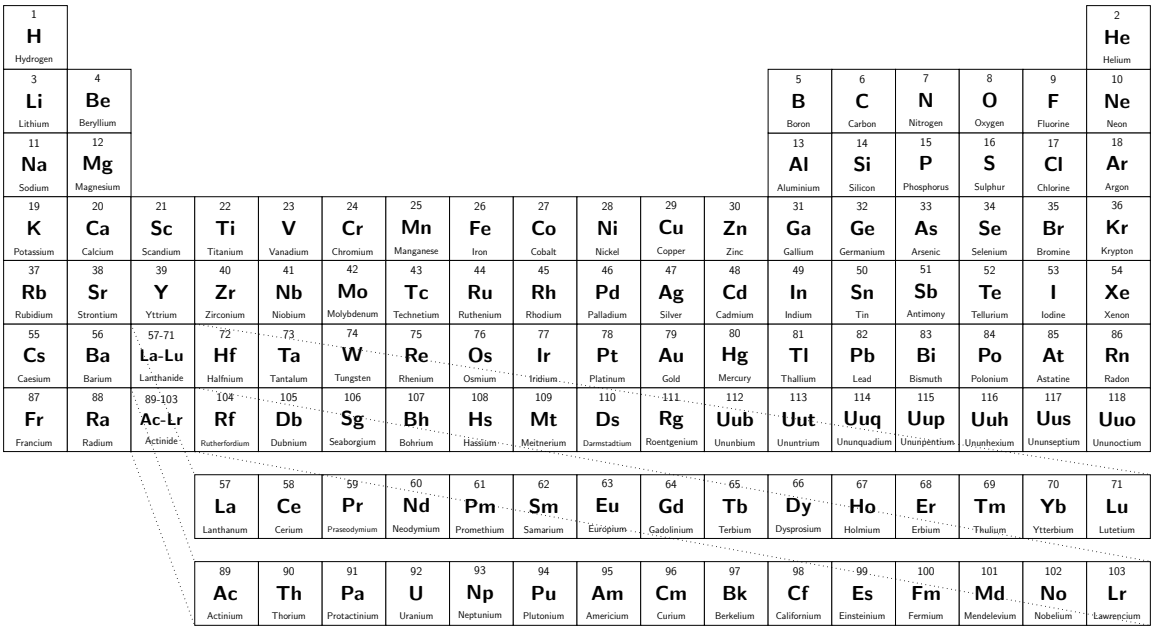

Figure 1.3 The Periodic Table of the elements.

extremely high neutron densities, allowing seed nuclei to quickly capture neutrons to reach highly unstable nuclei before the neutron flux is shut off. Once the neutron flux is gone, the unstable isotopes quickly decay back to stable isotopes. For these reasons, the *r*-process requires considerably higher neutron densities, on the order of 10^{23} to 10^{28} n cm^{-3} (Kratz et al. 2007), compared to $\lesssim 10^{14}$ n cm^{-3} for the *s*-process (Fishlock et al. 2014a).

There is strong observational evidence to suggest that the *s*-process takes place in low- to intermediate-mass stars during the AGB phase (e.g., Abia et al. 2002). The *s*-process is responsible for producing the majority of a number of elements from Ga to Bi such as Sr, Y, Zr, Ba, La, and Pb (Sneden et al. 2008). The formation site(s) of the *r*-process is still unknown but is most likely related to massive stars due to the timescales required for enrichment (for a review, see Arnould et al. 2007). The *r*-process predominantly produces elements such as Te, Eu, and Os (Sneden et al. 2008). In the Solar System, Sr and Ba were predominately produced through the *s*-process while Eu is predominately produced through the *r*-process. Elements such as Rb and Pd are produced almost equally by both processes (Sneden et al. 2008). The lifetime of a star provides further complications in the determining the origin of the elements as it affects how soon enriched material is recycled to form the next generation of stars.

Currently, theoretical predictions of neutron-capture elemental yields from AGB stars only exist in the literature for a few initial masses and metallicities. In Table 1.1 we list the studies that present yields of neutron-capture elements for at least two masses. Only the grid of $Z = 0.0003$ calculated by Straniero et al. (2014) has initial masses that expand the full range of AGB stars at a sufficient mass resolution. Other grids either focus on the low-mass models of less than 3 $M_\odot$ (Cristallo et al. 2011; Karakas et al. 2014) or have a low mass resolution (Pignatari et al. 2013).

As evidenced by Table 1.1, the reason that few studies have focused on calculating yields

Table 1.1 List of stellar models with tables of yields of neutron-capture elements available prior to this work. Only studies with more than one mass at each metallicity are listed.

Reference	Mass ($M_\odot$)	Metallicity, Z
Cristallo et al. (2011)	1.3, 1.5, 2, 2.5, 3	0.0001[a], 0.001, 0.003, 0.006, 0.008, 0.01, 0.014, 0.02
Pignatari et al. (2013)	1.65, 2, 3, 5	0.01, 0.02
Karakas et al. (2014)	1.7, 2.36	0.0003, 0.0006
Straniero et al. (2014)	1.3, 1.5, 2, 2.5, 3, 4, 5, 6	0.0003[a]

NB. – Table adapted from Karakas & Lattanzio (2014).
[a] Does not include [α/Fe] = +0.5

for neutron-capture elements is that it is computationally intensive. In addition, predictions of stellar yields are subject to numerous modelling uncertainties such as the treatment of convection, mass loss, and reaction rates[8] (e.g., Lugaro et al. 2003; Stancliffe & Jeffery 2007; Cristallo et al. 2009; Karakas 2010; Doherty et al. 2014a). Some studies have presented surface abundances of neutron-capture elements (e.g., Bisterzo et al. 2010; Lugaro et al. 2012) however these results are not suitable as input into chemical evolution models. For a detailed summary on the availability of stellar yields and the related uncertainties, see Karakas & Lattanzio (2014).

Chemical evolution models can provide valuable insight into the evolution of elements in a stellar system (e.g., Kobayashi et al. 2011a; Cescutti et al. 2012; Bisterzo et al. 2014). When used in conjunction with observations, chemical evolution models can provide constraints on the yields of elements by adjusting the yields included in chemical evolution models to match observations (e.g., Francois et al. 2004). The chemical evolution models of Lanfranchi et al. (2008) follow the accumulation of Y, Ba, La, and Eu in the Milky Way and a number of dSphs. As only empirical *r*-process predictions presently exist, assumptions about the stellar yields were made in order to account for the production of these elements in massive stars. The production of neutron-capture elements in intermediate-mass stars between 3 and 12 $M_\odot$ was not included in the chemical evolution models. Lanfranchi et al. (2008) found that a slow star formation rate and the presence of strong galactic winds, influences the abundances of neutron-capture elements in dSphs. In particular, lower enrichment of *r*-process elements by massive stars occurs in dSphs. The study of the Sagittarius dSph by McWilliam et al. (2013) attributes the high [La/Y] ratio observed to a 'leaky-box chemical evolution' where enriched material from low-metallicity, low-mass AGB stars can dominate if outflows remove material from Type II supernovae. Outflows of gas are more likely in lower mass galaxies as gravity is unable to retain the high-velocity supernovae ejecta. In contrast, the winds from AGB stars are low velocity and should be able to be retained by low-mass systems such as dSph galaxies and globular clusters.

[8] See Section 3.8 for a discussion of uncertainties in modelling AGB stars.

1.3. Aim and structure of this thesis

The aim of this thesis is to investigate the role AGB stars have had in the chemical enrichment of halo stars that were either accreted from dwarf galaxies or formed in-situ in the Galaxy. Through an analysis of potential chemical differences we seek to determine the extent to which the chemical properties of the surviving galaxies are similar to the satellite galaxies that were accreted long ago. With this analysis, we hope to reveal how environmental differences such as the star formation rate have influenced the observed abundance ratios. The sample compiled by Nissen & Schuster (2010) presents a unique opportunity to further investigate the chemical evolution of neutron-capture elements in dwarf galaxies and the Galactic halo through a comparison of the low- and high-α populations.

In order to understand the influence of AGB stars on the chemical enrichment of the low-α stars, we need to calculate detailed theoretical models of AGB stars at the metallicity of the low- and high-α population. We present stellar yields, including neutron-capture elements, for low- to intermediate-mass stars of $Z = 0.001$ ([Fe/H] = -1.2 using scaled-solar abundances), the mean metallicity of the Nissen & Schuster (2010) sample. Neutron-capture elemental yields for intermediate-mass models of this metallicity are presented for the first time in literature.

At the commencement of the research project, we were successful in receiving two nights on Magellan to observe a subset of the Nissen & Schuster (2010) sample. Until the data were obtained and reduced, we focussed on the calculation of the theoretical stellar models that would aid in the interpretation of the observational results. Additionally, these models will be extremely useful in studies of the chemical enrichment of globular clusters (e.g., Shingles et al. 2014) as well as comparisons to low-metallicity post-AGB stars (e.g., Fishlock et al. 2014a).

When calculating the intermediate-mass stellar models of 4 to 7 $M_{\odot}$, we noted that the surface C/O ratio decreases to below its initial value as a result of hot bottom burning (HBB) destroying C. Low-temperature opacities depend on the C/O ratio in the envelope and any changes in the composition as a result of stellar nucleosynthesis and mixing should be accounted for in the opacity (e.g., Ventura & Marigo 2009). The previous opacity treatment for the intermediate-mass models in the Mt Stromlo stellar evolutionary code did not include C/O values lower than the initial value. Therefore, the effects of HBB were not being accounted for in the low-temperature opacity treatment. We updated the stellar evolution code to include a low-temperature opacity treatment that follows the increases *and* decreases in the C/O ratio and the abundances of C, N, and O. The low-mass models that do not experience HBB are unaffected by this change in the opacity treatment. In Chapter 2, we investigate the effect that the updated opacity treatment has on the evolution and stellar yields of two intermediate-mass AGB stellar models of two different metallicities. We find the use of a low-temperature opacity treatment that follows the depletion and enhancement in the surface abundances of C, N, and O in intermediate-mass AGB stars is important in reducing the uncertainties in yield predictions. This chapter has been published as Fishlock et al. (2014b).

In Chapter 3, we present the results of the stellar models of 1 to 7 $M_\odot$ with $Z = 0.001$ ([Fe/H] $= -1.2$). The intermediate-mass models make use of the updated opacity treatment described in Chapter 2. We detail evolutionary properties, final surface abundances, and stellar net yields for each model. Additionally, we compare the final surface abundances of the low-mass models to the abundances observed in three Magellanic Cloud post-AGB stars of approximately the same metallicity. This chapter has been published as Fishlock et al. (2014a).

In Chapter 4, we present further details on the evolution and nucleosynthesis of the stellar models presented in Chapter 3. This chapter presents further results not discussed in Chapter 3 such as pre-AGB evolution. The pre-AGB phase dictates the stellar properties at the start of the AGB phase.

In Chapter 5, we present the results of extending the study of Nissen & Schuster (2010) and Nissen & Schuster (2011) by measuring abundances for Zr, La, Ce, Nd, Eu, and Sc using the differential analysis detailed in Nissen & Schuster (2010). For the first time, abundances of an *r*-process element, Eu, are determined for the low- and high-α populations. With these measurements, we aim to identify the rise of the *s*-process where the contribution of AGB stars starts to dominate over the *r*-process (Simmerer et al. 2004). This paper presenting the results of Chapter 5 is currently in preparation to be published.

We conclude with a summary drawing on the results of each chapter. We discuss future work that would further our understanding of how the Galactic halo formed through the accretion of dwarf galaxies. We also comment on how theoretical stellar models can be improved to provide insights into the origin and evolution of the elements.

CHAPTER 2

Molecular opacities and the evolution of intermediate-mass AGB stars

This chapter has been previously published as 'The effect of including molecular opacities of variable composition on the evolution of intermediate-mass AGB stars', Fishlock, C. K., Karakas, K. I., Stancliffe, S. J., 2014, MNRAS, 438, 1741. The work is presented here in an updated form.

Calculations from stellar evolutionary models of low- and intermediate-mass asymptotic giant branch (AGB) stars provide predictions of elemental abundances and yields for comparison to observations. However, there are many uncertainties that reduce the accuracy of these predictions. One such uncertainty involves the treatment of low-temperature molecular opacities that account for the surface abundance variations of C, N, and O. A number of prior calculations of intermediate-mass AGB stellar models that incorporate both efficient third dredge up and hot bottom burning include a molecular opacity treatment which does not consider the depletion of C and O due to hot bottom burning. Here we update the molecular opacity treatment and investigate the effect of this improvement on calculations of intermediate-mass AGB stellar models. We perform tests on two masses, 5 $M_{\odot}$ and 6 $M_{\odot}$, and two metallicities, $Z = 0.001$ and $Z = 0.02$, to quantify the variations between two opacity treatments. We find that several evolutionary properties are dependent on the opacity treatment including the mass-loss rate. Larger structural differences occur for the $Z = 0.001$ models compared to the $Z = 0.02$ models indicating that the opacity treatment has a more significant effect at lower metallicity. As a consequence of the structural changes, the predictions of isotopic yields are slightly affected. Despite this moderate effect, we conclude that it is more fitting to use variable molecular opacities for models undergoing hot bottom burning.

2.1. Introduction

The asymptotic giant branch (AGB) phase is the last nuclear burning stage for low- and intermediate-mass stars with initial masses of between approximately 0.8 $M_\odot$ to $\sim$ 8 $M_\odot$ (see Herwig 2005, for a review). During their evolution on the AGB, stars in this mass range experience mixing episodes that dredge up newly synthesised material which contains the products of He-burning and neutron-capture nucleosynthesis into the convective envelope (see Busso et al. 1999, for a review). Combined with strong mass loss that ejects the stellar envelope into the interstellar medium, low- and intermediate-mass AGB stars are important contributors to the chemical evolution of the Galaxy (for example, Romano et al. 2010; Kobayashi et al. 2011b; Recio-Blanco et al. 2012). This study is concerned with the evolution of intermediate-mass stars on the AGB with an initial mass $\gtrsim 4$ $M_\odot$. These stars produce substantial primary[1] nitrogen and are predicted to produce nitrogen enhanced metal poor stars in the early Galaxy (e.g. Pols et al. 2012). Intermediate-mass AGB stars are also implicated in the chemical evolution of globular clusters (Gratton et al. 2004; Ventura et al. 2011). However, the modelling of the evolution and nucleosynthesis of low- and intermediate-mass AGB stars is dependent on highly uncertain input physics including convection, mass loss, reaction rates and opacity.

AGB stars are an important site for the production of a number of light elements including lithium, carbon, nitrogen and fluorine as well as the elements heavier than iron produced by the slow neutron-capture process. Briefly, the structure of an AGB star consists of an electron-degenerate CO core surrounded by a He-burning shell and a H-burning shell which are separated by the He-intershell. This is encompassed by a deep convective envelope. During the thermally-pulsing AGB (TP-AGB) phase, the star undergoes periodic thermal pulses (TPs) due to instabilities in the He-burning shell (Herwig 2005; Busso et al. 1999). During the evolution of a TP-AGB star, two known mechanisms can occur which can periodically alter the surface composition: third dredge-up (TDU) and hot bottom burning (HBB). When the He-burning shell becomes unstable it drives an expansion of the star in order to release the energy generated by He-burning. A flash driven convection zone forms in the He-intershell mixing material, mainly ^{12}C, from the base of the He-shell throughout the intershell region. The outer layers have been cooled by the expansion and the H-burning shell has been almost extinguished which allows the outer convective envelope to move inwards. If the convective envelope reaches into the He-intershell, ^{12}C and *s*-process material are mixed to the surface. This process of TDU can occur multiple times and is responsible for creating carbon rich stars with a C/O ratio greater than unity.

HBB occurs in stars with masses greater than approximately 4 $M_\odot$ depending on metallicity and the input physics used. HBB takes place during the interpulse phase between TPs when the base of the outer convective envelope penetrates into the H-burning shell and becomes hot enough to sustain proton-capture nucleosynthesis. The CNO cycle converts ^{12}C and ^{16}O that has been mixed into the envelope by TDU into predominately ^{14}N. Therefore HBB can

[1] Primary elements can be synthesised from only H and He. Therefore the element does not depend on the initial composition of the star in which synthesis takes place.

prevent the stellar surface from becoming carbon rich by decreasing the ^{12}C abundance in the envelope. Frost et al. (1998) presented evolutionary calculations of intermediate-mass AGB stellar models and found that the surface C/O ratio initially decreases due to HBB. However mass loss slowly erodes the envelope causing a decrease in envelope mass. This results in a lower temperature at the base of the convective envelope which causes HBB to cease. There is also less dilution of the dredged-up material. This means that the C/O ratio starts to increase at the end of the TP-AGB phase, and in some cases to reach above unity.

The treatments of mass loss and convection have been shown to dominate modelling uncertainties in intermediate-mass AGB models (Ventura & D'Antona 2005a,b; Stancliffe & Jeffery 2007; Karakas et al. 2012). However, other uncertainties including reaction rates and opacities have been shown to affect the stellar structure and therefore the yields (Izzard et al. 2007; Ventura & Marigo 2009). In recent years there has been considerable work developing accurate low-temperature molecular opacities for stellar evolution calculations (Marigo & Aringer 2009). Due to these improvements to the opacity input physics it is now possible to quantify the effect of the updated opacities on the stellar evolution calculations and yield predictions (Ventura & Marigo 2009; Weiss & Ferguson 2009).

Intermediate-mass AGB stars have been shown to have effective temperatures cool enough for dust and molecule formation at solar metallicity and in the Magellanic Clouds (Garcia-Hernandez et al. 2009). In particular, we also show in this study that low-metallicity AGB stars become cool enough to form molecules particularly once they become carbon rich. The opacity tables of Alexander & Ferguson (1994), and later Ferguson et al. (2005), include a detailed treatment of the inclusion of molecules to the total opacity at low temperatures where $T \lesssim 10^4$ K. These tables, however, are only available for solar or scaled-solar composition. As previously mentioned, low- and intermediate-mass AGB stars undergo mixing episodes that alter their surface composition in a complex way. In particular, low-mass AGB stars can become carbon rich and intermediate-mass stars can display a range of behaviours for the C/O ratio. Marigo (2002) shows that at the transition point when the C/O ratio goes from below unity to above unity the dominant source of molecular opacity changes from oxygen-bearing molecules to carbon-bearing molecules. In AGB models, this causes a sudden decrease of the effective temperature and an expansion in radius which in turn increases the rate of mass loss. It is therefore necessary to use low-temperature molecular opacities that follow the change in the C/O ratio with time. The low-temperature opacity tables of Lederer & Aringer (2009) only account for an enhancement in C and N compared to initial abundances whereas the ÆSOPUS opacity tables of Marigo & Aringer (2009) are able to account for the depletion and enhancement of C, N, and the C/O ratio.

Using the ÆSOPUS molecular opacity tables, the effects of molecular opacities on the evolution of AGB stellar models have been investigated by Ventura & Marigo (2009) and Ventura & Marigo (2010). Using two different opacity treatments they determine that the yields of C, N, O and Na can be significantly altered depending on the opacity prescription used. Ventura & Marigo (2010) stress that it is important to use a molecular opacity treatment that accounts for variations in the surface CNO abundance when the C/O ratio exceeds unity. They find a minimum threshold mass for AGB stellar models ($\geq 3.5\,M_\odot$ for $Z = 0.001$)

where the use of opacity tables that account for the variations in the surface CNO abundance becomes less important. This is because HBB prevents the C/O ratio from exceeding unity for all their models with a mass greater than 3.5 $M_{\odot}$ rather than the models not being cool enough to form molecules. The models of Ventura & Marigo (2010) have a very efficient HBB owing to their choice of convective model, the Full Spectrum of Turbulence prescription (FST, Canuto & Mazzitelli 1991) and little TDU due to how they treat the convective borders.

As intermediate-mass AGB stars can experience both TDU and HBB, the complex interplay between the two processes can cause the star to become either oxygen rich or carbon rich. Stellar models calculated with different stellar evolution codes can display varied behaviours including differences in the efficiency of TDU and HBB which can alter the surface C/O ratio allowing for either carbon- or oxygen-rich compositions. This in turn means that the effect of the molecular opacities on the stellar evolution can vary greatly depending on model assumptions. In contrast, low-mass AGB stars only experience TDU which serves to increase the surface C/O ratio.

The aim of this paper is to expand upon the work of Ventura & Marigo using intermediate-mass AGB models that show a different evolution of the surface C/O ratio. In particular, our low-metallicity models show very deep dredge up and become carbon rich during the AGB phase in contrast to the models of, for example, Ventura & Marigo (2010). Therefore, their conclusions are not necessarily applicable to our models. In Section 2 we describe the method of calculation we use to model an AGB star and detail the molecular opacities used in the investigation. In Section 3 we present the results of the stellar models and in Section 4 we present the effect on the yields between the two opacity treatments. Section 5 we compare with previous studies and summarise our results.

2.2. Numerical method

A two step procedure is used to calculate each AGB stellar model. Firstly, we use the Mt Stromlo stellar evolutionary code (Karakas 2010, and references therein) to calculate the stellar evolutionary sequences. Each stellar model was evolved from the zero-age main sequence to near the end of the TP-AGB phase when the majority of the convective envelope is lost by strong stellar winds. For convective regions we use the standard mixing length theory (Böhm-Vitense 1958) with a mixing length parameter of $\alpha = 1.86$. The details of the procedure and the evolution code is described in Karakas (2010) with the following differences. We update the low-temperature molecular opacities (described in detail in Section 2.2.2) and the high-temperature radiative opacity tables. To be consistent with the molecular opacity tables, we use OPAL radiative tables (Iglesias & Rogers 1996) with a Lodders (2003) scaled-solar abundance. We do not include convective overshoot in the formal sense in order to obtain the third dredge-up. However we follow the method described by Lattanzio (1986) and Frost & Lattanzio (1996) to determine a neutral border to each convective boundary.

The calculated stellar evolutionary sequences are used as input into a post-processing nucleosynthesis code (see Cannon 1993; Lugaro et al. 2004). The nuclear network we use is

based on the JINA Reaclib[2] database as of May 2012 (Cyburt et al. 2010). It includes 589 reactions of 77 species from hydrogen to sulphur with a small group of iron-peak elements (Fe, Co, and Ni). An additional 'species' g is included in the network to account for the number of neutron captures occurring beyond ^{62}Ni; this g species simulates the s-process as a neutron sink. We use a scaled-solar initial composition from Asplund et al. (2009) and assume a solar global metallicity of $Z_{\odot} = 0.015$ which is comparable to the solar global metallicity recommended by Asplund et al. (2009) of $Z_{\odot} = 0.0142$. All abundance ratios are by number whereas individual species are in mass fraction. We assume the envelope abundances are equivalent to surface abundances.

2.2.1. Mass loss

Mass loss prior to the AGB phase is included using the Reimers (1975) formula with $\eta_R = 0.4$. This leads to very little mass being lost before the AGB phase. For example, the intermediate-mass models presented here lose less than 1 per cent of their initial mass before they reach the early AGB phase. Mass loss is included during the AGB phase using the Vassiliadis & Wood (1993) mass-loss prescription where only their equation 2 is used. The empirical formula of Vassiliadis & Wood (1993) was determined using a sample of oxygen- and carbon-rich AGB stars in the Milky Way and Magellanic Clouds which cover a range of luminosities and pulsation periods. In addition, the effective temperatures reached by intermediate-mass AGB models are on the order of $\log(T_{\rm eff}) \approx 3.45$ which is comparable to low-mass AGB models.

2.2.2. Molecular opacities

Bound-bound absorption by molecules becomes an important contribution to the total opacity at temperatures below 5000 K (Alexander & Ferguson 1994). The abundance of carbon relative to oxygen in the stellar envelope can significantly influence the formation of molecules and has a substantial effect on the opacity at low temperatures. Changes in the molecular opacity occur when the stellar envelope transitions from an oxygen-rich (C/O < 1) to a carbon-rich (C/O > 1) chemical composition (Marigo & Aringer 2009). This is due to the excess of carbon atoms allowing for the formation of carbon-bearing molecules such as, for example, HCN, CN, C_2 and SiC.

The intermediate-mass stellar models of Karakas et al. (2012) use low-temperature molecular opacity tables from Lederer & Aringer (2009) that account for only an increase in C due to TDU. For low-mass AGB stellar models that do not undergo HBB this method is sufficient as TDU will only increase the C abundance in the envelope. However, for intermediate-mass stars, CNO cycling during HBB causes a decrease in the C abundance (as well as the O abundance) in the envelope and it is possible that the C abundance will become lower than the initial C abundance. The subsequent decrease in O along with C can still cause the star to have a C/O ratio above unity. Current opacity tables used in Karakas et al. (2012) do

[2]https://groups.nscl.msu.edu/jina/reaclib/db/

Table 2.1 Values of f_i factors for the calculation of molecular opacity for the κ_C and κ_{CO} stellar models. The additional values included in the κ_{CO} treatment are shown in bold.

Z	X	$\log(f_{C/O})$	$\log(f_C)$	$\log(f_N)$	C/O
0.001	0.5	**−1.00**	**−1.00**	0.00	**0.050**
	0.6	**−0.35**	**−0.35**	0.60	**0.224**
	0.7	0.00	0.00	1.20	0.501
	0.8	0.17	0.17		0.741
		0.30	0.30		1.000
		0.35	0.35		1.122
		0.90	0.90		3.980
		1.55	1.55		17.779
		2.17	2.17		74.114
0.02	0.5	**−1.00**	**−1.00**	0.00	**0.050**
	0.6	**−0.35**	**−0.35**	0.60	**0.224**
	0.7	0.00	0.00	0.30	0.501
	0.8	0.17	0.17		0.741
		0.25	0.25		0.891
		0.30	0.30		1.000
		0.35	0.35		1.122
		0.50	0.50		1.585
		0.70	0.70		2.511

not account for this. In order to account for these variations we include low-temperature opacity tables to follow the decrease in C and O due to HBB.

For the stellar models presented here we use the ÆSOPUS low-temperature molecular opacity tables (Marigo & Aringer 2009) with a Lodders (2003) scaled-solar abundance. The low-temperature opacity tables have been calculated to follow the variations in the chemical composition of C, N and O in the envelope due to TDU and HBB. The tables use Rosseland mean opacities and are a function of temperature $\log(T)$ and $\log(R)$ where $R = \rho/(T/10^6\ \mathrm{K})^3$ for an arbitrary chemical composition (Marigo & Aringer 2009). We use tables with $\log(T)$ from 3.2 to 4.05 in steps of 0.05 dex and $\log(R)$ from −7.0 to 1.0 in steps of 0.5 dex.

To account for the changes in C, N and O in the envelope due to TDU and HBB, a variation factor f_i is used,

$$X_i = f_i X_{i,\mathrm{ref}}, \tag{2.1}$$

where X_i is the current abundance of species i in mass fraction and $X_{i,\mathrm{ref}}$ is the initial reference abundance of species i. A value of $f_i > 1$ indicates an enhancement in the abundance whereas $f_i < 1$ indicates a depletion in the abundance compared to the initial reference abundance. The increase (or decrease) in abundance for C, N and O can be described using the following equations from Ventura & Marigo (2009):

$$\left(\frac{X_C}{X_O}\right) = f_{C/O}\left(\frac{X_{C,\mathrm{ref}}}{X_{O,\mathrm{ref}}}\right), \tag{2.2}$$

$$X_C = f_C\, X_{C,\mathrm{ref}}, \tag{2.3}$$

$$X_N = f_N\, X_{N,\mathrm{ref}}. \tag{2.4}$$

The helium abundance is then given by $Y = 1 - X - Z$ so that the composition conserves mass where X is the hydrogen abundance and Z is the global metallicity.

We perform tests using two opacity treatments: one which only accounts for the increase in C (referred to as κ_{C}) and another where the increase and decrease in C and O are accounted for (referred to as κ_{CO}). We use the same scaled-solar *Æ*SOPUS opacity tables as Kamath et al. (2012) for the κ_{C} models (detailed in Table 2.1). In the κ_{CO} models we incorporate two additional variation factors for C and the C/O ratio and explicitly follow the envelope C/O ratio to account for a possible reduction in C and O abundances due to HBB for the κ_{CO} models (detailed in Table 2.1). The variations in abundance of N are treated the same for all models.

2.3. Stellar models

2.3.1. Stellar structure

We model two stellar masses, namely 5 $\mathrm{M}_\odot$ and 6 $\mathrm{M}_\odot$, with two metallicities, $Z = 0.001$ and $Z = 0.02$, to determine the effect of the two different opacity treatments, κ_{C} and κ_{CO}. All other input parameters in the stellar evolution code are kept to be the same so any differences in the stellar structure can be attributed to the different treatments of molecular opacity. There are negligible differences in the evolution of the stellar structure during the pre-AGB phase between the two opacity treatments and therefore only differences in the stellar models during the AGB phase will be discussed. Relevant properties of the stellar structure calculations for each of the models are summarised in Table 2.2 and includes the number of TPs calculated, final core mass (M_{core}) at the end of calculations, final envelope mass (M_{env}), maximum temperature reached at the base of the convective envelope ($T_{\mathrm{bce}}^{\mathrm{max}}$), and the total amount of material dredged-up due to TDU ($M_{\mathrm{dred}}^{\mathrm{tot}}$).

$Z = 0.001$ models

Figure 2.1(a) shows the evolution of the H-exhausted core with time for the 5 $\mathrm{M}_\odot$, $Z = 0.001$ model. The H-exhausted core mass at the beginning of the TP-AGB phase is slightly higher for the κ_{C} models, around 0.001 $\mathrm{M}_\odot$ for the 5 $\mathrm{M}_\odot$ model. This can be attributed to minor differences during core He-burning evolution. It can be seen that the updated opacity treatment κ_{CO} reduces the number of TPs during the AGB phase for the $Z = 0.001$ models.

Table 2.2 Properties of the calculated stellar models.

Opacity[a]	Mass[b] ($M_\odot$)	Z[c]	TPs[d]	Final M_{core}[e] ($M_\odot$)	Final M_{env}[f] ($M_\odot$)	T_{bce}^{max}[g] ($\times 10^6$ K)	M_{dred}^{tot}[h] ($M_\odot$)
κ_C	5.0	0.001	108	0.940	0.960	92.99	0.216
	6.0	0.001	126	1.018	0.888	104.91	0.127
	5.0	0.02	30	0.868	0.713	63.29	0.088
	6.0	0.02	41	0.907	1.084	81.59	0.090
κ_{CO}	5.0	0.001	96	0.938	1.035	92.47	0.192
	6.0	0.001	112	1.015	0.662	104.79	0.107
	5.0	0.02	29	0.867	1.013	63.95	0.083
	6.0	0.02	42	0.908	1.352	82.30	0.092

[a] Opacity treatment [b] Initial mass [c] Initial global metallicity [d] Number of TPs calculated [e] Final core mass [f] Final envelope mass [g] Maximum temperature reached at the base of the convective envelope [h] Total amount of material dredged up as a result of TDU

The 5 $M_\odot$, $Z = 0.001$ κ_{CO} model has 12 fewer TPs while the 6 $M_\odot$, $Z = 0.001$ κ_{CO} model has 14 fewer TPs when compared to the κ_C models. This means that less enriched material is dredged up to the surface as demonstrated in Table 2.2 where the total amount of He-intershell material decreases by around 15 per cent for the κ_{CO} models. The $Z = 0.001$ κ_C models each dredge up approximately 0.02 $M_\odot$ more material over the lifetime of the AGB phase compared to the κ_{CO} models.

The evolution of the temperature at the base of the convective envelope for each model is shown in Figure 2.2. HBB is evident as the temperature reaches higher than the $(50 - 80) \times 10^6$ K required for CNO cycling at the base of the convective envelope. Figure 2.2 for the $Z = 0.001$ models shows that, when using the updated opacity tables κ_{CO}, HBB is extinguished earlier. This is because the κ_{CO} models become more extended in radius and therefore cooler. This change due to the increased molecular opacity leads to an enhanced mass-loss rate which ejects the envelope sooner.

Figures 2.3(a) and 2.3(c) compare the evolution of the C/O ratio between the two opacity treatments for both $Z = 0.001$ models. For a period during the AGB phase, the competing effects of TDU and HBB can cause the C/O ratio to fluctuate between below unity and above unity. For a brief time during this period the ^{12}C surface abundance is below the initial ^{12}C surface abundance while the C/O ratio is greater than unity. The molecular opacity is then underestimated in the κ_C model as the fact that the C/O ratio exceeds unity has not been taken into account during these conditions. This omission in the determination of the opacity results in the discrepancies seen in the stellar evolution between the κ_C and κ_{CO} models in Figure 2.4. Figure 2.4 shows the temporal evolution of the C/O ratio, ^{12}C surface abundance, ^{16}O surface abundance, effective temperature and mass-loss rate for the 5 $M_\odot$, $Z = 0.001$ models.

As mentioned by Marigo (2002), the consequences of using opacity tables that do not correctly follow the variation of the C/O ratio when the star is carbon rich include an

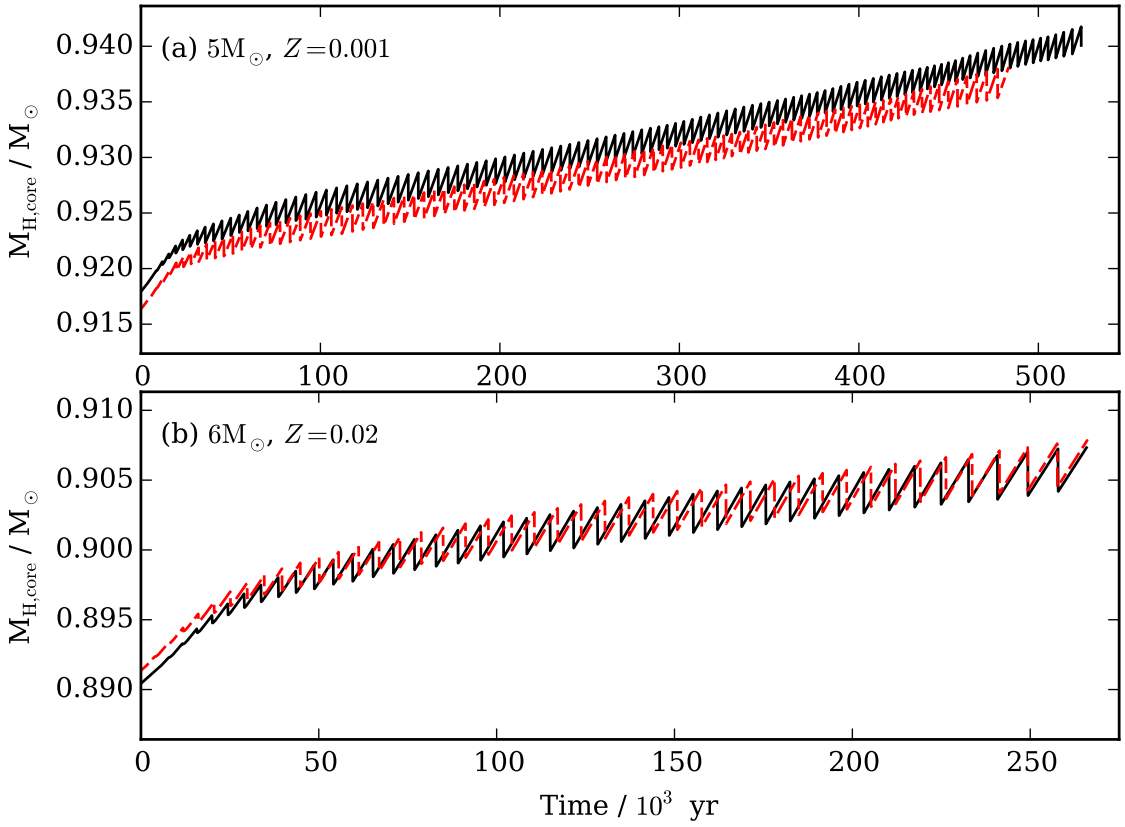

Figure 2.1 Evolution of the H-exhausted core ($M_{\rm H,core}$) from the start of the TP-AGB phase (t = 0) for two of the stellar models calculated. The solid (black) lines show the $\kappa_{\rm C}$ models while the dashed (red) lines show the $\kappa_{\rm CO}$ models.

inaccurate effective temperature. Figure 2.4 shows that the difference between the $\kappa_{\rm C}$ and $\kappa_{\rm CO}$ models is not due to a slightly different core mass at the beginning of the TP-AGB phase. The lower effective temperature (Figure 2.4(d)) and higher mass-loss rate (Figure 2.4(e)) for the $\kappa_{\rm CO}$ models starts to become significant when the surface C/O ratio for the models changes from below unity to above. This is where the $\kappa_{\rm CO}$ molecular opacity treatment more realistically follows the increase in the C/O ratio.

Z = 0.02 models

The effect of the different opacity treatment on the number of TPs is less pronounced for the Z = 0.02 models than for the Z = 0.001 models. Figure 2.1(b) shows that the difference in the evolution of the mass of the hydrogen exhausted core between the two opacity treatments is very slight for the 6 M$_\odot$ model. The differences between the two opacity treatments are minimal and the C/O ratio of the models does not exceed unity which would result in a higher molecular opacity where carbon-bearing molecules dominate. Compared to the Z = 0.001 models, there are fewer TPs with a shorter lifetime of the TP-AGB phase. The 5 M$_\odot$ $\kappa_{\rm CO}$ model experiences one less TP while the 6 M$_\odot$ $\kappa_{\rm CO}$ model experiences one more TP than the $\kappa_{\rm C}$ models. We conclude that the differences in the number of TPs are insignificant.

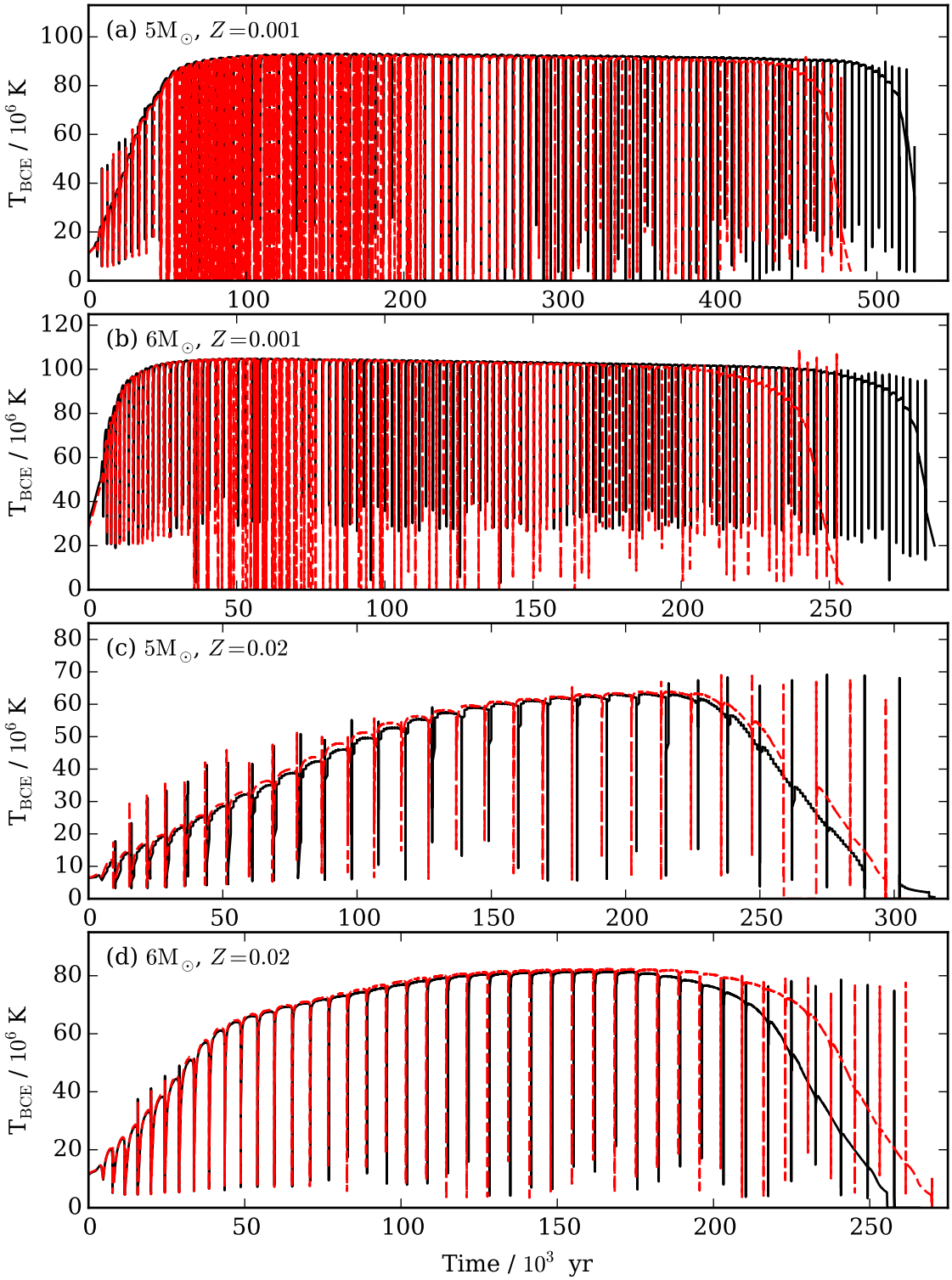

Figure 2.2 Evolution of the temperature at the base of the convective envelope from the start of the TP-AGB phase (t = 0) for each stellar model calculated. The solid (black) lines show the $\kappa_{\rm C}$ models while the dashed (red) lines show the $\kappa_{\rm CO}$ models.

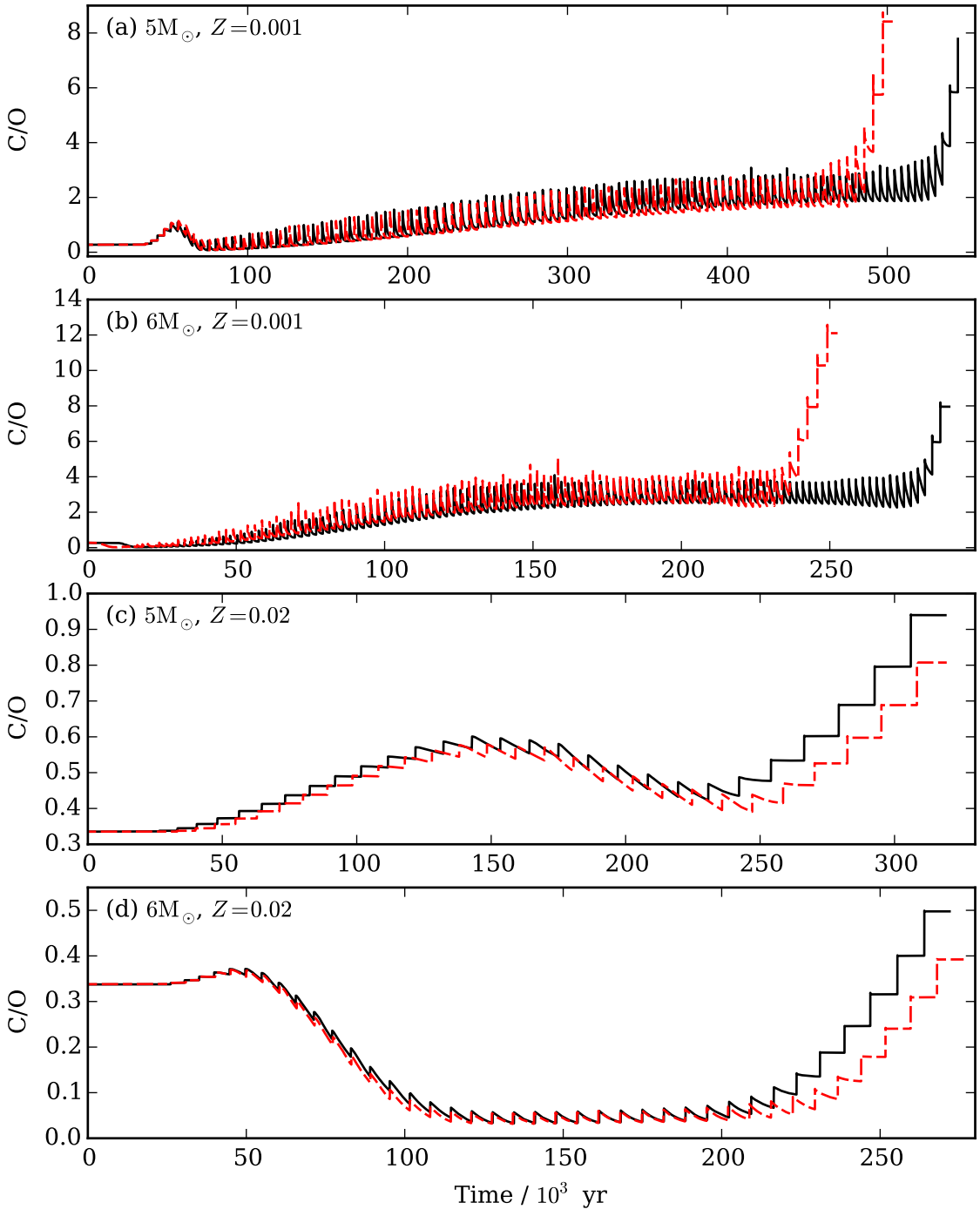

Figure 2.3 The variation in the C/O ratio with time for each of the stellar models calculated from the start of the TP-AGB phase (t = 0). The solid (black) lines show the κ_C models while the dashed (red) lines show the κ_{CO} models.

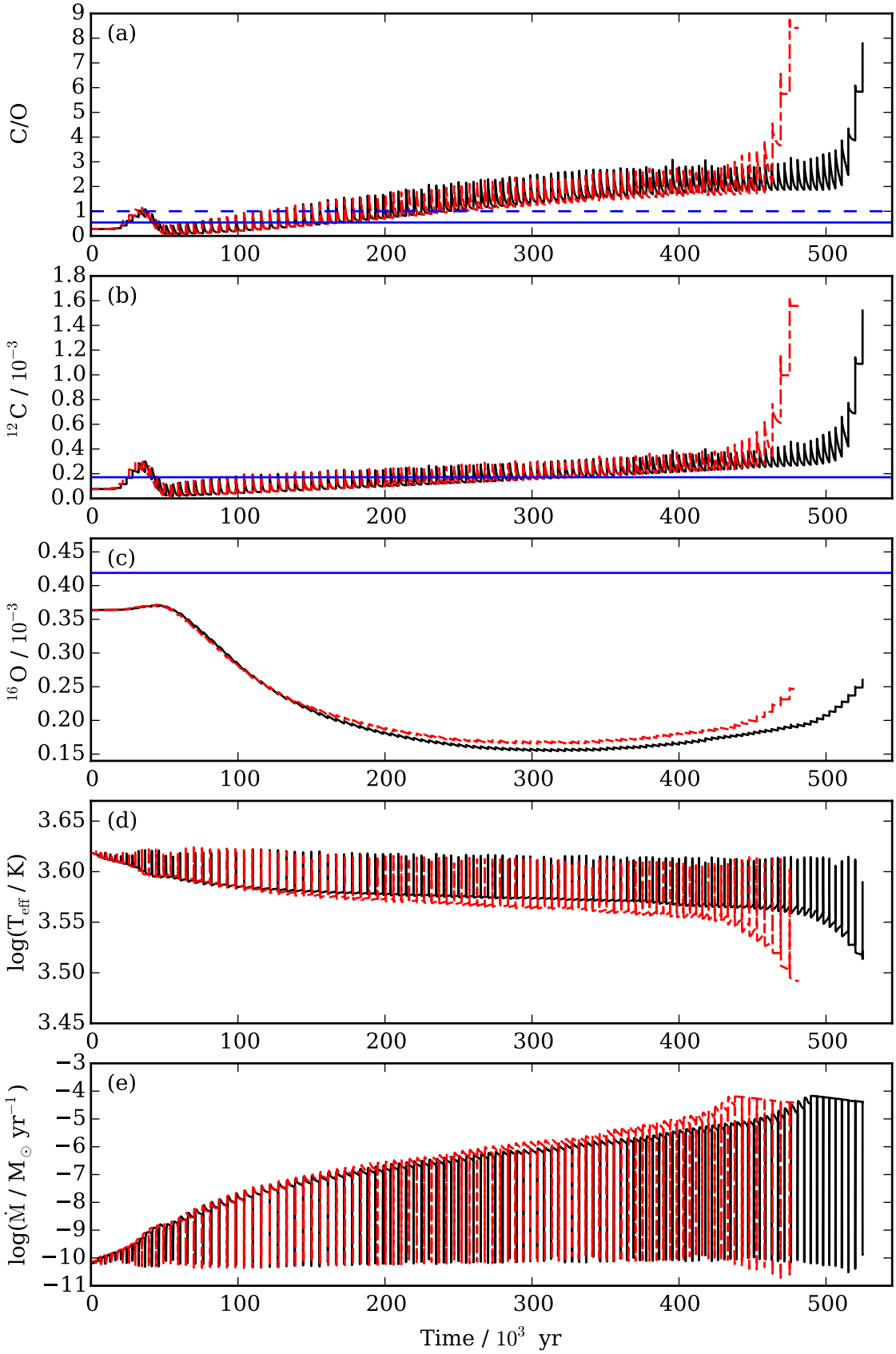

Figure 2.4 The 5 $M_\odot$, $Z = 0.001$ stellar model showing the variation in (*a*) C/O, (*b*) ^{12}C surface abundance, (*c*) ^{16}O surface abundance, (*d*) $\log_{10}(T_{\rm eff})$, and (*e*) $\log_{10}(\dot{M})$ with time from the start of the TP-AGB phase ($t = 0$). The dashed (blue) line shows a C/O ratio of unity while the solid (blue) lines show the initial ^{12}C and ^{16}O abundance.

Figure 2.5 shows the evolution of the C/O ratio, ^{12}C surface abundance, ^{16}O surface abundance, effective temperature and mass-loss rate for the TP-AGB phase for the 6 $M_\odot$ model. Pre-AGB evolution mixing episodes cause the surface ^{12}C and ^{16}O abundances to decrease below initial values. This causes the C/O ratio to decrease with the C/O ratio being below the initial value at the start of the TP-AGB phase. HBB is only active for part of the TP-AGB evolution in the 6 $M_\odot$, $Z = 0.02$ models. This is illustrated in Figure 2.5(a) where the C/O ratio initially increases, albeit with a shallow gradient and then decreases once the temperature at the base of the envelope becomes hot enough for proton captures onto ^{12}C. Eventually HBB is extinguished and the C/O ratio increases to almost unity owing to the continuation of TDU. It is when HBB is active that the κ_C model does not accurately follow the variation of the C and O abundance as only the increase in the ^{12}C abundance is taken into account.

For the κ_C 6 $M_\odot$ model this situation where the current C/O, C, and O abundances are never greater than the initial abundances is treated as if the surface abundance has a scaled-solar composition. The opacity does not vary for a given temperature and density with the variation factors being $f_C = f_O = 0$. Figure 2.6 shows the opacity below $\log(T) \lesssim 4$ in the 6 $M_\odot$ κ_C and κ_{CO} models for the same total stellar mass of approximately 2.3 $M_\odot$. This snapshot was chosen where the opacity difference is largest. At $\log(T) \lesssim 3.5$ near the stellar surface, the opacity is lower for the κ_{CO} model compared to the κ_C model. This decrease in opacity leads to a higher effective temperature (as seen in the bottom panel of Figure 2.5) and as a consequence the mass-loss rate is lower and HBB ceases slightly later. The sustained level of HBB causes a lower final C/O ratio compared to the κ_C models as seen in Figure 2.5(a).

2.3.2. Stellar yields

In order to determine the total amount of material ejected into the interstellar medium during the lifetime of the stellar model, we calculate the yield to be,

$$M_i = \int_0^\tau [X(i) - X_0(i)] \frac{dM}{dt} dt, \tag{2.5}$$

where M_i is the yield of species i in solar masses, dM/dt is the current mass-loss rate in $M_\odot$ yr^{-1}, $X(i)$ and $X_0(i)$ are the current and initial mass fraction of species i, and τ is the total lifetime of the stellar model in years. After calculating the stellar yields we calculate the percentage change for each stable isotope where $M_{i,C}$ is the yield for species i using the κ_C models and $M_{i,CO}$ is the yield for species i using the κ_{CO} models. The percentage change in yields between the κ_C and κ_{CO} models for each mass and metallicity is shown in Figure 2.7. The changes in surface abundance, and consequently the final net yield, are dependent on the amount of material dredged up from the He-intershell as well as the maximum temperature and duration of HBB. Yields for selected isotopes are presented in Table 2.3 for the two opacity treatments, κ_C and κ_{CO}.

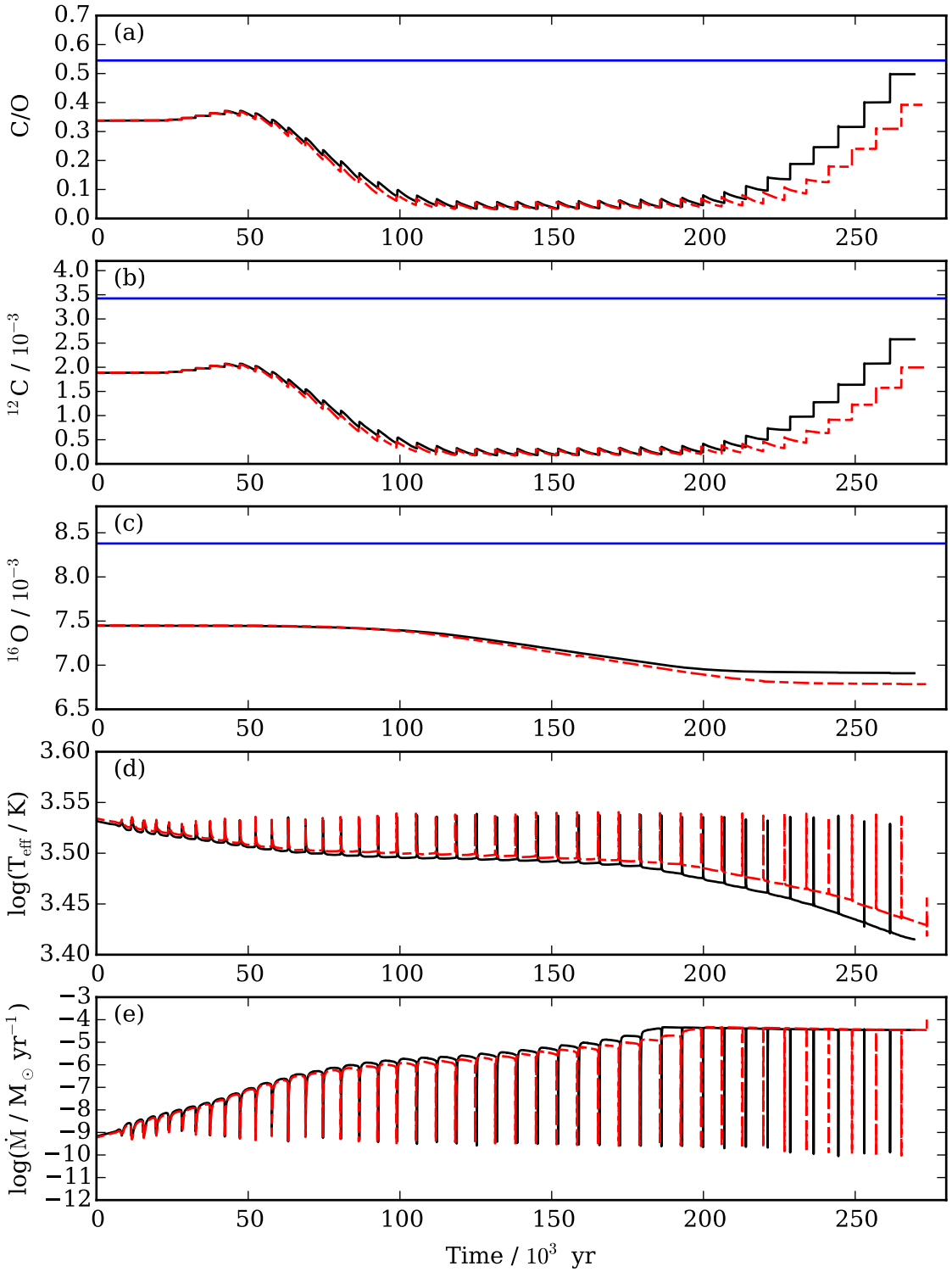

Figure 2.5 The 6 $M_\odot$, $Z = 0.02$ stellar model showing the variation in (*a*) C/O, (*b*) ^{12}C surface abundance, (*c*) ^{16}O surface abundance, (*d*) $\log_{10}(T_{\rm eff})$, and (*e*) $\log_{10}(\dot{M})$ with time from the start of the TP-AGB phase ($t = 0$). The solid (blue) lines show the initial ^{12}C and ^{16}O mass fraction.

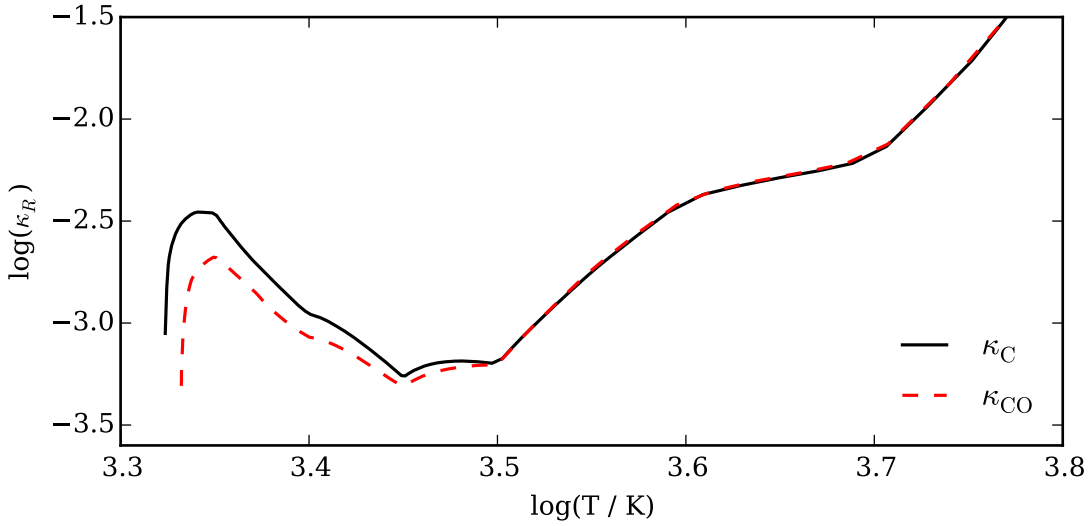

Figure 2.6 The difference in opacity κ_R between the 6 $M_\odot$, $Z = 0.02$ κ_C (solid black line) and κ_{CO} (dashed red line) models for the same total mass (approximately 2.3 $M_\odot$). The opacity is noticeably different for $\log(T) \lesssim 3.5$ near the stellar surface between the two opacity treatments.

Z = 0.001 yields

Figures 2.7(a) and 2.7(c) show that the 5 $M_\odot$ and 6 $M_\odot$, $Z = 0.001$ models display a similar trend in yield differences between the two opacity treatments, κ_C and κ_{CO}. The reduced number of TDU episodes for the κ_{CO} influences the changes seen in the yields. A higher percentage change is seen in the yields for the 6 $M_\odot$ model compared to the 5 $M_\odot$ model. This is caused by a larger decrease in the number of TPs as well as the duration of HBB between the κ_C and κ_{CO} models.

The isotopes ^{12}C and ^{16}O are produced in the intershell region through partial He-burning and are brought to the surface by repeated TDU. During the interpulse period, HBB produces ^{14}N at the expense of ^{12}C and ^{16}O. Due to a shorter period of HBB for the κ_{CO} models, the ^{12}C yield is higher despite these models dredging up less material (see Table 2.2). Therefore the ^{14}N yield is also lower for the κ_{CO} models for the same reason. The majority of ^{13}C is produced during HBB through the CN cycle before being destroyed via the ^{13}C(p,γ)^{14}N reaction. The ^{13}C yield decreases for the κ_{CO} models due to a shorter period of HBB combined with a slightly lower temperature at the base of the convective envelope. Even though ^{16}O is being dredged up to the surface the amount is much less than ^{12}C as the intershell composition comprises of $\lesssim 1$ per cent ^{16}O and around 25 per cent ^{12}C. The majority of the ^{16}O is destroyed through HBB and the net yield of ^{16}O is negative for both opacity treatments.

The isotope ^{22}Ne is produced in the intershell via α-captures onto ^{14}N. The amount of ^{22}Ne mixed into the envelope affects the yields of isotopes in the Ne-Na chain. For example, ^{23}Na is formed by proton captures onto ^{22}Ne. As the κ_{CO} models experience fewer TDU episodes, the yields of ^{22}Ne and ^{23}Na are lower than for the κ_C models by around 20 per cent each for the 5 $M_\odot$ model. For the 6 $M_\odot$ κ_{CO} model the yield of ^{22}Ne is lower by around

20 per cent and for ^{23}Na, the yield decreases by around 60 per cent as seen in Figure 2.7. The isotopes ^{25}Mg and ^{26}Mg are produced through the ^{22}Ne(α,n)^{25}Mg and ^{22}Ne(α,γ)^{26}Mg reactions which are activated at temperatures above 3×10^8 K. These conditions occur during the convective region that develops during a TP.

Less synthesised ^{25}Mg and ^{26}Mg reaches the surface for the $\kappa_{\rm CO}$ models resulting in lower yields with an approximately 10 to 30 per cent decrease compared to the $\kappa_{\rm C}$ models. Any change in the abundance of the iron group isotopes is due to neutron-capture through the *s*-process. The isotope ^{56}Fe is used as a seed for the *s*-process during a convective TP where neutrons are released by the ^{22}Ne(α,n)^{25}Mg reaction. Any neutron captures onto ^{56}Fe or isotopes heavier than ^{56}Fe are accounted for by the neutron sink g. Therefore g can be thought of as the sum of abundances for the *s*-process isotopes. For the $\kappa_{\rm CO}$ models the yield of the neutron sink g is lower for the $\kappa_{\rm CO}$ models compared to the $\kappa_{\rm C}$ models. These yield changes can all be attributed to the reduced number of TDU episodes.

Z = 0.02 yields

In Figures 2.7(b) and 2.7(d) we show the percentage change in yields for the $Z = 0.02$ models. From this figure we can see that the relative size of the yield changes between the $\kappa_{\rm C}$ and $\kappa_{\rm CO}$ models are smaller than for the $Z = 0.001$ model. This is mainly because the $\kappa_{\rm C}$ and $\kappa_{\rm CO}$ models experience almost the same number of TPs (as shown in Table 2.2). In Table 2.3 we see that the ^{12}C yields of the 5 $M_\odot$ models are positive compared to the negative ^{12}C yields of the 6 $M_\odot$ models. This indicates that there is an overall net production of carbon in the 5 $M_\odot$ models. While the amount of material dredged into the envelope is similar in both the 5 $M_\odot$ and 6 $M_\odot$ models (e.g., see Table 2.2), the maximum temperature at the base of the envelope in the 5 $M_\odot$ is considerably lower. This means that HBB is not very efficient in the 5 $M_\odot$ as shown in Figure 2.2, where the maximum temperature is only 64×10^6 K and this temperature is only sustained for about 5 TPs. This means that the carbon dredged to the surface is not as efficiently burnt via the CNO cycles at the base of the envelope.

However, both $\kappa_{\rm CO}$ models have a decrease in the ^{12}C yields compared to the $\kappa_{\rm C}$ models. This can be attributed to the longer duration, as well the higher temperatures, of HBB. This is despite the slight differences in the number of TDU episodes. The negative yield of ^{16}O indicates that more is being destroyed through HBB than being mixed from the intershell region to the surface. The longer duration of HBB also explains the increase in the ^{14}N yield as more ^{12}C is burnt to produce ^{14}N via the CNO cycles.

In summary, as shown in Figure 2.7, we find yield differences of up to 20 per cent for lighter isotopes with atomic mass up to about 18 including the CNO isotopes. For ^{19}F we found a difference of around 15 per cent for the 6 $M_\odot$ model with a smaller difference for the 5 $M_\odot$ model. For the intermediate-mass isotopes, which include here ^{22}Ne, ^{23}Na, ^{25}M, ^{26}Mg and ^{26}Al^g we found very small yield differences of less than 10 per cent for both the 5 $M_\odot$ and 6 $M_\odot$ models as illustrated in Figure 2.7. There is a negligible effect on the net yield of the neutron sink g with a percentage change of less than 5 per cent.

Table 2.3 Net yields of selected isotopes for each model.

Op.	Mass	Z	^{12}C	^{13}C	^{14}N	^{16}O	^{22}Ne	^{23}Na	^{25}Mg	^{26}Mg	g
$\kappa_{\rm C}$	5.0	0.001	1.652(−3)	5.718(−4)	5.715(−2)	−8.273(−4)	1.845(−3)	4.725(−5)	3.399(−4)	2.866(−4)	1.793(−6)
	6.0	0.001	9.784(−4)	4.298(−4)	3.806(−2)	−1.547(−3)	5.404(−4)	6.487(−6)	2.197(−4)	1.279(−4)	1.241(−6)
	5.0	0.02	1.864(−3)	3.476(−3)	1.971(−2)	−2.831(−3)	1.720(−3)	9.558(−5)	1.563(−4)	8.990(−5)	8.321(−7)
	6.0	0.02	−1.112(−2)	5.849(−4)	4.305(−2)	−7.224(−3)	1.637(−3)	1.350(−4)	2.039(−4)	1.248(−4)	1.268(−6)
$\kappa_{\rm CO}$	5.0	0.001	2.101(−3)	5.447(−4)	5.030(−2)	−8.422(−4)	1.495(−3)	3.763(−5)	2.991(−4)	2.292(−4)	1.473(−6)
	6.0	0.001	1.309(−3)	3.877(−4)	3.091(−2)	−1.621(−3)	4.166(−4)	2.717(−6)	1.989(−4)	8.397(−5)	8.665(−7)
	5.0	0.02	3.780(−4)	3.238(−3)	2.156(−2)	−2.862(−3)	1.691(−3)	9.566(−5)	1.512(−4)	8.759(−5)	8.183(−7)
	6.0	0.02	−1.207(−2)	5.589(−4)	4.509(−2)	−7.817(−3)	1.665(−3)	1.332(−4)	2.281(−4)	1.239(−4)	1.304(−6)

NB. – Yields are in solar masses and are expressed in the form $n(m) = n \times 10^m$.

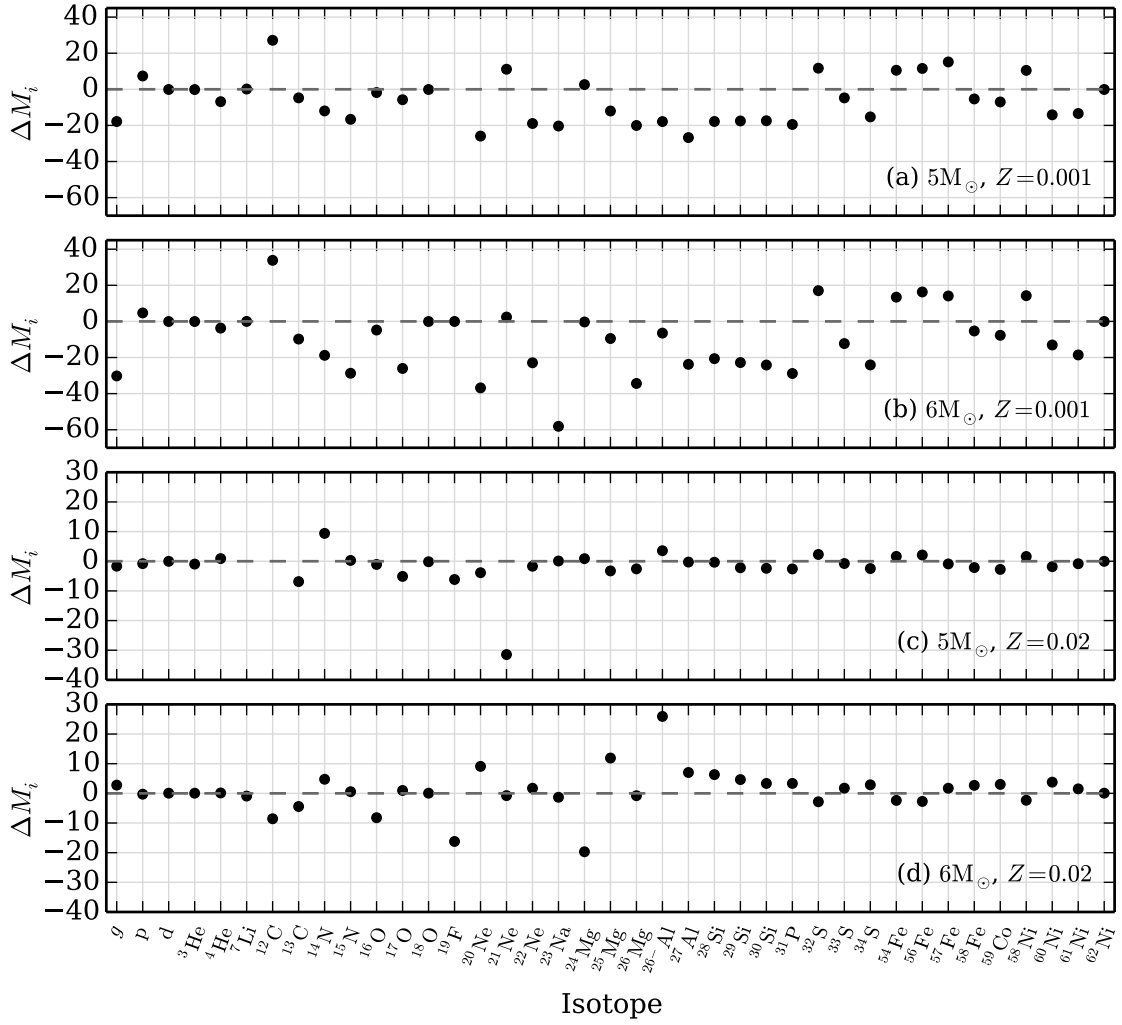

Figure 2.7 The percentage change in yield for species *i* between the κ_C and κ_{CO} models for each model calculated where $\Delta M_i = 100(M_{i,CO} - M_{i,C})/|M_{i,C}|$. For the 5 $M_\odot$, $Z = 0.001$ model the percentage change for ^{19}F is not shown. For the κ_{CO} model, the ^{19}F yield decreases by around 250 per cent. For the 5 $M_\odot$, $Z = 0.02$ models the percentage change in ^{7}Li and ^{12}C is not shown. For the κ_{CO} model the yield of ^{7}Li decreases by around 100 per cent while the yield of ^{12}C decreases by around 80 per cent compared to the κ_C model. Each plot has the same *y*-axis scale for each metallicity for ease of comparison.

2.4. Discussion and conclusions

The demand for accurate AGB models requires a more thorough understanding of the uncertainties in the input physics which play a role in determining the stellar evolution of AGB stars. We present new detailed evolutionary models of two masses, 5 $M_\odot$ and 6 $M_\odot$, and two metallicities, $Z = 0.001$ and $Z = 0.02$. These models are used to investigate the uncertainties in the stellar evolution when using two differing molecular opacity treatments, κ_C and κ_{CO}, as well as investigating the effects of differing molecular opacity on mass and metallicity. We determine that the AGB lifetime for the lower metallicity models is affected by the choice of the molecular opacity prescription. The increased molecular opacity has the effect of lowering the effective temperature in the low-metallicity AGB models which, in turn, has the consequence of increasing the mass-loss rate. This consequence is confirmed

by Marigo (2002) where the increase in the mass-loss rate due to increased molecular opacity serves to better explain the presence of carbon-rich stars in a population of Galactic giant stars. In addition, previous studies by Ventura & Marigo (2009) and Ventura & Marigo (2010) highlight the importance of using variable abundance molecular opacities only if the C/O ratio exceeds unity. For low-mass AGB models where HBB does not occur it is sufficient for the molecular opacity to only follow the increase in carbon due to TDU as with the $\kappa_{\rm C}$ opacity tables.

Previous studies such as the stellar models by Karakas et al. (2012) calculate the evolution of intermediate-mass AGB stars using the Mt Stromlo stellar evolutionary code but utilise opacity tables that only account for an increase in carbon due to TDU. This situation has been modelled here using the $\kappa_{\rm C}$ opacity tables. For the case when the surface C/O ratio does not exceed the initial C/O ratio, the $\kappa_{\rm C}$ opacity is calculated as if scaled-solar opacity tables had been used. The $\kappa_{\rm CO}$ opacity tables are able to interpolate between lower values and as a consequence of the decreased opacity the stellar structure is affected. The 6 $M_{\odot}$, $Z = 0.02$ model suffers from this omission of lower values below the scaled-solar composition in the low-temperature molecular opacity tables. However, as mentioned by Marigo (2007), the evolution depends on the sensitivity of the mass-loss prescription to the effective temperature.

The studies by Stancliffe et al. (2004) and Pignatari et al. (2013) calculate $Z = 0.02$ intermediate-mass AGB models which experience efficient TDU. Our study finds that with efficient TDU the surface C/O ratio for the low-metallicity models can exceed unity even with the presence of efficient HBB. The study by Herwig (2004a) of $Z = 0.0001$ intermediate-mass AGB models also finds efficient TDU where the C/O ratio exceeds unity for periods of time despite efficient HBB. This is in contrast to Ventura & Marigo (2010) who find a threshold at $M \geq 3.5$ $M_{\odot}$ for a metallicity of $Z = 0.001$ where, above this mass limit, the final C/O ratio of the models does not exceed unity. However, the Ventura & Marigo models use an α-enhanced composition and this could affect the ability of the models to become carbon rich.

In addition, we investigate the effect of the two different molecular opacity treatments on the stellar yield predictions for 77 species. As illustrated in Figure 2.7 the low-metallicity models that the net yields are affected by changes in the stellar evolution due to opacity. The changes in the net yields of the $Z = 0.02$ models are negligible when using the updated $\kappa_{\rm CO}$ opacity treatment. This result indicates the possibility that the changes in yield could be more considerable at a lower metallicity than $Z = 0.001$. The $Z = 0.001$ models of Marigo (2007) utilise synthetic TP-AGB models to investigate the effects of variable molecular opacity tables. Marigo (2007) concludes that the use of variable molecular opacities should not considerably affect the stellar yields in massive AGB models with $Z \leq 0.001$ as effective temperatures may be so high that the molecules cannot form. We do not find this to be the case for our models as the effective temperatures are comparable to low-mass AGB models at the same metallicity.

The treatment of molecular opacity along with other input physics such as the choice of the mass-loss rate, reaction rates and treatment of convection all contribute to the uncertainty

in AGB models. These uncertainties can have a larger effect at $Z = 0.02$ when compared to the opacity treatment. Ventura & D'Antona (2005a) investigate the effect of the treatment of convection on a 5 $M_\odot$, $Z = 0.001$ model. They find that the yields strongly depend on the convection model used with significant yield differences between MLT and FST. A previous study on the choice of mass-loss prescription by Stancliffe & Jeffery (2007) finds yield changes of around 15 to 80 per cent for the light elements when investigating the effect on the yields for a 1.5 $M_\odot$, $Z = 0.008$ model. These differences are comparable to the results presented in this paper for the $Z = 0.001$ models. The investigation on mass loss by Karakas et al. (2006) finds yield changes of up to 90 per cent for a 5 $M_\odot$, $Z = 0.0001$ model. When looking at uncertainties in reaction rates for the Ne-Na and Mg-Al chains, Izzard et al. (2007) find variations of up to two orders of magnitude for some species in the synthetic models. The models of Karakas et al. (2006) find maximum yield differences up to 350 per cent when looking at different ^{22}Ne + α reaction rates for a 5 $M_\odot$, $Z = 0.02$ model using the Reimers (1975) mass-loss prescription which is different to that used in this study. The yield differences due to reaction rate uncertainties are significantly higher when compared to uncertainties found here due to the treatment of molecular opacities. However, with all these sources of inaccuracies, mass loss and convection are thought to dominate the uncertainties in stellar modelling.

One use of stellar models is to provide theoretical predictions of chemical yields for comparison to observational data. Chemical yields are incorporated into chemical evolution models in order to understand the contribution of stellar populations to, for example, the Galaxy or globular clusters (Kobayashi et al. 2011b; Cescutti et al. 2012). We have shown that the yields of intermediate-mass AGB stars can be affected by the treatment of molecular opacity in quite a complex way with changes of up to 20 per cent for most isotopes. These results also show that the degree of the difference depends on mass and metallicity. Therefore it is more suitable to update current stellar models that experience HBB and become carbon rich to include molecular opacity tables that account for the changes in the surface abundances of C and O, as well as N, due to the CNO cycle that occurs during HBB.

CHAPTER 3

Evolution and nucleosynthesis of AGB stellar models of low metallicity

This chapter has been previously published as 'Evolution and nucleosynthesis of asymptotic giant branch stellar models of low metallicity', Fishlock, C. K., Karakas, K. I., Lugaro, M., Yong, D., 2014, ApJ, 797, 44. The work is presented here in an updated form.

We present stellar evolutionary tracks and nucleosynthetic predictions for a grid of stellar models of low- and intermediate-mass asymptotic giant branch (AGB) stars at $Z = 0.001$ ([Fe/H] = -1.2). The models cover an initial mass range from 1 $M_\odot$ to 7 $M_\odot$. Final surface abundances and stellar yields are calculated for all elements from hydrogen to bismuth as well as isotopes up to the iron group. We present the first study of neutron-capture nucleosynthesis in intermediate-mass AGB models, including a super-AGB model, of [Fe/H] = -1.2. We examine in detail a low-mass AGB model of 2 $M_\odot$ where the $^{13}C(\alpha,n)^{16}O$ reaction is the main source of neutrons. We also examine an intermediate-mass AGB model of 5 $M_\odot$ where intershell temperatures are high enough to activate the ^{22}Ne neutron source, which produces high neutron densities up to $\sim 10^{14}$ n cm^{-3}. Hot bottom burning is activated in models with $M \geq 3$ $M_\odot$. With the 3 $M_\odot$ model we investigate the effect of varying the extent in mass of the region where protons are mixed from the envelope into the intershell at the deepest extent of each third dredge-up. We compare the results of the low-mass models to three post-AGB stars with a metallicity of [Fe/H] $\simeq -1.2$. The composition is a good match to the predicted neutron-capture abundances except for Pb and we confirm that the observed Pb abundances are lower than what is calculated by AGB models.

3.1. Introduction

Stars with an initial mass of between ~0.8 and ~8 $M_\odot$, depending on initial metallicity, evolve through the asymptotic giant branch (AGB) phase. This is the last stage of nuclear burning for these stars (for a review, see Herwig 2005; Straniero et al. 2006; Karakas & Lattanzio 2014). AGB stars are an observationally confirmed site for the *slow* neutron-capture process (the *s*-process, e.g. Abia et al. 2001), which is responsible for the production of around half of the abundance of the heavy elements beyond Fe (Gallino et al. 1998). AGB stars also produce a number of light elements such as lithium (e.g., Ventura & D'Antona 2010), carbon (e.g., Izzard et al. 2009), fluorine (e.g., Abia et al. 2010; Recio-Blanco et al. 2012), and nitrogen (e.g., Johnson et al. 2007). Through nucleosynthesis and strong mass loss, AGB stars contribute to the chemical evolution of galaxies (Meléndez & Cohen 2007; Romano et al. 2010; Letarte et al. 2010; Kobayashi et al. 2011b) as well as globular clusters (Ventura & D'Antona 2008; Meléndez & Cohen 2009; Marino et al. 2011).

The stellar structure of an AGB star consists of an electron degenerate CO core surrounded by a He-burning shell and a H-burning shell. These shells are separated by the He-intershell which consists of approximately 75% ^{4}He, 22% ^{12}C, and 2% ^{16}O left over from partial He-burning. Surrounding the H-exhausted core (hereafter core) is a large convective envelope. Neutron-capture nucleosynthesis via the *s*-process takes place in the He-intershell where the abundance of ^{4}He is high and (α,n) reactions can be efficiently activated releasing free neutrons that are then captured by the abundant ^{56}Fe seed nuclei. The *s*-process terminates at Pb and Bi, the heaviest stable elements that can be produced with the low neutron densities that occur in AGB stars. For a review on *s*-process nucleosynthesis in AGB stars see Busso et al. (1999).

During the thermally-pulsing AGB phase, the star undergoes periodic thermal pulses (TPs) caused by instabilities in the thin He-burning shell. In order to liberate the energy that accumulates during He-burning, the He-burning shell drives a pulse-driven convective zone, which mixes ashes from the He-burning shell into the He-intershell. The energy released results in an expansion of the stellar layers above the CO core that effectively extinguishes the H-burning shell. This allows the convective envelope to move inwards in mass. If the convective envelope moves into the He-intershell, material enriched from partial He-burning and *s*-process nucleosynthesis is mixed to the surface. This mixing mechanism is known as the third dredge-up (TDU) and is one way of altering the surface composition of an AGB star. Another important product that is mixed into the envelope is ^{12}C from partial He-burning. Therefore the TDU is responsible for increasing the surface C/O ratio with the possibility of creating carbon-rich stars that have a C/O ratio greater than unity.

Nucleosynthesis in intermediate-mass AGB stars ($M \geq 3\ M_\odot$ at $Z = 0.001$) can also occur via proton captures at the base of the convective envelope. This mechanism is known as hot bottom burning (HBB). The temperature at the base of the convective envelope becomes sufficiently high which activates H-burning via the CNO cycle. If the temperature increases further, the Ne-Na chain and Mg-Al chain can also be activated (Arnould et al. 1999). One

important consequence of HBB is the production of ^{14}N at the expense of ^{12}C and ^{16}O, as well as decreasing the C/O ratio.

There are two main neutron source reactions in AGB stars: ^{13}C(α,n)^{16}O and ^{22}Ne(α,n)^{25}Mg. The ^{22}Ne neutron source is efficiently activated at temperatures higher than approximately 300×10^6 K. These temperatures are easily attained in the convective region that develops in the intershell during a TP for intermediate-mass stars. For low-mass stars, the ^{22}Ne neutron source is only marginally activated and is ineffective in producing the neutrons required for substantial *s*-process nucleosynthesis. However, the ^{13}C(α,n)^{16}O reaction is activated at temperatures as low as 90×10^6 K, which means it can be ignited in low-mass stars (Straniero et al. 1995). In canonical stellar models there is not enough ^{13}C from the ashes of H-burning for it to be an efficient source of neutrons. In order to increase the abundance of ^{13}C in the He-intershell, it is hypothesised that extra mixing of protons occurs at the deepest extent of the convective envelope during TDU. This is when a sharp composition discontinuity forms where the H-rich envelope and He-intershell meet. Protons that have been mixed downwards are captured by ^{12}C forming a 'pocket' of ^{13}C which usually burns in radiative conditions during the interpulse via the ^{13}C(α,n)^{16}O reaction before the next TP. This releases free neutrons at densities of $\lesssim 10^8$ n cm^{-3}; much lower than the neutron densities reached by the ^{22}Ne source of up to $\sim 10^{14}$ n cm^{-3}. The total number of neutrons released (the neutron exposure), however, is higher for the ^{13}C neutron source than the ^{22}Ne neutron source because the neutron flux lasts for roughly 10^4 years. For low-mass AGB stars, the ^{13}C pocket is responsible for producing the bulk of the abundances of the *s*-process elements (e.g. Bisterzo et al. 2014).

The AGB phase terminates once the stellar envelope has been ejected as a result of strong mass loss with the CO core remaining as a white dwarf. The ejected material enriches the interstellar medium from which the next generation of stars form.

The aim of this paper is to provide a self-consistent set of low- and intermediate-mass AGB models with [Fe/H][1] = −1.2 appropriate for the study of dwarf spheroidal galaxies and globular clusters as well as direct comparison to post-AGB stars. The models can also provide input for synthetic and parametric studies (e.g. Izzard et al. 2004). The models presented here are also applicable to investigating the pollution of Galactic halo stars by AGB stars and studies of galactic chemical evolution. We present evolution and nucleosynthesis results, including neutron-capture elements, for AGB models of 1 to 7 M$_\odot$ for an initial metallicity of [Fe/H] = −1.2. The models presented here cover the most extensive mass range of AGB stars at [Fe/H] = −1.2. In Section 2 we present the numerical details required for calculating the AGB stellar models. In Section 3 we present the stellar evolution results. The calculated models presented here provide the first detailed study of the TDU for an extended grid of AGB stars from 1 to 7 M$_\odot$ at [Fe/H] = −1.2. In Section 4 we explore in more detail the evolution and nucleosynthesis results of a typical low-mass model (2 M$_\odot$) and a typical intermediate-mass model (5 M$_\odot$). In Section 5 we present the nucleosynthesis results including final surface abundances and stellar yields. In Section 6 we present the effect of varying the extent in mass of the region where protons are mixed from the envelope into the

[1] [X/Y] = $\log_{10}(N_X/N_Y)_\star - \log_{10}(N_X/N_Y)_\odot$ where N_X and N_Y are the abundances of elements X and Y.

intershell for the 3 $M_\odot$ model. In Section 7 we present a comparison between the low-mass model predictions and the observed abundances of three post-AGB stars. In Section 8 we discuss uncertainties in the stellar abundances and stellar yields as a result of assumptions in the input physics and we end with discussion and conclusions in Section 9.

3.2. Evolutionary and nucleosynthesis codes

We calculate AGB stellar models for a range of initial masses from 1 $M_\odot$ to 7 $M_\odot$ with a metallicity of $Z = 0.001$ ([Fe/H] = −1.2) and a helium abundance of $Y = 0.25$. For the purposes of this study, we define the low-mass models to be those with an initial mass up to and including 3 $M_\odot$, and the intermediate-mass models, 3.25 $M_\odot$ and above. Each stellar model is evolved from the zero-age main sequence to near the end of the AGB phase when the majority of the convective envelope is lost by stellar winds. A two-step procedure is performed to calculate the structure and detailed nucleosynthesis for each stellar model.

First, we use the Mt Stromlo Stellar Evolutionary code (Karakas et al. 2010, and references therein) to calculate the stellar evolutionary sequences. The details of the procedure and evolution code are as described in Karakas et al. (2010) except for the differences described below. For the low-mass models, we use the C and N enhanced ÆSOPUS low-temperature molecular opacity tables (Marigo & Aringer 2009) as used in Kamath et al. (2012). For the intermediate-mass models, we use updated Lodders (2003) scaled-solar ÆSOPUS low-temperature molecular opacity tables (Marigo & Aringer 2009), which account for the depletion and enhancement of C and C/O. The opacity treatment utilised for the intermediate-mass models is described in detail in Fishlock et al. (2014b). We use OPAL tables (Iglesias & Rogers 1996) updated to a Lodders (2003) scaled-solar abundance for consistency with the low-temperature opacity tables.

To model convective borders we follow the method described by Lattanzio (1986) and Frost & Lattanzio (1996) which employs the Schwarzschild criterion but searches for a neutral border when ∇_{ad}/∇_{rad}, the ratio of the adiabatic and radiative temperature gradients, is discontinuous such as during TDU. For convective regions we use the standard mixing length theory (Böhm-Vitense 1958) with a mixing length parameter of $\alpha = 1.86$. We use a solar global metallicity of $Z_\odot = 0.015$ with a scaled-solar initial composition from Asplund et al. (2009) which has a protosolar metallicity of 0.0142. As with Karakas et al. (2010), mass loss prior to the AGB phase is included using the Reimers (1975) formula with $\eta_R = 0.4$. Mass loss during the AGB phase is included using the Vassiliadis & Wood (1993) mass-loss prescription.

Second, detailed nucleosynthesis calculations are performed using the stellar evolutionary sequences as input into a post-processing nucleosynthesis code (see Lugaro et al. 2004, 2012, and references therein for details). The nucleosynthesis code calculates nuclear reactions and mixing simultaneously to solve for the abundances. A post-processing code is necessary as the stellar evolutionary code only accounts for the major energy generating reactions involving H, ^{3}He, ^{4}He, ^{12}C, ^{14}N, and ^{16}O. We assume the additional reactions included in

the post-processing code produce negligible energy and do not affect the stellar structure (see Doherty et al. 2014a).

The updated nuclear network incorporated into the nucleosynthesis code is based on the JINA Reaclib[2] database as of May 2012 with the modifications as detailed in Lugaro et al. (2014). The reaction rate of ^{13}C(α,n)^{16}O is taken from Heil et al. (2008b) while the reaction rates for ^{22}Ne(α,n)^{25}Mg and ^{22}Ne(α,γ)^{26}Mg are taken from Iliadis et al. (2010). The network, which considers 2336 reactions, includes 320 species from neutrons to polonium and comprises all the stable and unstable isotopes relevant for *s*-process nucleosynthesis (for example, we do not include the long-lived isotope ^{130}Te, because it is not reached by the *s*-process). We further include two species for the unstable isotope ^{85}Kr, the ground state ^{85}Kr^{g} and the short-lived metastable state ^{85}Kr^{m}, due to their location at an *s*-process branching point. When determining surface abundances and yields, we assume that long-lived isotopes have decayed (e.g. ^{99}Tc to ^{99}Ru).

For the low-mass models a partial mixing zone (PMZ) is included in the post-processing nucleosynthesis code[3]. Protons are artificially added to the top layers of the He-intershell at the deepest extent of TDU where they are captured by ^{12}C leading to the production of the ^{13}C pocket (see Lugaro et al. 2012). This produces the free neutrons required for *s*-process nucleosynthesis. For the low-mass models with an initial mass less than 2.75 M$_\odot$, we choose the mass of the added PMZ to be 2×10^{-3} M$_\odot$. For the 2.75 and 3 M$_\odot$ models we choose a PMZ mass of 1×10^{-3} M$_\odot$ and 5×10^{-4} M$_\odot$, respectively. We choose a lower PMZ mass for the 2.75 and 3 M$_\odot$ models because of the effect of a decreasing intershell mass with initial mass. We discuss the uncertainty related to the choice of the PMZ mass in Section 3.6. We set the mass to remain constant for every PMZ added during TDU. As the intershell mass reduces with each TP we take the neutron-capture abundances to be an upper limit.

3.3. Stellar evolution results

In Table 3.1 we provide a summary of the structural properties relevant for nucleosynthesis for each of the AGB models. The AGB phase is terminated when the stellar envelope is removed through mass loss. The low-mass models, excluding the 1 M$_\odot$ model, experience the superwind phase in the final few TPs during which the mass-loss rate reaches a plateau of approximately 10^{-5} M$_\odot$ yr^{-1}. The 1 M$_\odot$ model loses the majority of its stellar envelope before it reaches the superwind phase. The intermediate-mass models experience the superwind phase well before most of the envelope has been lost.

For models with an initial mass up to (and including) 2 M$_\odot$, we are able to evolve the envelope mass to less than 0.02 M$_\odot$ which puts the model just beyond the tip of the AGB towards the post-AGB phase (Blöcker 2001). The models with $M \gtrsim 2$ M$_\odot$ suffer from convergence problems towards the end of the AGB (see Lau et al. 2012, for more details). For the models between 2 and 4 M$_\odot$ we are able to evolve the envelope mass to less than 0.6 M$_\odot$. However,

[2]https://groups.nscl.msu.edu/jina/reaclib/db/

[3]See Section 4.4.3 for a discussion of the need for a PMZ.

Table 3.1 Evolutionary properties of the calculated $Z = 0.001$ stellar models.

$M_{\rm initial}$[a] ($M_\odot$)	$M_{\rm final}$[b] ($M_\odot$)	$M_{\rm core}$[c] ($M_\odot$)	$M_{\rm env}$[d] ($M_\odot$)	TPs[e]	TDUs[f]	$\lambda_{\rm max}$[g]	$T_{\rm BCE}^{\rm max}$[h] (10^6 K)	$T_{\rm He}^{\rm max}$[i] (10^6 K)	$M_{\rm TDU}$[j] ($M_\odot$)
1.00	0.678	0.667	0.011	17	2	0.08	1.4	284.1	0.002
1.25	0.669	0.649	0.020	14	8	0.16	2.2	271.8	0.009
1.50	0.657	0.646	0.011	14	10	0.37	6.7	275.4	0.026
2.00	0.668	0.661	0.007	17	14	0.73	4.2	294.2	0.095
2.25	0.839	0.673	0.166	17	16	0.82	5.6	305.4	0.132
2.50	0.948	0.709	0.239	17	16	0.92	9.2	318.5	0.138
2.75	1.057	0.746	0.312	18	18	0.97	15.8	320.8	0.138
3.00	1.189	0.792	0.397	22	20	1.00	28.3	332.5	0.124
3.25	1.403	0.843	0.561	23	22	1.00	48.9	350.5	0.093
3.50	1.176	0.857	0.319	27	27	0.99	58.5	361.3	0.104
4.00	1.726	0.883	0.843	68	68	1.02	82.9	361.3	0.231
4.50	1.659	0.908	0.750	79	78	0.97	87.6	356.6	0.210
5.00	1.740	0.938	0.802	94	93	0.95	92.5	361.2	0.194
5.50	1.962	0.972	0.990	100	99	0.93	98.1	363.0	0.151
6.00	1.725	1.015	0.709	108	105	0.92	104.8	376.5	0.107
7.00	2.062	1.145	0.917	135	132	0.86	125.0	392.4	0.034

[a] Initial mass [b] Final mass [c] Final core mass [d] Final envelope mass [e] Number of TPs computed [f] Number of TDU episodes [g] Maximum efficiency of TDU [h] Maximum temperature reached at the base of the convective envelope [i] Maximum temperature reached at the base of the He-intershell [j] Total amount of mass mixed into the envelope through TDU

for the models between 4 $M_\odot$ and 7 $M_\odot$, we are able to evolve the envelope mass to less than 1 $M_\odot$.

Since some envelope mass still remains, it is possible that additional TDU episodes could occur which would further enrich the envelope prior to being ejected into the interstellar medium (see Karakas & Lattanzio 2007). If we assume that the mass lost during the final calculated interpulse period is taken as representative of the mass to be lost before the next possible TP, the models with $M \leq 3.5$ $M_\odot$ cannot experience another TDU episode as there is not enough envelope mass left. The more massive models, however, retain sufficient mass to experience at least one more TDU episode. For example, the 6 $M_\odot$ model has an envelope mass of 0.709 $M_\odot$ remaining when calculations cease due to convergence issues. To estimate the number of remaining of TPs we assume the mass lost during the preceding TP is taken as representative of the mass to be lost in the following TPs (approximately 1.5×10^{-1} $M_\odot$). This leaves a minimum of an additional 4 TPs (possibly with TDU) that could take place. We remove the remaining envelope without taking into account the possibility for extra TDU(s). Therefore, the final surface abundance and yield predictions of the neutron-capture elements are a lower limit for the intermediate-mass models. Additionally, the termination of the intermediate-mass models occurs after HBB has ceased.

In Table 3.2 we identify models which experience a core He-flash, the first dredge-up (FDU; after core H-burning at the base of the RGB), the second dredge-up (SDU; after core He-burning on the early AGB), TDU and/or HBB. All the models calculated with an initial

Table 3.2 A tick (✓) means the phenomenon occurred in each model, a cross (×) if it did not.

Mass ($M_\odot$)	Core He-flash	FDU	SDU	TDU	HBB
1.00	✓	✓	×	✓	×
1.25	✓	✓	×	✓	×
1.50	✓	✓	×	✓	×
2.00	×	✓	×	✓	×
2.25	×	✓	×	✓	×
2.50	×	✓	×	✓	×
2.75	×	✓	✓	✓	×
3.00	×	✓	✓	✓	✓
3.25	×	✓	✓	✓	✓
3.50	×	✓	✓	✓	✓
4.00	×	×	✓	✓	✓
4.50	×	×	✓	✓	✓
5.00	×	×	✓	✓	✓
5.50	×	×	✓	✓	✓
6.00	×	×	✓	✓	✓
7.00	×	×	✓	✓	✓

mass less than 2 $M_\odot$ develop an electron degenerate core and experience a core He-flash at the onset of core He-ignition. A core He-flash removes this degeneracy and the luminosity of the H-shell briefly reaches up to 10^9 $L_\odot$. FDU is experienced in all models $\leq$ 3.5 $M_\odot$ (Table 3.2). The intermediate-mass models with $M \geq 4$ $M_\odot$ do not experience FDU as core He-burning is ignited before the model reaches the first giant branch; these stars experience SDU as their first mixing episode. We find that SDU occurs in models with $M \geq 2.75$ $M_\odot$. The 2.75 to 3.5 $M_\odot$ models are the only models to experience both FDU and SDU.

All the stellar models experience TDU on the AGB and the efficiency of TDU is quantified by the parameter,

$$\lambda = \frac{\Delta M_{\rm dredge}}{\Delta M_{\rm c}}, \tag{3.1}$$

where $\Delta M_{\rm dredge}$ is the mass of the material mixed into the convective envelope by the TDU episode and $\Delta M_{\rm c}$ is the mass growth of the core due to H-burning during the preceding interpulse period. The 1 $M_\odot$ model experiences the fewest number of TDUs with only six episodes which brings a total of 0.0016 $M_\odot$ of enriched material to the stellar surface. The largest total amount of material that is mixed to the surface is 0.232 $M_\odot$, which occurs for the 4 $M_\odot$ model. Despite having more TDU episodes than the 4 $M_\odot$ model, the 4.5, 5, 5.5, 6, and 7 $M_\odot$ models dredge up a smaller amount of material. This is because the intershell region is not as massive and TDU is less efficient in these models compared to the 4 $M_\odot$ model.

Figure 3.1(a) illustrates the evolution of λ with core mass for each model and the range

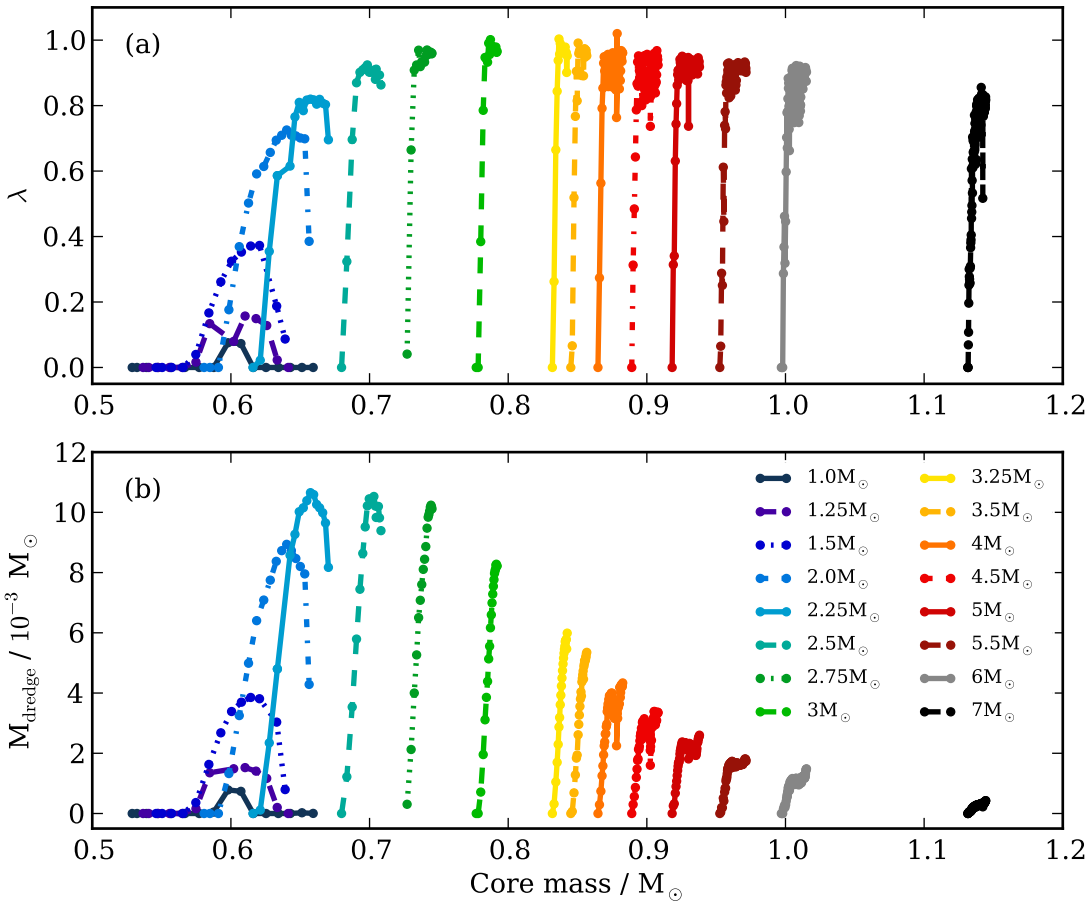

Figure 3.1 The evolution of (*a*) the efficiency of TDU, λ and (*b*) $M_{\rm dredge}$ with core mass for each model.

of core masses produced by the models. The TDU efficiency gradually increases with increasing core mass. Overall, the efficiency of TDU increases with initial mass with the maximum λ values occurring for the 3 and 3.25 $M_\odot$ models. The overall efficiency then decreases for the 4.5, 5, 5.5, 6, and 7 $M_\odot$ models. Figure 3.1(b) reveals that the low-mass models, with the lowest λ values, mix up more material per TDU as a result of a larger intershell mass compared to the intermediate-mass models. However, $M_{\rm dredge}$ does not correlate with λ value. The increase in the core mass during the AGB phase is higher for the low-mass models as a result of a low λ. The mass of the core of the 1 $M_\odot$ model increases by 0.14 $M_\odot$ while the core mass of the 7 $M_\odot$ model only increases by 0.014 $M_\odot$, a factor of ten lower. This is a result of the high efficiency of TDU ($\lambda \approx 1$) and shorter interpulse periods in the intermediate-mass models leading to minimal core growth.

The maximum temperature reached at the base of the convective envelope increases with increasing initial mass reaching up to 125×10^6 K for the 7 $M_\odot$ model (see Table 3.1). While we find the lower initial stellar mass limit for HBB to be 3 $M_\odot$ (Table 3.2) there is only mild activation of HBB for a few TPs in models less than 4 $M_\odot$. The lower initial mass limit for efficient HBB with $T_{\rm bce} \gtrsim 60 \times 10^6$ K is 4 $M_\odot$. The $Z = 0.001$ models with an initial mass ≤ 2.5 $M_\odot$ of Ventura & Marigo (2010) do not experience HBB where they define the onset of

HBB to be $T_{\rm bce} \gtrsim 60 \times 10^6$ K.

The 6 and 7 $M_\odot$ models experience hot TDU where HBB takes place during TDU as C and O is mixed the surface. The studies by Goriely & Siess (2004) and Herwig (2004b) demonstrated that hot TDU can inhibit *s*-process nucleosynthesis. For these models, and the other intermediate-mass models, we do not include a PMZ.

The 7 $M_\odot$ model is characterised as a super-AGB star as it experiences off-centre carbon ignition which produces an ONe core at the end of the AGB phase (Siess 2007). Super-AGB stars also experience high mass-loss rates with the 7 $M_\odot$ model reaching a maximum rate of 1.3×10^{-3} $M_\odot$ yr^{-1} after around 60 TPs. In comparison, the 6 $M_\odot$ reaches a maximum mass-loss rate of 8.8×10^{-4} $M_\odot$ yr^{-1} after around 80 TPs. The grid of super-AGB models calculated by Doherty et al. (2014b) includes a 7 $M_\odot$ model of $Z = 0.001$. A comparison between these two models finds similar final core masses (1.14 $M_\odot$ compared to 1.145 $M_\odot$ for the model presented here), maximum temperature at the base of the convective envelope (120 MK compared to 125 MK), and total mass of material dredged up (3.97×10^{-2} $M_\odot$ compared to 3.4×10^{-2} $M_\odot$). The 7 $M_\odot$ model presented here experiences 135 TPs, whereas the Doherty et al. (2014b) model experiences 126 TPs and is evolved to a smaller envelope mass.

3.4. Details of a low- and intermediate-mass model

3.4.1. The 2 $M_\odot$ model

The 2 $M_\odot$ model was chosen as a representative case of low-mass AGB evolution at $Z = 0.001$ as we are able to compare our results with the calculations of Cristallo et al. (2009, 2011). Furthermore, we were able to evolve this model to a low envelope mass of 0.007 $M_\odot$. In Table 3.3 we present, for each TP, the total mass ($M_{\rm tot}$), the core mass ($M_{\rm core}$), the mass of material mixed to the surface due to TDU ($M_{\rm dredge}$), the efficiency of TDU (λ), the interpulse period ($\tau_{\rm ip}$), the maximum surface luminosity ($L_{\rm max}$), the effective temperature ($T_{\rm eff}$), the maximum radius ($R_{\rm max}$), and the surface C/O ratio (C/O). The model experiences 17 TPs with 14 of these TPs followed by TDU.

In Figure 3.2(a), we plot the temporal evolution of three different mass boundaries during the AGB phase: the inner edge of the convective envelope, the mass of the H-exhausted core, and the mass of the He-exhausted core. The mass of the He-exhausted core remains constant during the interpulse because the He-burning shell is mostly inactive. It is only during a TP that the He-exhausted core increases in mass. The mass of the H-exhausted core grows during the interpulse period when the H-burning shell is active. Following a TP the convective envelope moves inwards in mass and, if TDU occurs, H-rich material is mixed into the H-exhausted core thus reducing the mass of the core.

The first TDU episode occurs after the fourth TP (once λ is greater than zero). The dredge-up efficiency increases for each successive TP until it reaches a maximum value of $\lambda = 0.73$. TDU causes the C/O ratio to increase above unity by the sixth TP changing the envelope

Table 3.3 Properties of each TP for the 2 $M_\odot$ model.

TP	$M_{\rm tot}$[#] ($M_\odot$)	$M_{\rm core}$ ($M_\odot$)	$M_{\rm dredge}$ ($\times 10^{-3} M_\odot$)	λ	$\log_{10}\tau_{\rm ip}$ (yr)	$\log_{10} L_{\rm max}$ ($L_\odot$)	$\log_{10} T_{\rm eff}$ (K)	$R_{\rm max}$ ($R_\odot$)	C/O
1	1.9737	0.581	0.00	0.00	–	3.36	3.64	85.41	0.29
2	1.9737	0.585	0.00	0.00	5.06	3.55	3.62	115.58	0.29
3	1.9737	0.591	0.00	0.00	5.22	3.62	3.62	128.64	0.29
4	1.9737	0.599	1.33	0.18	5.24	3.68	3.61	141.77	0.29
5	1.9737	0.606	3.25	0.37	5.21	3.74	3.61	156.02	0.83
6	1.9736	0.613	4.99	0.50	5.18	3.80	3.59	177.78	2.34
7	1.9736	0.619	6.40	0.59	5.15	3.85	3.58	202.51	4.43
8	1.9736	0.624	7.09	0.61	5.12	3.89	3.57	224.31	6.75
9	1.9735	0.628	7.75	0.66	5.09	3.92	3.55	246.33	8.78
10	1.9734	0.633	8.37	0.69	5.06	3.94	3.54	270.05	10.64
11	1.9730	0.637	8.73	0.71	5.04	3.96	3.53	291.06	12.41
12	1.9721	0.640	8.94	0.73	5.02	3.98	3.52	311.25	13.99
13	1.9702	0.644	8.73	0.71	4.99	4.00	3.52	330.66	15.54
14	1.9658	0.647	8.47	0.71	4.97	4.01	3.51	348.69	16.85
15	1.9543	0.650	8.20	0.70	4.94	4.03	3.50	367.14	18.03
16	1.9156	0.653	7.96	0.70	4.91	4.04	3.49	388.99	19.20
17	1.3980	0.656	4.29	0.39	4.89	4.05	3.45	518.40	20.20

[#] NB. – The final mass is given in Table 3.1.

composition from oxygen rich to carbon rich (see Table 3.3). The C/O ratio is approximately 20 by the last TP. A total amount of 0.0945 $M_\odot$ of enriched material is mixed into the envelope through TDU (Table 3.1), compared to 0.1313 $M_\odot$ for the model calculated by Cristallo et al. (2011).

Appreciable envelope mass loss does not occur until the penultimate TP where the mass-loss rate increases to approximately 2×10^{-5} $M_\odot$ yr^{-1} during the superwind phase. The superwind phase is where the majority of the envelope, around 1 $M_\odot$, is lost. This is shown along with the temporal evolution of total mass and core mass in Figures 3.2(b) and 3.2(c).

The composition profiles after the last TDU episode are presented in Figure 3.3 and focus on the region where the PMZ is added at the deepest extent of TDU. Key isotopes (p, ^{12}C, ^{13}C, ^{16}O, ^{14}N, ^{88}Sr, ^{138}Ba, and ^{208}Pb) involved in s-process nucleosynthesis are presented. When the convective envelope reaches its most inward point in mass during TDU, a PMZ of 2×10^{-3} $M_\odot$ is added to the top of the He-intershell (illustrated in Figure 3.3(a)). At the beginning of the interpulse, the ^{13}C pocket forms along with a pocket of ^{14}N. The mass of the ^{13}C pocket is approximately 1×10^{-3} $M_\odot$. Later, the ^{13}C(α,n)^{16}O reaction is activated increasing the neutron abundance. In the regions where the ^{14}N abundance is higher than the ^{13}C abundance, no s-process nucleosynthesis can occur as ^{14}N acts as a neutron poison via the ^{14}N(n,p)^{14}C reaction (illustrated in Figure 3.3(b)). Elements from the first peak, such as Sr, are produced first, followed by the second-peak elements such as Ba. Pb is then produced at the expense of these elements (illustrated in Figure 3.3(c)). Eventually the

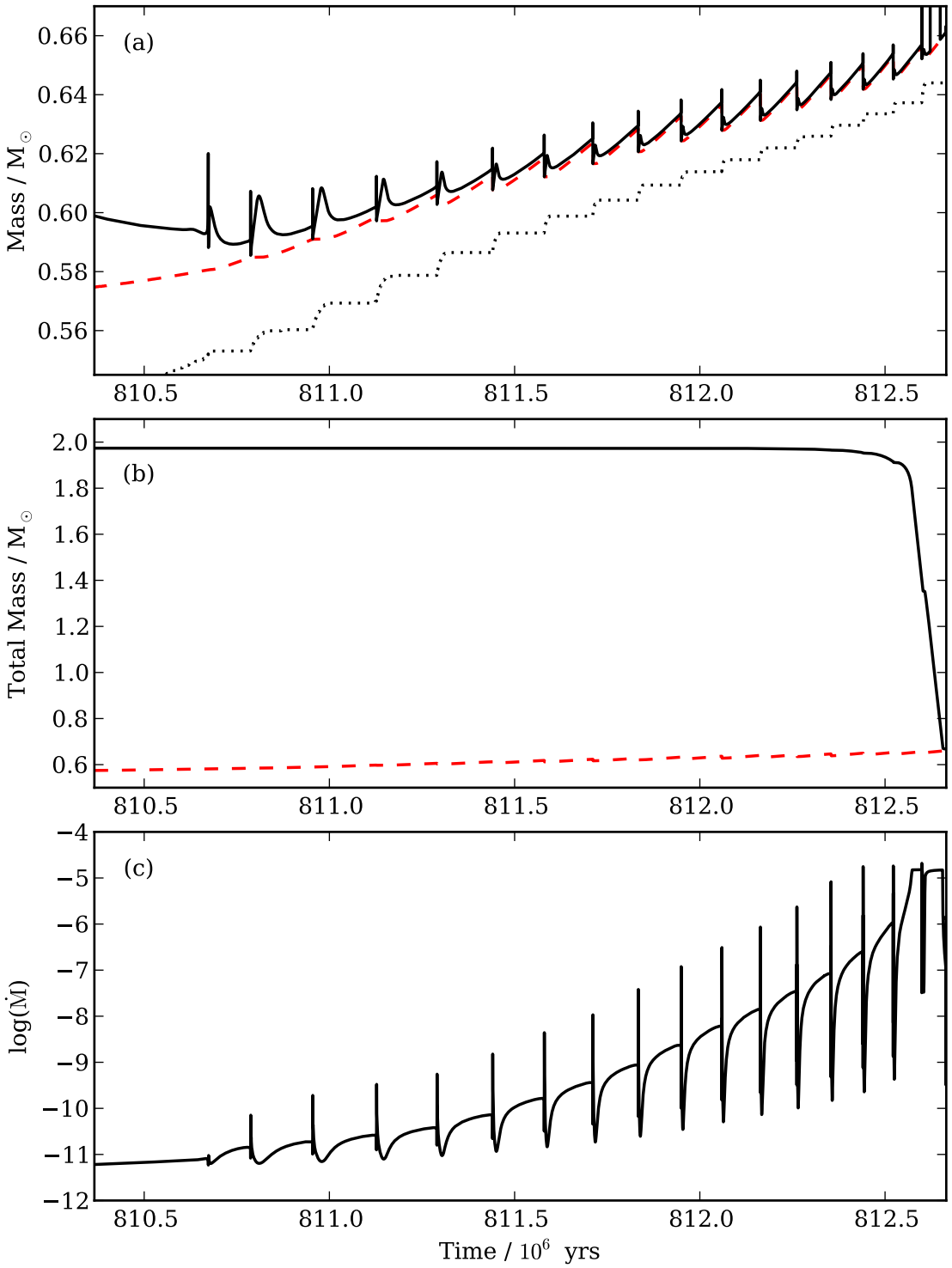

Figure 3.2 The temporal evolution from the start of the AGB phase for the 2 $M_\odot$ model of (*a*) the inner edge of the convective envelope (solid line), the mass of the H-exhausted core (dashed line) and the mass of the He-exhausted core (dotted line), (*b*) total mass (solid line) and the mass of the H-exhausted core (dashed line) and (*c*) the mass-loss rate.

abundance of ^{13}C reduces to below that of ^{14}N and *s*-process nucleosynthesis terminates. The enriched material is then mixed into the following TP and then to the stellar surface through the next TDU.

Figure 3.4 highlights the distribution of the surface abundance ratios relative to Fe for all elements from C to Bi. The 'Initial' line is the initial composition on the main sequence. The 'Pre-AGB' line is the pre-AGB composition as a result of FDU where the surface abundance of carbon, measured by [C/Fe], decreases by 0.28 dex while [N/Fe] increases by 0.49 dex. The ratio of [Na/Fe] also increases by 0.22 dex. The remaining lines illustrate the surface abundances at the end of each TDU episode. The final abundances calculated by Cristallo et al. (2009) are also plotted.

Among the light elements, [C/Fe], [F/Fe], [Ne/Fe], and [Na/Fe] are enhanced by over 1 dex by the end of the AGB phase. The final [C/Fe] ratio is 1.88 as a result of TDU mixing up the products of partial He-burning. The [F/Fe] ratio increases from slightly below the solar value at the start of the AGB phase to 2.10, higher than the enhancement of [C/Fe]. The [O/Fe] value increases marginally as a result of partial He-burning to 0.30 while the abundance of [N/Fe] only increases by 0.05 dex during the AGB phase. The final surface abundances of [Ne/Fe] and [Na/Fe] are enhanced to 1.3 and 1.2, respectively. The Cristallo et al. (2009) model has a higher enhancement in [Ne/Fe] and [Mg/Fe] with values up to 1.60 and 1.28, respectively. For the Fe-peak elements, there are minimal changes in the abundances. Both Co and Cu experience an enhancement of 0.2 dex while Sc increases by 0.14 dex and Zn by 0.1 dex.

The surface abundance of the neutron-capture elements only increases after the second TDU episode (Figure 3.4). The ^{13}C pocket burns during the interpulse period once protons are added at the deepest extent of the first TDU. The newly synthesised neutron-capture elements are then mixed to the surface during the next TDU. The *s*-process abundance for each element asymptotically approaches its final value as each TDU brings more *s*-process enriched material to the surface. By the end of the AGB phase, the ratios of [Rb/Fe], [Zr/Fe], [Ba/Fe], and [Pb/Fe] are enhanced by 0.70, 1.53, 2.02, and 2.95 dex, respectively. These values follow a characteristic abundance distribution of neutron-capture elements for a low-metallicity low-mass AGB model where the production of Pb is favoured over the other neutron-capture elements (Busso et al. 2001). The model of Cristallo et al. (2009) produces 1.41, 1.99, and 2.87, respectively for [Zr/Fe], [Ba/Fe], and [Pb/Fe] and these values are comparable to those presented here despite a different treatment of the inner border of the convective envelope. The Cristallo et al. (2009) model has a noticeably higher enhancement of Rb as seen in Figure 3.4 as a result of neutron densities greater than 10^{12} n cm^{-3} occurring during a TP. The neutron densities in our model peak at less than 10^{11} n cm^{-3} during a TP (see Figure 3.5) and have a minimal contribution to the abundance of Rb.

The surface abundance distribution for the neutron-capture elements exhibits three main peaks (around Sr, Ba, and Pb as seen in Figure 3.4) corresponding to the isotopes with a magic number[4] of neutrons ($N = 50, 82, 126$). The average abundances of the neutron-capture elements at the first two of these points are called light *s* (*ls*) and heavy *s* (*hs*), respectively.

[4]The number of nucleons required to form complete shells within a nucleus.

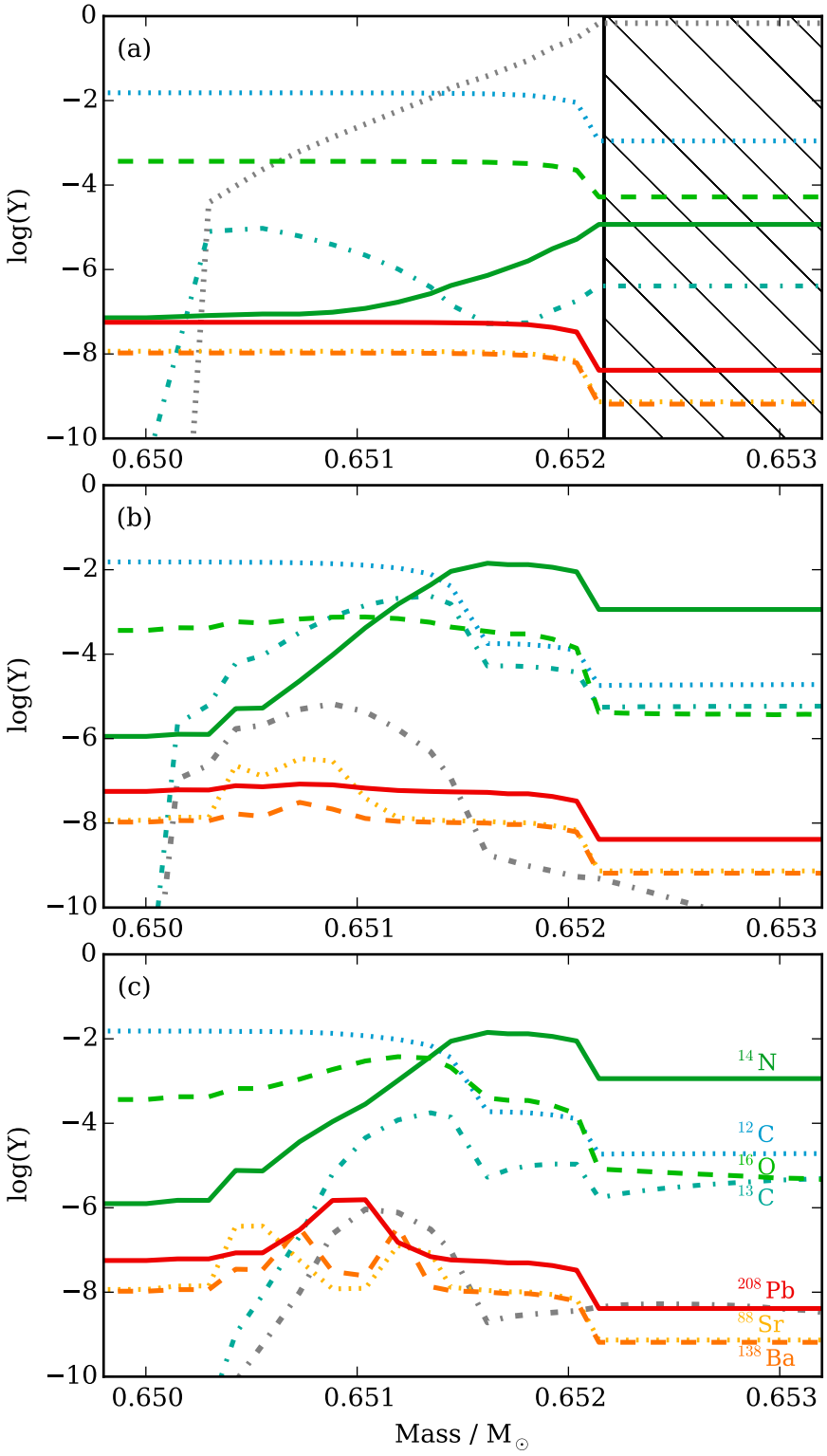

Figure 3.3 Composition profiles for three snapshots in the 2 $M_\odot$ model after the last TDU episode. Abundances are given in units of log(Y), where $Y = X/A$ and X is the mass fraction and A is the atomic mass. Protons are shown by the grey dotted line. Neutrons are shown by the grey dash-dotted line and are offset in log(Y) by +15. The hatched region represents the convective envelope. Panel (*a*): the proton profile of the added PMZ just after the deepest extent of the last TDU. Panel (*b*): the ^{13}C pocket has formed along with a ^{14}N pocket with the ^{13}C(α,n)^{16}O reaction producing a peak of neutrons. The neutron-capture elements are starting to be synthesised. Panel (*c*): Pb is created at the expense of Ba and the abundance of ^{13}C is now below that of ^{14}N so no more neutrons can be produced.

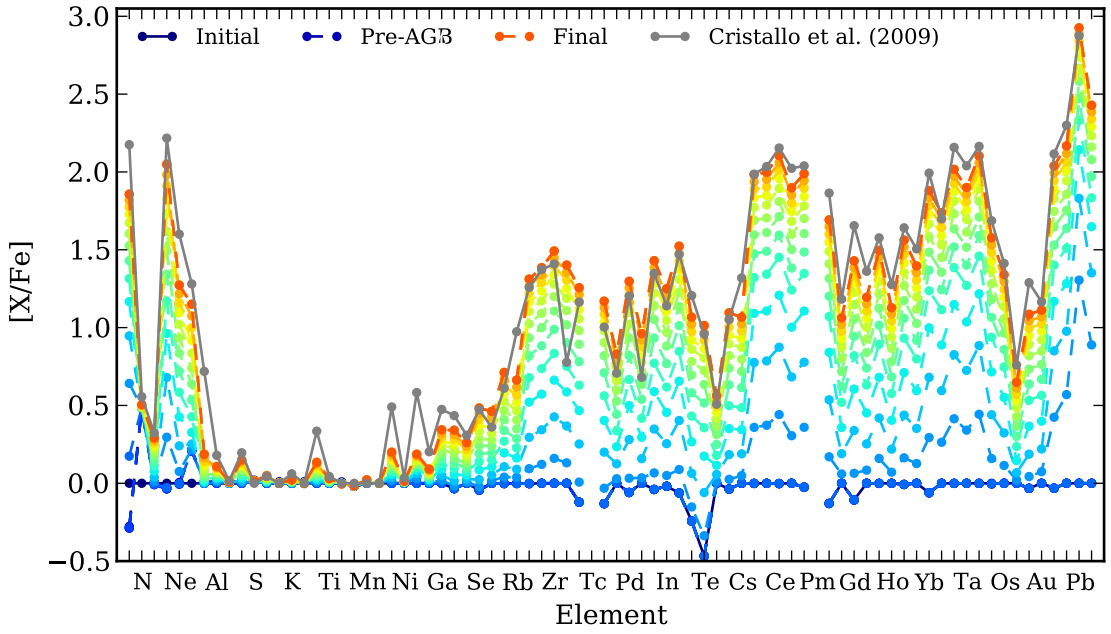

Figure 3.4 The surface abundance ratio for each of the elements after each TDU for the 2 $M_\odot$ model. Each line connects the [X/Fe] abundance after each TDU. The initial and pre-AGB compositions are also shown. The initial composition shows that some elements have a value less than solar. This is a result of a few stable isotopes not being considered in the nuclear network as they are not accessible by the *s*-process (see Section 3.2). For comparison, the final surface abundance distribution for the 2 $M_\odot$ model of Cristallo et al. (2009) is shown as a solid grey line. The elements are ordered by increasing atomic number.

The third peak is given as the abundance of [Pb/Fe]. As in Cristallo et al. (2011), the [*ls*/Fe] abundance is given by,

$$[ls/\mathrm{Fe}] = ([\mathrm{Sr/Fe}] + [\mathrm{Y/Fe}] + [\mathrm{Zr/Fe}])/3, \tag{3.2}$$

and the [*hs*/Fe] abundance,

$$[hs/\mathrm{Fe}] = ([\mathrm{Ba/Fe}] + [\mathrm{La/Fe}] + [\mathrm{Nd/Fe}] + [\mathrm{Sm/Fe}])/4. \tag{3.3}$$

As the neutron exposure increases, the *ls* elements are produced first, then the *hs* elements, and finally Pb. For the 2 $M_\odot$ model, the final surface abundance values of [*ls*/Fe], [*hs*/Fe], and [Pb/Fe] are 1.43, 1.95, and 2.95, respectively. Combinations of these ratios include [*hs*/*ls*] and [Pb/*hs*] and these *s*-process indicators are independent of the efficiency of TDU and the mass-loss rate for the low-mass models. For the model presented here the final [*hs*/*ls*] and [Pb/*hs*] values are 0.52 and 1.00. These values are reached by the sixth TDU episode and remain constant until the end of the AGB phase.

The abundance distribution of the neutron-capture elements is predominately controlled by the neutron density, along with the neutron exposure. In Figure 3.5, we plot, against time, the temperature of the He-burning shell and the maximum neutron density reached for each of the TPs. Notably, the first interpulse period with a ^{13}C pocket has a neutron

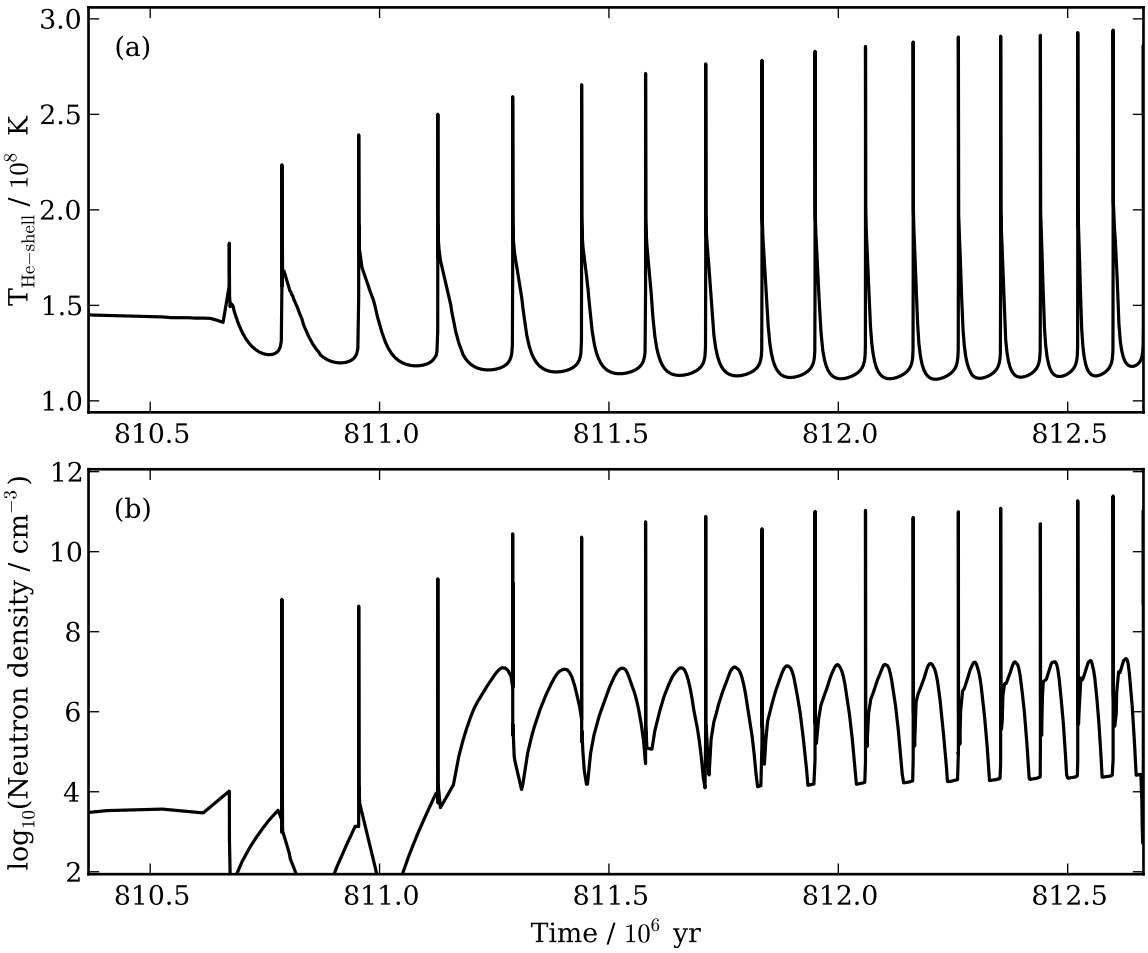

Figure 3.5 (a) The temperature at the top of the He-shell and (b) the maximum neutron density as a function of time from the start of the AGB phase for the 2 $M_\odot$ model.

density around 10^7 n cm^{-3}. During this interpulse, not all of the ^{13}C is burned under radiative conditions and is later engulfed by the subsequent TP, resulting in convective ^{13}C burning. This condition is described by Lugaro et al. (2012) as Case 3. For the remaining ^{13}C pockets, all the ^{13}C is burned radiatively before the subsequent TP in accordance with Case 2 as described by Lugaro et al. (2012). A peak in the neutron density occurs at each TP where there is a marginal activation of the ^{22}Ne neutron source (Gallino et al. 1998). The production of the neutron-capture elements from the ^{22}Ne source is negligible compared to those produced from the ^{13}C neutron source but elements produced via branching points such as Rb can be affected by this neutron flux.

3.4.2. The 5 $M_\odot$ model

We examine the 5 $M_\odot$ model as a representative case of an intermediate-mass AGB model. In contrast to a low-mass AGB model, the intermediate-mass models experience more efficient HBB and the ^{22}Ne neutron source is more efficiently activated. We do not add a PMZ for the reasons presented in detail by Garcia-Hernandez et al. (2013).

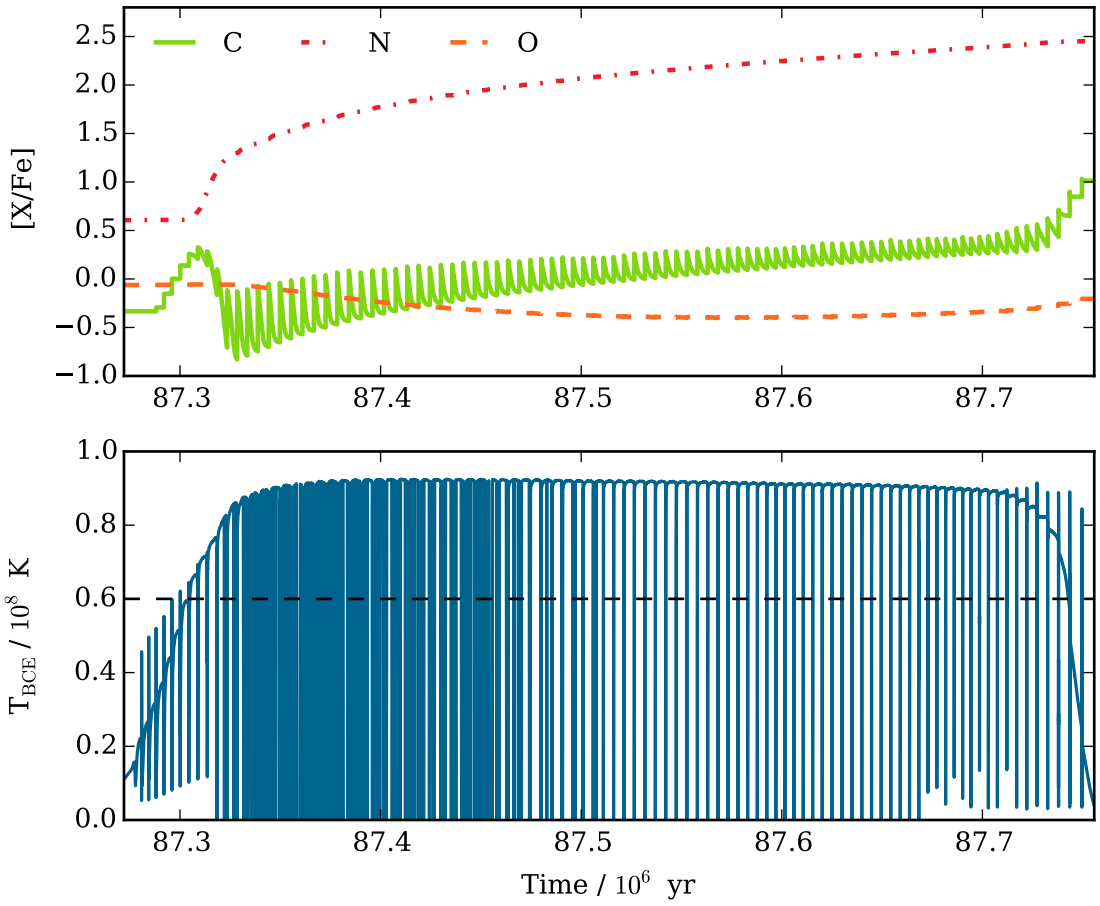

Figure 3.6 The evolution of [C/Fe], [N/Fe], and [O/Fe] (top) and the temperature at the base of the convective envelope (bottom) with respect to time from the start of the AGB phase for the 5 $M_\odot$ model. The dashed line illustrates the temperature above which HBB is efficiently activated.

Figure 3.6 illustrates (a) the effect of HBB on the C, N, and O surface abundance relative to Fe and (b) the temperature at the base of the convective envelope. Initially, when the temperature at the base of the convective envelope has not reached the value required for CNO cycling, the ratio of [C/Fe] increases due to TDU while [N/Fe] remains constant. When temperatures at the base of the convective envelope reach approximately 60×10^6 K the CNO cycle is activated with C and O being converted to N. This destruction of C and O, along with the competing effect of TDU, causes the evolution of the C/O ratio to fluctuate about unity. From a certain point onwards, the model remains carbon rich. Eventually HBB is extinguished and [C/Fe] and [O/Fe] once again increases for the last few TDU episodes.

This fluctuating behaviour in the C/O ratio is also a feature in the 5 $M_\odot$, $Z = 0.001$ model of Marigo et al. (2013). Marigo et al. (2013) also noted that the last few TPs do not experience HBB and the surface C/O ratio increases significantly to a final value of ~ 10. This value is comparable to the final C/O ratio of ~ 9 for the 5 $M_\odot$ model presented here. One difference, however, is that prior to HBB the Marigo et al. (2013) model does not exhibit an increase in the C/O ratio in contrast to our model in which this ratio increases above unity before the onset of HBB (Figure 3.6).

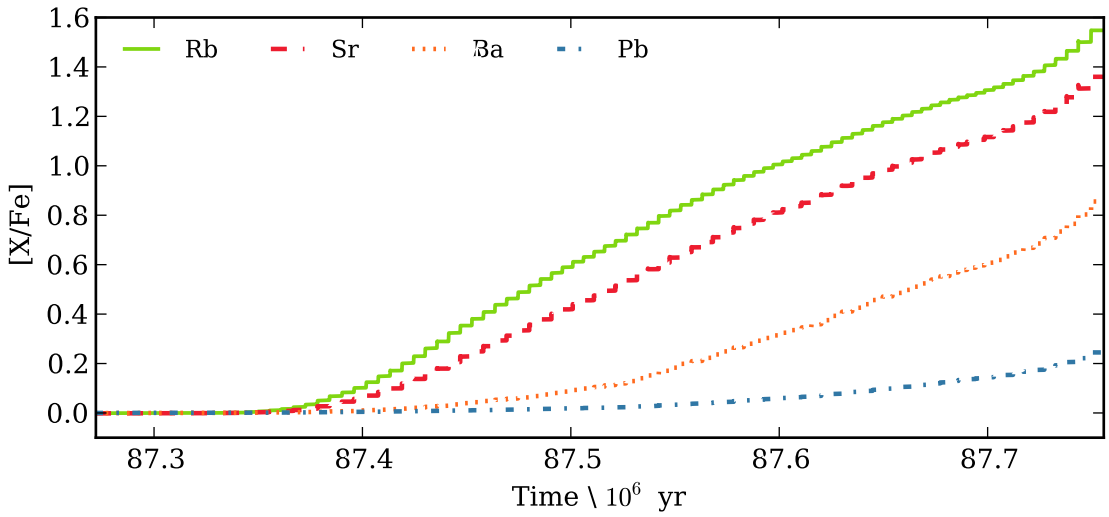

Figure 3.7 The surface abundance of four neutron-capture elements (Rb, Sr, Ba, and Pb) as a function of time from the start of the AGB phase for the 5 $M_\odot$ model.

The efficiency of TDU in the 5 $M_\odot$ model increases with each TP until it reaches a plateau of $\lambda \approx 0.95$ and the amount of material brought to the surface gradually increases until it reaches a value of approximately 2.5×10^{-3} $M_\odot$. Despite the high efficiency of TDU, the amount of material mixed to the surface through each TDU is lower for the 5 $M_\odot$ model compared to the low-mass model of 2 $M_\odot$. This is a result of the He-intershell region having approximately ten times less mass. However, the higher number of TDU episodes (93 compared to 14) means that the overall amount of the material being brought to the surface during the AGB phase is larger, 0.194 $M_\odot$ compared to 0.095 $M_\odot$ for the 2 $M_\odot$ model (see Table 3.1).

Figure 3.7 presents the evolution of Rb, Sr, Ba, and Pb relative to Fe. These elements are representative of the three *s*-process peaks. Rb exhibits the greatest enhancement and Pb the least and this situation is opposite to what the low-mass models display. The intermediate-mass models do not attain the neutron exposure required to produce elements such as Ba and Pb to the level produced by the low-mass models. However, the models are able to produce the high neutron densities required to bypass unstable isotopes (e.g., ^{85}Kr) at branching points resulting in a higher abundance of Rb (cf. van Raai et al. 2012). The final [Rb/Fe] surface abundance is around 1.6 whereas [Pb/Fe] only increases by approximately 0.2 dex.

Figure 3.8(a) illustrates the maximum neutron density reached for each TP as a function of time. The peak neutron density is approximately 10^{13} n cm^{-3}. The neutron density stays above 10^{12} n cm^{-3} for approximately 30 days within each TP. As the temperature of the He-burning shell decreases, the neutron density also decreases. During the interpulse, the neutron density remains constant just below 10^6 n cm^{-3} due to the release of neutrons during radiative burning in the He-intershell. However, this neutron flux is not high enough to activate *s*-process nucleosynthesis.

The surface [*hs*/*ls*] and [Pb/*hs*] ratios from the beginning of the AGB phase are presented in Figures 3.8(b) and 3.8(c). The behaviour of the *s*-process indicators for the 5 $M_\odot$ model (and all the intermediate-mass models) differs from the low-mass models due to the different neutron source. For the 5 $M_\odot$ model, the ratios of [*ls*/Fe], [*hs*/Fe], [*hs*/*ls*], and [Pb/*hs*] remain constant during the AGB phase until the neutron density reaches above 10^{12} n cm^{-3}. Once the neutron density exceeds this value the ratios of [*ls*/Fe] and [*hs*/Fe] increase while [*hs*/*ls*] and [Pb/*hs*] decrease. Unlike in the low-mass models, the values of [*hs*/*ls*] and [Pb/*hs*] never reach an equilibrium value.

3.4.3. Comparison with different metallicities

We briefly compare our 2 and 5 $M_\odot$ models of [Fe/H] = −1.2 to the models of [Fe/H] = −2.3 presented in Lugaro et al. (2012) and the models of [Fe/H] = −1.7 presented in Straniero et al. (2014). As the models of Straniero et al. (2014) are α enhanced we only examine the neutron-capture elements (Ga to Bi) which are unaffected by the initial abundance of α elements.

Figure 3.9 illustrates the final neutron-capture surface abundances in [X/Fe] for each of the models. Both the models calculated here and in Lugaro et al. (2012) use the same evolutionary and post-processing codes, while the models of Cristallo et al. (2011) and Straniero et al. (2014) use the FUNS code. The dip in abundance at Nb for the Cristallo et al. (2011) and Straniero et al. (2014) models is due to the unstable isotope ^{93}Zr ($\tau_{1/2} = 1.53 \times 10^6$ years) not being decayed to the stable isotope ^{93}Nb. We include the 2 $M_\odot$, $Z = 0.001$ model from Cristallo et al. (2011) in Figure 3.9 for completeness.

Table 3.4 presents a number of abundance ratios including the *s*-process indicators. The models of Straniero et al. (2014) have a [Fe/H] value in between the other models and we would expect them to show intermediate abundance values. However, the 2 $M_\odot$ model appears to have essentially the same abundance pattern of the other models but with overall lower abundances. This is possibly the result of a lower amount of mass dredged up (0.075 $M_\odot$) for their model, probably a consequence of the α enhancement employed in these models. The 5 $M_\odot$ model of Straniero et al. (2014) has a higher surface abundance of Pb compared to the 5 $M_\odot$ model presented here and in Lugaro et al. (2012). This is due to the contribution of a small ^{13}C pocket activated after each TDU in the model of Straniero et al. (2014), which is not included in the other 5 $M_\odot$ models.

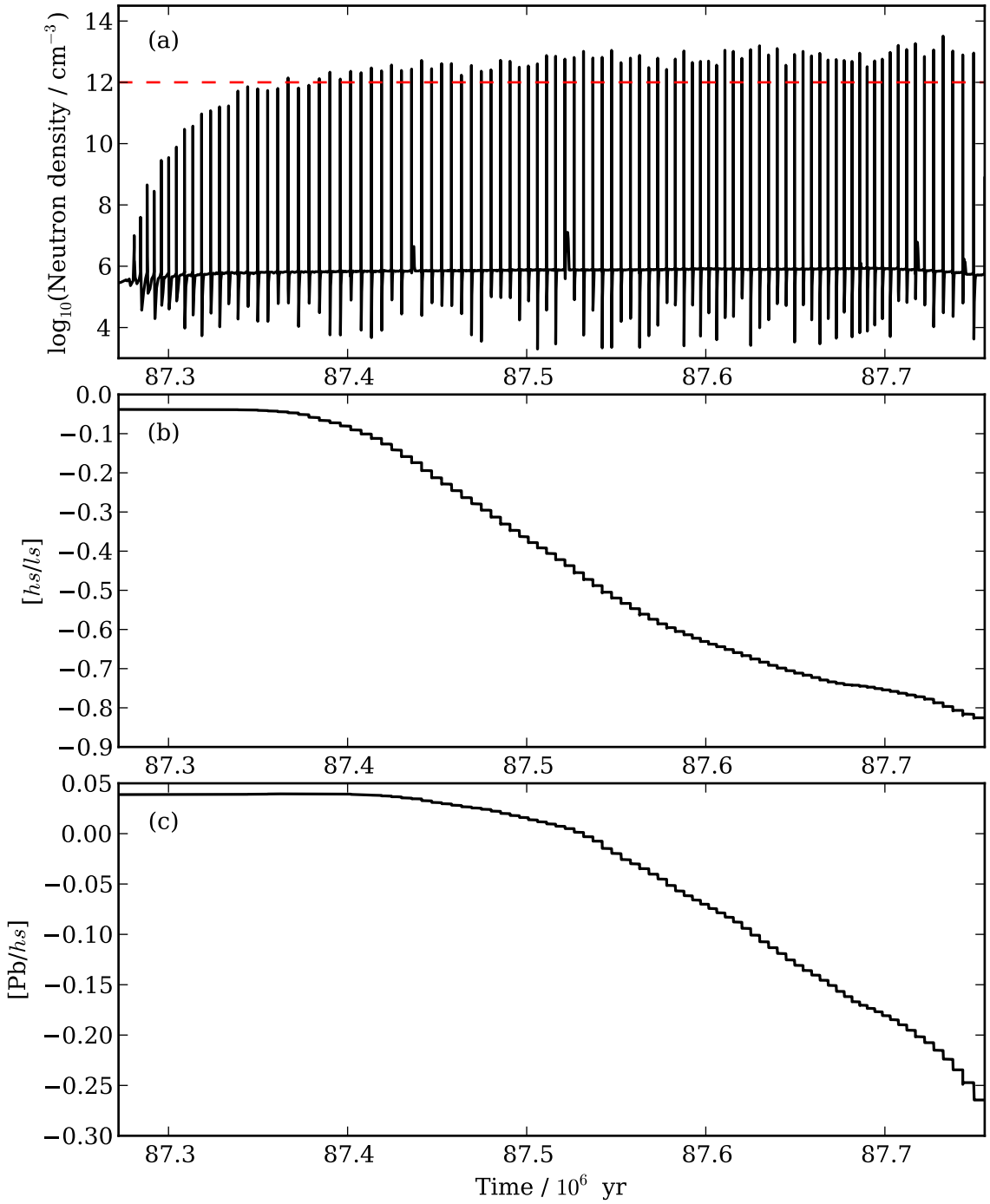

Figure 3.8 (*a*) The maximum neutron density (the red dashed line shows the density where the ^{22}Ne neutron source is efficient), (*b*) the surface [*hs*/*ls*] ratio, and (*c*) the surface [Pb/*hs*] ratio as a function of time for the 5 $M_\odot$ model from the beginning of the AGB phase.

Table 3.4 Final surface abundances of the 2 and 5 $M_\odot$ models for a number of neutron-capture elemental ratios for each metallicity.

	L12		S14		F14	
	[Fe/H] = −2.3		[Fe/H] = −1.7		[Fe/H] = −1.2	
[Rb/Fe]	1.47	1.86	0.60	1.37	0.70	1.55
[Zr/Fe]	1.96	1.74	0.94	0.98	1.53	1.32
[Rb/Zr]	−0.49	0.12	−0.34	0.39	−0.83	0.24
[*ls*/Fe]	1.87	1.72	0.89	1.00	1.43	1.34
[*hs*/Fe]	2.36	1.07	1.40	0.63	1.95	0.52
[Pb/Fe]	3.24	0.71	2.77	1.43	2.95	0.25
[*hs*/*ls*]	0.49	−0.66	0.51	−0.37	0.52	−0.82
[Pb/*hs*]	0.88	−0.36	1.37	0.80	1.01	−0.27

NB. – L12 (Lugaro et al. 2012), S14 (Straniero et al. 2014), F14 (models presented here).

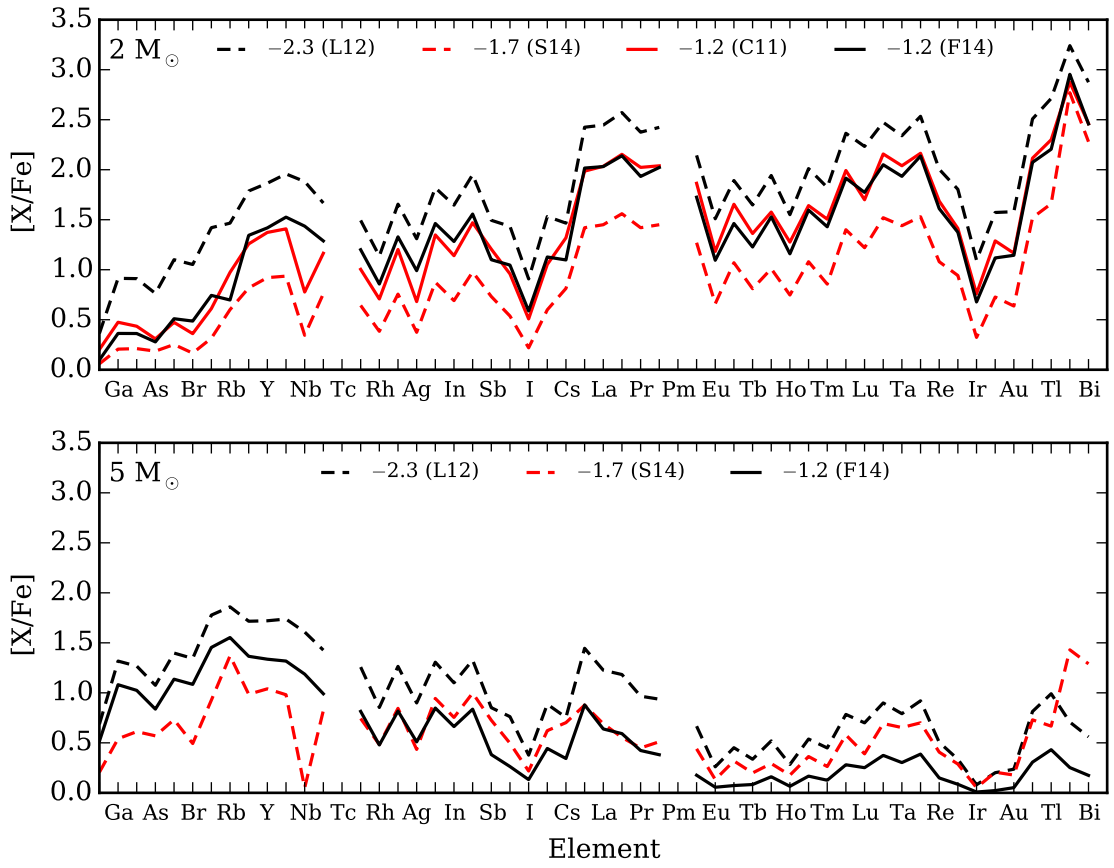

Figure 3.9 Final surface abundance ratios of neutron-capture elements for three different [Fe/H] ratios for the 2 $M_\odot$ models (top) and 5 $M_\odot$ models (bottom). Legend is as follows: C11 (Cristallo et al. 2011), L12 (Lugaro et al. 2012), S14 (Straniero et al. 2014), F14 (models presented here). The elements are ordered by increasing atomic number.

3.5. Abundance and stellar yield results

In this section we present final surface abundances and elemental stellar yields for each of the calculated models. We calculate the net stellar yield M_i (in $M_\odot$) to be,

$$M_i = \int_0^\tau [X(i) - X_0(i)] \frac{dM}{dt} dt, \tag{3.4}$$

where dM/dt is the current mass-loss rate in $M_\odot$ yr^{-1}, $X(i)$ and $X_0(i)$ are the current and initial mass fraction of species i, and τ is the total lifetime of the stellar model (Karakas 2010). For a negative net yield, the species is destroyed whereas a positive net yield indicates that the species is produced. Tables 3.5 and 3.6 present net yields of select elements for each model.

3.5.1. The light elements

In this section we present final surface abundances and yields for the light elements up to the Fe group. We discuss He, C, N, O, F, Ne, Na, Mg, and Al in detail. These elements are well known to be produced or destroyed in AGB stars (Busso et al. 1999). In Figure 3.10 we present the final surface abundances of select light elements (in [X/Fe]) for each of the models. Table 3.7 presents the final surface abundances for the ^{4}He mass fraction, C/O ratio, ^{12}C/^{13}C ratio, and [X/Fe] for the selected light elements.

He, C, N, O, and F

As presented in Table 3.7, the final ^{4}He surface abundance for the low-mass models reaches a peak value of 0.31 for the 2.25 $M_\odot$ model. This is a result of the 2.25 $M_\odot$ model experiencing the deepest extent of FDU and efficient TDU. The 2.25 $M_\odot$ model also has the highest He yield of the low-mass models with a value of 8.48×10^{-2} $M_\odot$ (see Table 3.5). The ^{4}He abundance reaches a maximum of 0.36 for the 5, 5.5, 6, and 7 $M_\odot$ models and the yield increases with increasing initial mass, with a maximum He yield of 6.06×10^{-1} $M_\odot$ for the 7 $M_\odot$ model.

The highest final surface abundance of [C/Fe] occurs for the 2.25 $M_\odot$ model with a value of 1.94. The 7 $M_\odot$ has the lowest final abundance due to very efficient HBB and a low $M_{\rm TDU}$ value (see Table 3.1). The C yield increases with increasing initial mass for the models up to 2.75 $M_\odot$. This increase in the yield follows the increase in the value of $M_{\rm TDU}$ where more C is mixed to the surface. The highest yield of C occurs for the 2.75 $M_\odot$ model as it has the maximum $M_{\rm TDU}$ for the low-mass models. For the intermediate-mass models, the yield on the whole decreases with the 7 $M_\odot$ model having the lowest yield of 2.56×10^{-4} $M_\odot$.

In Table 3.7 we present the final ^{12}C/^{13}C ratio at the surface. The ^{12}C/^{13}C ratio can be determined observationally and is a key observational constraint for stellar models. For the low-mass models, the ^{12}C/^{13}C ratio increases as TDU brings ^{12}C synthesised from He-burning to the surface. The 3 $M_\odot$ model has very inefficient HBB which results in a

Table 3.5 Net stellar yield results of selected light and neutron-capture elements for each low-mass model.

El.	1 $M_\odot$	1.25 $M_\odot$	1.25 $M_\odot$	1.5 $M_\odot$	2 $M_\odot$	2.25 $M_\odot$	2.5 $M_\odot$	3 $M_\odot$
He	8.56(-3)	2.08(-2)	3.16(-2)	6.76(-2)	8.48(-2)	8.22(-2)	8.25(-2)	7.63(-2)
C	1.92(-4)	1.57(-3)	4.94(-3)	1.65(-2)	2.22(-2)	2.34(-2)	2.53(-2)	2.44(-2)
N	1.95(-5)	5.11(-5)	8.09(-5)	1.49(-4)	1.72(-4)	1.69(-4)	1.85(-4)	2.34(-4)
O	3.59(-6)	6.82(-5)	2.16(-4)	5.34(-4)	6.32(-4)	6.34(-4)	5.17(-4)	4.71(-4)
F	5.63(-9)	1.86(-7)	7.27(-7)	3.77(-6)	6.40(-6)	7.52(-6)	6.56(-6)	4.00(-6)
Ne	5.05(-6)	1.41(-4)	5.56(-4)	2.45(-3)	3.64(-3)	4.03(-3)	2.99(-3)	2.01(-3)
Na	1.37(-7)	1.49(-6)	6.52(-6)	3.65(-5)	5.24(-5)	4.29(-5)	2.64(-5)	2.09(-5)
Mg	−2.17(-8)	1.33(-6)	6.49(-6)	3.86(-5)	6.92(-5)	1.18(-4)	1.44(-4)	1.77(-4)
Al	6.74(-8)	1.80(-7)	3.75(-7)	1.36(-6)	2.68(-6)	6.14(-6)	7.46(-6)	6.56(-6)
Si	1.22(-8)	7.36(-8)	1.82(-7)	5.84(-7)	1.16(-6)	3.46(-6)	5.99(-6)	9.09(-6)
Rb	2.69(-11)	5.76(-10)	2.51(-9)	6.89(-9)	1.40(-8)	3.41(-8)	2.62(-8)	2.41(-8)
Sr	5.51(-10)	6.55(-9)	2.68(-8)	8.65(-8)	1.25(-7)	1.37(-7)	8.33(-8)	5.44(-8)
Y	1.15(-10)	1.65(-9)	6.29(-9)	2.24(-8)	3.36(-8)	4.02(-8)	2.52(-8)	1.55(-8)
Zr	2.33(-10)	4.64(-9)	1.65(-8)	6.23(-8)	9.57(-8)	1.19(-7)	8.14(-8)	5.41(-8)
Ba	1.35(-10)	9.32(-9)	3.09(-8)	1.32(-7)	2.02(-7)	2.23(-7)	1.34(-7)	8.69(-8)
La	1.44(-11)	9.23(-10)	3.14(-9)	1.35(-8)	2.07(-8)	2.28(-8)	1.30(-8)	7.81(-9)
Ce	5.85(-11)	2.87(-9)	1.04(-8)	4.49(-8)	7.03(-8)	8.00(-8)	4.80(-8)	2.94(-8)
Pb	4.69(-9)	1.19(-7)	4.14(-7)	1.27(-6)	1.65(-6)	1.64(-6)	1.27(-6)	9.11(-7)

NB. – Yields are in solar masses and are expressed in the form $n(m) = n \times 10^m$.

final $^{12}C/^{13}C$ ratio of 89. As a result of the CN cycle during HBB the $^{12}C/^{13}C$ ratio for the intermediate-mass models reaches an equilibrium value of approximately 3. This is in agreement with the value found by Frost et al. (1998). The final $^{12}C/^{13}C$ ratio is greater than 3 as it increases as a result of HBB ceasing while TDU continues.

All the models become carbon-rich with the C/O ratio increasing to above unity. The low-mass models have a high final C/O ratio. This is because the surface abundance of O only increases slightly compared to the increase of C. Despite the more massive models having a higher $T_{\rm bce}$ and more efficient HBB, the 4 $M_\odot$ model has the lowest C/O ratio of 3.38 of all the intermediate-mass models.

The final surface abundance of N is reasonably constant for the low-mass models, with the increase in [N/Fe] to $\sim$ 0.5 a result of FDU. The N yield increases with increasing initial mass from 1.95×10^{-5} $M_\odot$ for the 1 $M_\odot$ model to 2.34×10^{-4} $M_\odot$ for the 3 $M_\odot$ model. The intermediate-mass models experience HBB and, as such, have a higher final surface abundance of N compared to the low-mass models. The 4 $M_\odot$ model has the highest [N/Fe] ratio (with a value of 2.62) and N yield (5.94×10^{-2} $M_\odot$) of all the models. This is a result of the 4 $M_\odot$ model having the largest amount of material brought to the surface, which provides additional primary C to be converted to N.

The low-mass models between 2 and 2.5 $M_\odot$ have a similar final surface abundance of O, with an [O/Fe] ratio of around 0.3. The final O abundance is lower for the intermediate-

Table 3.6 Net stellar yield results of selected light and neutron-capture elements for each intermediate-mass model.

El.	3.25 $M_\odot$	3.5 $M_\odot$	4 $M_\odot$	4.5 $M_\odot$	5 $M_\odot$	5.5 $M_\odot$	6 $M_\odot$	7 $M_\odot$
He	6.89(-2)	1.01(-1)	2.66(-1)	3.57(-1)	4.39(-1)	5.01(-1)	5.48(-1)	6.06(-1)
C	1.95(-2)	1.56(-2)	2.39(-3)	3.04(-3)	2.63(-3)	1.80(-3)	1.74(-3)	2.56(-4)
N	1.24(-3)	8.53(-3)	5.94(-2)	5.61(-2)	5.22(-2)	4.33(-2)	3.29(-2)	1.26(-2)
O	2.19(-4)	2.99(-4)	3.09(-4)	−2.62(-4)	−8.28(-4)	−1.24(-3)	−1.61(-3)	−2.20(-3)
F	1.27(-6)	1.28(-6)	1.45(-7)	7.97(-8)	−4.54(-9)	−6.43(-8)	−1.02(-7)	−1.41(-7)
Ne	6.58(-4)	6.77(-4)	2.93(-3)	2.21(-3)	1.64(-3)	9.32(-4)	4.84(-4)	5.81(-5)
Na	1.04(-5)	1.26(-5)	7.57(-5)	5.94(-5)	3.86(-5)	1.64(-5)	3.65(-6)	−8.63(-6)
Mg	9.45(-5)	1.02(-4)	7.53(-4)	6.56(-4)	4.47(-4)	2.75(-4)	1.39(-4)	−6.84(-5)
Al	3.14(-6)	3.15(-6)	4.01(-5)	4.88(-5)	5.86(-5)	6.89(-5)	8.55(-5)	7.00(-5)
Si	6.73(-6)	7.63(-6)	3.37(-5)	3.19(-5)	2.68(-5)	2.22(-5)	2.57(-5)	7.73(-5)
Rb	1.48(-8)	1.72(-8)	1.53(-7)	1.64(-7)	1.38(-7)	1.12(-7)	8.50(-8)	2.41(-8)
Sr	1.72(-8)	2.05(-8)	2.20(-7)	2.38(-7)	2.04(-7)	1.67(-7)	1.22(-7)	3.06(-8)
Y	2.96(-9)	3.56(-9)	4.40(-8)	4.85(-8)	4.05(-8)	3.38(-8)	2.40(-8)	5.79(-9)
Zr	5.23(-9)	6.28(-9)	8.99(-8)	1.01(-7)	8.27(-8)	6.93(-8)	4.78(-8)	1.09(-8)
Ba	7.75(-10)	9.17(-10)	2.01(-8)	2.28(-8)	1.78(-8)	1.50(-8)	9.15(-9)	1.77(-9)
La	3.26(-11)	4.03(-11)	1.06(-9)	1.17(-9)	8.93(-10)	7.55(-10)	4.46(-10)	8.11(-11)
Ce	7.83(-11)	9.41(-11)	2.41(-9)	2.71(-9)	2.01(-9)	1.68(-9)	9.64(-10)	1.75(-10)
Pb	1.60(-10)	1.79(-10)	2.51(-9)	2.90(-9)	2.27(-9)	1.82(-9)	9.65(-10)	1.72(-10)

NB. – Yields are in solar masses and are expressed in the form $n(m) = n \times 10^m$.

mass models due to its destruction from HBB. For the models with a mass of 4.5 $M_\odot$ and higher, the [O/Fe] abundances are negative, down to −0.64 for the 7 $M_\odot$ model. As expected, the 7 $M_\odot$ model has the lowest net yield of O with -2.20×10^{-3} $M_\odot$. The highest yield of 6.34×10^{-4} $M_\odot$ occurs for the 2.5 $M_\odot$ model.

There is only one stable isotope of F (^{19}F) which is produced through the ^{15}N(α,γ)^{19}F reaction in the He-intershell (Jorissen et al. 1992; Mowlavi et al. 1996; Lugaro et al. 2004; Abia et al. 2009). The F synthesised during the preceding TP is mixed to the surface during TDU. The final F surface abundance increases for each model, with [F/Fe] up to 2.27 for the 2.5 $M_\odot$, before decreasing to sub-solar values for the 6 and 7 $M_\odot$ models. The decrease in F is caused by the destruction of ^{19}F through α capture to produce ^{22}Ne. In the more massive models, the F yield also decreases as temperatures during HBB allow for the destruction of F to take place via the ^{19}F(p,α)^{16}O reaction. The 5, 5.5, 6, and 7 $M_\odot$ models have a negative F yield, with the lowest net yield of -1.41×10^{-7} $M_\odot$ occurring for the 7 $M_\odot$ model.

Ne, Na, Mg, and Al

Only Ne and Na are noticeably affected by FDU and SDU whereas the surface abundances of Mg and Al do not change during FDU for the low-mass models and changes by only 35 per cent for ^{27}Al for the intermediate-mass models. Of all the models, the 2.25 $M_\odot$ has the highest final surface abundance of [Ne/Fe] and [Na/Fe] as a result of FDU and TDU with

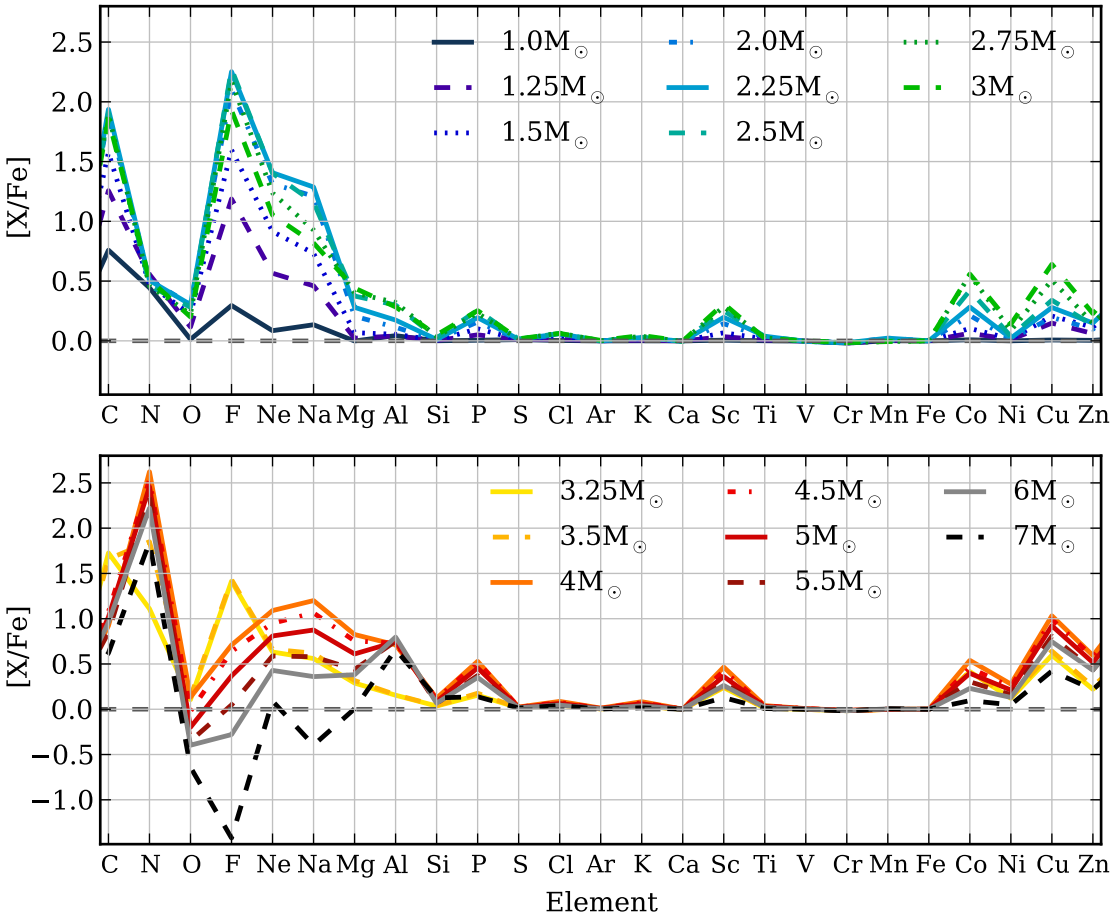

Figure 3.10 Final surface abundances relative to Fe for each of the models for the light elements from C to Zn. The elements are ordered by increasing atomic number.

1.41 and 1.29, respectively (Table 3.7). The Ne-Na chain is activated during HBB for the intermediate-mass models and the main result of the Ne-Na chain is the production of ^{23}Na, the only stable isotope of Na, at the expense of ^{22}Ne. The 4 $M_\odot$ model has the highest yield of Na with 7.57×10^{-5} $M_\odot$. The 7 $M_\odot$ model is the only model with a negative Na yield.

The highest final surface abundances of Mg and Al occur for the 4 and 6 $M_\odot$ models, respectively. This is also reflected in the net yields. The yield of Mg increases with increasing initial mass before decreasing once the peak yield of 7.53×10^{-4} $M_\odot$ is reached for the 4 $M_\odot$ model. The 3.25 and 3.5 $M_\odot$ models are exceptions to this trend. This is because the models (compared to lower and higher mass models) have less TDU, the absence of a PMZ resulting in fewer neutron captures onto ^{24}Mg, lower activation of the ^{22}Ne + α reaction compared to intermediate-mass models, and the Mg-Al chain is not activated. The production of Al increases with increasing mass for the intermediate-mass models however the 7 $M_\odot$ model has a lower Al yield than the 6 $M_\odot$ due to HBB temperatures being high enough for the production of ^{28}Si to occur at the expense of ^{27}Al.

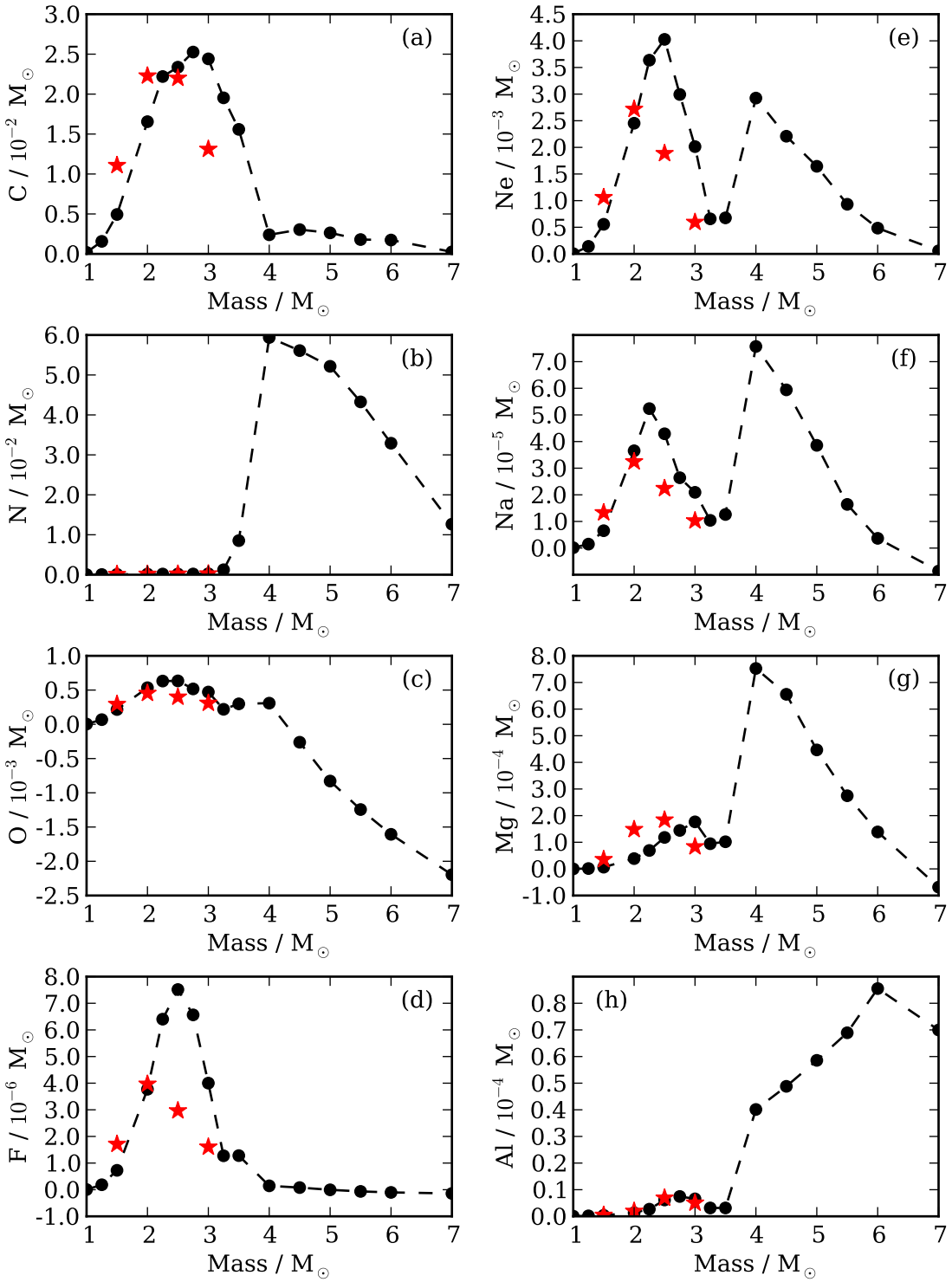

Figure 3.11 Net yields of select elements lighter than Si as a function of initial mass. Results from Cristallo et al. (2011) are shown as red stars.

Table 3.7 Final surface ^{4}He mass fraction, C/O ratio, ^{12}C/^{13}C ratio, and [X/Fe] ratios for selected light elements.

Mass	^{4}He	C/O	^{12}C/^{13}C	[C/Fe]	[N/Fe]	[O/Fe]	[F/Fe]	[Ne/Fe]	[Na/Fe]	[Mg/Fe]	[Al/Fe]
1.00	0.28	3.07	160	0.76	0.44	0.01	0.30	0.09	0.13	0.00	0.04
1.25	0.29	7.67	575	1.26	0.45	0.12	1.19	0.57	0.40	0.02	0.04
1.50	0.29	12.47	1232	1.58	0.47	0.22	1.60	0.91	0.73	0.07	0.05
2.00	0.30	21.04	2687	1.88	0.51	0.30	2.10	1.31	1.21	0.21	0.11
2.25	0.31	23.80	3129	1.94	0.51	0.30	2.25	1.41	1.29	0.28	0.17
2.50	0.30	23.47	2752	1.91	0.46	0.28	2.27	1.40	1.16	0.37	0.30
2.75	0.29	26.02	2355	1.90	0.46	0.22	2.17	1.24	0.93	0.40	0.32
3.00	0.29	24.82	89	1.85	0.51	0.19	1.92	1.05	0.81	0.44	0.28
3.25	0.28	22.93	11	1.72	1.11	0.10	1.41	0.63	0.56	0.29	0.15
3.50	0.29	18.32	6.27	1.66	1.85	0.13	1.43	0.66	0.62	0.31	0.16
4.00	0.34	3.38	5.97	0.91	2.62	0.12	0.70	1.08	1.19	0.82	0.70
4.50	0.35	6.91	7.99	1.07	2.53	−0.03	0.63	0.94	1.06	0.75	0.72
5.00	0.36	9.07	7.56	1.01	2.45	−0.20	0.36	0.80	0.87	0.61	0.74
5.50	0.36	8.69	6.11	0.84	2.34	−0.35	0.04	0.58	0.58	0.44	0.75
6.00	0.36	12.58	8.53	0.96	2.22	−0.40	−0.28	0.43	0.36	0.38	0.79
7.00	0.36	10.09	6.65	0.62	1.84	−0.64	−1.42	0.09	−0.40	0.00	0.66

Other light elements

There is a slight enhancement of up to approximately 0.15 dex for Si, S, Cl, and Ar. The 7 $M_\odot$ model produces the most Si with a net yield of 7.73×10^{-5} $M_\odot$ (Table 3.6). [P/Fe] increases by around 0.5 dex for the intermediate-mass models with the maximum enhancement occurring for the 4 $M_\odot$ model. Sc is produced with the 4 $M_\odot$ model showing the largest enhancement of [Sc/Fe] ($\approx$ 0.4 dex). Of the Fe-group elements, Cu is enhanced the most in the 4 $M_\odot$ model increasing by 1.03 dex for [Cu/Fe]. The abundance of [Zn/H] has been proposed to be a good proxy of [Fe/H] in planetary nebulae (e.g. Dinerstein & Geballe 2001; Smith et al. 2014). The low-mass models have [Zn/Fe] enhancements between 0 and 0.32 dex with the 1 $M_\odot$ model having no increase and the 3 $M_\odot$ model having the largest increase. The smallest enhancement for the intermediate-mass models occurs for the 7 $M_\odot$ model with a [Zn/Fe] ratio of 0.22 whereas the 4 $M_\odot$ model has [Zn/Fe] increase by 0.59 dex.

Comparison with Cristallo et al. (2011)

Figure 3.11 also presents the net yields of Cristallo et al. (2011) for each of the initial stellar masses in common with the models presented here: 1.5, 2, 2.5, and 3 $M_\odot$. For these low masses, the net yield of C (and O) follows the total amount of material mixed to the surface by TDU. The 2.5 and 3 $M_\odot$ models of Cristallo et al. (2011) have a lower value of $M_{\rm TDU}$, which results in a lower C (and O) yield in Figure 3.11(a); with the largest yield difference ΔM_i being 1.13×10^{-2} $M_\odot$ for the 3 $M_\odot$ model.

The net yield of N agrees with the predictions of Cristallo et al. (2011), with the N yield

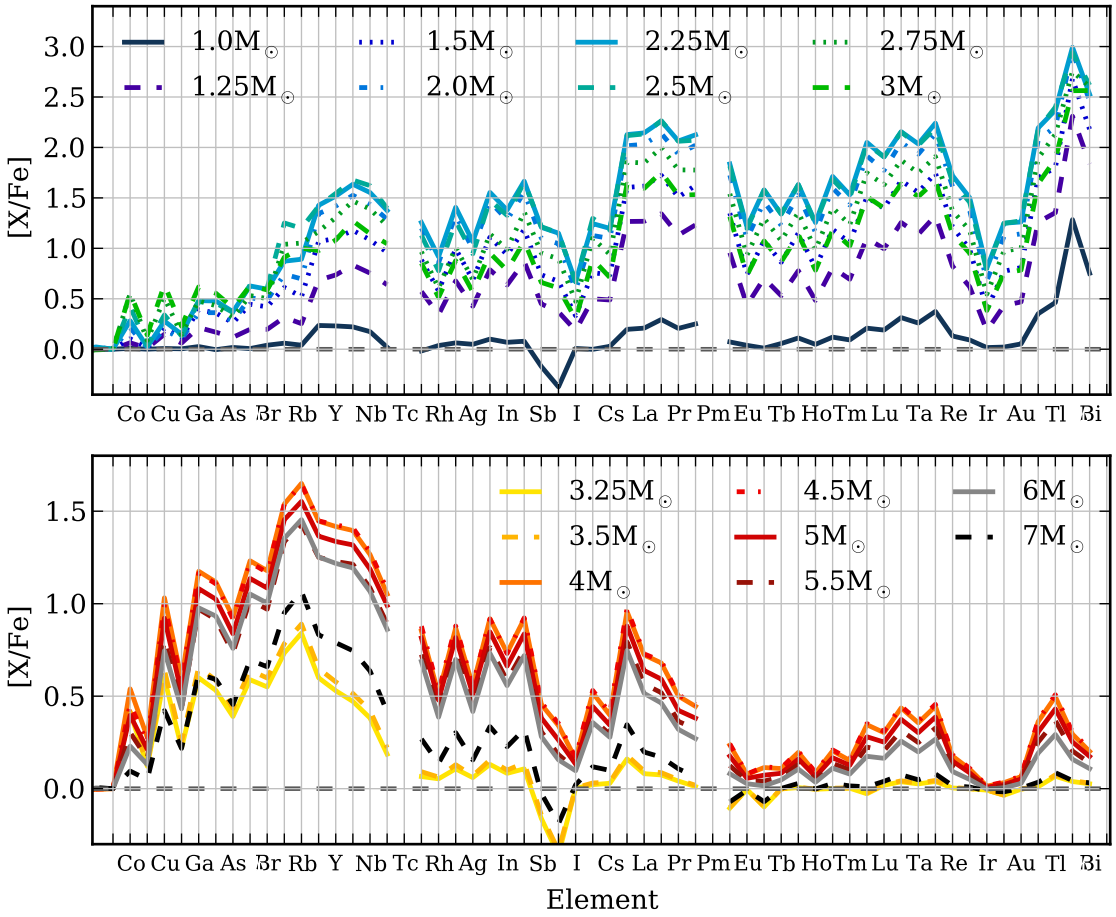

Figure 3.12 Final surface abundances relative to Fe for each of the models for the elements heavier than Mn. Low-mass models are presented in the top plot while intermediate-mass models are presented in the bottom plot. The elements are ordered by increasing atomic number. For an explanation of why some abundances have a value less than solar, see the caption of Figure 3.4 and Section 3.2.

increasing with increasing initial mass as a result of FDU. For the Cristallo et al. (2011) yields of F, Ne, and Na, the 2 $M_\odot$ model has the largest net yield as a result of having the largest value of $M_{\rm TDU}$. For the models presented here, the yields peak at 2.5 $M_\odot$ except for Na which peaks at 2.25 $M_\odot$. The yields of Mg and Al peak at 3 $M_\odot$ and 2.75 $M_\odot$, respectively.

3.5.2. The neutron-capture elements

In this section we present final surface abundances and net stellar yield predictions for selected neutron-capture elements (Rb, Sr, Y, Zr, Ba, La, Ce, and Pb). Table 3.8 presents the final surface abundances for selected neutron-capture elements and *s*-process indicators. The distribution of the final surface abundances [X/Fe] for these elements is shown in Figure 3.12.

As illustrated in Figure 3.12, the low-mass models produce a final surface abundance distribution of the neutron-capture elements that has peaks at Sr, Zr, Ba, and Pb as discussed for the case of the 2 $M_\odot$ model. In comparison the intermediate-mass models produce a

Table 3.8 Final surface abundances for select neutron-capture elements and *s*-process indicators.

Mass	[Rb/Fe]	[Sr/Fe]	[Y/Fe]	[Zr/Fe]	[Ba/Fe]	[La/Fe]	[Ce/Fe]	[Pb/Fe]	[*ls*/Fe]	[*hs*/Fe]
1.00	0.04	0.24	0.23	0.22	0.20	0.21	0.29	1.28	0.23	0.18
1.25	0.25	0.68	0.74	0.83	1.27	1.27	1.34	2.31	0.75	1.18
1.50	0.52	1.07	1.10	1.18	1.60	1.62	1.72	2.68	1.11	1.55
2.00	0.70	1.34	1.42	1.53	2.02	2.03	2.14	2.95	1.43	1.95
2.25	0.89	1.43	1.52	1.64	2.13	2.14	2.26	2.99	1.53	2.06
2.50	1.20	1.42	1.54	1.68	2.12	2.13	2.26	2.94	1.55	2.03
2.75	1.05	1.17	1.30	1.47	1.85	1.85	2.00	2.75	1.31	1.75
3.00	1.00	0.98	1.08	1.27	1.64	1.59	1.75	2.56	1.11	1.51
3.25	0.84	0.60	0.53	0.47	0.16	0.08	0.07	0.04	0.53	0.03
3.50	0.89	0.65	0.58	0.51	0.18	0.10	0.09	0.04	0.58	0.04
4.00	1.65	1.45	1.42	1.40	0.96	0.72	0.68	0.29	1.41	0.58
4.50	1.65	1.45	1.43	1.41	0.97	0.73	0.69	0.31	1.42	0.59
5.00	1.55	1.37	1.34	1.32	0.88	0.64	0.59	0.25	1.33	0.51
5.50	1.43	1.25	1.23	1.21	0.79	0.57	0.52	0.20	1.23	0.44
6.00	1.45	1.25	1.22	1.19	0.75	0.52	0.46	0.16	1.22	0.40
7.00	1.07	0.83	0.79	0.75	0.35	0.20	0.17	0.04	0.79	0.13

peak at Rb. This difference is due to a combination of the addition of a PMZ for the low-mass models and the activation of the ^{22}Ne neutron source for the intermediate-mass models.

The final surface abundance of Rb increases with increasing initial mass for the low-mass models, up to 1.20 for the 2 $M_\odot$ model before decreasing slightly for the 2.75 and 3 $M_\odot$ models. This increase is mainly the result of the mild activation of the ^{22}Ne neutron source. For the intermediate-mass models, the highest final surface abundance and yield of all the neutron-capture elements occurs for Rb where branching points are activated and the total neutron exposure is lower than in the low-mass models. The highest final surface abundance for Rb occurs for the 4 and 4.5 $M_\odot$ models where both have a final [Rb/Fe] value of 1.65. The 4.5 $M_\odot$ model has the highest yield of Rb with 1.64×10^{-7} $M_\odot$.

Each model has a similar final abundance for [Sr/Fe], [Y/Fe], and [Zr/Fe], three first *s*-process peak elements. Of the three elements, Sr has the lowest final abundance and Zr has the highest for each of the low-mass models. For the intermediate-mass models, the trend is reversed with Sr having the highest abundance and Zr, the lowest of the three elements. Of the intermediate-mass models, the 4.5 $M_\odot$ model has the highest abundances with 1.45, 1.43, and 1.41 for Sr, Y, and Zr, respectively. This is also reflected in the yields of the 4.5 $M_\odot$ model where it has the highest Sr and Y yields of all the models, 2.38×10^{-7} and 4.85×10^{-8} $M_\odot$, respectively. For Zr, the 2.5 $M_\odot$ model has the highest yield of 1.19×10^{-7} $M_\odot$.

For the low-mass models, the final surface abundances of Ba, La, and Ce are higher than the abundances of Sr, Y, and Zr. The 2.25 $M_\odot$ model has the highest final [Ba/Fe], [La/Fe], and [Ce/Fe] values of all the models (see Table 3.8). The abundances of Ba, La, and Ce for the intermediate-mass models never reach above enhancements of 1 dex. The 4.5 $M_\odot$ model once again has the highest final abundances of the intermediate-mass models for

these three elements whereas the 7 $M_\odot$ has the lowest. Of all the models, the 2.5 $M_\odot$ model has the highest yields for Ba, La, and Ce with 2.23×10^{-7}, 2.28×10^{-8}, and 8.00×10^{-8} $M_\odot$, respectively.

The low-mass models produce more Pb compared to the intermediate-mass models (Figure 3.12). Once the first and second *s*-process peaks reach equilibrium, any increase in their abundance is prevented and only the abundance of Pb increases. The value of [Pb/Fe] reaches a maximum value of 2.99 for the 2.25 $M_\odot$ model. The intermediate-mass models produce minimal Pb as discussed in the case of the 5 $M_\odot$ model, with the final surface abundance ranging from 0.04 for the 3.25 $M_\odot$ model to 0.31 for the 4.5 $M_\odot$ model. For the low-mass models, the Pb yield increases with increasing mass before reaching a plateau of approximately 1.7×10^{-6} $M_\odot$ for the 2.25 to 2.5 $M_\odot$ models (see Figure 3.13). The Pb yield then drops below approximately a few times 10^{-9} $M_\odot$ for the intermediate-mass models.

Figure 3.14 presents the distribution of the final surface abundance of the *s*-process indicators [*ls*/Fe], [*hs*/Fe], [Pb/Fe], [*hs*/*ls*], [Pb/*hs*], and [Rb/Zr] with initial mass. The [*ls*/Fe] ratio increases with increasing initial mass for the low-mass models up to 2.5 $M_\odot$ before decreasing for the 2.75, 3, and 3.25 $M_\odot$ models. The [*ls*/Fe] ratio then increases to 1.43 for the 4.5 $M_\odot$ model before decreasing again with increasing initial mass. The [*hs*/Fe] and [Pb/Fe] values for the intermediate-mass models are less than 0.6.

Figures 3.14(d) and 3.14(e) illustrate the trend of the *s*-process indicators [*hs*/*ls*] and [Pb/*hs*] with initial mass. These intrinsic *s*-process indicators are independent of the amount of TDU and help constrain the neutron source and neutron exposure for the *s*-process. The low-mass models, excluding the 1 $M_\odot$ model, plateau at approximately 0.5 for [*hs*/*ls*] while the intermediate-mass plateau at a sub-solar value of around −0.8. For [Pb/*hs*], the low-mass models fluctuate between $\sim$ 0.9 and 1.2. The intermediate-mass models have a sub-solar value of approximately −0.2 with the 3.25 and 3.5 $M_\odot$ models having a value close to solar.

Figure 3.14(f) illustrates the trend of the final surface [Rb/Zr] ratio with initial mass, where Rb and Zr are both first peak neutron-capture elements. This ratio is an indicator of the neutron density with a positive ratio resulting from higher densities produced by the ^{22}Ne neutron source. The intermediate-mass models show a fairly constant [Rb/Zr] ratio; between 0.2 and 0.4. The low-mass models, however, first decrease with increasing initial mass from −0.2 for the 1 $M_\odot$ model to −0.8 for the 2 $M_\odot$ model, then increase to approximately −0.3 dex for the 3 $M_\odot$ model. The increase in [Rb/Zr] is due to temperatures increasing in the pulse-driven convective zone so that the ^{22}Ne neutron source is mildly activated.

Comparison with Cristallo et al. (2011)

Figure 3.13 also presents the yield predictions from Cristallo et al. (2011) for the 1.5, 2, 2.5, and 3 $M_\odot$ models. With the exception of Rb and Zr, the Cristallo et al. (2011) yields for the *s*-process elements shown in Figure 3.13 have the highest value for the 2 $M_\odot$, which has the largest $M_{\rm TDU}$ value of the four models. In contrast, the yield predictions of the models presented here peak at 2.5 $M_\odot$ except for Pb which peaks at 2.25 $M_\odot$. The yield of Pb reaches

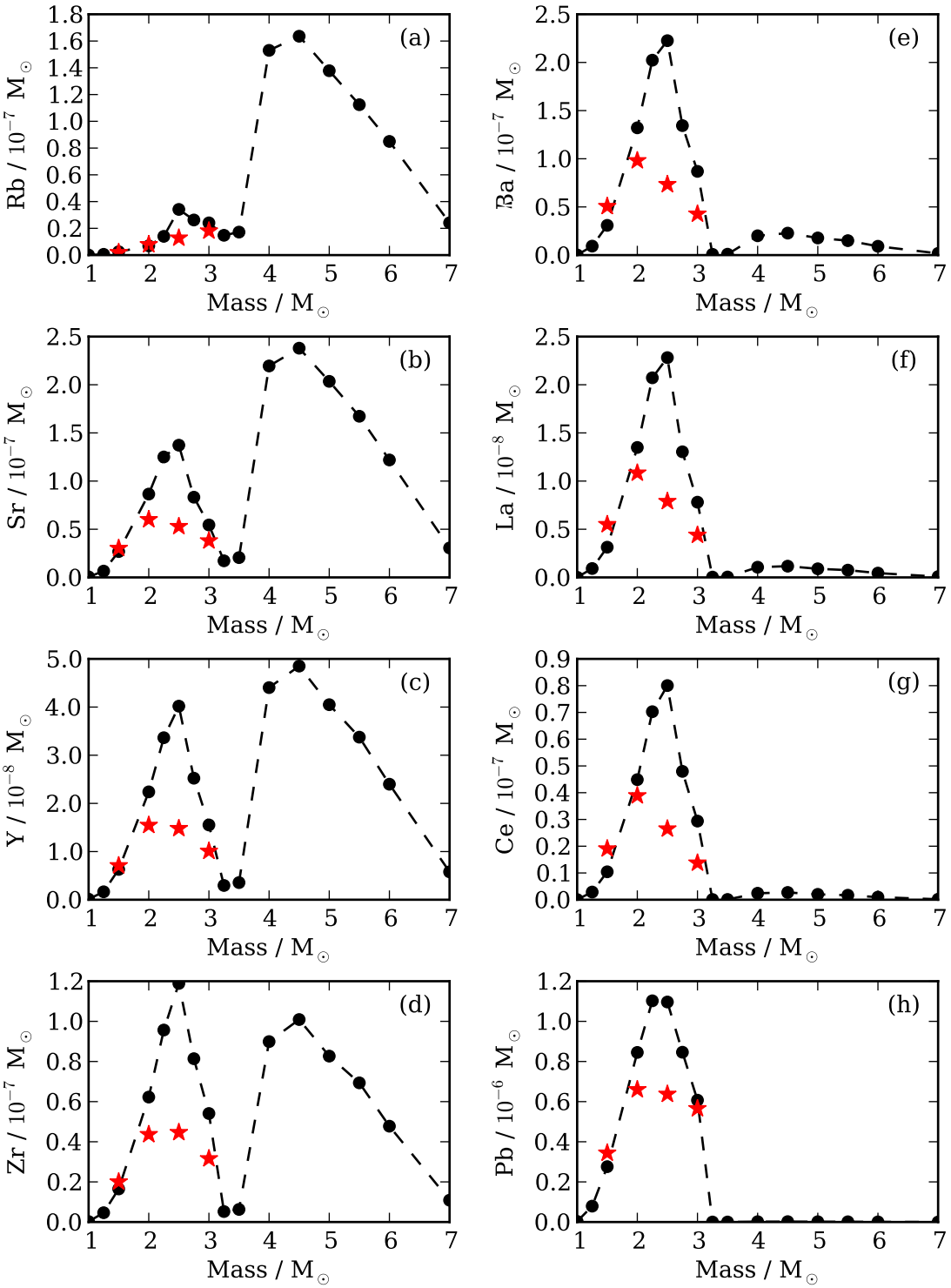

Figure 3.13 Net yields of select neutron-capture elements as a function of initial mass. Results from Cristallo et al. (2011) are shown as red stars.

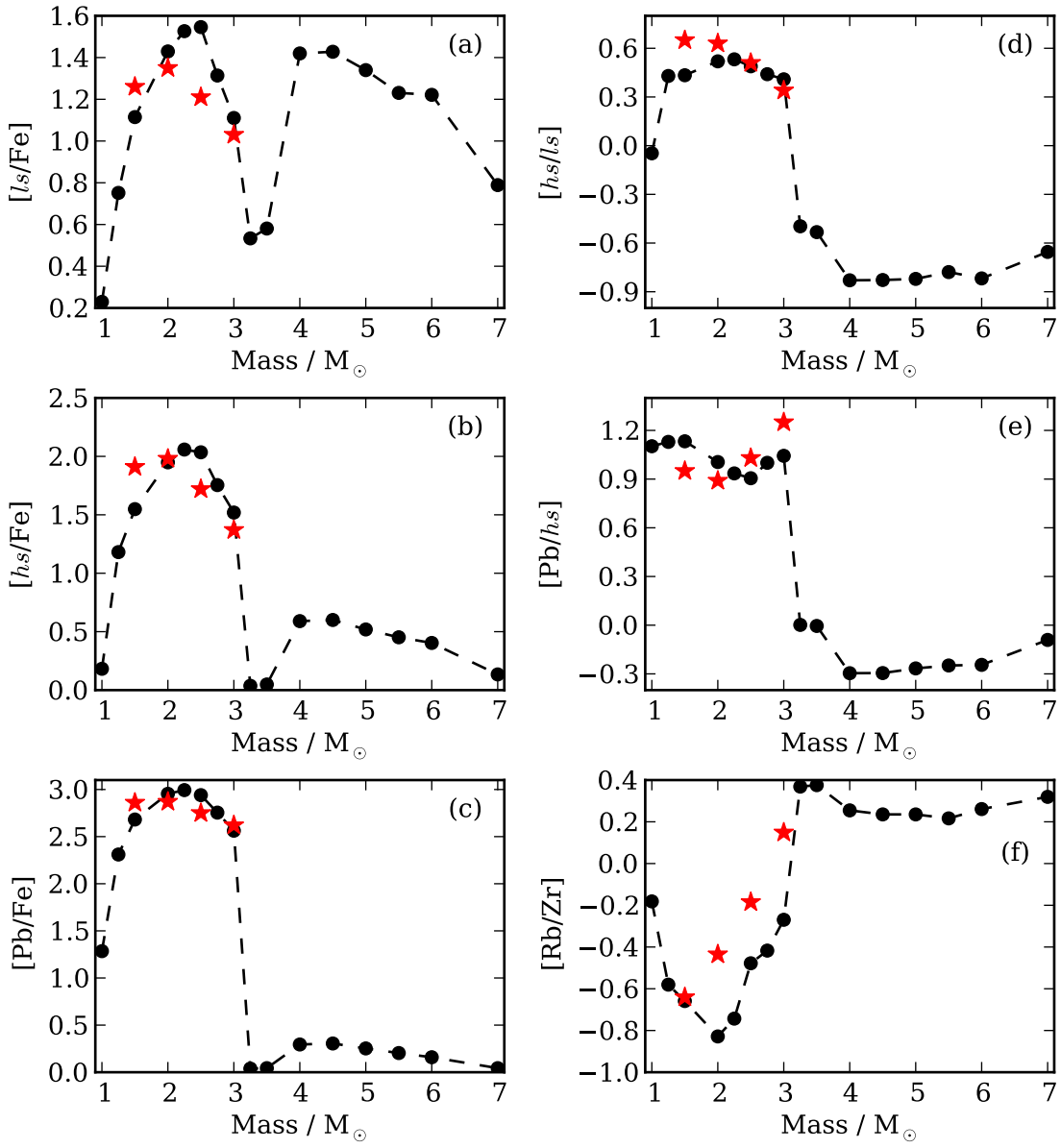

Figure 3.14 Distribution of [*hs*/*ls*] and [Pb/*hs*] with initial mass. Results from Cristallo et al. (2011) are shown as red stars.

a plateau between 2.25 $M_\odot$ and 2.5 $M_\odot$. The largest difference in the yield predictions occurs for the 2.5 $M_\odot$ model.

Figure 3.14 presents *s*-process indicator predictions for the Cristallo et al. (2011) models. The *s*-process indicators show a similar trend with mass between the Cristallo et al. (2011) models and the models presented here. The [*ls*/Fe], [*hs*/Fe], and [Pb/Fe] increase with increasing mass before reaching a peak and decreasing. The low-mass models presented here show a flat distribution for [*hs*/*ls*] of approximately 0.5 dex whereas the [*hs*/*ls*] predictions of Cristallo et al. (2011) decrease with increasing initial mass, from 0.65 dex to 0.34 dex. The values of [Pb/*hs*] fluctuate between $\sim$ 0.9 and 1.2 however the models of Cristallo et al. (2011) have [Pb/*hs*] mostly increasing with increasing initial mass. The [Rb/Zr] ratios are higher for the Cristallo et al. (2011) models, due to higher peak temperatures during TPs (see Table 3.1). Note that the rate of the ^{22}Ne source we use from Iliadis et al. (2010) is comparable to the Jaeger et al. (2001) rate used by Cristallo et al. (2011). The final abundances of [Zr/Fe] are lower for the Cristallo et al. (2011) models (excluding the 1.5 $M_\odot$ model) further increasing the final [Rb/Zr] ratio.

3.6. Effects of varying the mass of the PMZ

The extent in mass of the PMZ and the profile of the proton abundance in the PMZ are unknown parameters which introduce additional uncertainty into the elemental abundances and stellar yields for the low-mass AGB stellar models (Straniero et al. 2009). Here, we investigate the effect of varying the extent in mass of the PMZ, while keeping fixed the exponential profile of the proton abundance. We have computed the 3 $M_\odot$ model using three different values for the extent in mass of the PMZ: $(0.5, 1, 2) \times 10^{-3}$ $M_\odot$ as well as a model without the inclusion of a PMZ.

The difference in the final surface abundances of the light elements compared to the standard PMZ mass of 5×10^{-4} $M_\odot$ is shown in Figure 3.15. The model with a PMZ of 2×10^{-3} $M_\odot$ has the largest increase in [X/Fe] for elements lighter than Fe (excluding C) with respect to the standard case; the largest increase is exhibited by Ne, Na, and P where Δ[Ne/Fe], Δ[Na/Fe], and Δ[P/Fe] are approximately +0.3. Between the model with the standard PMZ and the Cristallo et al. (2011) model, the [F/Fe] ratio shows the largest difference of 0.4 dex. The final abundances of [Ne/Fe] and [Na/Fe] are also lower by approximately 0.2 dex in the Cristallo et al. model compared to our standard PMZ case.

As a larger PMZ extends over a larger mass range in the intershell, it reaches into regions of higher temperature. The higher temperatures cause the ^{13}C pocket to form sooner and deeper in the intershell for the models with a more massive PMZ compared with the standard PMZ mass. The larger PMZ also results in larger ^{13}C and ^{14}N pockets forming in the intershell. The extra ^{14}N is captured by α particles during subsequent TPs to produce ^{22}Ne. The increases in Ne and Na are therefore the result of the increased production of ^{22}Ne, where the ^{22}Ne is dredged to the surface. Some of the newly synthesised ^{22}Ne is captured by protons in the H-shell during the next interpulse period to make extra ^{23}Na.

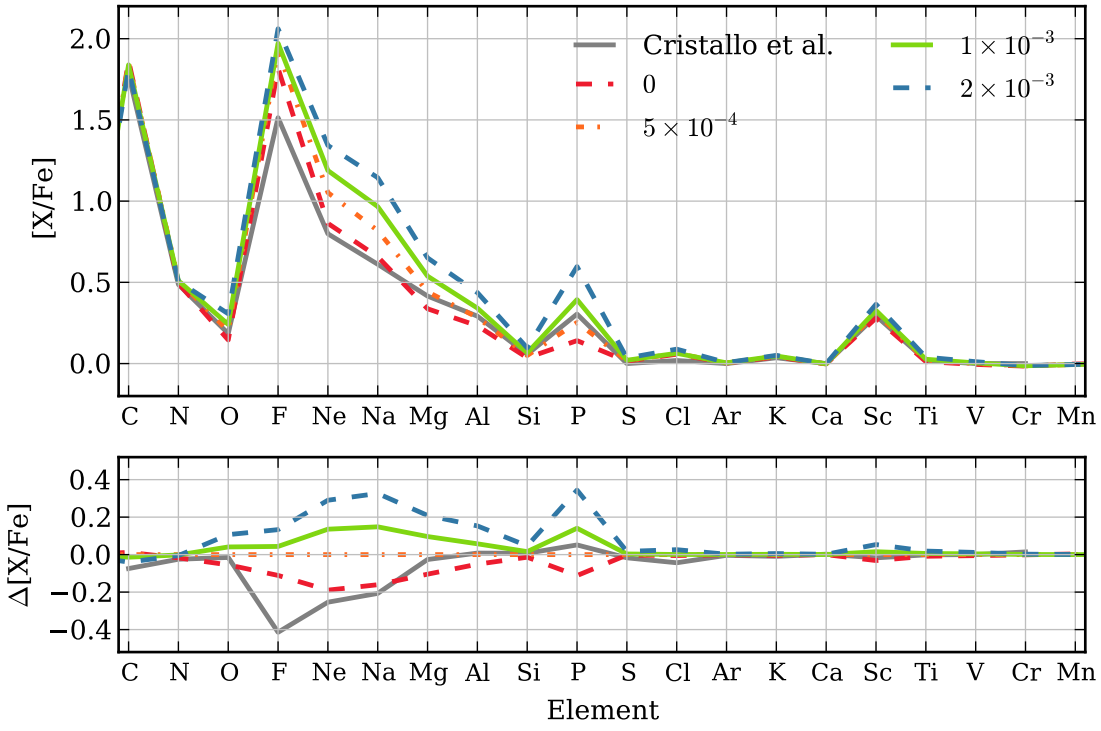

Figure 3.15 Final surface abundance ratios for each 3 $M_\odot$ model with a different PMZ mass (in units of $M_\odot$ as indicated in the legend) for the elements lighter than Fe. The final surface abundances for the 3 $M_\odot$ model of Cristallo et al. (2011) are also presented. The bottom panel illustrates the absolute difference between each model and the standard PMZ mass, 5×10^{-4} $M_\odot$. The elements are ordered by increasing atomic number.

When compared to the standard case, the model without a PMZ produces lower abundances with [Ne/Fe] and [Na/Fe] showing deficiencies of approximately −0.2 dex.

Of the elements between Si and Mn, only P shows a non-negligible production due to the increase in the mass of the PMZ. There is only one stable isotope of P (^{31}P) and it can be produced through neutron capture in AGB stars. The increase in [P/Fe] with increasing PMZ mass is due to the increased number of neutrons available for neutron capture.

The effect of the PMZ mass on the final surface abundance distribution for the neutron-capture elements is illustrated in Figure 3.16. The height of the abundance peaks increases with increasing PMZ mass with the general shape of the distribution of the *ls* and *hs* elements remaining the same. The higher temperatures reached by a more massive PMZ increases the rate of the ^{13}C(α,n)^{16}O reaction resulting in a higher peak neutron density. This has the effect of increasing the efficiency of the branching points at ^{85}Kr and ^{86}Rb producing more ^{86}Kr and ^{87}Rb, both of which have a magic number of neutrons. Figure 3.16 shows that [Kr/Fe] has the largest increase between the model with a PMZ mass of 2×10^{-3} $M_\odot$ and the model with the standard PMZ.

We attribute the smaller increase in the Pb abundance with increasing PMZ mass (compared to the *ls* and *hs* elements) to the lower neutron exposure experienced in each ^{13}C pocket (see e.g., Gallino et al. 1998). Compared to the model with the standard PMZ mass, the neutron exposures for models with a more massive PMZ become increasingly lower with

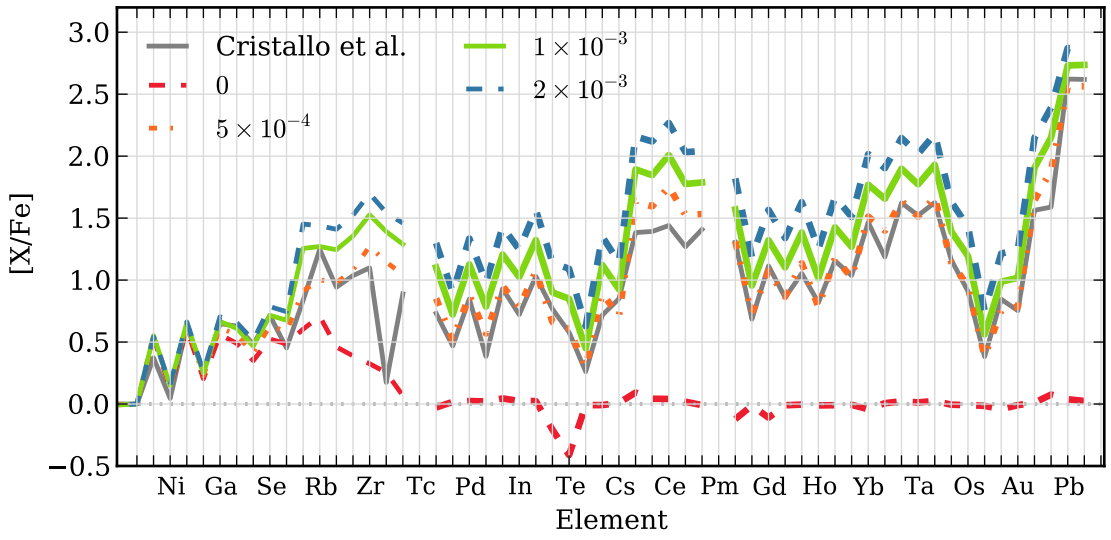

Figure 3.16 Final surface abundance ratios for each 3 $M_\odot$ model with a different PMZ mass (in units of $M_\odot$ as indicated in the legend) for the elements heavier than Fe. The final surface abundances for the 3 $M_\odot$ model of Cristallo et al. (2011) are also presented. The elements are ordered by increasing atomic number. For an explanation of why some abundances have a value less than solar, see the caption of Figure 3.4 and Section 3.2.

each interpulse period. Another result of increased ^{13}C burning temperatures is that the ^{13}C nuclei are consumed faster and the duration of the ^{13}C pocket is shorter for the models with a more massive PMZ.

When a PMZ is not added in the post-processing nucleosynthesis calculations, the effect of the ^{22}Ne neutron source is more evident. In this case, the largest final abundance occurs for [Rb/Fe] due to branching points opening in the *s*-process path at Rb. The much lower neutron exposure however implies minimal production of second *s*-process peak elements and Pb.

In contrast to our models with a PMZ, the model of Cristallo et al. (2011) has Rb as the most enhanced first *s*-process peak element. However, our 3 $M_\odot$ model (with the standard PMZ mass) has a slightly higher Rb yield than the Cristallo et al. (2011) model, with a net yield of 2.41×10^{-8} $M_\odot$ compared to 1.81×10^{-8} $M_\odot$. This is due to the faster increase in Rb with TP number where [Rb/Fe] asymptotically approaches 0.8 and more of this enriched material is then ejected through mass loss. The Cristallo et al. (2011) model has a lower abundance of second *s*-process peak elements but a higher Pb abundance than the model with the standard PMZ mass of 5×10^{-4} $M_\odot$.

All the models with a PMZ produce relatively high abundances of neutron-capture elements (Figure 3.17) and the values of [*ls*/Fe], [*hs*/Fe], and [Pb/Fe] increase with increasing PMZ mass. When comparing the model with a PMZ of 2×10^{-3} $M_\odot$ to the model with the standard PMZ, [*ls*/Fe] increases by 0.43 dex while for [*hs*/Fe] the increase is 0.52 dex. For [Pb/Fe] there is an increase of 0.3 dex.

Figure 3.17 also highlights the effect of changing the mass of the PMZ on the intrinsic

s-process indicators [*hs*/*ls*] and [Pb/*hs*]. For the models with a PMZ, there is an absolute difference of only 0.08 for the [*hs*/*ls*]. The small change in [*hs*/*ls*] is due to the abundances reaching equilibrium (see Lugaro et al. 2012). For [Pb/*hs*] there is a decrease of 0.21 dex when increasing the PMZ mass from 5×10^{-4} to 2×10^{-3} $M_{\odot}$. This is a result of the lower neutron exposure when the PMZ mass is higher.

Despite the different approaches, there is a reasonable agreement between the two groups, as testified by the *s*-process indicators reported in Figure 3.17. However, there is a disagreement between the final abundance of [Rb/Zr] between the Cristallo et al. (2011) model and our models with a PMZ. The models presented here have a sub-solar [Rb/Zr] ratio of approximately −0.25 whereas the Cristallo et al. (2011) model has a ratio of ~ 0.6 due to the higher predicted Rb abundance. The model without a PMZ is the only model that shows a [Rb/Zr] ratio above solar which is a consequence of the ^{22}Ne(α, n)^{25}Mg reaction being the only source of neutrons.

Using our method for including a ^{13}C pocket, it is difficult to select an appropriate mass (and profile) for the PMZ in models in the transition phase between low- and intermediate-mass. The models of Cristallo et al. (2009, 2011) use convective boundary mixing with an exponential decline in velocity to handle the discontinuity in the radiative gradient due to the abrupt change in opacities due to the TDU episodes. This leads to a deeper TDU and to protons being partially mixed into the core. The formation of a ^{13}C pocket then follows. Such a treatment of convective boundary mixing results in deeper TDU relative to our models. The mixing of protons inwards in mass makes use of a free parameter β, with higher values of β resulting in more efficient TDU. However, the effective mass of the ^{13}C pocket does not increase with increasing values of β. The mass of the ^{13}C pocket is at its largest when $\beta = 0.1$. A lower or higher value of β results in a lower abundance of neutron-capture elements. Our PMZ, which is added during post-processing calculations, assumes a constant mass for the proton profile at each TDU episode. In contrast, the ^{13}C pockets of Cristallo et al. (2009, 2011) reduce in mass along the AGB, following the progressive shrinking in mass of the He-intershell.

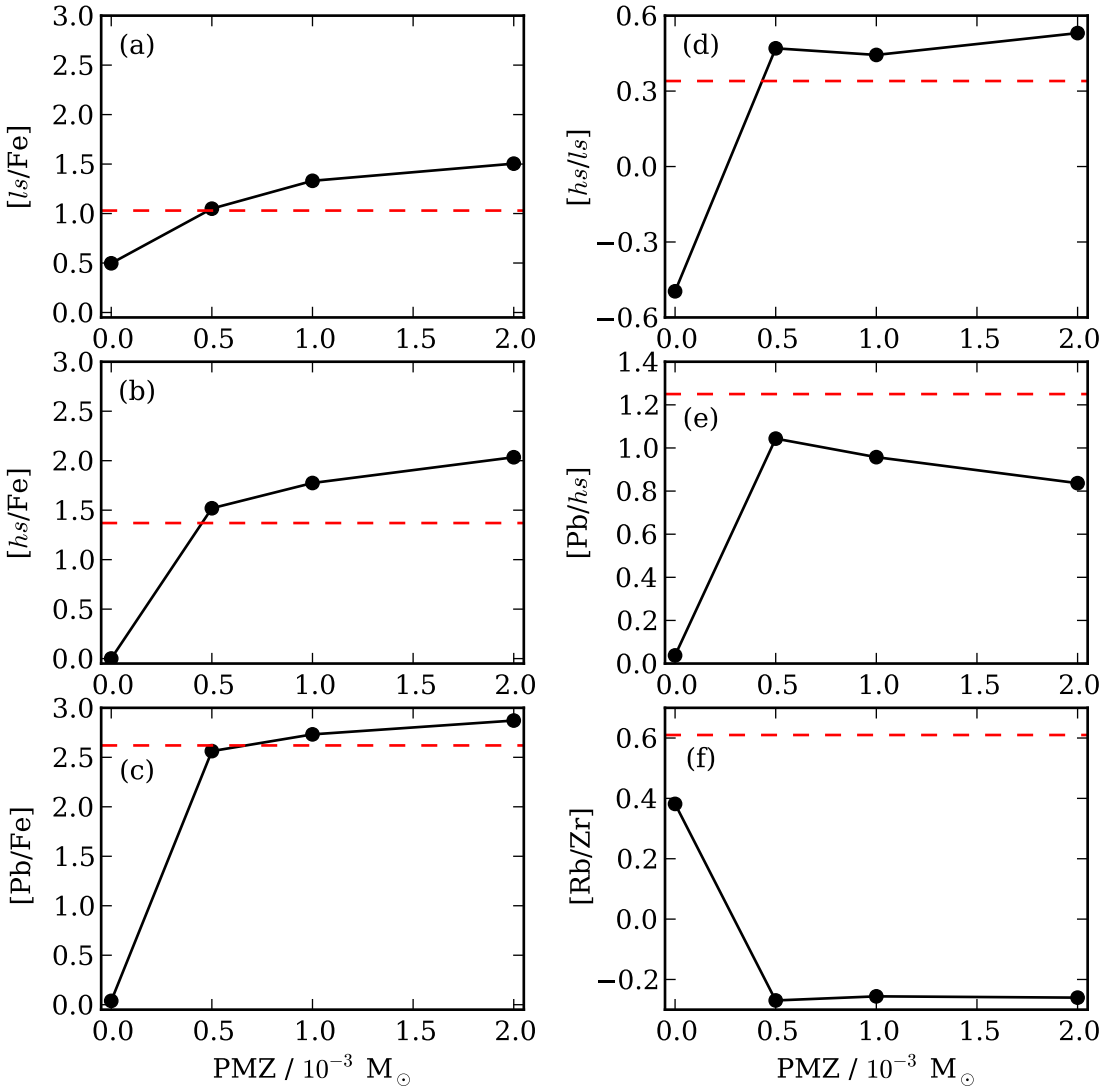

Figure 3.17 Distribution of [*ls*/Fe], [*hs*/Fe], [Pb/Fe], [*hs*/*ls*], [Pb/*hs*], and [Rb/Zr] with varying PMZ mass for each 3 $M_\odot$ model showing the behaviour of the *s*-process peaks. The results from Cristallo et al. (2011) are shown as a horizontal dashed line.

3.7. Comparison to post-AGB stars

We compare the final surface abundance predictions to three *s*-process rich post-AGB stars in the Large Magellanic Cloud (van Aarle et al. 2013; De Smedt et al. 2014): J050632.10-714229.8, J052043.86-692341.0, and J053250.69-713925.8. The post-AGB stars have a metallicity of [Fe/H] ≈ -1.2 and their initial masses are between 1 and 1.5 $M_\odot$ (van Aarle et al. 2013). In Figure 3.18 we present the abundances determined by van Aarle et al. (2013) with upper limits of the Pb abundance from De Smedt et al. (2014) and the predicted final surface abundances from the models between 1 and 2 $M_\odot$.

For J052043 and J053250, the 2 $M_\odot$ model is the best match to the neutron-capture abundances of the *ls* and *hs* elements. These initial masses are higher than the 1 to 1.5 $M_\odot$ estimated by van Aarle et al. (2013). The abundances of the *ls* elements for J050632 also match the 2 $M_\odot$

predictions however the *hs* elements are better matched by the 1.25 or 1.5 $M_{\odot}$ models.

As noted by De Smedt et al. (2014), the observed upper limits of the Pb abundance are well below the predicted values. This is in conflict with calculations of AGB models including those presented here. Model predictions of low-metallicity AGB stars suggest that the Pb abundance should be higher than that of the second *s*-process peak (Gallino et al. 1998). Piersanti et al. (2013) noted, using theoretical models of AGB stars, that rotation could decrease the final [Pb/Fe] abundance, down to a value of 1.6 (from 2.8 for the model with no rotation) for a 1.5 $M_{\odot}$ model with a rotation velocity of 120 km s^{-1} and [Fe/H] of −1.7. The presence of rotation also decreases the [*hs*/*ls*] and [Pb/*hs*] ratios.

The observed values for [C/Fe] are lower than the predictions of the best-matched model whereas [O/Fe] is observed to be overabundant. One possibility for the high [O/Fe] abundance is that the initial composition for the post-AGB stars was enhanced in O and Si compared to the scaled-solar initial composition used in the models. The required enhancements in the initial composition of [O/Fe] to match the abundances of the post-AGB stars range from 0.41 to 0.58. High abundances of other α elements (Mg, Ca, and Ti) are not observed in the post-AGB stars.

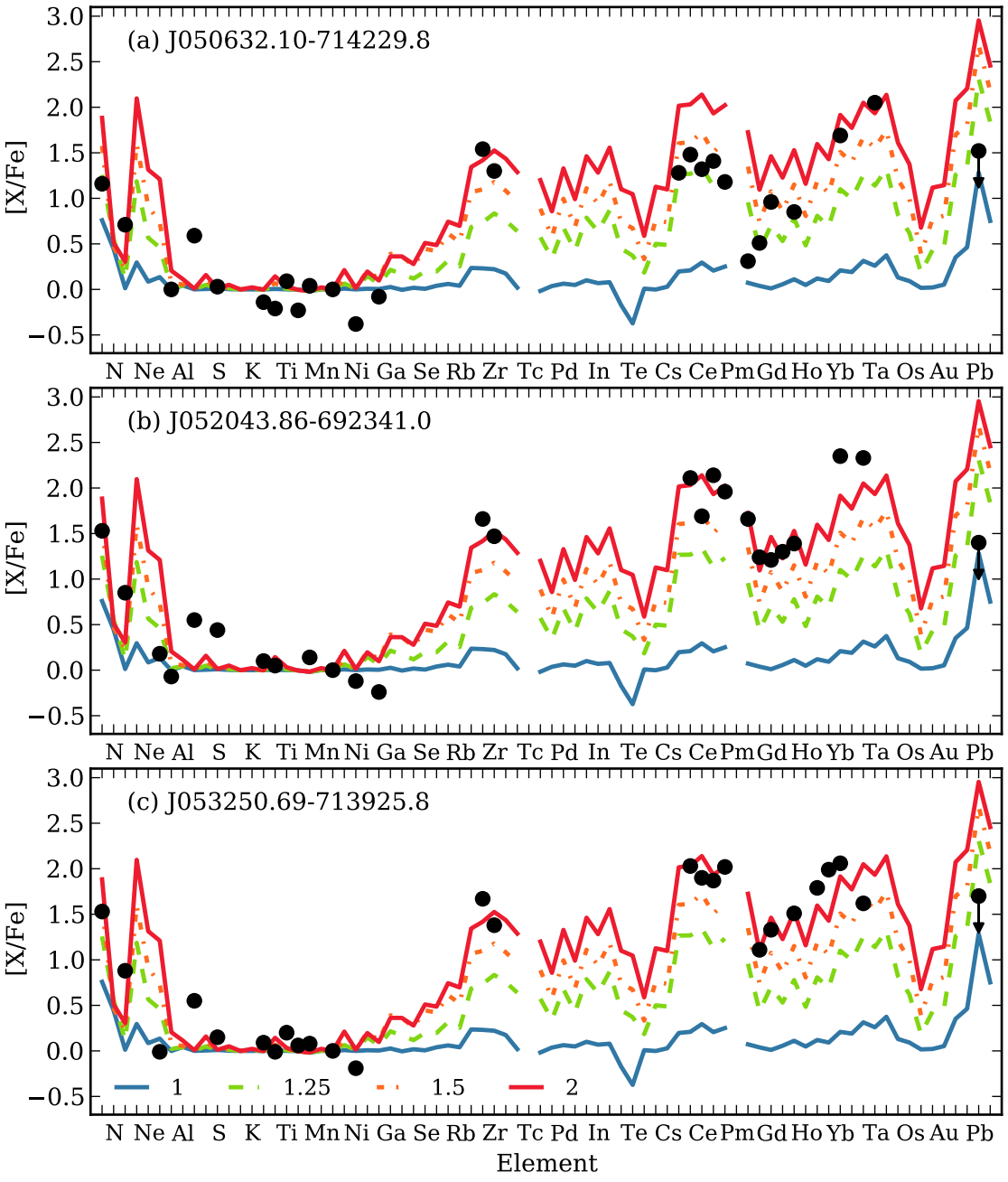

Figure 3.18 Comparison of three post-AGB stars (van Aarle et al. 2013; De Smedt et al. 2014) to four low-mass AGB models (1, 1.25, 1.5, and 2 $M_{\odot}$). The legend (in units of $M_{\odot}$) is shown in the bottom panel. The post-AGB abundances are shown as black points with the Pb abundance being only an upper limit.

3.8. Discussion of uncertainties

There are many uncertainties in the input physics used for modelling AGB stars including convection, mass loss, extra mixing, reaction rates, rotation, and low-temperature opacities. It is therefore important to understand the role that these uncertainties have on the theoretical predictions. In this section we focus on a few uncertainties that can substantially affect the calculation of yields for neutron-capture elements; namely, mass loss, reaction rates, convection (and TDU), and the addition of a ^{13}C pocket.

The mass-loss rate affects the lifetime of the AGB phase and the number of TDU episodes experienced. Therefore, mass loss plays a key role in influencing the chemical yields (cf. Stancliffe & Jeffery 2007; Karakas 2010). With a more efficient mass-loss rate, and hence a shorter AGB phase, lower yields of neutron-capture elements are expected as a smaller amount of enriched material is dredged to the surface to be expelled into the interstellar medium. Mass-loss rates are difficult to determine from observations and require the modelling of dust properties and radiative transfer. Cristallo et al. (2009) compared models of 2 $M_\odot$ with $Z = 0.0001$ using two different mass-loss prescriptions: one with a Reimers (1975, $\eta = 0.4$) prescription, and the standard case which uses a prescription similar to Vassiliadis & Wood (1993) but updated with more recent infrared observations (see Straniero et al. 2006). The model with the Reimers (1975) prescription shows an increase in the final surface abundance of the neutron-capture elements as a result of a longer AGB lifetime. However, it was found that the *s*-process indicators, [*hs*/*ls*] and [Pb/*hs*], are less sensitive to the duration of the AGB phase as the largest ^{13}C pockets occur in the first few TPs and produce the largest increase in the *s*-process abundances. This sets the abundance ratio of the *s*-process indicators early in the AGB phase for the low-mass models. For the intermediate-mass models presented here, the values of the *s*-process indicators decrease over time and do not reach a constant ratio (see Figure 3.11).

The uncertainties in the reaction rates can also have an impact on the production of the neutron-capture elements. In particular for *s*-process nucleosynthesis, the reaction rates of the neutron sources, ^{13}C(α,n)^{16}O and ^{22}Ne(α,n)^{25}Mg, can affect the number of neutrons produced per Fe seed. The ^{13}C(α,n)^{16}O reaction can only be measured experimentally at high energies and extrapolated to energies that occur during *s*-process nucleosynthesis. Guo et al. (2012) present an updated measurement for the reaction rate of ^{13}C(α,n)^{16}O and compares to previous measurements using AGB models with *s*-process nucleosynthesis. Relative to the reaction rates from Caughlan & Fowler (1988) and Angulo et al. (1999), they find that if all the ^{13}C is destroyed in radiative conditions minimal variations of up to 5 per cent occur for the neutron-capture elements. If some ^{13}C is destroyed inside a convective TP, the updated reaction rate has a larger effect on the abundance of the neutron-capture elements, with up to 25 per cent variation for Pb. The conditions where ^{13}C is burnt convectively occur in low-mass stars when there is incomplete radiative burning of ^{13}C during an interpulse or if there is proton ingestion in a TP. In the models presented here, we use the ^{13}C(α,n)^{16}O reaction rate taken from Heil et al. (2008b) which is consistent with the updated measurement presented by Guo et al. (2012).

Concerning the uncertainties associated with convection and mixing length theory, a different α value will alter the amount of material mixed to the surface (cf. Boothroyd & Sackmann 1988). Cristallo et al. (2009) investigated a 2 $M_\odot$ model of $Z = 0.0001$ with two different α values: 1.8 and 2.15. The lower α value resulted in lower temperatures at the bottom of the pulse driven convective zone produced by a TP. Another consequence of the lower α value was less efficient TDU with 9.54×10^{-2} $M_\odot$ dredged up compared to 1.6×10^{-1} $M_\odot$. This decrease in $M_{\rm TDU}$ occurs despite the standard model having one extra TP and results in lower final abundances. The *s*-process indicators for the low-mass models are less affected as they are more sensitive to the metallicity and to the mass of the ^{13}C pocket.

As mentioned in Section 1, low-mass models require extra mixing of protons to form the ^{13}C pocket (Karakas & Lattanzio 2014). We have shown in Section 3.6 that changing the PMZ mass has an effect on the final surface abundances, particularly on the abundance of the neutron-capture elements. Shingles & Karakas (2013) investigated varying the mass of the PMZ to match abundances in planetary nebulae and found that the predicted Ne abundance is sensitive to the size of the ^{13}C pocket. The lack of understanding of the mechanism responsible for the formation of the ^{13}C pocket highlights the uncertainties related to predicting yields of *s*-process nucleosynthesis. We refer the reader to Bisterzo et al. (2014) and Trippella et al. (2014) for further discussion on this point. It is important to note that TDU and the formation of the ^{13}C pocket should not be treated separately as is done with an added PMZ, particularly if the timescale for burning is shorter than the mixing timescale (Goriely & Siess 2004).

The effect of rotation on the production of neutron-capture elements in AGB models has been studied by Herwig et al. (2003), Siess et al. (2004), and Piersanti et al. (2013). It was determined that rotation reduces the neutron flux as the ^{13}C pocket is mixed with the neutron poison ^{14}N. This reduction in the number of neutrons in turn may hinder the synthesis of the neutron-capture elements. The presence of rotation offers a possible solution to the lower than predicted Pb abundances in post-AGB stars. We do not consider rotation in our models.

3.9. Conclusions

We have presented new AGB stellar models for a range of initial masses from 1 $M_\odot$ to 7 $M_\odot$ for a metallicity of $Z = 0.001$ ([Fe/H] = −1.2) and a scaled-solar initial composition. In particular, *s*-process nucleosynthesis predictions for intermediate-mass AGB models of $Z = 0.001$ are presented for the first time in the literature. We also present neutron-capture abundances and yields for a super-AGB model of 7 $M_\odot$ for the first time. Online tables are available presenting (for each stellar mass) evolutionary properties, final surface abundances (including [X/H] and [X/Fe]) and yields for all elements, as well as isotope final surface abundances and yields for elements up to the Fe group.

We have presented in detail two representative AGB models, one low-mass model of 2 $M_\odot$ and one intermediate-mass model of 5 $M_\odot$. As a result of the activation of different neutron

sources these models produce dissimilar abundance distributions. The low-mass models favour the production of Pb due to the $^{13}C(\alpha,n)^{16}O$ reaction whereas the intermediate-mass models favour the production of Rb over other neutron-capture elements due to the activation of branching points by the $^{22}Ne(\alpha,n)^{25}Mg$ reaction. The [Rb/Zr] ratio, comparing two first *s*-process peak elements, is mass dependent with the intermediate-mass models showing an enhancement of ~ 0.4 dex. The low-mass models show a sub-solar value down to -0.8 dex for the 2 $M_\odot$ model.

The new predictions are compared to the $Z = 0.001$ models of Cristallo et al. (2009, 2011) and Marigo et al. (2013) for masses in common between the various studies. The differences in the final surface abundances and yields between the calculations can be attributed to the choice of input physics such as the treatment of convective borders. The elemental yield predictions of the models presented here are comparable to those by Cristallo et al. (2011). The *s*-process indicators [*ls*/Fe] and [*hs*/Fe] agree to within 0.36 dex, with the largest difference occurring for the 1.5 $M_\odot$ models for [*hs*/Fe]. For [Pb/Fe], the difference is less than 0.19 dex.

We also investigated the uncertainty in the addition of a ^{13}C pocket by varying the mass of the PMZ in the 3 $M_\odot$ model. The 3 $M_\odot$ model is in the transition zone between the lower mass models and the more massive models. Increases in the mass of the PMZ result in enhancements in the abundances of neutron-capture elements and a number of light elements (O, F, Ne, Na, Mg, Al, and P). The intrinsic *s*-process indicator [*hs*/*ls*] is shown to be weakly dependent on the mass of the PMZ whereas [Pb/*hs*] decreases with increasing PMZ mass for the 3 $M_\odot$ model due to lower neutron exposures.

One application of the AGB stellar models presented is a comparison of three low-metallicity post-AGB stars to the model predictions. Other applications include chemical evolution studies (e.g. Bisterzo et al. 2014) and the study of planetary nebulae in our Galaxy (e.g. Karakas & Lugaro 2010) as well as external galaxies. The models presented here have been used in the interpretation of measured abundances of globular cluster stars (Yong et al. 2014a,b), a chemically peculiar star in the Aquarius co-moving group (Casey et al. 2014), and the *s*-process component of M4 and M22 (Shingles et al. 2014).

CHAPTER 4

AGB evolution and nucleosynthesis

We present additional details of the $Z = 0.001$ stellar models presented in Fishlock et al. (2014a), expanding on the results of Chapter 3. The stellar evolution and nucleosynthesis during the pre-AGB phase is discussed where mixing episodes alter the surface composition of a number of light elements. We also provide further details of the AGB phase including stellar properties of interest such as the mass of the H-exhausted core and the temperature at the base of the convective envelope for each model. The nucleosynthesis of the light and heavy elements as a result of HBB and TDU is summarised along with the reactions responsible for producing the required neutrons for neutron-capture nucleosynthesis.

4.1. Numerical modelling details

As detailed in Chapter 3, we use an initial He mass fraction of $Y = 0.25$ and a metallicity of $Z = 0.001$. The initial He abundance was determined using $\Delta Y/\Delta Z$ of 2.1 (Casagrande et al. 2007) and a primordial He abundance Y_P of 0.2485 (Cyburt 2004).

For all elements heavier than He, we use scaled-solar abundances from Asplund et al. (2009) and a solar metallicity of $Z_\odot = 0.015$. The solar abundances of C, N, O, Ne, Mg, Si, S, Ar, and Fe are the pre-solar nebula values from Asplund et al. (2009) and the abundance of F is the meteoritic value (due to its lower uncertainty). For a number of elements heavier than Fe the meteoritic values are used for the solar abundances (e.g., Zr, La, Eu, and Pb). Tables 4.1 and 4.2 detail the 320 species in the nuclear network and their initial abundances (in mole number Y_A). The nuclear network does not include stable isotopes that are not reached by the *s*-process to reduce computational time. These isotopes, such as ^{84}Sr, ^{132}Ba, and ^{154}Sm, are shielded by a neighbouring short-lived isotope.

The nuclear reaction rates were obtained from the Joint Institute for Nuclear Astrophysics REACLIB project[1] (Cyburt et al. 2010) as of May 2012. The REACLIB database also includes neutron-capture cross sections from the KADoNis database (Dillmann et al. 2006). A number

[1] https://groups.nscl.msu.edu/jina/reaclib/db/

of cross sections in the KADoNis database are not well determined for temperatures achieved in AGB stars and therefore we use rates labelled *ka02* instead of the updated *kd02* rates. For more details on the nuclear network see Lugaro et al. (2014).

Table 4.1 Species of light elements included in the nuclear network. For stable isotopes, the initial abundance (in mole number) is given in brackets.

Element	A (initial abundance Y_A)
n	1
H	$1(7.49 \times 10^{-1})$, $2(1.63 \times 10^{-6})$
He	$3(6.90 \times 10^{-6})$, $4(6.25 \times 10^{-2})$
Li	$7(8.22 \times 10^{-11})$
Be	7
B	8
C	$12(1.43 \times 10^{-5})$, $13(1.60 \times 10^{-7})$, 14
N	13, $14(3.61 \times 10^{-6})$, $15(8.07 \times 10^{-9})$
O	14, 15, $16(2.62 \times 10^{-5})$, $17(9.95 \times 10^{-9})$, $18(5.25 \times 10^{-8})$, 19
F	17, 18, $19(1.29 \times 10^{-9})$, 20
Ne	19, $20(4.24 \times 10^{-6})$, $21(1.02 \times 10^{-8})$, $22(3.12 \times 10^{-7})$, 23
Na	21, 22, $23(8.49 \times 10^{-8})$, 24
Mg	23, $24(1.68 \times 10^{-6})$, $25(2.13 \times 10^{-7})$, $26(2.35 \times 10^{-7})$, 27
Al	25, 26, $27(1.38 \times 10^{-7})$, 28
Si	27, $28(1.60 \times 10^{-6})$, $29(8.12 \times 10^{-8})$, $30(5.35 \times 10^{-8})$
P	$31(1.26 \times 10^{-8})$, 32, 33
S	$32(6.70 \times 10^{-7})$, $33(5.37 \times 10^{-9})$, $34(3.03 \times 10^{-8})$, 35, $36(1.41 \times 10^{-10})$
Cl	$35(6.29 \times 10^{-9})$, 36, $37(2.01 \times 10^{-9})$
Ar	$36(1.14 \times 10^{-7})$, 37, $38(2.07 \times 10^{-8})$, 39, $40(3.31 \times 10^{-11})$
K	$39(5.47 \times 10^{-9})$, $40(8.64 \times 10^{-13})$, $41(3.95 \times 10^{-10})$
Ca	$40(9.24 \times 10^{-8})$, 41, $42(6.16 \times 10^{-10})$, $43(1.29 \times 10^{-10})$, $44(1.99 \times 10^{-9})$, 45, $46(3.81 \times 10^{-12})$, 47, $48(1.78 \times 10^{-10})$
Sc	$45(5.48 \times 10^{-11})$, 46, 47, $48(3.24 \times 10^{-32})$
Ti	$46(3.28 \times 10^{-10})$, $47(2.95 \times 10^{-10})$, $48(2.93 \times 10^{-09})$, $49(2.15 \times 10^{-10})$, $50(2.06 \times 10^{-10})$
V	$51(4.45 \times 10^{-10})$
Cr	$52(1.79 \times 10^{-8})$, $53(2.03 \times 10^{-9})$, $54(5.04 \times 10^{-10})$
Mn	$55(1.48 \times 10^{-8})$
Fe	$54(9.90 \times 10^{-8})$, 55, $56(1.55 \times 10^{-6})$, $57(3.59 \times 10^{-8})$, $58(4.78 \times 10^{-9})$, 59, 60
Co	$59(3.62 \times 10^{-9})$, 60
Ni	$58(5.27 \times 10^{-8})$, 59, $60(2.03 \times 10^{-8})$, $61(8.83 \times 10^{-10})$, $62(2.81 \times 10^{-9})$, 63, $64(7.17 \times 10^{-10})$
Cu	$63(6.01 \times 10^{-10})$, 64, $65(2.68 \times 10^{-10})$
Zn	$64(1.01 \times 10^{-9})$, 65, $66(5.82 \times 10^{-10})$, $67(8.55 \times 10^{-11})$, $68(3.91 \times 10^{-10})$, 69, $70(1.29 \times 10^{-11})$

Table 4.2 Species of neutron-capture elements included in the nuclear network. For stable isotopes, the initial abundance (in mole number) is given in brackets.

Element	A (initial abundance Y_A)
Ga	$69(3.53\times10^{-11})$, 70, $71(2.34\times10^{-11})$
Ge	$70(3.87\times10^{-11})$, 71, $72(5.12\times10^{-11})$, $73(1.44\times10^{-11})$, $74(6.74\times10^{-11})$
As	$75(9.75\times10^{-12})$
Se	$76(1.00\times10^{-11})$, $77(8.16\times10^{-12})$, $78(2.54\times10^{-11})$, 79, $80(5.30\times10^{-11})$
Br	$79(8.59\times10^{-12})$, 80, $81(8.35\times10^{-12})$
Kr	$80(2.02\times10^{-12})$, 81, $82(1.01\times10^{-11})$, $83(1.00\times10^{-11})$, $84(4.94\times10^{-11})$, 85, $86(1.50\times10^{-11})$
Rb	$85(1.15\times10^{-11})$, 86, $87(4.72\times10^{-12})$
Sr	$86(3.66\times10^{-12})$, $87(2.56\times10^{-12})$, $88(3.06\times10^{-11})$, 89, 90
Y	$89(7.92\times10^{-12})$, 90, 91
Zr	$90(8.52\times10^{-12})$, $91(1.86\times10^{-12})$, $92(2.84\times10^{-12})$, 93, $94(2.88\times10^{-12})$, 95, $96(4.64\times10^{-13})$
Nb	$93(1.26\times10^{-12})$, 94, 95
Mo	$94(3.89\times10^{-13})$, $95(6.74\times10^{-13})$, $96(7.10\times10^{-13})$, $97(4.09\times10^{-13})$, $98(1.04\times10^{-12})$
Tc	99
Ru	$99(3.59\times10^{-13})$, $100(3.54\times10^{-13})$, $101(4.80\times10^{-13})$, $102(8.87\times10^{-13})$
Rh	$103(5.61\times10^{-13})$
Pd	$104(2.43\times10^{-13})$, $105(4.87\times10^{-13})$, $106(5.97\times10^{-13})$, 107, $108(5.78\times10^{-13})$
Ag	$107(4.01\times10^{-13})$, 108, $109(3.73\times10^{-13})$
Cd	$108(2.23\times10^{-14})$, 109, $110(3.13\times10^{-13})$, $111(3.21\times10^{-13})$, $112(6.05\times10^{-13})$, $113(3.06\times10^{-13})$, $114(7.20\times10^{-13})$
In	$115(2.69\times10^{-13})$
Sn	$116(8.35\times10^{-13})$, $117(4.41\times10^{-13})$, $118(1.33\times10^{-12})$, $119(4.93\times10^{-13})$, $120(1.87\times10^{-12})$
Sb	$121(2.86\times10^{-13})$
Te	$122(1.89\times10^{-13})$, $123(6.58\times10^{-14})$, $124(3.51\times10^{-13})$, $125(5.23\times10^{-13})$, $126(1.39\times10^{-12})$
I	$127(1.73\times10^{-12})$
Xe	$128(1.86\times10^{-13})$, $129(2.31\times10^{-12})$, $130(3.72\times10^{-13})$, $131(1.84\times10^{-12})$, $132(2.25\times10^{-12})$, 133, $134(8.31\times10^{-13})$
Cs	$133(5.87\times10^{-13})$, 134, 135, 136, 137
Ba	$134(1.79\times10^{-13})$, $135(4.88\times10^{-13})$, $136(5.81\times10^{-13})$, $137(8.31\times10^{-13})$, $138(5.30\times10^{-12})$
La	$139(7.22\times10^{-13})$
Ce	$140(1.64\times10^{-12})$, 141, $142(2.06\times10^{-13})$
Pr	$141(2.81\times10^{-13})$
Nd	$142(3.72\times10^{-13})$, $143(1.66\times10^{-13})$, $144(3.27\times10^{-13})$, $145(1.21\times10^{-13})$, $146(2.36\times10^{-13})$, 147, $148(7.87\times10^{-14})$
Pm	147, 148
Sm	$147(6.38\times10^{-14})$, $148(4.78\times10^{-14})$, $149(5.88\times10^{-14})$, $150(3.14\times10^{-14})$, 151, $152(1.14\times10^{-13})$
Eu	$151(7.56\times10^{-14})$, 152, $153(8.25\times10^{-14})$, 154, 155
Gd	$152(1.10\times10^{-15})$, 153, $154(1.20\times10^{-14})$, $155(8.11\times10^{-14})$, $156(1.12\times10^{-13})$, $157(8.58\times10^{-14})$, $158(1.36\times10^{-13})$
Tb	$159(1.02\times10^{-13})$
Dy	$160(1.54\times10^{-14})$, $161(1.25\times10^{-13})$, $162(1.68\times10^{-13})$, $163(1.64\times10^{-13})$, $164(1.86\times10^{-13})$
Ho	$165(1.44\times10^{-13})$
Er	$166(1.36\times10^{-13})$, $167(9.29\times10^{-14})$, $168(1.10\times10^{-13})$, 169, $170(6.06\times10^{-14})$
Tm	$169(6.44\times10^{-14})$, 170, 171
Yb	$170(1.21\times10^{-14})$, $171(5.73\times10^{-14})$, $172(8.82\times10^{-14})$, $173(6.54\times10^{-14})$, $174(1.30\times10^{-13})$
Lu	$175(5.84\times10^{-14})$, $176(1.70\times10^{-15})$, 177
Hf	$176(1.30\times10^{-14})$, $177(4.66\times10^{-14})$, $178(6.84\times10^{-14})$, $179(3.42\times10^{-14})$, $180(8.80\times10^{-14})$
Ta	$181(3.71\times10^{-14})$, 182, 183
W	$182(5.78\times10^{-14})$, $183(3.12\times10^{-14})$, $184(6.69\times10^{-14})$, 185, $186(6.21\times10^{-14})$
Re	$185(3.17\times10^{-14})$, 186, $187(5.72\times10^{-14})$
Os	$186(1.75\times10^{-14})$, $187(1.39\times10^{-14})$, $188(1.46\times10^{-13})$, $189(1.78\times10^{-13})$, $190(2.89\times10^{-13})$, 191, $192(4.49\times10^{-13})$
Ir	$191(3.81\times10^{-13})$, 192, $193(6.40\times10^{-13})$
Pt	$192(1.59\times10^{-14})$, 193, $194(6.72\times10^{-13})$, $195(6.89\times10^{-13})$, $196(5.14\times10^{-13})$
Au	$197(3.08\times10^{-13})$
Hg	$198(7.21\times10^{-14})$, $199(1.22\times10^{-13})$, $200(1.67\times10^{-13})$, $201(9.53\times10^{-14})$, $202(2.16\times10^{-13})$
Tl	$203(8.49\times10^{-14})$, 204, $205(2.03\times10^{-13})$
Pb	$204(1.07\times10^{-13})$, 205, $206(9.96\times10^{-13})$, $207(1.10\times10^{-12})$, $208(3.15\times10^{-12})$
Bi	$209(2.18\times10^{-13})$, 210
Po	210

Table 4.3 Half-lives for long-lived isotopes.

Isotope	Half-life[#]	Reaction
^{36}Cl	301,000 y	^{36}Cl(β^-)^{36}Ar
^{39}Ar	269 y	^{39}Ar(β^-)^{39}K
^{41}Ca	103,000 y	^{41}Ca(e^-,ν_e)^{41}K
^{26}Al[†]	717,000 y	^{26}Al(β^-)^{26}Mg
^{60}Fe	2,620,000 y	^{60}Fe(β^-)^{60}Co
^{60}Co	1925.1 d	^{60}Co(β^-)^{60}Ni
^{59}Ni	76,000 y	^{59}Ni(β^-)^{59}Co
^{63}Ni	100.1 y	^{63}Ni(β^-)^{63}Cu
^{79}Se	$\leq$ 650,000 y	^{79}Se(β^-)^{79}Br
^{93}Zr	1,530,000 y	^{93}Zr(β^-)^{93}Nb
^{99}Tc	211,100 y	^{99}Tc(β^-)^{99}Ru
^{107}Pd	6,500,000 y	^{107}Pd(β^-)^{107}Ag
^{135}Cs	2,300,000 y	^{135}Cs(β^-)^{135}Ba
^{205}Pb	15,300,000 y	^{205}Pb(e^-,ν_e)^{205}Tl
^{210}Po	138.376 d	^{210}Po(α)^{206}Pb

[#] Half-lives taken from `http://atom.kaeri.re.kr/`
[†] Ground state of ^{26}Al.

Some unstable isotopes have long half-lives and these isotopes are decayed to their daughter isotopes before final surface abundances and stellar yields are determined. Table 4.3 presents the unstable isotopes that are forced to decay, their half-life, and the associated reaction.

Uncertainties in nuclear reaction rates determined either theoretically or experimentally reduce the accuracy of model predictions. Previous studies have shown that revised reaction rates can influence structural properties and abundance predictions (e.g., Suda et al. 2011; Guo et al. 2012). Here we perform a comparison between the updated network against the previously used 2009 nuclear network (Lugaro et al. 2012) for the 3 $M_\odot$ model of $Z = 0.001$. Figure 4.1 presents the final surface abundances for each model with a different nuclear network. We find the largest change in the final surface abundance occurs for F where the model using the updated 2012 nuclear network produces 0.33 dex more F than the model using the 2009 network.

The difference in F is a result of the updated ^{19}F(α,p)^{22}Ne reaction rate from Ugalde et al. (2008). The 2009 network uses the ^{19}F(α,p)^{22}Ne reaction from Caughlan & Fowler (1988). At temperatures lower than 10^9 K, this reaction rate is slower than the Ugalde et al. (2008) rate. To confirm that it is the ^{19}F(α,p)^{22}Ne reaction that causes the large difference in the final abundance of F between the two networks, we incorporate the previously used Caughlan & Fowler (1988) rate into the 2012 network using a reduced number of species (which does not include the neutron-capture elements). Figure 4.1 confirms that the abundance of F determined using the reduced network matches the F abundance when using the 2009 network.

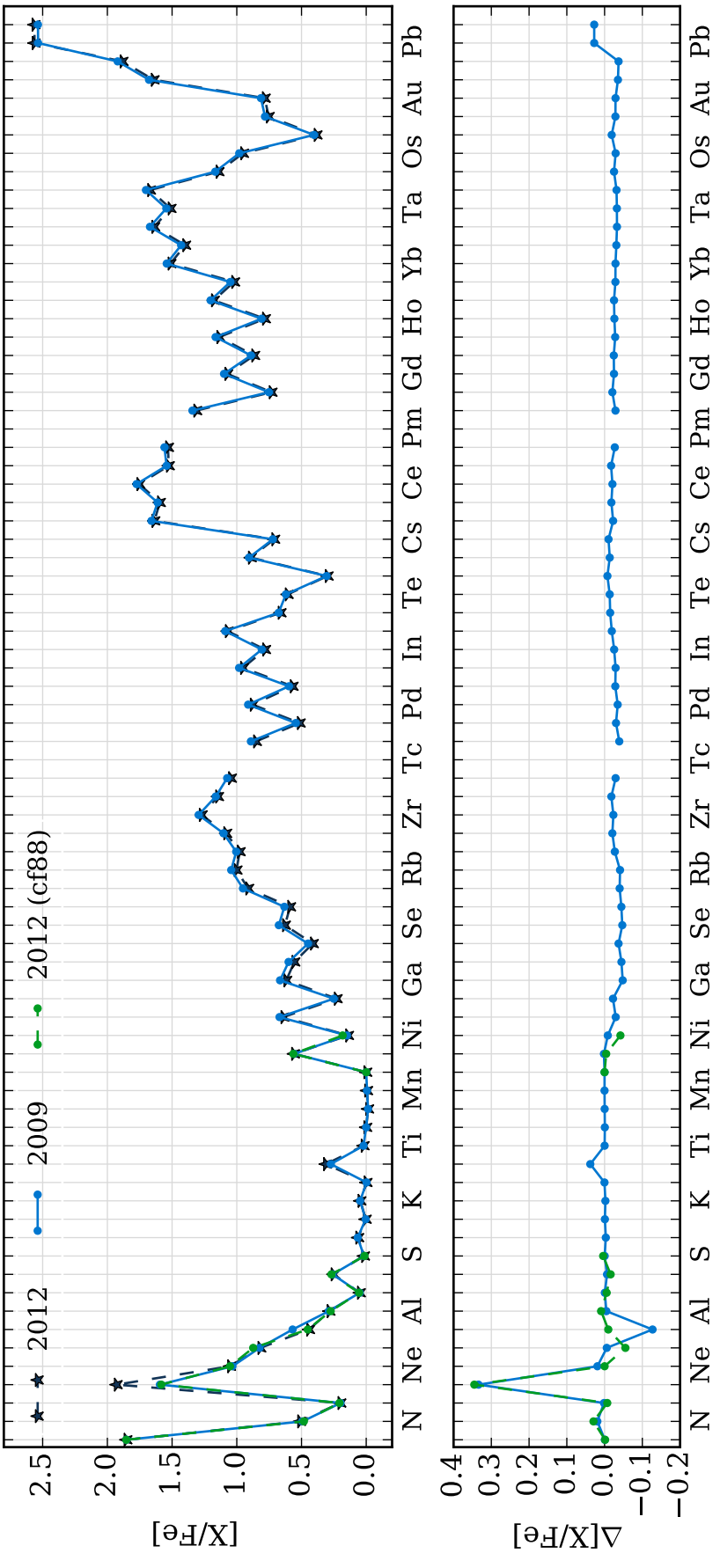

Figure 4.1 Comparison of the predictions from the 2009 and 2012 nuclear networks for the 3 $M_\odot$ model of $Z = 0.001$ as well as the 2012 network with the Caughlan & Fowler (1988) $^{19}F(\alpha,p)^{22}Ne$ reaction from the 2009 network. The bottom panel shows the difference between the full 2012 network and the 2009 and 2012 networks with the Caughlan & Fowler (1988) reaction.

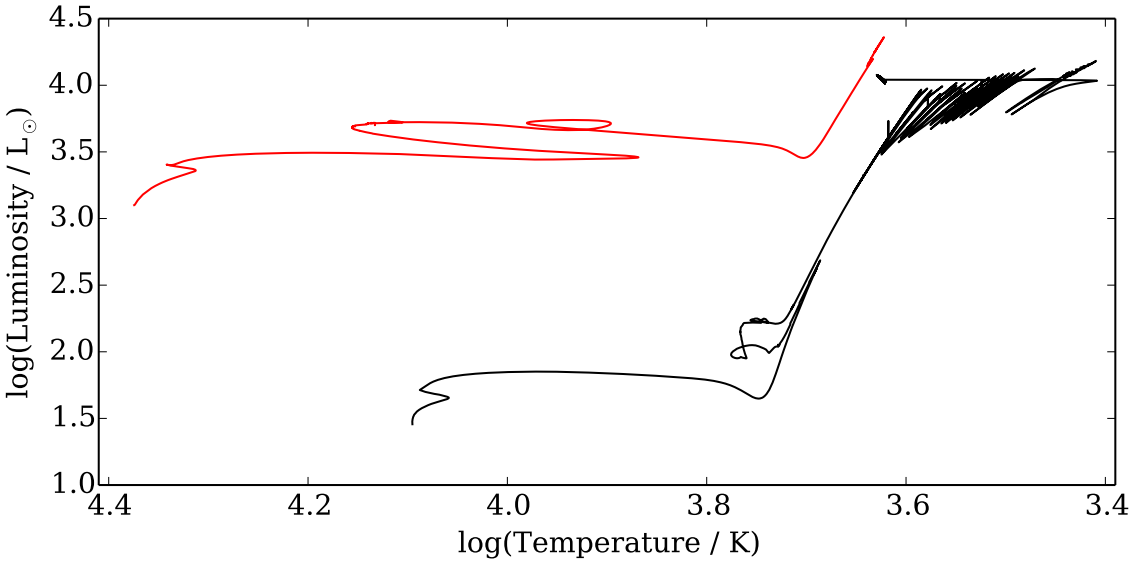

Figure 4.2 Hertzsprung-Russell diagram for the 2 $M_\odot$ model from the zero-age main sequence to the post-AGB phase (black line) and the 6 $M_\odot$ from the zero-age main sequence to the early-AGB phase (red line). For clarity, the AGB phase for the 6 $M_\odot$ model is not shown.

4.2. Pre-AGB evolution and nucleosynthesis

The evolution prior to the AGB phase is important as it dictates the structure and composition of a star at the beginning of the TP-AGB phase. The evolution of a star is strongly dependent on the initial stellar mass whereas the initial composition plays a lesser role. The following section describes the pre-AGB evolution of the $Z = 0.001$ models of low- to intermediate-mass presented in Chapter 3.

Figure 4.2 presents the Hertzsprung-Russell diagram for the 2 $M_\odot$ model from the zero-age main sequence to the post-AGB phase and the 6 $M_\odot$ model from the zero-age main sequence to the early-AGB phase. For clarity, the AGB phase for the 6 $M_\odot$ model is not shown.

The main sequence is where a star spends the majority of its lifetime converting H to He through core hydrogen-burning (H-burning). There are two main processes that convert H to He: the proton-proton (p-p) chain and the CNO cycle. The first of the p-p chain reactions to take place and produce ^{3}He are:

$$^1\mathrm{H}(p,\gamma)^2\mathrm{He}(\beta^+)^2\mathrm{H}(p,\gamma)^3\mathrm{He} \tag{4.1}$$

After this ^{3}He can undergo one of three reactions. The first branch of the p-p chain (ppI) is:

$$^3\mathrm{He}(^3\mathrm{He},2p)^4\mathrm{He} \tag{4.2}$$

In the Sun, the ppI chain occurs 85% of the time (Ryan & Norton 2010). The second branch

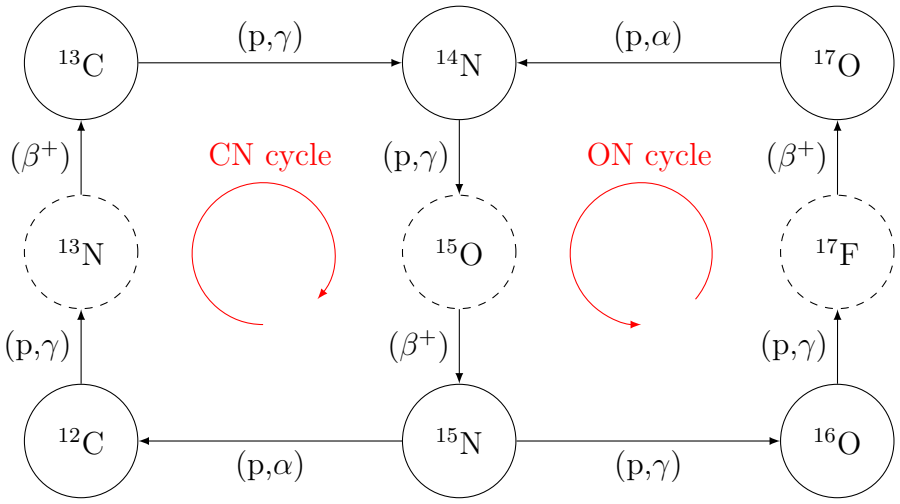

Figure 4.3 Schematic of the CNO cycle with the CN cycle (left) and the ON cycle (right). Dashed circles represent unstable isotopes.

of the p-p chain (ppII) is:

$$^3\mathrm{He}(\alpha,\gamma)^7\mathrm{Be} \tag{4.3}$$
$$^7\mathrm{Be}(e^-,\nu_e)^7\mathrm{Li} \tag{4.4}$$
$$^7\mathrm{Li}(p,\alpha)^4\mathrm{He} \tag{4.5}$$

The third branch of the p-p chain (ppIII), which rarely occurs in the Sun, is:

$$^3\mathrm{He}(\alpha,\gamma)^7\mathrm{Be} \tag{4.6}$$
$$^7\mathrm{Be}(p,\gamma)^8\mathrm{B} \tag{4.7}$$
$$^8\mathrm{B}(\beta^+)^8\mathrm{Be} \tag{4.8}$$
$$^8\mathrm{Be}(\alpha)^4\mathrm{He} \tag{4.9}$$

When ^{12}C is present in the initial composition and the core temperature is sufficiently high, around $(15-20)\times10^6$ K, the CNO cycle can dominate a star's energy production over the p-p chains (Ryan & Norton 2010). The energy generation rate for the CNO cycle is proportional to T^{18} at around $T \approx 10\times10^6$ K compared to approximately T^4 for the p-p chain (Salaris & Cassisi 2006; Karakas & Lattanzio 2014). The CNO cycle consists of two cycles: the CN cycle and the ON cycle. The CN cycle occurs where ^{12}C is used as a catalyst in the conversion of protons to ^{4}He (Figure 4.3). The ON cycle requires higher temperatures than the CN cycle and the capture of a proton onto $^{15}_{7}$N produces $^{16}_{8}$O + γ rather than $^{12}_{6}$C + α (Figure 4.3). Eventually the majority of the isotopes involved in the CNO cycle will be converted to ^{14}N because, during hydrostatic burning, the ^{14}N + p reaction is the slowest of all the CNO cycle reactions and acts as a bottleneck in the cycle. At this point, the CNO cycle reaches equilibrium where the rate of the production equals the rate of destruction. Additionally, the total sum of C+N+O nuclei does not change as a result of the CNO cycle (Iben 2013a).

When the mass of the He core reaches about 10 percent of the total stellar mass (the

Schönberg-Chandrasekhar limit), the core starts to contract and core H-burning ceases. The star leaves the main sequence, crosses the Hertzsprung gap, and moves up the red giant branch (RGB). During this time, H-burning (via the CNO cycle) continues in a shell around the H-exhausted core and the star's radius and luminosity increase while its effective temperature decreases. As the star evolves up the RGB, the deep convective envelope moves inwards in mass and mixes material from partial H-burning up to the stellar surface. This process is known as the first dredge-up (FDU) and, for some stars, is the first mixing episode to alter the surface composition. For more details on FDU, including the changes in the surface composition for a number of light element isotopes, see Section 4.2.1.

The contraction of the core on the RGB steadily increases the core temperature. For stars with an initial mass of less than approximately 2 $M_\odot$ (at $Z = 0.001$), the He core becomes electron degenerate before He can be ignited. Neutrino energy losses from the centre of the core move the mass of maximum core temperature outwards resulting in He-burning being ignited off-centre under degenerate conditions. In this case, the temperature and density are essentially decoupled leading to a violent He ignition called a core helium flash. During the core He-flash, the He-burning luminosity reaches up to 10^{10} $L_\odot$. A number of flashes of lower luminosity occur after the main He-flash before quiescent core He-burning settles in. Despite the increase in the He-burning luminosity, the surface luminosity does not change considerably as the energy goes into removing the degeneracy.

The surface luminosity at the start of core He-burning is approximately constant for stars that undergo a core He-flash. This is a result of these stars reaching a similar core mass required to remove the degeneracy. Therefore it is possible to use the tip of the RGB branch as a distance indicator for resolved stellar systems such as globular clusters or galaxies (e.g., Lee et al. 1993). Stars with a initial mass of 2 $M_\odot$ or more are able to ignite core He-burning in the centre of the core under non-degenerate conditions and have a lower surface luminosity at the tip of the RGB. For stars more massive than 4 $M_\odot$ at $Z = 0.001$, quiescent core He-burning starts before reaching the RGB. This also means that these stars do not experience FDU as their first mixing episode.

Once He is ignited the core a star moves onto the horizontal branch, or experiences a blue loop in the case of intermediate-mass stars, and its effective temperature increases. During this phase, H-burning continues in a shell around the core. The reactions that take place during He-burning are independent of stellar mass. The production of ^{12}C occurs through the fusion of three ^4He nuclei. This process is called the triple-α reaction and consists of two steps:

$$^4He(\alpha,\gamma)^8Be \tag{4.10}$$

$$^8Be(\alpha,\gamma)^{12}C \tag{4.11}$$

However, as ^8Be is unstable it is possible that it will decay back into two α particles before it can capture another α particle. Therefore, in order for the triple-α reaction to be efficient and release a sizeable amount of energy, core temperatures of approximately 120×10^6 K are

required (Salaris & Cassisi 2006). The triple-α process is strongly dependent on density and temperature with the energy released proportional to $\sim T^{40}$ at 10^8 K (Iben 2013b). This high temperature dependence results in a convective core on the horizontal branch. The other reaction that takes place in the He-burning core, $^{12}C(\alpha,\gamma)^{16}O$, converts ^{12}C to ^{16}O which leaves the star with an electron-degenerate CO core. The $^{12}C(\alpha,\gamma)^{16}O$ reaction rate is subject to uncertainties and the C/O ratio in the core can vary depending on the adopted reaction rate (Herwig et al. 2006).

After core He-exhaustion, a He-burning shell is established around the electron-degenerate CO core. This causes structural changes where the star expands and the H-burning shell is extinguished, moving the star up the early-AGB. During this stage of evolution, the He-burning shell provides the majority of the surface luminosity.

Models more massive, and including, 4 $M_\odot$ (at $Z = 0.001$) do not reach the RGB and maintain their initial surface composition until the early-AGB where second dredge-up (SDU) occurs. During the ascent of the early-AGB the convective envelope can move inwards and, depending on the initial stellar mass, reach the H-exhausted core mixing material from partial H-burning to the surface. This has the effect of reducing the mass of the H-exhausted core. In agreement with the models presented in this study, the 6.5 to 7.5 $M_\odot$ models of $Z = 0.001$ calculated by Doherty et al. (2014b) do not experience FDU and experience SDU as their first mixing episode. For more details on the changes in the surface composition as a result of SDU, see Section 4.2.1. After SDU the H-shell is re-ignited and the star moves onto the thermally-pulsing AGB (TP-AGB) phase with the first He-shell instability occurring. For a description of the TP-AGB phase see Section 4.3.

4.2.1. First and second dredge-up

As previously mentioned, before a star reaches the TP-AGB phase it will experience either the FDU (on the RGB), the SDU (on the early-AGB), or possibly both. These mixing episodes change the surface composition of a number of light element isotopes left over from partial H-burning such as ^{4}He, ^{12}C, ^{13}C, and ^{14}N.

Figure 4.4 presents the innermost mass layer reached by FDU and/or SDU relative to the initial mass for each model. For models with an initial mass less than 2.5 $M_\odot$, the convective envelope during the early-AGB phase does not reach as deep as FDU. The 2 and 2.25 $M_\odot$ models experience the deepest FDU relative to their initial mass. For the most massive models of 5.5 to 7 $M_\odot$, the convective envelope does not move inwards in mass before core He-burning starts and the models of 4 to 5$M_\odot$ do not experience changes in the surface composition. The $Z = 0.001$ models of Boothroyd & Sackmann (1999) also show a maximum FDU depth for the 2 and 2.25 $M_\odot$ models with a decrease in the relative depth of FDU with increasing stellar mass. For models with a higher metallicity at the same initial mass, the convective envelope moves in further resulting in deeper FDU (Boothroyd & Sackmann 1999).

The FDU leaves behind a sharp composition discontinuity above the H-burning shell. For the lowest mass stars the time spent on the RGB is long enough for the H-burning shell to

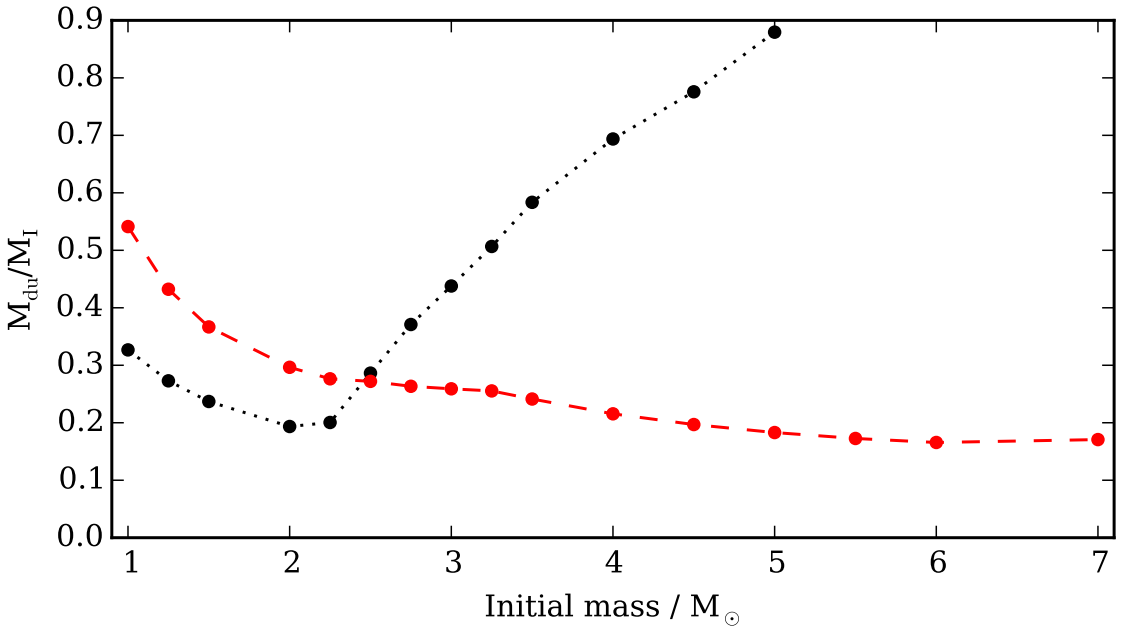

Figure 4.4 Innermost mass layer reached by the convective envelope (M_{du}) relative to the initial stellar mass (M_I) during FDU (black dotted line) and SDU (red dashed line). In models with an initial mass less than 2.5 $M_\odot$ the convective envelope during the early-AGB phase does not reach as deep as FDU.

move outwards in mass and erase this discontinuity. When the H-burning shell reaches this increased abundance of H, the efficiency of H-burning increases, causing the surface luminosity to decrease. Once the H-burning shell crosses this discontinuity, the surface luminosity starts to increase again and the star moves up the RGB once again. The location of this feature on the RGB is known as the RGB bump. The RGB bump is observable in most globular clusters (e.g., Nataf et al. 2013) and can help constrain theoretical details of stellar evolution models such as mixing (e.g., Cassisi et al. 2002). For the models presented here, the RGB bump is experienced before the ignition of core He-burning in models up, and including, 2 $M_\odot$. For the 1.5 $M_\odot$ model, the RGB bump occurs at $\log(L/L_\odot) \approx 2.4$. The luminosity of the RGB bump also increases with increasing initial mass.

Figure 4.5 presents the composition profile of select isotopes of C, N, and O for the 2 $M_\odot$ model just before FDU. The deepest extent of FDU is also shown. The region of partial H-burning between 0.5 and 1 $M_\odot$ shows where the CN cycle is active. In this region, ^{16}O is the most abundant isotope after ^{1}H and ^{4}He. It is only in the inner 0.5 $M_\odot$ region that the ON cycle becomes active, increasing the abundance of ^{14}N to above the abundance of ^{16}O. In the 2 $M_\odot$ model, FDU is only just able to reach into this region processed by the ON cycle.

Figure 4.6 presents enhancements of post-FDU surface abundances for select isotopes affected by the occurrence of FDU. FDU increases the abundance of ^{4}He at the expense of H by mixing up material processed by the p-p chain and/or the CNO cycle. The 1.25 $M_\odot$ model shows the highest enhancement of He of all the models that experience FDU. The ^{4}He enhancement then decreases with increasing initial mass. Cristallo et al. (2011) present the ^{4}He surface mass fraction after the occurrence of FDU for their $Z = 0.001$ models. Figure 4.6 shows the results of Cristallo et al. (2011) are comparable where the enhancement

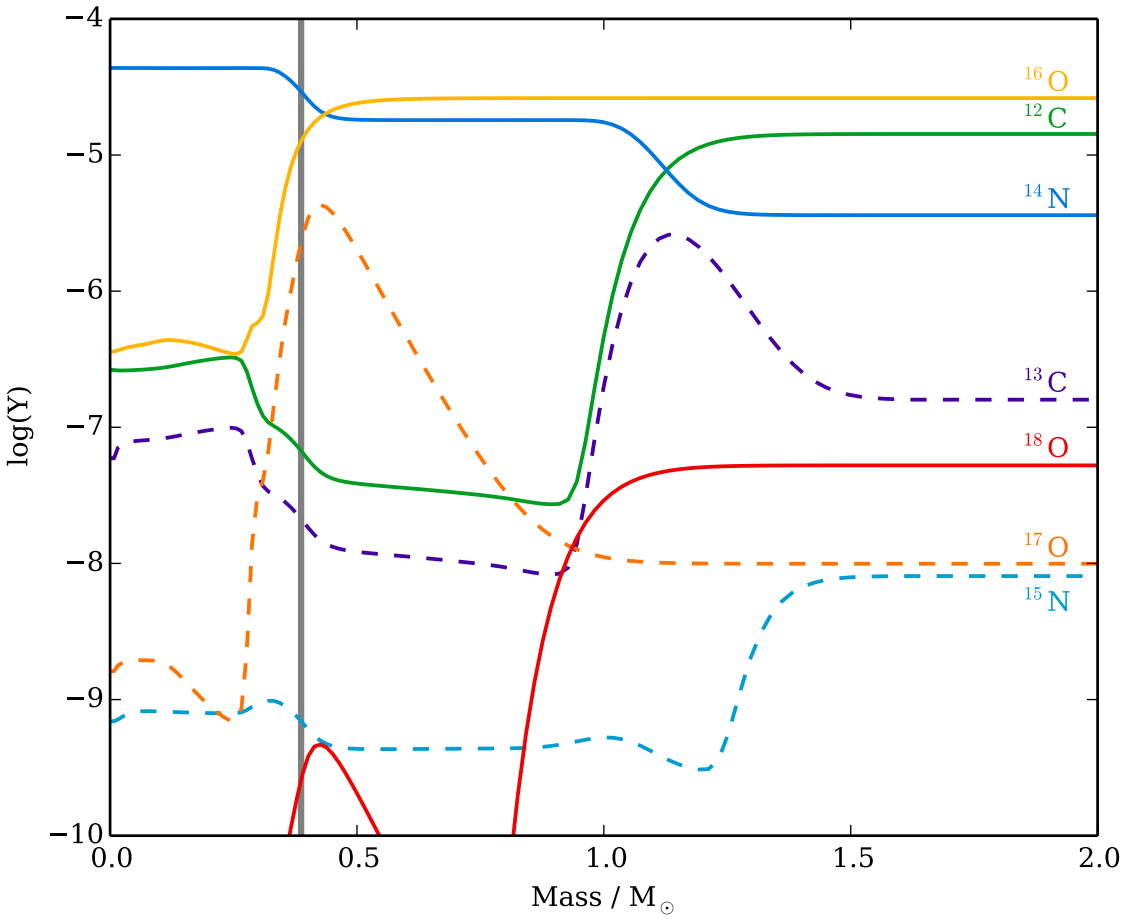

Figure 4.5 The composition profile of C, N, and O isotopes for the 2 $M_\odot$ model just before FDU. The solid grey line shows the deepest extent of the convective envelope during FDU.

of He decreases with increasing initial mass. This is despite the slightly lower initial He abundance of 0.245 for the Cristallo et al. (2011) models.

The decrease in the surface abundance of ^{12}C occurs as FDU reaches into a region of partial H-burning depleted in ^{12}C by the CN cycle. The 2 and 2.25 $M_\odot$ models, with the deepest FDU, have the highest decrease of ^{12}C, down to nearly half of the initial ^{12}C abundance. During FDU the convective envelope reaches a 'pocket' of ^{13}C left over from H-burning (Boothroyd & Sackmann 1999). This pocket causes an increase in the surface abundance of ^{13}C. The location of the pocket is above the region depleted in ^{12}C (Figure 4.5). The 3.5 $M_\odot$ model has the largest enhancement of ^{13}C due to FDU as the 'width' of the ^{13}C pocket generally increases with increasing initial mass for the low-mass models. The lower mass models with deep FDU reach into regions below the ^{13}C pocket that are depleted in ^{13}C (Figure 4.5). Therefore, during FDU, the surface abundance of ^{13}C increases first before decreasing again. However, the net result is that the abundance of ^{13}C is always enhanced compared to the initial abundance.

The abundance of ^{14}N increases towards the core as a result of the active CNO cycle (Figure 4.5). Therefore, FDU increases the abundance of ^{14}N with the enhancement relative to the initial peaking at nearly 3 for the 2 and 2.25 $M_\odot$ models which have the deepest FDU.

The other stable isotope of N, ^{15}N, decreases due to FDU. The surface abundance of ^{15}N displays the opposite trend to ^{14}N where the 2.25 and 2.5 $M_\odot$ models have the highest depletions of around 0.4 times the initial abundance.

When considering the O isotopes, only ^{17}O increases after FDU as it is possible for the convective envelope to reach a pocket of ^{17}O. However, due to the depth of the pocket, only the models with deep FDU are able to consume the pocket. As the ^{17}O pocket is deeper than the ^{13}C pocket, models with shallow FDU show an increase in ^{13}C and not in ^{17}O. The 2 and 2.25 $M_\odot$ models have deep enough FDU to show a decrease in the surface abundance of ^{16}O. In the other models, the convective envelope is not able to reach into regions processed by the ON cycle and that are depleted in ^{16}O. The region depleted in ^{18}O is able to be reached more easily in the low-mass models and the surface abundance of ^{18}O decreases.

The convective envelope in the 5.5 to 7 $M_\odot$ models does not move inwards in mass on the RGB as core He-burning is ignited before this occurs. This is a result of core temperatures reaching above the required 10^8 K to ignite core He-burning before the RGB phase. Therefore, they experience SDU as their first mixing episode (see Figure 4.2).

Figure 4.7 presents the mass of the inner edge of the convective envelope, the mass at the top of the H-shell, and the mass of the H-exhausted core for the 2.5 $M_\odot$ and 2.75 $M_\odot$ models during the early-AGB phase. The convective envelope of the 2.5 $M_\odot$ model moves inwards in mass but is not able to reach the top of the H-shell whereas the convective envelope of the 2.75 $M_\odot$ model reaches the H-exhausted core. This causes H-rich material to be mixed downwards into regions depleted in H, thus reducing the core mass. Here we define the occurrence of SDU to be the reduction in mass of the H-exhausted core.

The occurrence of SDU on the early-AGB changes the composition of a number of isotopes as the convective envelope reaches regions altered by partial H-burning. The changes in surface abundance for isotopes of He, C, N, and O as a result of SDU are presented in Figure 4.6. The surface abundance of ^{4}He increases during SDU with the most massive AGB models having the highest enhancements (relative to the initial abundance). The 6 $M_\odot$ model has the highest enhancement of 1.356 compared to the 7 $M_\odot$ model with 1.354. As a comparison, the 6 and 7 $M_\odot$ models of Boothroyd & Sackmann (1999) with $Z = 0.001$ show post-SDU He enhancements of 1.403 and 1.407, respectively. The models of Boothroyd & Sackmann (1999) have a lower initial He abundance ($Y = 0.24$).

For the models that experience SDU, the post-SDU ^{12}C surface abundance decreases with increasing initial mass. For the models that experience both FDU and SDU, the surface abundance of ^{13}C decreases further from the post-FDU abundance as SDU reaches into the region depleted in ^{13}C that was not reached by FDU. For the models that do not experience FDU, SDU is able to erase the pocket of ^{13}C resulting in an increase in the surface abundance of ^{13}C.

SDU increases the abundance of ^{14}N, with the enhancement increasing with increasing initial mass. The 7 $M_\odot$ model has the highest increase in ^{14}N with a post-SDU abundance just over 4.5 times the initial abundance. SDU decreases the surface abundance of ^{15}N, opposite to the behaviour of ^{14}N.

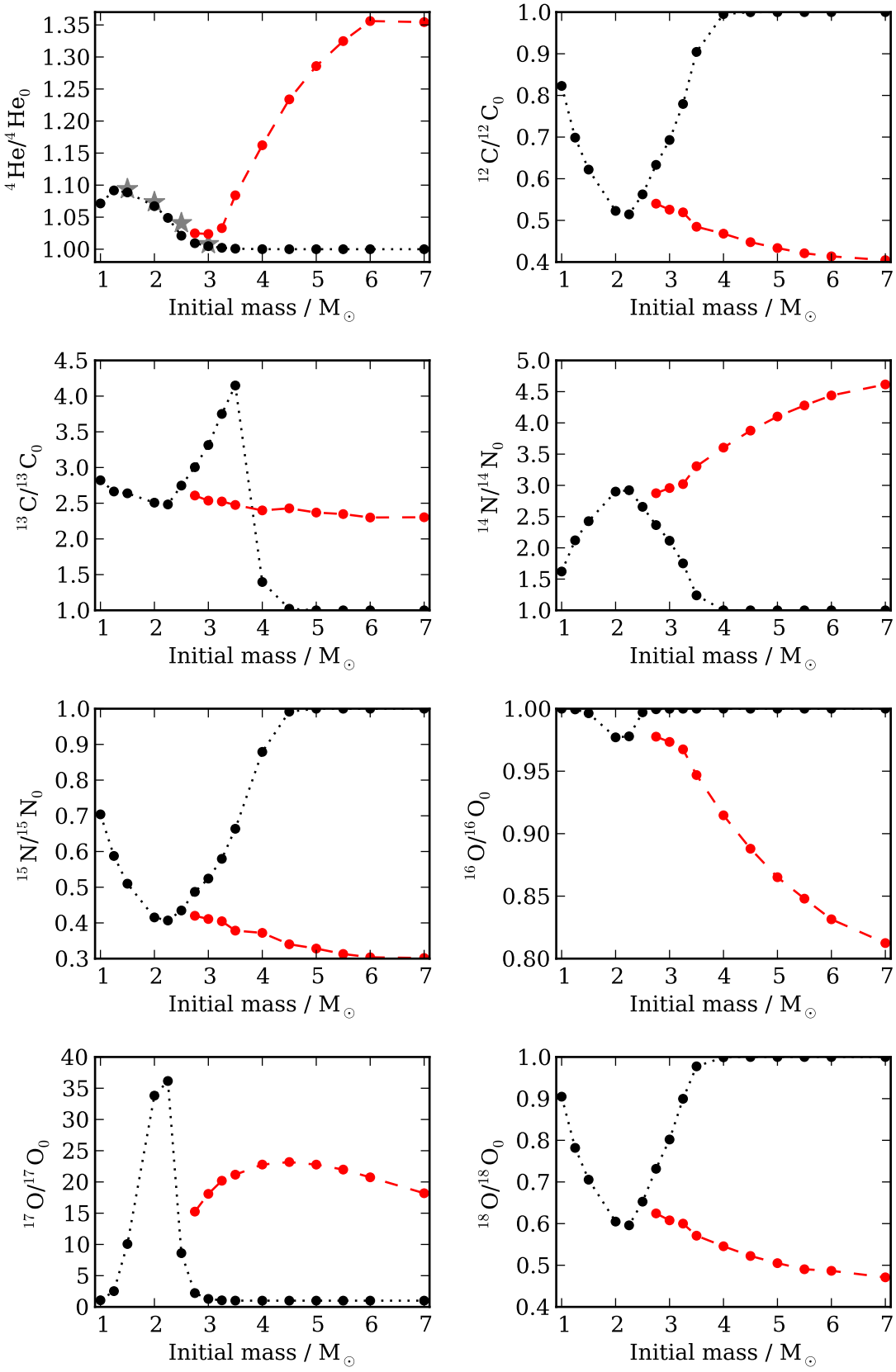

Figure 4.6 Surface abundances for a number of isotopes of He, C, N, and O relative to the initial abundance after FDU (black dotted line) and SDU (red dashed line). The post-FDU ^{4}He enhancements of Cristallo et al. (2011) are shown as grey stars.

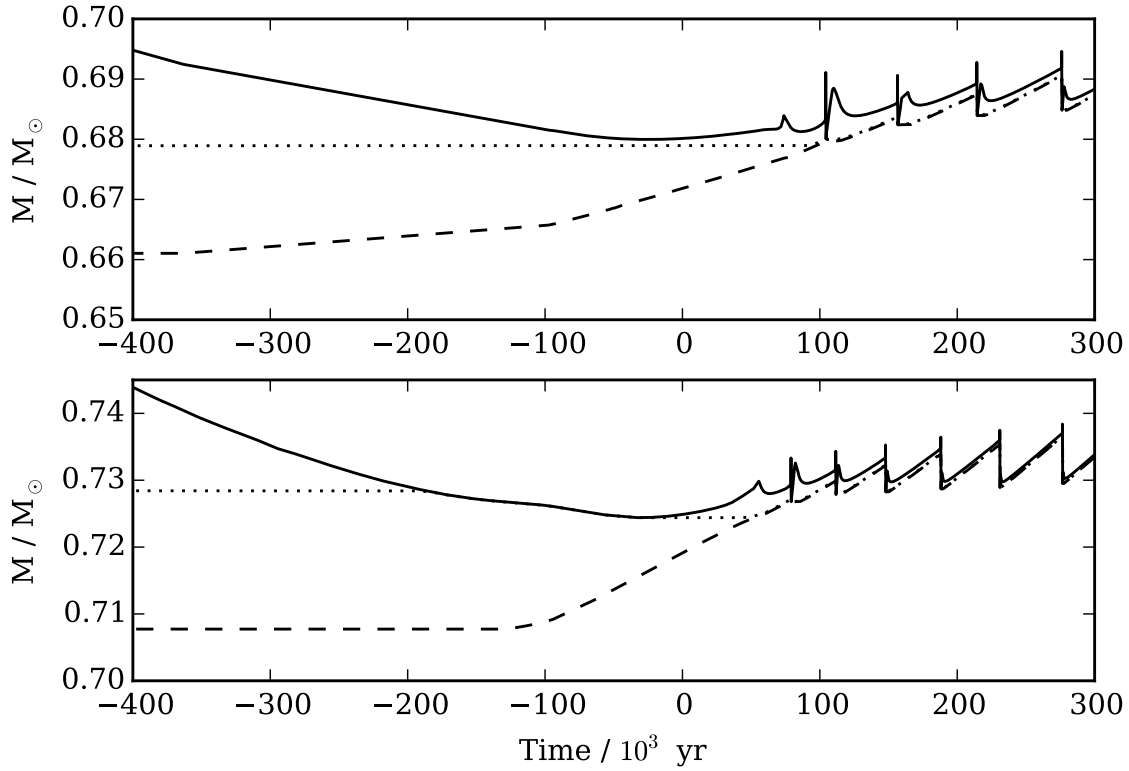

Figure 4.7 The mass of the inner edge of the convective envelope, the mass at the top of the H-shell, and the mass at the bottom of the H-shell for the 2.5 $M_\odot$ (top) and 2.75 $M_\odot$ (bottom) models. SDU is experienced in models with an initial mass $\geq$ 2.75 $M_\odot$ where the mass of the H-exhausted core is reduced.

SDU is able to erase the ^{17}O pocket (if it was not already reached by FDU) as the convective envelope moves further inwards during SDU than FDU. In contrast to other C, N, and O isotopes that either increase or decrease with increasing initial mass, ^{17}O reaches a peak enhancement for the 4.5 $M_\odot$. However, the models that experience SDU do not reach the high ^{17}O enhancements observed in the 2 and 2.25 $M_\odot$ models as the size of the ^{17}O pocket decreases before the occurrence of SDU on the early-AGB.

The surface abundance changes due to FDU and SDU of selected isotopic ratios of C, N, and O are presented in Figure 4.8. The surface abundance of ^{12}C/^{13}C can be used as a tracer of stellar evolution and the mixing processes that occur in the interior of a star (e.g., Charbonnel 1995). FDU and SDU further decrease the abundance of ^{12}C whereas the abundance of ^{13}C increases. This has the effect of decreasing the ^{12}C/^{13}C ratio from an initial value of $\sim$ 90 to between 10 and 30. The decrease is a consequence of the CNO cycle moving towards an equilibrium value of $\sim$ 3.5 for ^{12}C/^{13}C.

Measurements of the ^{12}C/^{13}C ratio in the interstellar medium have found a range of values from approximately 40 to 110 (Sheffer et al. 2007). Therefore, the use of a scaled-solar initial composition for AGB models is not necessarily valid. The initial composition of a model can affect a number of properties during stellar evolution. For example, VandenBerg et al. (2012) used low-mass stellar models to investigate the effect of an increased initial abundance of C, N, and O abundances. They found that the turnoff from the main sequence occurs sooner as

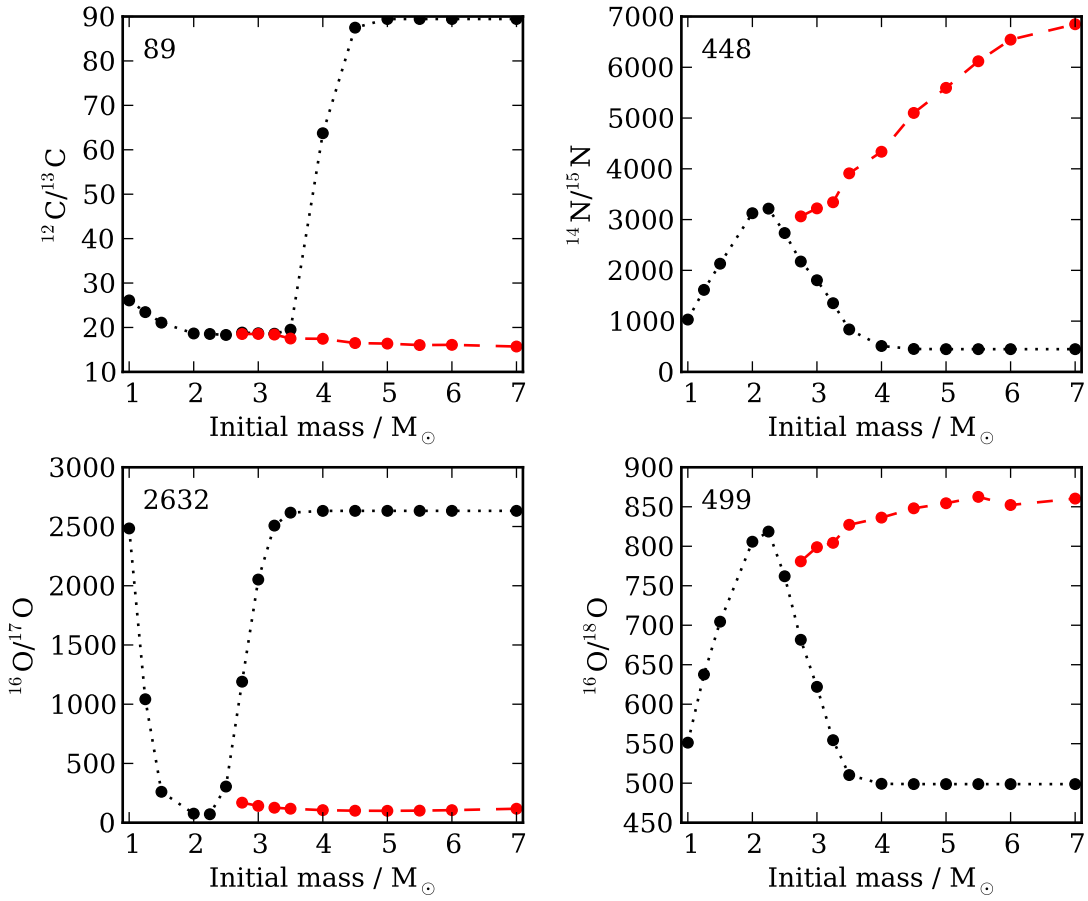

Figure 4.8 Surface abundances for a number of isotopic ratios after FDU (black dotted line) and SDU (red dashed line). The initial value for each isotopic ratio is given in the top-left of each plot.

the CNO cycle becomes more dominant resulting in more centrally concentrated burning.

The study of the globular cluster M4 by Shetrone (2003) found $^{12}C/^{13}C$ values between 4 and 25 (neglecting uncertainties) where the $^{12}C/^{13}C$ ratio increases with decreasing stellar magnitude. Stellar models do not predict $^{12}C/^{13}C$ values as low 4 and the presence of extra mixing has been put forward as a possible solution. When utilising extra mixing during the RGB phase, Boothroyd & Sackmann (1999) are able to reduce the $^{12}C/^{13}C$ ratio to below 5 for the lowest mass models ($\leq 1.8\ M_\odot$ at $Z = 0.001$). The form of extra mixing that Boothroyd & Sackmann (1999) uses involves material at the base of the convective envelope being mixed into regions hot enough for H-burning via the CNO cycle before being mixed back to the surface. The FDU occurs before the RGB bump near the base of the RGB. However, some observations suggest that extra mixing should take place after the RGB bump. For example, in M4, stars below the RGB bump have a high $^{12}C/^{13}C$ ratio whereas stars near the tip of the RGB have low $^{12}C/^{13}C$ ratios (Shetrone 2003).

The $^{14}N/^{15}N$ ratio increases as a result of FDU and SDU mixing up the products of CNO cycling. During SDU in the intermediate-mass, the convective envelope is able to reach the region processed by the ON cycle and, as such, these models have the largest values

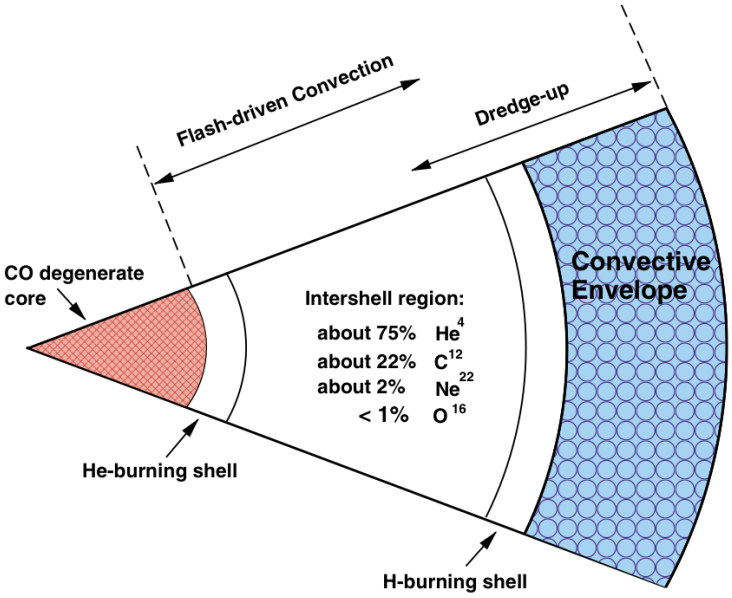

Figure 4.9 The interior structure of an AGB star showing the CO core surrounded by a He-shell and H-shell separated by the He-intershell. Encompassing the core is a deep convective envelope. Note that the schematic is not to scale. Figure from Karakas et al. (2002).

of $^{14}N/^{15}N$. The 7 $M_\odot$ model has the value of nearly 7×10^3 after SDU, up from an initial ratio of 448. The increase in $^{14}N/^{15}N$ with increasing mass follows the same trend as the AGB models of Karakas & Lattanzio (2007) despite the models presented here being of a lower metallicity.

FDU decreases the ratio of $^{16}O/^{17}O$ at the surface with the models with the deepest FDU having the lowest values. This is a result of the large increase in ^{17}O compared to the slight decrease in ^{16}O. The value also depends on the depth of FDU and/or SDU. The mass of the model with the minimum $^{16}O/^{17}O$ value after the FDU is 2.25 $M_\odot$ which has very deep FDU. This is in very good agreement with the $Z = 0.001$ models of Boothroyd & Sackmann (1999) whose minimum $^{16}O/^{17}O$ value occurs for the 2.2 $M_\odot$ model. SDU further decreases the $^{16}O/^{17}O$ ratio from the initial ratio of 2632 to approximately 100. The ratio of $^{16}O/^{18}O$ increases due to FDU and/or SDU from an initial value of 499. The convective envelope is able to move into regions highly depleted in ^{18}O but only into regions slightly depleted in ^{16}O (see Figure 4.8). The intermediate-mass models have the largest increase where the ratio after SDU is approximately 850 at the surface.

4.3. AGB evolution

As described previously in Chapter 3, an AGB star consists of an electron degenerate CO core surrounded by a He-burning shell and a H-burning shell. These shells are separated by the He-intershell and surrounding the core is a large convective envelope. A schematic of the structure of an AGB star is illustrated in Figure 4.9.

During the TP-AGB phase, the H-shell burns for long periods and is periodically interrupted

by a thermally unstable He-shell. As the H-burning shell moves outwards in mass it compresses and heats the He ashes below in the He-intershell. When the mass of this ash reaches a critical point, the He-burning shell is able to ignite making the triple-α reaction the dominant energy source (Salaris & Cassisi 2006). This increase in temperature from the He-burning shell drives a pulse-driven convection zone (PDCZ) in the intershell (see Figure 4.9). This process, called a thermal pulse (TP), mixes material from partial He-burning and neutron-capture nucleosynthesis at high temperatures. For a brief discussion on the nucleosynthesis that takes place in the intershell see Section 4.4.2.

The majority of the energy produced by the He-burning shell (up to 10^9 $L_\odot$) does not increase the surface luminosity but goes into driving an expansion of the star. This expansion moves the H-burning shell into a region of cooler temperature and lower density effectively extinguishing it. At this point, the convective envelope is able to move inwards. If the envelope reaches the He-intershell, material from partial He-burning (mostly ^{4}He and ^{12}C) and neutron-capture nucleosynthesis is mixed to the surface (Herwig 2005). This phenomenon is called the third dredge-up (TDU).

The efficiency of TDU depends on the strength of the previous TP which is linked to the core mass and initial metallicity. However, Karakas et al. (2002) find that the efficiency of TDU does not decrease with TP number if mass loss on the AGB is not considered. The low-mass models presented here with an initial mass of ≤ 2.5 $M_\odot$ reach a peak value of λ before decreasing again[2] (see Figure 1 in Chapter 3). However, it must be noted that these models are able to be evolved to a lower envelope mass than the intermediate-mass models.

At the end of each TDU episode, the star contracts and the H-burning shell re-ignites. The time period between successive TPs is referred to as the interpulse. During the interpulse in intermediate-mass AGB models, the convective envelope is able to move into the top of the H-burning shell resulting in nuclear burning at the base of the convective envelope. This phenomenon, known as hot bottom burning (HBB), can activate the CNO cycle along with the Ne-Na and Mg-Al chains depending on the temperatures reached. Efficient HBB requires temperatures at the base of the convective envelope to be greater than 60×10^6 K (e.g., Ventura & Marigo 2010). These temperatures are higher than the temperatures required for CNO cycling in the H-burning shell as the densities in the convective envelope are lower.

One of the major uncertainties in modelling the AGB phase is the treatment of mass loss (e.g., Stancliffe & Jeffery 2007; Ventura & Marigo 2010) and there are a number of parameterised prescriptions available to model mass loss (e.g., Reimers 1975; Vassiliadis & Wood 1993; Blöcker 1995). For the models presented here, we use the Vassiliadis & Wood (1993) mass-loss prescription on the AGB which is based on observations of carbon- and oxygen-rich stars in the Galaxy and the Large and Small Magellanic Clouds. It also predicts the superwind phase where mass-loss rates reach up to 10^{-4} $M_\odot$ yr^{-1}. Mass loss in low-metallicity AGB stars is one of the largest uncertainties when using mass-loss rates based on observations. Mattsson et al. (2008) concluded that low-metallicity AGB stars have similar mass-loss rates to higher metallicity AGB stars due to the energy injection of pulsations being comparable.

[2]see Chapter 3 for a definition of λ.

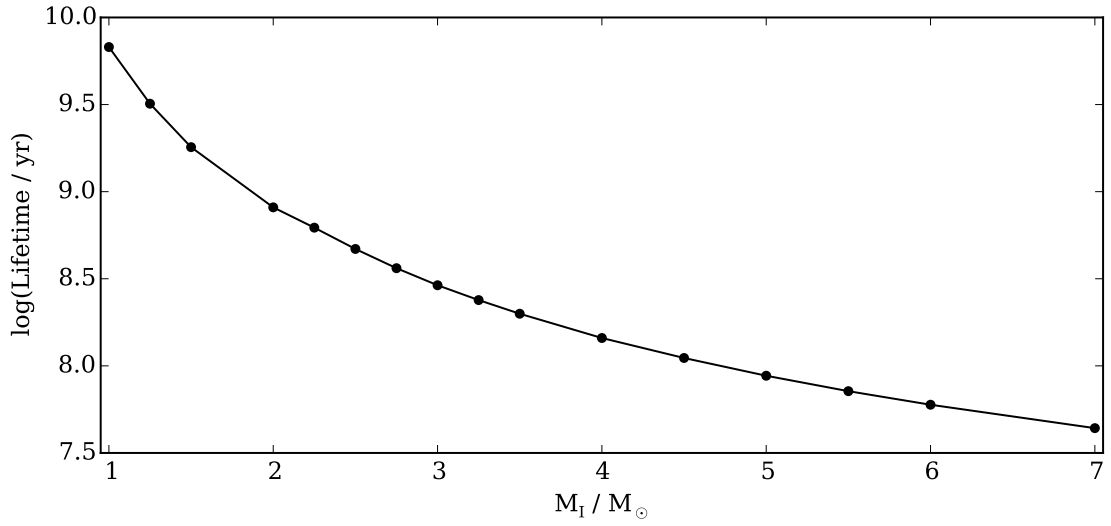

Figure 4.10 Stellar lifetimes for each model with initial mass $M_{\rm I}$.

For further discussion on the uncertainties related to mass loss see Karakas & Lattanzio (2014).

The cycle of He-shell instabilities continues until mass loss erodes the stellar envelope. The star then moves into the post-AGB phase before ending its life as a white dwarf. For further details on the post-AGB phase, see the reviews of Blöcker (2001) and Van Winckel (2003).

4.3.1. Properties of the AGB phase

Here we present in detail a number of stellar properties that influence the nucleosynthesis that takes place during the AGB phase.

Stellar lifetime

The lifetimes of low- to intermediate-mass stars affect how soon these stars will contribute to the chemical evolution of a galaxy. The lifetime of a star is strongly dependent on its initial mass with intermediate-mass stars evolving faster than low-mass stars. This is illustrated in Figure 4.10 for the $Z = 0.001$ stellar models. The lowest mass models ($\lesssim 1.5$ M$_\odot$) have lifetimes greater than a Gyr however all the models have a lifetime less than the age of the Galaxy (Kalirai 2012). AGB stars with an initial mass less than 1 M$_\odot$ at $Z = 0.001$ are unlikely to contribute to the chemical evolution of a stellar system as their lifetimes are likely to be longer than the age of the Universe. It is also possible that these stars will never experience TDU to further enrich the interstellar medium (see Section 4.4.2).

Modelling uncertainties, such as the treatment of convection, can affect the calculated lifetimes (e.g., Alongi et al. 1991). The chemical composition of a model can also alter the predicted lifetimes. Karakas et al. (2014) investigated the role that He enrichment has on the stellar lifetime of low-mass, low-metallicity AGB models. They found that the models

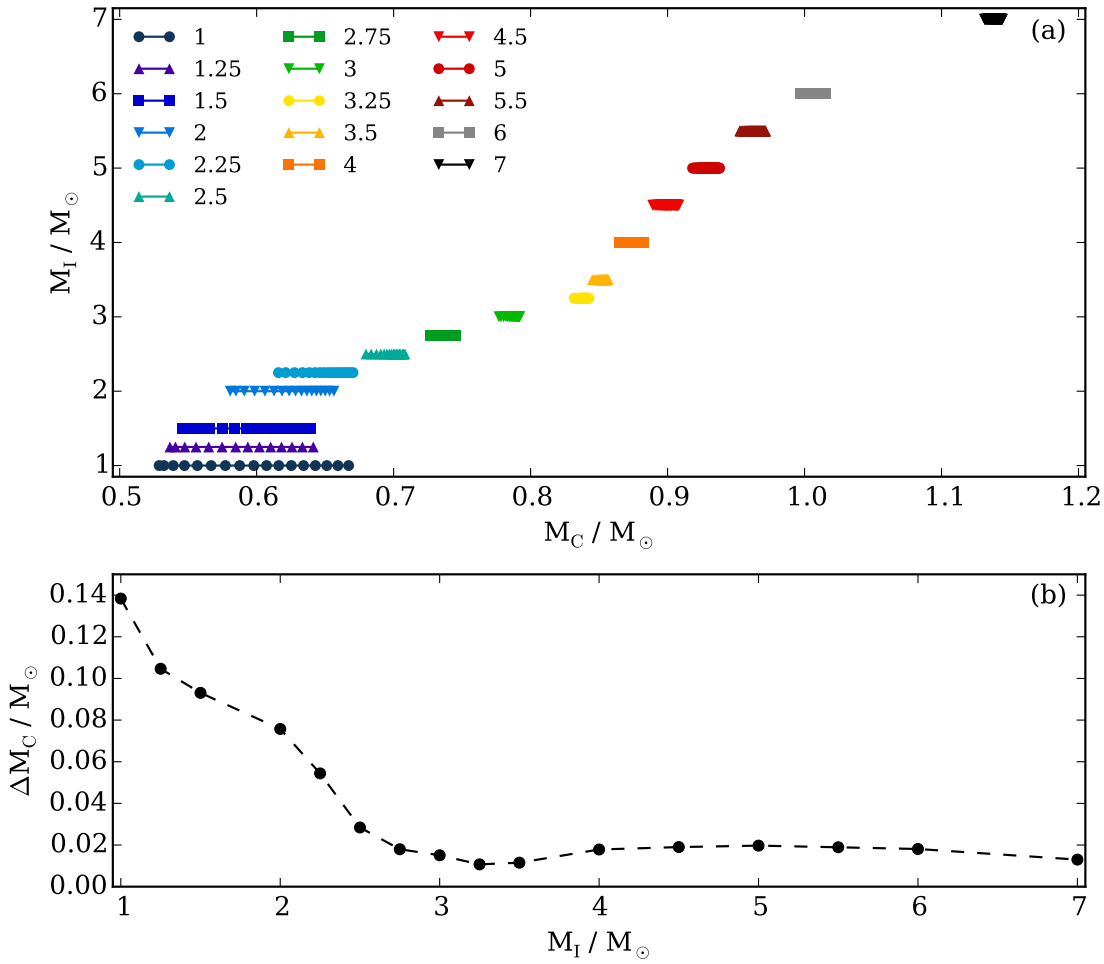

Figure 4.11 *(a)* The growth of the core mass M_C during the AGB phase for each model with initial mass M_I. Each point represents the core mass at each TP. The final core mass is not shown. *(b)* The change in core mass between the first TP and the last TP for each model.

with a higher initial He abundance evolve faster than a primordial He model. Therefore, low-mass models that are He enhanced will be able to contribute to the chemical evolution of a stellar system sooner. We do not investigate the effects due to He enrichment in the models presented here, however, it is expected that models of $Z = 0.001$ with enhanced He would experience the same effect.

Intermediate-mass models, towards the end of the AGB phase, are subject to instabilities that cause divergence issues and terminate calculations (Lau et al. 2012). For the models that experience divergence issues before most of the stellar envelope is ejected, a number of TPs could still occur. However, even if a few TPs are not calculated, the total lifetime will not change greatly as the interpulse period is considerably shorter than the total lifetime. For example, if the 7 $M_\odot$ model was to experience 5 more TPs, the lifetime would only increase by ~ 0.0046 Myr compared to the total calculated lifetime of 44 Myr.

Mass of the H-exhausted core

The growth in the mass of the H-exhausted core over the lifetime of the AGB phase for each model is presented in Figure 4.11. The growth in the mass of the core is a result of the active H-burning shell moving outwards in mass during the interpulse period. Its growth is inhibited if TDU occurs which mixes H-rich material downwards causing the mass of the core to be reduced. The mass of the core affects many properties such as the occurrence of TDU, the strength of the TP, and the efficiency of the H-burning shell. The mass of the core at the end of the TP-AGB phase also determines the mass of the white dwarf remnant and studies of white dwarf populations in nearby open clusters have helped put constraints on TDU and mass loss on the AGB (e.g., Kalirai et al. 2014). The investigation by Kalirai et al. (2014) found that the choice of mass-loss rate on the AGB affects the growth of the core more strongly than TDU which plays a secondary but non-negligible effect.

The core mass at the start of the TP-AGB phase increases with increasing initial mass and, excluding the 1 and 1.25 $M_\odot$ models, the core mass at the end of the TP-AGB increases with increasing initial mass. The 1 and 1.25 $M_\odot$ models experience minimal TDU (with low values of λ) and long interpulse periods which allow the core mass to increase more per TP compared to the other low-mass models.

The low-mass models have the greatest growth in core mass compared to the intermediate-mass models as a result of longer interpulse periods and less efficient TDU (see Figure 4.11). The change in the core mass on the AGB decreases with increasing initial mass for the low-mass models. For the 1 $M_\odot$ model which has the fewest number of TDU episodes, the core mass increases by 0.14 $M_\odot$ from the first TP to the last. In comparison, the core of the 3 $M_\odot$ increases by 0.015 $M_\odot$.

All the intermediate-mass models have a core mass greater than 0.8 $M_\odot$ at the start of the TP-AGB phase. The 7 $M_\odot$ model ends the TP-AGB phase with the most massive core of all the models calculated (1.145 $M_\odot$). The core mass at the start of the AGB is also above the minimum core mass of 1.06 $M_\odot$ required for an ONe core to form (Doherty et al. 2014b, 2015) where core temperatures are high enough to start C-burning. Stars that ignite off-centre core C-burning are known as super-AGB stars (Siess 2007). We find that the 7 $M_\odot$ model presented here ends the TP-AGB phase with an ONe core and is classified as a super-AGB.

The core mass of the 7 $M_\odot$ super-AGB model of $Z = 0.001$ calculated by Doherty et al. (2014b) grows from 1.13 $M_\odot$ after SDU to 1.14 $M_\odot$ at the end of the calculation. This core growth is very similar to our 7 $M_\odot$ model where the core increases from 1.129 $M_\odot$ after SDU to 1.145 $M_\odot$ at the end of calculations after experiencing 135 TPs. The small increase in core mass is the result of short interpulse periods along with efficient TDU inhibiting core growth. Doherty et al. (2014b) found that the final core mass in super-AGB stars is not affected by an increased mixing length theory α value (Böhm-Vitense 1958) or the choice of mass-loss rate.

The interplay of mass loss and low-temperature opacities can also affect the growth of the core in AGB stars. Constantino et al. (2014) determined that accounting for the change in the abundance of C, N, and O in the low-temperature opacity treatment causes the core

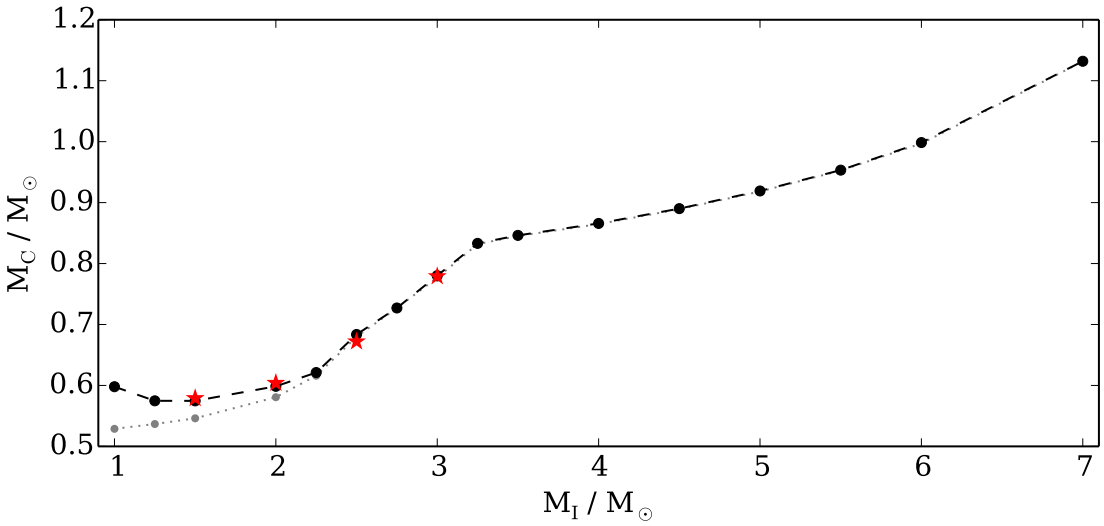

Figure 4.12 The minimum core mass required for TDU (black dashed line) and the core mass at the first TP (grey dotted line) for each model with initial mass $M_{\rm I}$. The red stars show the minimum core mass required for TDU for the $Z = 0.001$ models of Cristallo et al. (2011).

at the end of the AGB phase to be less massive than if a composition-independent opacity treatment is used. This is due to a shorter AGB lifetime as the mass-loss rate increases. These conclusions were also found in the investigation of Fishlock et al. (2014b) using $Z = 0.001$ models of 5 and 6 $M_{\odot}$.

All the models experience TDU during the TP-AGB phase and the minimum core mass required for TDU along with the core mass at the first TP in each model is presented in Figure 4.12. The minimum core mass required for TDU dictates whether an AGB star, particularly one of low mass, will experience TDU at all. Observations of the carbon star luminosity function of the Large and Small Magellanic Clouds suggest that AGB stellar models overestimate the core mass required for TDU. Studies have found that TDU in AGB models must be more efficient and begin earlier (ie. at a lower core mass) in order to explain carbon star luminosity function in the Magellanic Clouds (e.g., Stancliffe et al. 2005; Kamath et al. 2012).

We find the minimum core mass for the occurrence of TDU to be 0.575 $M_{\odot}$ for both the 1.25 and 1.5 $M_{\odot}$ models. For the 1.25 $M_{\odot}$ model, TDU first occurs at the sixth TP while for the 1.5 $M_{\odot}$ model TDU first occurs at the fifth TP. The minimum core mass required for TDU then increases with increasing initial mass. For the low-mass models less than 2.5 $M_{\odot}$, there is a noticeable increase in the core mass between the first TP and the first TDU episode (Figure 4.12). The core mass for the 1 $M_{\odot}$ model at the first TP is 0.529 $M_{\odot}$ whereas TDU does not occur until the core grows to 0.598 $M_{\odot}$. The intermediate-mass models do not experience their first TDU episode at the first TP but the increase in core mass after the first interpulse is negligible.

Figure 4.12 also presents the low-mass models of Cristallo et al. (2011) at $Z = 0.001$. The $Z = 0.001$ models of Cristallo et al. (2011) have a minimum core mass for TDU of 0.579 $M_{\odot}$

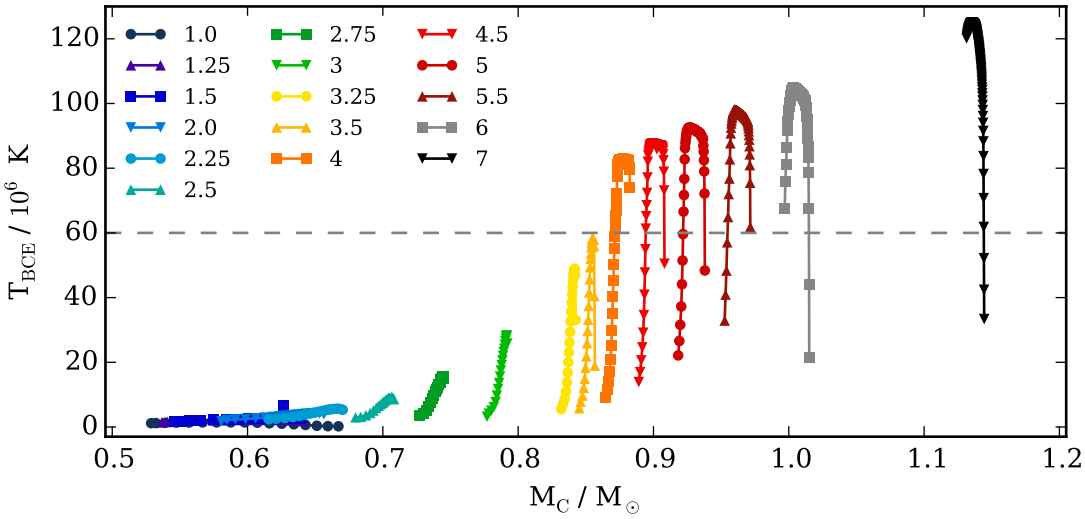

Figure 4.13 Temperature at the base of the convective envelope $T_{\rm BCE}$ (during the interpulse period) as a function of core mass for each stellar model. The dashed line shows the temperature at which HBB is efficiently activated.

in their 1.5 $M_\odot$ model which occurs at the third TP. Despite the difference in the treatment of convection compared to the models presented here, there is good agreement for the minimum core mass required for TDU between the different methods.

A number of factors, such as metallicity, can influence the minimum core mass at the first TDU episode (Karakas et al. 2002). Increasing the initial abundance of He at a given stellar mass increases the minimum core mass required for TDU as well as the core mass at the first TP (Karakas 2014). This is because models enriched in He reach the AGB with a higher core mass due to higher He-burning temperatures (Karakas et al. 2014).

Figure 4.12 demonstrates the same trend as seen in the models of Karakas et al. (2002) where the minimum core mass at the first TDU episode first decreases with increasing initial mass before increasing again. When considering the results of Karakas et al. (2002) and the results presented here, the initial mass of the model with the smallest core at TDU decreases with decreasing metallicity.

Temperature at the base of the convective envelope

Figure 4.13 shows the temperature at the base of the convective envelope ($T_{\rm BCE}$) during the interpulse period against core mass for each of the models. The presence of efficient HBB requires $T_{\rm BCE}$ to reach above 60×10^6 K. At these temperatures ^{7}Li can be produced and the CN cycle is activated with ^{14}N being produced at the expense of ^{12}C, ^{13}C, and ^{16}O.

In models less massive than 3 $M_\odot$, $T_{\rm BCE}$ never reaches above 20×10^6 K. Therefore the TDU is the only mixing episode during the TP-AGB phase that alters the surface composition. The 3 $M_\odot$ model experiences very minimal HBB which only slightly affects the ^{12}C / ^{13}C ratio and not ^{14}N. Of the models that experience HBB during the interpulse period, the

3.5 $M_\odot$ model only experiences minimal HBB for a few TPs (see Figure 4.14) whereas the more massive models have very efficient HBB.

The 7 $M_\odot$ model enters the TP-AGB phase with $T_{\rm BCE}$ already above 120×10^6 K. In this case, efficient HBB starts during the early-AGB phase converting C to N. The maximum $T_{\rm BCE}$ reached during the AGB phase is 125×10^6 K. For the 7 $M_\odot$ model of Doherty et al. (2014b) at the same metallicity, the maximum $T_{\rm BCE}$ reached is slightly lower at 120×10^6 K.

The grid of intermediate-mass AGB models and super-AGB models by Doherty et al. (2014a,b) demonstrates that the maximum $T_{\rm BCE}$ reached during the interpulse period increases with decreasing metallicity for a given initial mass. Despite this, the lower metallicity 6 $M_\odot$ model of Straniero et al. (2014) has a lower maximum $T_{\rm BCE}$ than the 6 $M_\odot$ model presented here (91×10^6 K compared to 105×10^6 K). This discrepancy may be the result of the different initial composition (as the model is α-enhanced) or the different treatment of convection. Straniero et al. (2014) state that instantaneous mixing can overestimate the effects of HBB as the timescales for nuclear burning are shorter than the timescales for convection.

The choice of α, the MLT parameter, affects the temperatures reached at the base of the convective envelope (Renzini & Voli 1981; Ventura & D'Antona 2005a; Doherty et al. 2014a). A higher α value increases $T_{\rm BCE}$ thus increasing the surface luminosity. With an increased surface luminosity, the rate of mass loss increases shortening the lifetime of the AGB phase and therefore the number of TDU episodes. As there are large uncertainties when modelling convection using the MLT, the choice of α is subjective and often calibration to a 'solar model' is used. However, the use of a solar model is not always appropriate as the evolution during the main sequence is different to that on the AGB phase.

There are additional factors that can affect the temperature at the base of the convective envelope. Ventura & Marigo (2009, 2010) found that including composition-dependent low-temperature opacities in low-mass AGB models of $Z = 0.001$ can dramatically lower the $T_{\rm BCE}$. Constantino et al. (2014) investigated the role of low-temperature opacity at even lower metallicities. They found that temperatures at the base of the convective envelope in the 2.5 $M_\odot$ models with [Fe/H] ≤ -2 exceed 60×10^6 K if changes in composition for the low-temperature opacities are disregarded. When the low-temperature opacities are correctly followed, the $T_{\rm BCE}$ lowers as a result of the higher mass loss rate. In the case of the [Fe/H] $= -2$ model of 2.5 $M_\odot$, the maximum $T_{\rm BCE}$ decreases from 72.6×10^6 K to 12.3×10^6 K. The models presented here use composition-dependent low-temperature opacities as described in Kamath et al. (2012) for the low-mass models and Fishlock et al. (2014b) for the intermediate-mass models.

The temperature at the base of the convective envelope is dependent on the mass-loss rate where a significant reduction in the envelope mass can terminate HBB (Frost et al. 1998). Therefore, the choice of mass-loss prescription on the AGB can alter the duration of HBB. For example, the study by Karakas et al. (2012) found that using a delayed superwind (where the superwind does not begin until the pulsation period increases further) will increase the duration of HBB which results in higher temperatures at the base of the convective envelope.

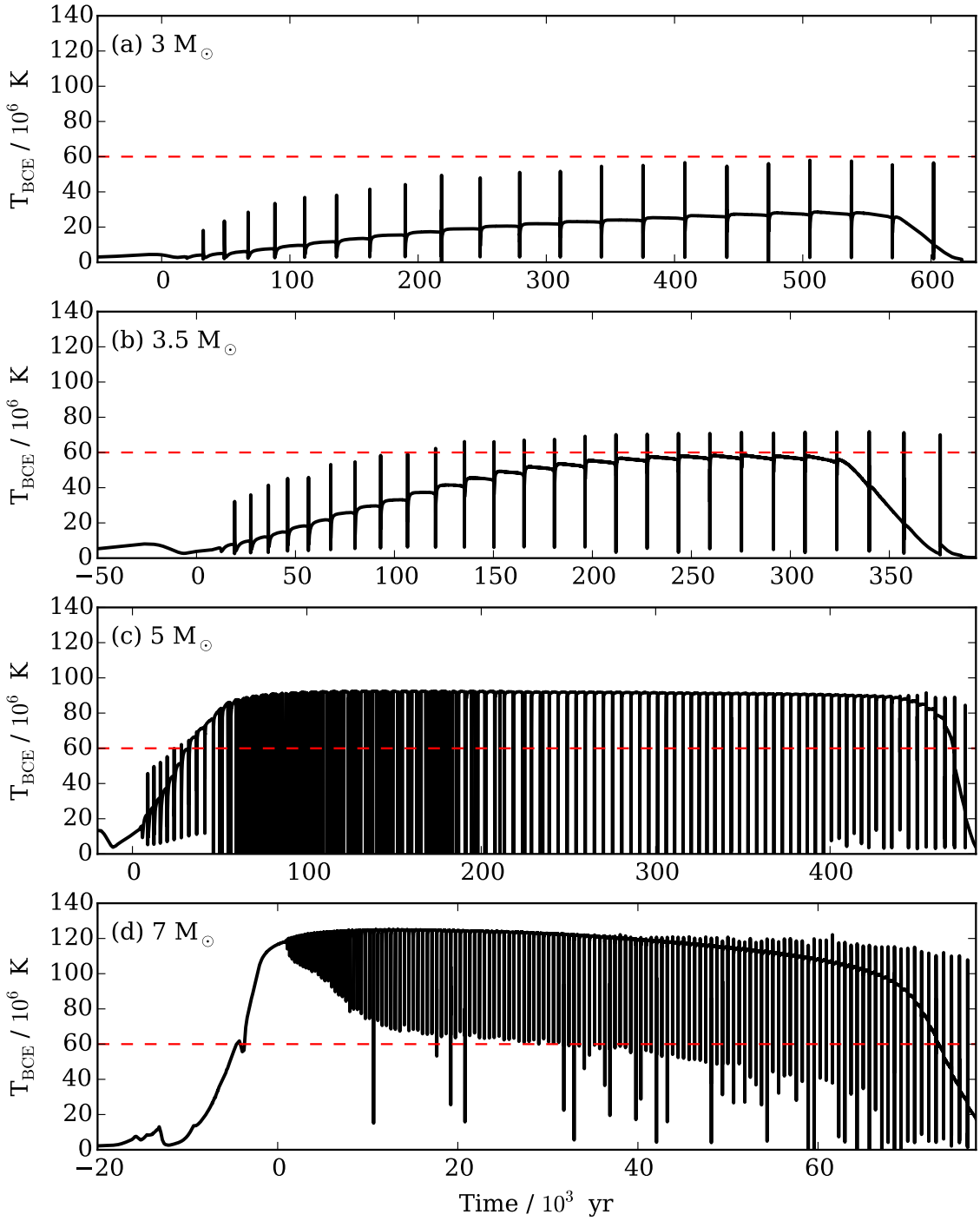

Figure 4.14 Temperature at the base of the convective envelope $T_{\rm BCE}$ from the start of the AGB phase for the (a) 3 $M_\odot$, (b) 3.5 $M_\odot$, (c) 5 $M_\odot$, and (d) 7 $M_\odot$ models of $Z = 0.001$. The dashed line shows the minimum temperature where efficient HBB takes place.

4.4. AGB nucleosynthesis

During the AGB phase, recurrent mixing episodes are able to enrich the stellar envelope with elements such as C, F, and the neutron-capture elements. High mass-loss rates eject the envelope which then pollutes the interstellar medium and consequently the next generation of stars. As mentioned in Section 4.3, two processes are able to alter the composition of elements at the stellar surface: HBB and TDU. The presence of HBB and TDU is strongly dependent on the initial mass and metallicity of a star where the prediction of stellar yields depends on the interplay between HBB and TDU. Input physics into the stellar models such as the treatment of convection, opacity, and mass-loss rate can also affect the occurrence of HBB and TDU (e.g., Marigo 2002; Stancliffe & Jeffery 2007; Marigo 2007; Doherty et al. 2014a).

The spectroscopic study by Merrill (1952) of S-type stars (C/O $\approx$ 1) uncovered the presence of the unstable element Tc where the longest-lived isotope of Tc produced by the *s*-process is ^{99}Tc which has a half-life of approximately 211,100 years. The discovery of Tc in the stellar atmospheres of these stars suggested that Tc had been recently produced in the stellar interior before being mixed to the surface. Further observational confirmation for the existence of AGB stars came through spectroscopic analyses of stars enhanced in C and *s*-process elements (e.g., Wallerstein & Knapp 1998; Abia et al. 2002).

In this section, we provide a summary of the nucleosynthesis as a result of HBB and TDU using the $Z = 0.001$ models presented in Chapter 3. For an in-depth review on nucleosynthesis and stellar yields in AGB stars, see Karakas & Lattanzio (2014).

4.4.1. Hot bottom burning

Observational evidence for HBB came from the lack of luminous carbon-rich stars in the Large and Small Magellanic Clouds (e.g., Wood et al. 1983). The discovery of luminous Li-rich stars in the Magellanic Clouds (e.g., Smith & Lambert 1989, 1990; Plez et al. 1993) further confirmed that HBB is taking place in intermediate-mass AGB stars. These stars also showed enhancements of *s*-process elements confirming them as intrinsic AGB stars.

As demonstrated in Figure 4.13, temperatures at the base of the convective envelope can reach above 60×10^6 K in models with an initial mass of 4 $M_\odot$ or more. At these temperatures, the surface abundances of elements such Li, C, N, O, Ne, Na, Mg, and Al can be altered (e.g., Mowlavi & Meynet 2000; Ventura & D'Antona 2010; Ventura et al. 2011, 2012; Doherty et al. 2014a,b).

Lithium

HBB is theorised to increase the surface abundance of the fragile isotope ^{7}Li through the Cameron-Fowler mechanism (Cameron & Fowler 1971). The process requires that a ^{3}He nuclei captures an α-particle producing ^{7}Be. The ^{7}Be nuclei can either capture a proton to complete the pp-III chain or capture an electron to produce ^{7}Li. The path that ^{7}Be takes

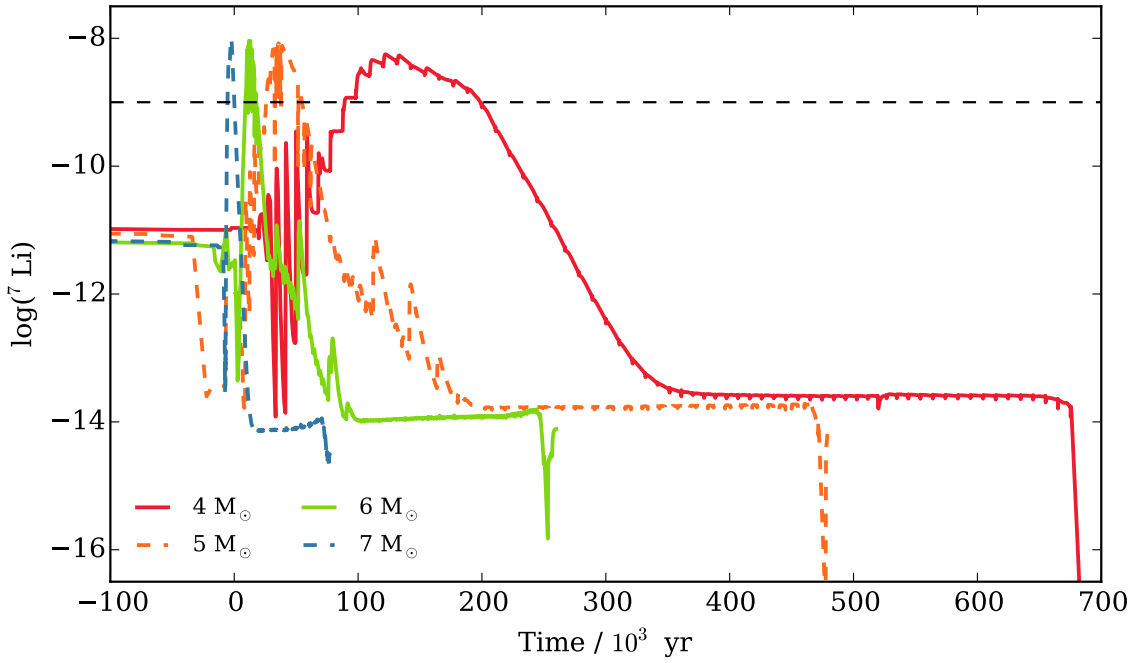

Figure 4.15 Surface abundance of ^{7}Li (in mole fraction) from the start of the AGB phase for four intermediate-mass models that experience efficient HBB. The dashed line shows the minimum abundance for a star to be defined as Li rich.

strongly depends on the temperature of the region. As a result of efficient mixing in the convective envelope, some ^{7}Be is mixed into cooler regions preventing proton capture and instead captures an electron to produce ^{7}Li. Once the envelope is depleted of ^{3}He, the production of ^{7}Li ceases.

All the models more massive than 3.25 $M_{\odot}$ become Li rich where $\log \epsilon(^{7}\mathrm{Li}) > -9$ at some point during the AGB phase. Figure 4.15 presents the surface abundance of ^{7}Li during the AGB phase for four intermediate-mass models that experience efficient HBB. The duration of the Li-rich phase decreases with increasing initial mass from approximately 190×10^{3} years for the 3.5 $M_{\odot}$ model to approximately 5×10^{3} years for the 7 $M_{\odot}$. Blöcker & Schoenberner (1991) predict that it would not be possible to observed Li-rich stars brighter than $M_{\mathrm{bol}} \gtrsim -7$ as the duration of the Li-rich phase would be too short. For the 7 $M_{\odot}$ model, the Li-rich phase starts before the TP-AGB phase.

There are many uncertainties in modelling the production and destruction of Li due to the timescales involved. The timescales for the reactions involved in the Cameron-Fowler mechanism are comparable to the timescales for mixing (Sackmann & Boothroyd 1992; Lattanzio 1992). This allows for ^{7}Li and ^{8}Be to move into regions of lower temperature preventing their destruction. Therefore, when modelling ^{7}Li, an approximation is needed for time-dependent mixing in the convective envelope.

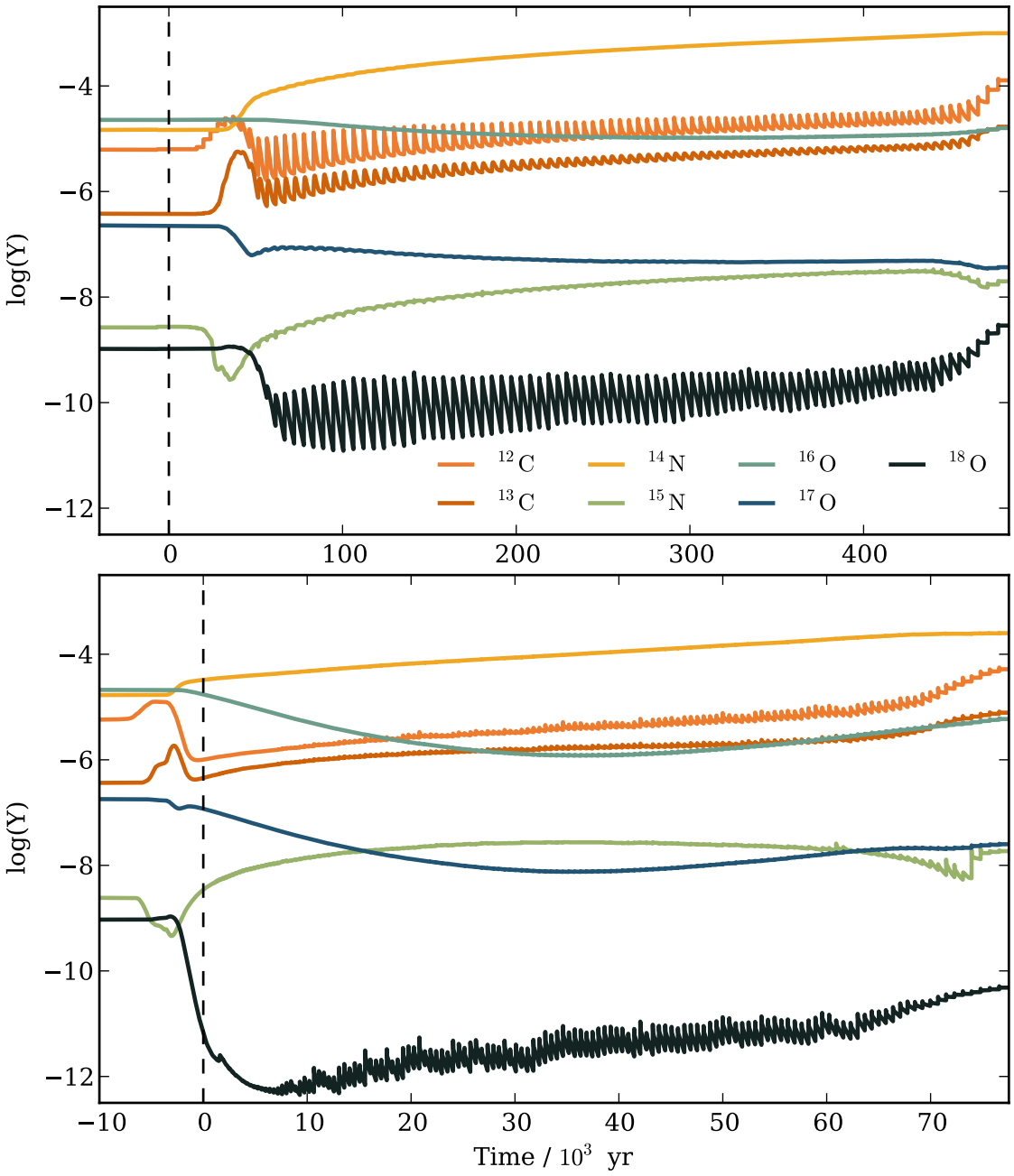

Figure 4.16 The surface abundance of select C, N, O, and F isotopes for the 5 $M_\odot$ model (top) and the 7 $M_\odot$ model (bottom). The dashed line marks the start of the AGB phase.

C, N, O, and F

Temperatures during HBB are high enough to activate the CNO cycle where the abundance of N increases at the expense of C and O (for more details see Section 4.2). Figure 4.16 illustrates the change in abundance of select C, N, O, and F isotopes during the AGB phase for the 5 $M_\odot$ and 7 $M_\odot$ models. The 7 $M_\odot$ model has the most extreme behaviour of all the models as a result of very efficient HBB.

In the 5 $M_\odot$ model, TDU starts before $T_{\rm BCE}$ becomes high enough to activate the CNO cycle. Therefore, the abundance of ^{12}C in the envelope increases. The increase in ^{13}C occurs when HBB activates the CN cycle and eventually ^{14}N is produced and the abundances of both ^{12}C and ^{13}C decrease. The competing effect of TDU and HBB results in a sawtooth pattern for ^{12}C, ^{13}C, and ^{19}F where TDU increases the surface abundance before it is depleted through HBB.

Each TDU episode increases the surface abundance of ^{12}C whereas HBB decreases its abundance during the interpulse. The ^{12}C/^{13}C ratio in the 5 $M_\odot$ model decreases from approximately 17 at the start of the AGB phase to the equilibrium value of ~ 3 during HBB with TDU periodically increasing the ^{12}C/^{13}C ratio. The 5 $M_\odot$ model then ends the AGB phase with a ^{12}C/^{13}C ratio of 7.6 as HBB ceases before TDU (see Frost et al. 1998).

HBB causes the surface abundance of ^{14}N to continually increase during the AGB phase through either ^{13}C(p,γ)^{14}N or ^{17}O(p,α)^{14}N. The 5 $M_\odot$ model ends the AGB phase with a higher surface abundance of ^{14}N than the 7 $M_\odot$ model with $\log(^{14}\mathrm{N}) \approx -3.0$, compared to $\log(^{14}\mathrm{N}) \approx -3.6$. This difference can be attributed to the longer duration of HBB for the 5 $M_\odot$ model. The abundance of ^{15}N decreases at the start of the AGB phase before increasing to a maximum. It then decreases slightly at the end of the AGB phase as HBB becomes less efficient.

The O isotopes, ^{16}O and ^{17}O, are destroyed via proton capture during HBB. The 5 and 7 $M_\odot$ models have a lower surface abundance of ^{16}O and ^{17}O at the end of the AGB phase than at the start. The more massive AGB models experience a larger decrease in the surface abundance of ^{16}O. This effect is seen when comparing the 5 $M_\odot$ model to the 7 $M_\odot$ model (Figure 4.16).

The destruction of ^{19}F at the base of the convective envelope is very efficient with the temperatures reached during HBB. Therefore, massive AGB stars are not expected to show enhancements of F (Mowlavi et al. 1996). The 7 $M_\odot$ model ends the AGB phase with a lower surface abundance of ^{19}F than the 5 $M_\odot$ model due to a higher $T_{\rm bce}$ and a lower $M_{\rm TDU}$. The peculiar Li-rich carbon star WZ Cas is observed to have a large enhancement of F with [F/Fe] = +1.15 (Abia et al. 2010). This is at odds of what is expected if the star is experiencing efficient HBB in order to produce Li.

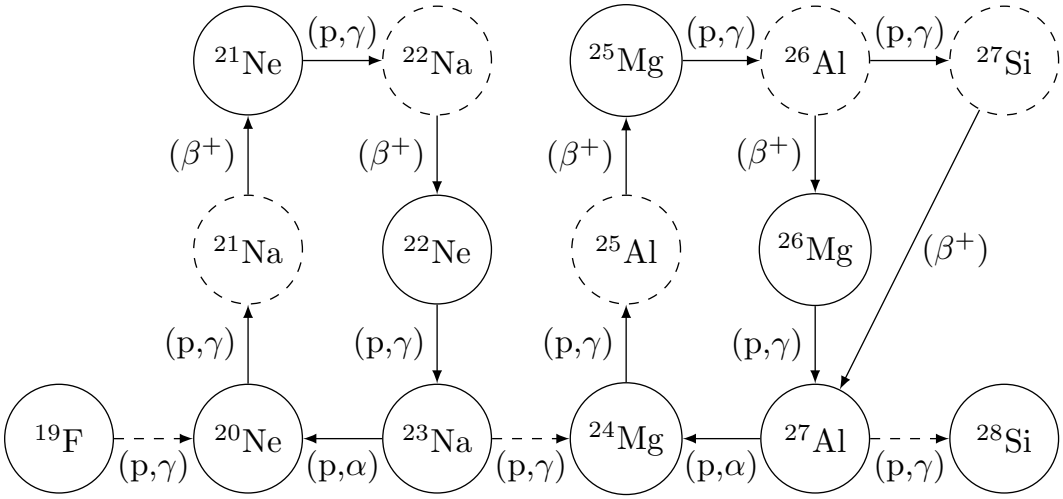

Figure 4.17 Schematic of the Ne-Na and Mg-Al chains. Dashed circles represent unstable isotopes.

Ne, Na, Mg and Al

The activation of the Ne-Na and Mg-Al chains through efficient HBB results in the enhancement of ^{23}Na, ^{25}Mg, ^{26}Mg, and ^{26}Al. Figure 4.17 presents the reactions involved in the Ne-Na and Mg-Al chains. The relative rates of ^{23}Na(p,α)^{20}Ne and ^{23}Na(p,γ)^{24}Mg control the rate of leakage from the Ne-Na chain to the Mg-Al chain. At even higher temperatures, such as those reached in super-AGB stars (Doherty et al. 2014b), ^{28}Si can be produced through the ^{27}Al(p,γ)^{28}Si reaction (e.g., Ventura et al. 2011).

Figure 4.18 illustrates the surface abundance of select Ne, Na, Mg, and Al isotopes during the AGB phase for the 5 $M_\odot$ and 7 $M_\odot$ models. The production of ^{23}Na occurs at the expense of ^{22}Ne through proton capture (Mowlavi 1999). In particular, AGB stars are able to produce primary ^{23}Na from primary ^{22}Ne produced in the intershell. Temperatures above $(70-80)\times10^6$ K destroy ^{23}Na through proton capture producing either ^{20}Ne or ^{24}Mg (Mowlavi 1999).

In general, HBB increases the surface abundance of ^{25}Mg and ^{26}Mg and decreases the abundance of ^{24}Mg (Karakas & Lattanzio 2003). Once HBB ceases, the surface abundance of ^{24}Mg can increase as TDU is able to mix freshly synthesised ^{24}Mg to the surface. The 7 $M_\odot$ super-AGB model experiences temperatures of up to 125×10^6 K at the base of the convective envelope that increase the rate of leakage from the Ne-Na chain into the Mg-Al chain. This causes the ^{25}Mg and ^{26}Mg surface abundances to decrease. The same trends are observed in the 7 $M_\odot$, $Z = 0.001$ model of Doherty et al. (2014b). The 5 $M_\odot$ model ends the AGB phase with a [Mg/Fe] ratio of 0.61 whereas the 7 $M_\odot$ model has a final [Mg/Fe] ratio of 0.

The long-lived unstable isotope ^{26}Al ($\tau_{1/2}\approx7.4\times10^5$ yr) is produced at the expense of ^{25}Mg through proton-capture nucleosynthesis where temperatures of over $(60-70)\times10^6$ K are required before ^{25}Mg is destroyed. We find the 5 $M_\odot$ model has a higher net yield of ^{26}Al than the 7 $M_\odot$ model with 3.1×10^{-5} $M_\odot$ compared to 1.4×10^{-5} $M_\odot$. Doherty et al. (2014b) also find a lower ^{26}Al yield for the 7 $M_\odot$ model of $Z = 0.001$ compared to their 6.5 $M_\odot$

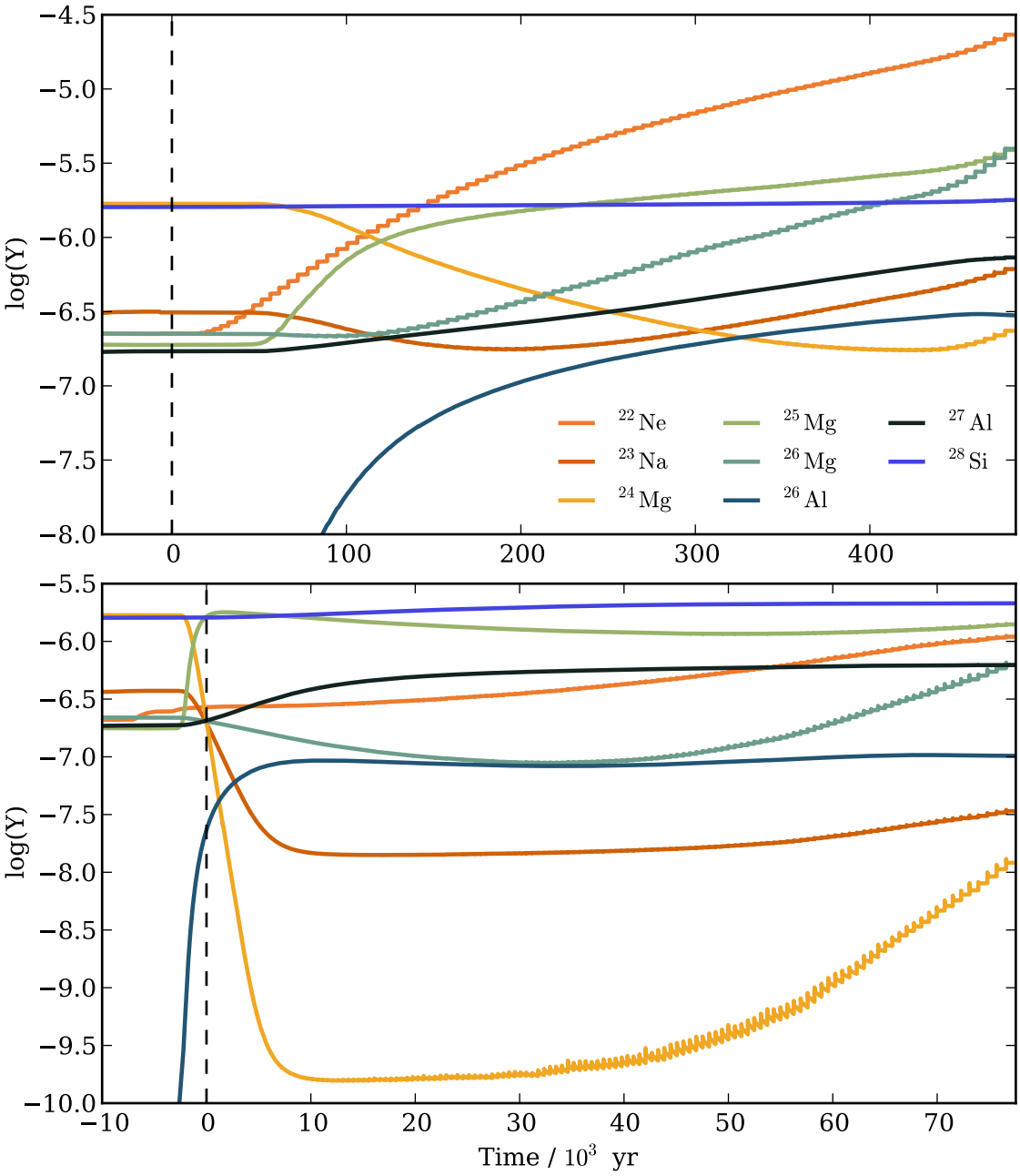

Figure 4.18 The surface abundance of select Ne, Na, Mg, and Al isotopes for the 5 $M_\odot$ model (top) and the 7 $M_\odot$ model (bottom). The dashed line marks the start of the AGB phase.

model. The lower ^{26}Al yield for the 7 $M_\odot$ model is a result of the base of the convective envelope reaching temperatures above 120×10^6 K. Eventually, ^{26}Al will decay to ^{26}Mg.

The abundance of ^{28}Si increases from proton captures on ^{27}Al when temperatures at the base of the convective exceed $(120 - 130) \times 10^6$ K (Doherty et al. 2014b). For the 5 $M_\odot$ model the surface abundance of ^{28}Si only slightly increases as a result of TDU whereas the 7 $M_\odot$ model is able to produce considerably more ^{28}Si through HBB (see Table 3.6).

4.4.2. Third dredge-up

TDU mixes the products of partial He-burning and H-burning to the surface. Additionally, the products remaining from the H-burning shell affect the products produced through He-burning. TDU is also responsible for the observed enhancements in the neutron-capture elements (e.g., Abia et al. 2002).

After ^{4}He, the most abundant isotope mixed to the surface is ^{12}C. This is demonstrated in Figure 4.19 using the 3 $M_\odot$ model. The He-burning shell is responsible for producing ^{12}C which is then diluted by the PDCZ before TDU mixes it to the surface. The surface abundance of ^{13}C increases as a result of mild HBB during each TDU episode. This is reflected in the low ^{12}C/^{13}C ratio of 89. In comparison, the 2.75 $M_\odot$ model has a final ^{12}C/^{13}C ratio of 2355 (see Table 3.7).

There is minimal production of ^{14}N in the low-mass models as it is destroyed in the PDCZ after being produced in the H-burning shell and the ^{14}N pocket that forms from the addition of a PMZ. This is also reflected in the net yield of ^{14}N in these models. ^{15}N is produced in the H-burning shell and the ^{13}C pocket. However, in the 3 $M_\odot$ model, ^{15}N is completely destroyed in the PDCZ. Therefore, the surface abundance of ^{15}N decreases with each TDU episode.

The only O isotope that increases as a result of TDU is ^{16}O. ^{16}O is produced in the He-burning shell before being mixed to the surface through TDU. However, the increase with each TDU episode in the surface abundance is only slight. Both ^{17}O and ^{18}O decrease slightly over the TP-AGB phase as they are destroyed in the PDCZ before the occurrence of TDU.

The increase in C above O during the TP-AGB phase results in the 3 $M_\odot$ model becoming carbon rich with a final surface C/O ratio of 24.82 (see Table 3.7). All the $Z = 0.001$ models become carbon rich with the 2.75 $M_\odot$ having the highest C/O ratio of 26. The 1 $M_\odot$ model has the lowest final C/O ratio of 3.1 as it only experiences two TDU episodes where it becomes carbon rich after the first TDU episode. The surface C/O ratio in the intermediate-mass models fluctuates around unity for a period due to the competing effects of HBB and TDU (Fishlock et al. 2014b). Eventually, TDU is able to overcome HBB and increases the C/O ratio to above unity. Once HBB ceases due to mass loss eroding the stellar envelope, the C/O ratio increases due to continuing TDU. With this in mind, Frost et al. (1998) were able to explain the presence of luminous carbon-rich stars in the Magellanic Clouds (van Loon et al. 1998).

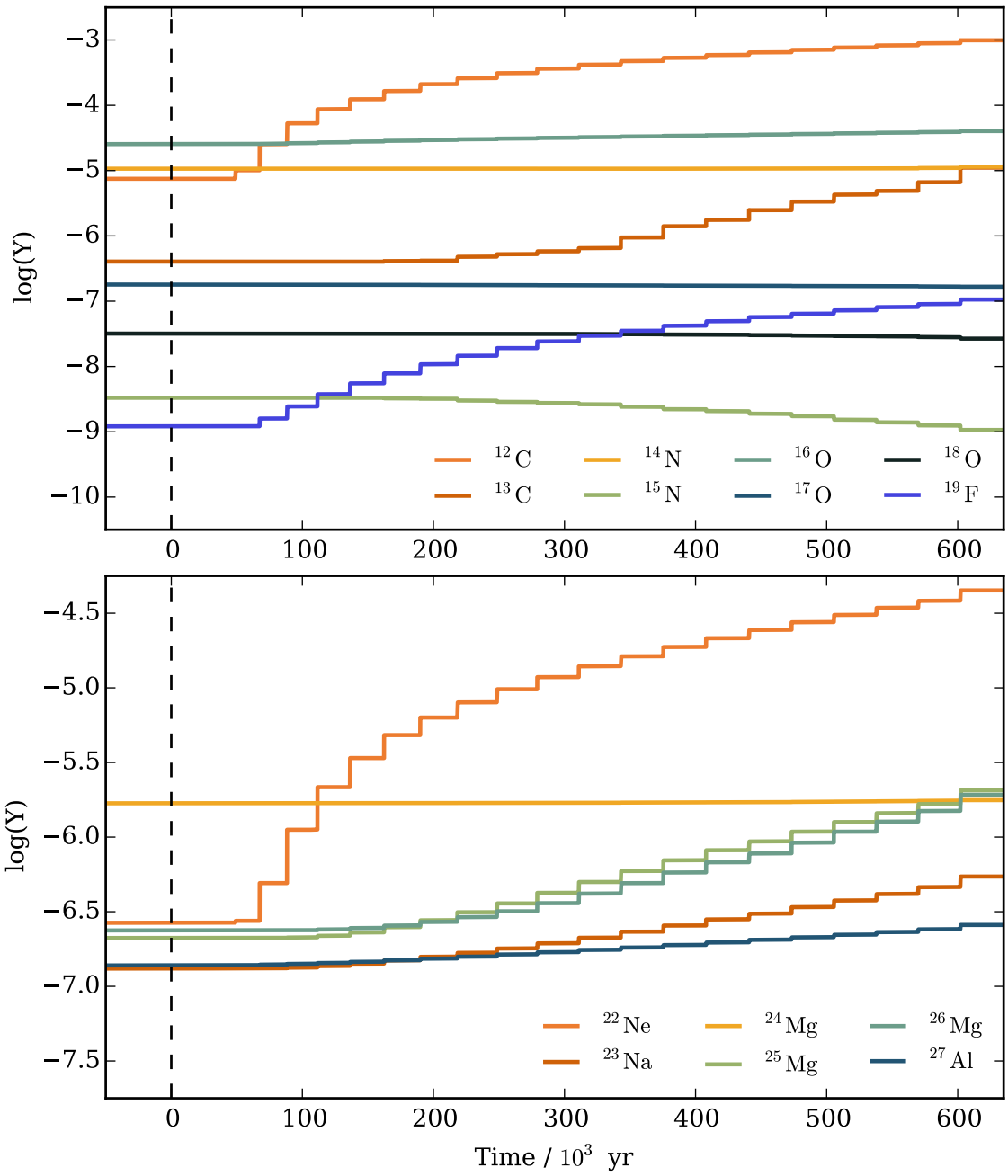

Figure 4.19 The surface abundance of select C, N, O, and F isotopes (top) and Ne, Na, Mg, and Al isotopes (bottom) for the 3 $M_\odot$ model. The dashed line marks the start of the AGB phase.

The abundance of F is observed to correlate with the abundance of C (Jorissen et al. 1992; Abia et al. 2011) providing observational evidence that AGB stars are a site of F production. Additionally, the F abundance is found to correlate with enhancements of *s*-process elements (Abia et al. 2010). The only stable isotope of F, ^{19}F, is produced in the He-intershell during He-burning via the pathway of ^{14}N(α,γ)^{18}F(β^+)^{18}O(p,α)^{15}N(α,γ)^{19}F (Jorissen et al. 1992). TDU then mixes the freshly synthesised ^{19}F to the surface. The presence of a PMZ greatly increases the abundance of ^{19}F as additional ^{14}N is consumed by the PDCZ. During the interpulse period ^{19}F is destroyed in the intershell via the ^{19}F(α,γ)^{22}Ne reaction (Forestini et al. 1992; Lugaro et al. 2004).

Along with the CNO cycle, the Ne-Na and Mg-Al chains also operate in the H-burning shell. However, there is a complex interplay between the H-burning and He-burning shells which affects the production and destruction of these elements.

The abundant Ne isotope ^{22}Ne is produced in the PDCZ from ^{14}N left from H-burning through the ^{14}N(α,γ)^{18}F(β^+)^{18}O(α,γ)^{22}Ne reactions (Wallerstein et al. 1997). A small amount of ^{22}Ne is destroyed by the H-burning shell during the interpulse. However, this amount is insignificant compared to the amount of ^{22}Ne produced in the PDCZ. The occurrence of TDU then increases the surface abundance of ^{22}Ne. As there is no HBB to destroy ^{22}Ne, low-mass AGB stars are predicted to produce considerable Ne (see Table 3.5).

Some ^{23}Na is produced by the H-burning shell in the intershell during the interpulse via the ^{22}Ne(p,γ)^{23}Na reaction (Mowlavi 1999). However, the majority of the ^{23}Na is produced in the PMZ region for the 3 $M_\odot$ model. At the proceeding TP, the ^{23}Na is then diluted by the PDCZ before being mixed into the envelope and increasing the surface abundance.

The abundance of Mg is affected by the activation of the Mg-Al chain in the H-burning shell. The first reaction to occur, at temperatures higher than 30×10^6 K, is the destruction of ^{25}Mg via proton capture to ^{26}Al^g (Arnould et al. 1999). However, the abundances of ^{25}Mg and ^{26}Mg increase as a result of α capture onto ^{22}Ne in the PDCZ. Therefore, despite ^{25}Mg being destroyed by the Mg-Al chain, the surface abundances of ^{25}Mg and ^{26}Mg increase with each TDU episode. As the reaction rates for α capture are similar, the increase of ^{25}Mg and ^{26}Mg are comparable. There is a very small increase in the surface abundance of ^{24}Mg. The majority of the ^{24}Mg produced is a result of the addition of a PMZ in the intershell. The H-burning shell provides the remaining fraction of the abundance.

There is a gradual increase in the surface abundance of ^{27}Al with each TDU episode due to the activation of the Mg-Al chain in the H-burning shell. The synthesised ^{27}Al is then diluted by the PDCZ before being mixed into the envelope. There is minimal production of ^{28}Si in the intershell.

4.4.3. Neutron-capture nucleosynthesis

The production of elements heavier than Fe through neutron capture was proposed by Cameron (1957, 1960). The the *s*-process occurs when the timescale for the decay of unstable isotopes (τ_β) is generally shorter than the timescale for neutron capture (τ_n). In contrast,

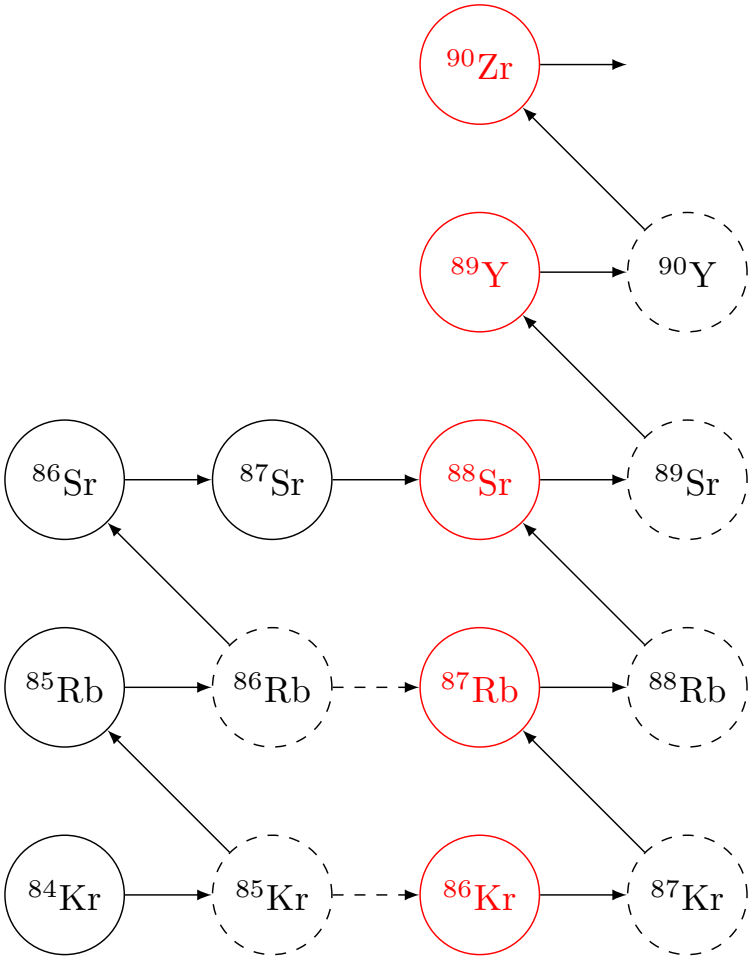

Figure 4.20 A section of the *s*-process path. Dashed circles represent unstable isotopes and red circles represent isotopes with a magic number of neutrons. Solid arrows indicate the *s*-process path accessible by low neutron densities. Dashed arrows indicate the branching points at ^{85}Kr and ^{86}Rb accessible at neutron densities above 10^8 n cm^{-3}.

the rapid neutron-capture process (the *r*-process) occurs when unstable isotopes are able to successively capture neutrons before decaying.

The *s*-process path follows the valley of β stability and long-lived isotopes such as ^{99}Tc. Figure 4.20 illustrates the *s*-process path where neutron densities of the order 10^6 to 10^{14} n cm^{-3} are required (Busso et al. 1999). In comparison, the *r*-process requires neutron densities above $\sim 10^{23}$ n cm^{-3} and isotopes out to the nuclear drip line can be formed.

The neutron capture cross section of an isotope dictates its willingness to capture a neutron. Isotopes with a magic number of neutrons (e.g. ^{88}Sr, ^{138}Ba, ^{208}Pb) have a very low neutron capture cross section (Bao et al. 2000) and act as a bottleneck for the neutron flux in the path taken by the *s*-process. When an isotope is reached in the *s*-process path that has a half-life that competes with neutron capture ($\tau_\beta \approx \tau_n$), it is possible for branching points in the *s*-process path to occur (Figure 4.20). When neutron densities exceed a few times 10^8 n cm^{-3}, branching points in the *s*-process path are able to be activated at ^{85}Kr and ^{86}Rb (Beer & Macklin 1989; Abia et al. 2001; Raut et al. 2013). This allows for the production of ^{87}Rb as the timescale for decay of the unstable isotope ^{86}Rb is greater than the timescale

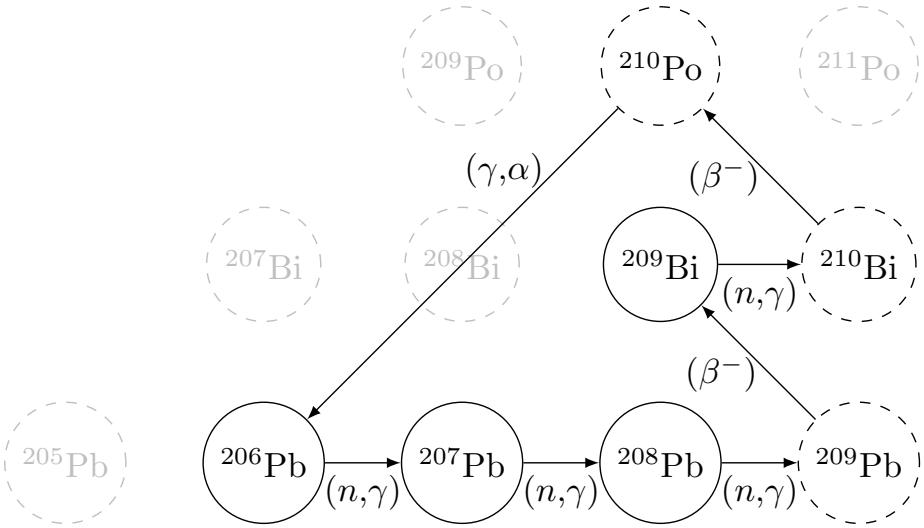

Figure 4.21 The Pb-Bi cycle at the termination of the *s*-process path. Dashed circles represent unstable isotopes.

to capture a neutron. ^{87}Rb has a magic number of neutrons and its neutron-capture cross section[3] is low with a value of 15.7 mbarn (at 30 keV, Heil et al. 2008a). Therefore, once ^{87}Rb is produced, it resists the capture of additional neutrons and accumulates.

The *s*-process terminates at Pb and Bi, the heaviest stable elements[4], where the unstable isotope ^{210}Po decays to the stable isotope ^{206}Pb in approximately 140 days (see Figure 4.21). As ^{208}Pb is doubly magic with a magic number of both protons and neutrons, it has an extremely low cross section of 0.36 mbarn (at 30 keV, Beer et al. 1997; Bao et al. 2000). This means the abundance of Pb only increases as it resists the capture of neutrons. In contrast, ^{138}Ba, which also has a magic number of neutrons, has a cross section of 4 mbarn at 30 keV.

In AGB stars, the *s*-process takes place in the He-intershell. TDU then brings up the products of neutron-capture nucleosynthesis to the surface. In low-mass AGB stars, a ^{13}C pocket forms in the intershell. The neutron-capture elements produced in this region are then diluted by the PDCZ before being mixed to the surface at the next TDU.

Temperatures at the base of the PDCZ in low-mass AGB stars are too low to efficiently activate the ^{22}Ne neutron source and produce the observed abundances of neutron-capture elements (e.g., Gallino et al. 1998; van Aarle et al. 2013). Furthermore, the large enhancements of Pb observed in some stars (e.g., Liu et al. 2012) cannot be explained with the neutron exposures achieved through the ^{22}Ne neutron source (cf. Busso et al. 1999).

The ^{13}C(α,n)^{16}O reaction takes place in the intershell where temperatures reach above the required 90×10^6 K (Truran & Iben 1977; Straniero et al. 1995). However, the amount of ^{13}C left over from CN cycling in the H-burning shell is insufficient to produce the neutron densities required for the *s*-process in low-mass AGB stars. In order to increase the abundance of ^{13}C in the intershell, some protons must be mixed down from the envelope and react with ^{12}C producing ^{13}C through the ^{12}C(p,γ)^{13}N(β^+)^{13}C reaction.

[3]The neutron-capture cross sectional area is given in mbarn where 1 barn is defined at 10^{-28} m^2.

[4]The isotope ^{209}Bi was recently found to be unstable with a half-life of 2×10^{19} yr, longer than the age of the Universe (`http://atom.kaeri.re.kr`).

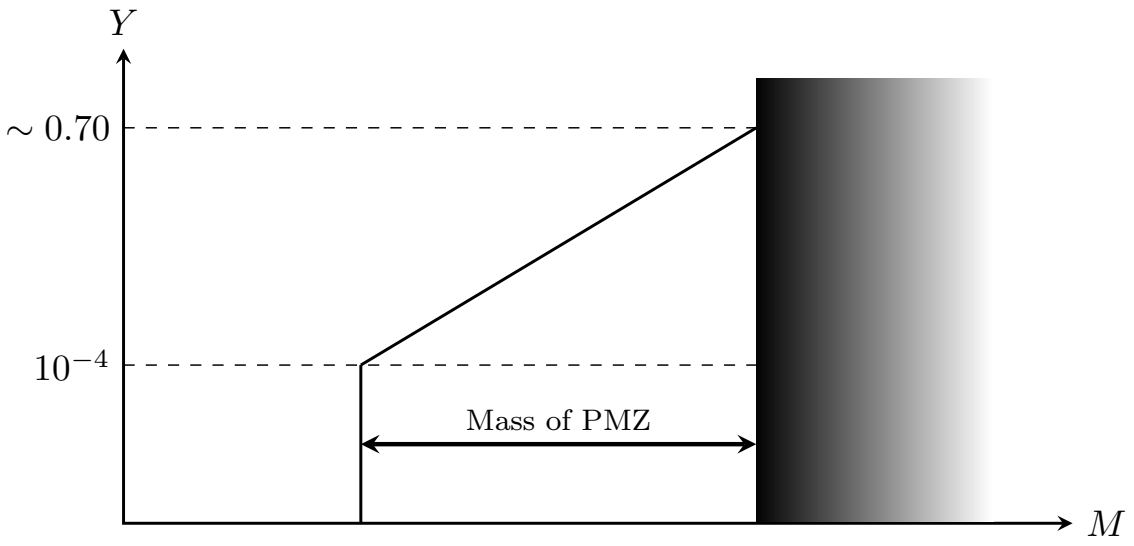

Figure 4.22 Schematic of the profile of the added PMZ where the mass coordinate (M) is given on the x-axis and the mole fraction (Y) on the y-axis. The arrows show the extent of the PMZ and the shaded region represents the convective envelope at the deepest extent of TDU.

In the low-mass models presented here, an exponential profile of protons (known as a partial mixing zone or PMZ) is added to the top of the He-intershell at the deepest extent of TDU where there is a sharp discontinuity between H and He. A schematic of the PMZ profile is illustrated in Figure 4.22. The additional protons in the intershell are captured by ^{12}C to produce ^{13}C. The ^{13}C is then converted to ^{16}O releasing neutrons during the interpulse. These neutrons are eventually captured by ^{56}Fe seeds to produce the neutron-capture elements observed in AGB stars. For the $Z = 0.001$ models, a PMZ is added for low-mass stars with an initial mass of 3 $M_\odot$ and lower. In these stars, the ^{13}C(α,n)^{16}O reaction is the dominant source of neutrons.

The ^{13}C pocket is of primary origin as it is produced from H and newly synthesised ^{12}C. Thus, it does not depend on the initial metallicity of a star and the neutron-to-seed ratio decreases with increasing metallicity. This affects the distribution of neutron-capture elements where lower metallicity models are able to produce more Pb relative to lighter neutron-capture elements than higher metallicity models (Busso et al. 1999).

In intermediate-mass stars, temperatures at the base of the PDCZ exceed the 300×10^6 K required for the activation of the ^{22}Ne(α,n)^{25}Mg reaction which produces the neutrons for neutron-capture nucleosynthesis (Truran & Iben 1977). The high abundance of ^{22}Ne is a product of the ^{14}N(α,γ)^{18}F(β^+)^{18}O(α,γ)^{22}Ne reactions where there is ^{14}N left over from the ashes of H-burning (Busso et al. 2001). Despite the high neutron densities experienced during the TP, the duration is quite short so that the neutron exposure remains low. The maximum temperature at the base of the PDCZ increases with each TP increasing the efficiency of the ^{22}Ne neutron source. The peak maximum temperature also, in general, increases with increasing initial stellar mass, core mass, and time.

Branching points in the s-process path are efficiently activated by the neutron densities produced from the ^{22}Ne(α,n)^{25}Mg reaction. This favours the production of neutron-capture

elements at the first *s*-process peak, in particular Rb. The initial metallicity strongly influences the enhancement of the first *s*-process peak compared to the second peak. The 5 $M_\odot$, $Z = 0.02$ model of Karakas et al. (2012) has a final [Rb/Fe] surface abundance of 0.76 whereas the final [Ba/Fe] ratio is lower at 0.08. In comparison, the 5 $M_\odot$, $Z = 0.0001$ model of Lugaro et al. (2012) has final [Rb/Fe] and [Ba/Fe] surface abundances of 1.86 and 1.45, respectively. This difference in final surface abundances is a consequence of the number of ^{56}Fe seeds available for neutron capture with lower metallicity models having a higher neutron-to-seed ratio. The 5 $M_\odot$, $Z = 0.001$ model presented here has a final [Rb/Fe] surface abundance of 1.55 whereas the [Ba/Fe] ratio is 0.88. These values are as expected as the metallicity is bracketed by the metallicity of the models of Karakas et al. (2012) and Lugaro et al. (2012) and are calculated with the same stellar evolution code.

The surface abundance distribution of the neutron-capture elements reflects the neutron densities reached in a model. The activation of branching points is dependent on the neutron density which determined by the initial stellar mass. chapter3/figures/ 4.23 and 4.24 present, for each model, the peak neutron densities reached during the AGB phase. We find that neutron densities in the most massive models presented here reach up to 10^{14} n cm^{-3} where the ^{22}Ne(α,n)^{25}Mg reaction is the dominant source of neutrons.

In the low-mass models, the addition of a PMZ causes the neutron density to increase above the required 10^6 n cm^{-3} for *s*-process nucleosynthesis during the interpulse. In a number of low-mass models the first few ^{13}C pockets do not burn completely in radiative conditions and are ingested into the following TP. The ^{13}C is mixed with the neutron poison ^{14}N reducing the number of neutrons available for neutron-capture nucleosynthesis. This situation is described in Lugaro et al. (2012). The intermediate-mass models without a PMZ do not show an increase in the neutron density during the interpulse.

All models show an increase in the neutron density during a TP. However, only the models more massive than 2.75 $M_\odot$ have the peak neutron density during a TP increase to above approximately 10^{12} n cm^{-3}. The high neutron densities achieved are reflected in the increase in the [Rb/Zr] ratio for the low-mass models as branching points are activated.

van Raai et al. (2012) find their 3 $M_\odot$, $Z = 0.02$ model reaches peak neutron densities of approximately 10^{11} n cm^{-3} via the ^{22}Ne neutron source during a TP. The 3 $M_\odot$, $Z = 0.001$ model presented here achieves peak neutron densities of approximately 10^{13} n cm^{-3} in the PDCZ towards the end of the AGB phase. The higher neutron density is due to higher peak temperatures experienced in the PDCZ. The 6.5 $M_\odot$, $Z = 0.02$ model of van Raai et al. (2012) reaches neutron densities of nearly 10^{13} n cm^{-3} due to the efficient ^{22}Ne neutron source.

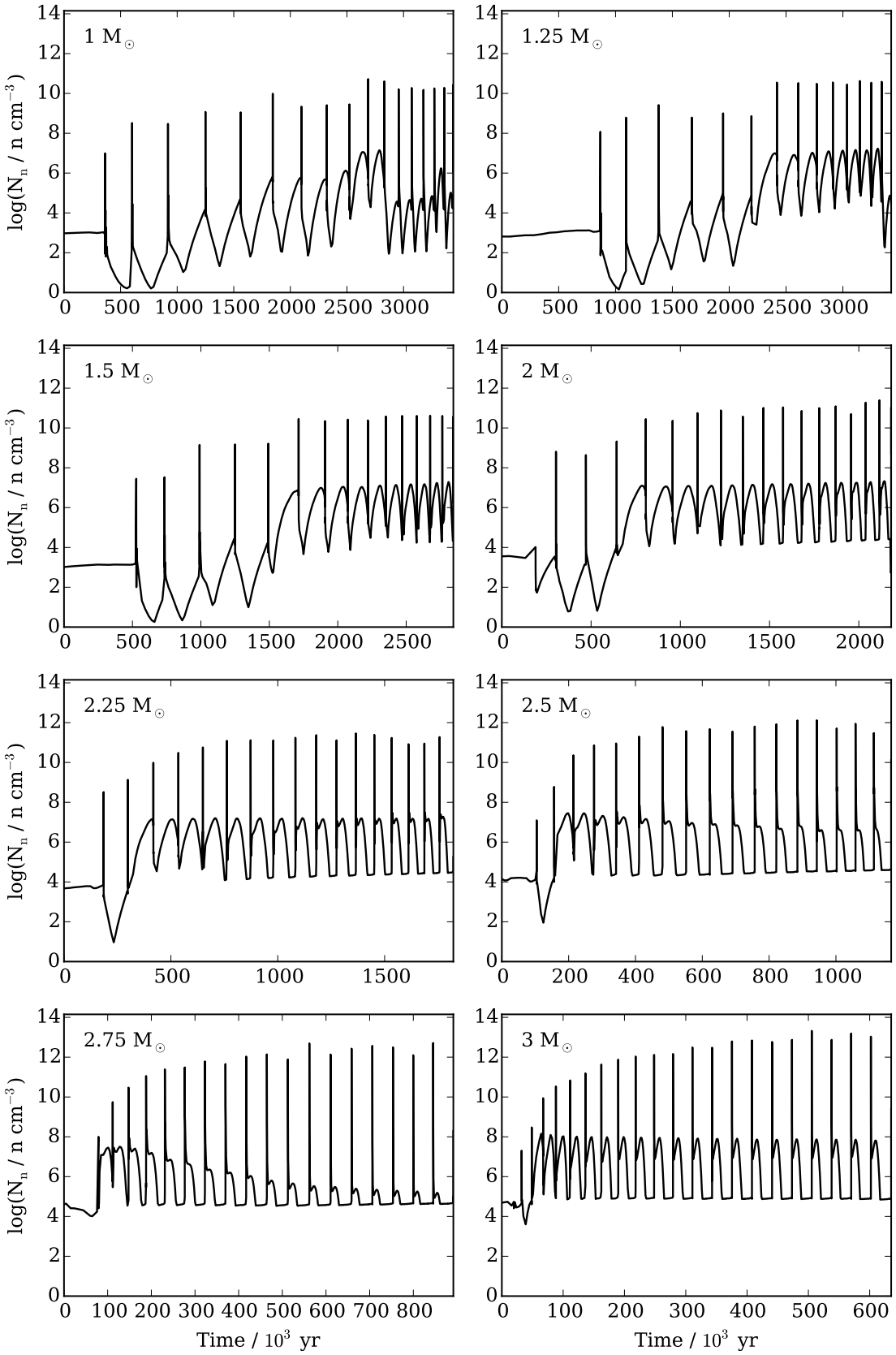

Figure 4.23 Peak neutron densities achieved in the intershell from the start of the AGB phase for the low-mass models.

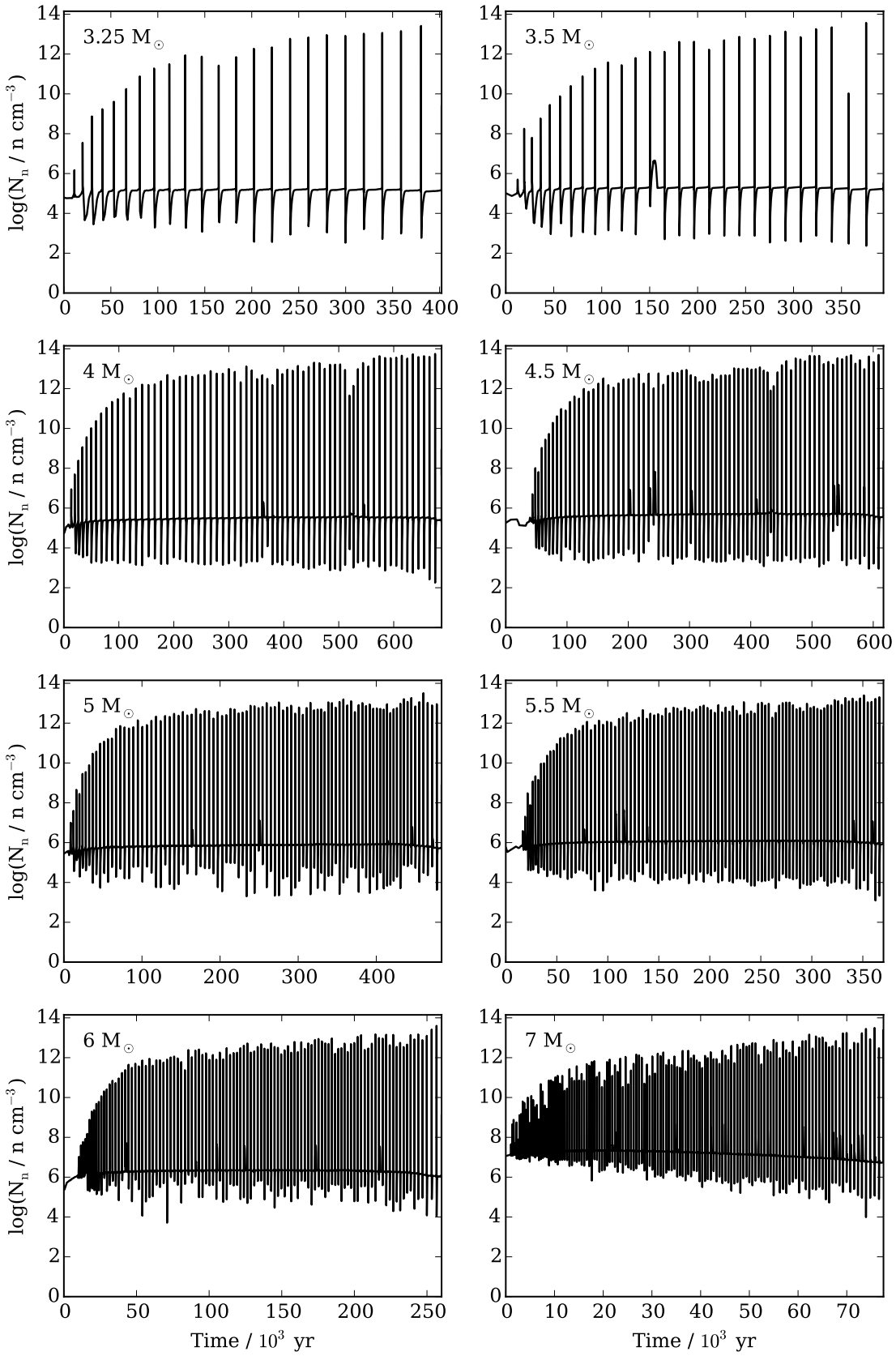

Figure 4.24 Peak neutron densities achieved in the intershell from the start of the AGB phase for the intermediate-mass models.

4.4.4. The PMZ in the 2 $M_\odot$ model

As discussed in Chapter 3, the choice of the PMZ mass affects the level of *s*-process nucleosynthesis that takes place in the intershell. Here we investigate the effect of including three different PMZ masses of (2, 4, 6) $\times 10^{-3}$ $M_\odot$ in the 2 $M_\odot$ model. Figures 4.25 and 4.26 present the composition profiles as a function of model number (a proxy for time) for ^{13}C and neutrons, respectively, for two TPs in two 2 $M_\odot$ models with a PMZ mass of 2×10^{-3} and 6×10^{-3} $M_\odot$, respectively. Note that chapter3/figures/ 4.25 and 4.26 exaggerate the duration of the TP as model number is used rather than time. For the boxed regions indicated, the duration of the first TP is approximately 140 years while the interpulse period is approximately 108,000 years.

As mentioned in Chapter 3, a more massive PMZ reaches into deeper regions of the He-intershell and of higher temperature. This causes the ^{13}C pocket to form sooner and deeper in the intershell. This is evident when comparing the ^{13}C abundance profiles in Figure 4.25a to Figure 4.25b. In addition, a more massive PMZ produces larger ^{13}C and ^{14}N pockets in the intershell. Figure 4.25 also illustrates that the ^{13}C nuclei are consumed faster in the model with the more massive PMZ. This is a result of the increased ^{13}C burning temperatures and therefore the lifetime of the ^{13}C pocket is shorter.

As the ^{13}C(α,n)^{16}O reaction takes place in regions of higher temperature for the model with a more massive PMZ, more neutrons can be released increasing the neutron density (see Figure 4.26). For the final seven ^{13}C pockets, the neutron density exceeds 10^8 n cm^{-3}, thus activating branching points at ^{85}Kr and ^{86}Rb. The effect of branching points being activated can be observed in the increased abundance of Rb (and Kr) where the 2 $M_\odot$ model with the 6×10^{-3} $M_\odot$ PMZ has a final surface abundance of $\log \epsilon(\mathrm{Rb}) = 2.5$ whereas the model with the standard PMZ has a value of $\log \epsilon(\mathrm{Rb}) = 2.1$.

At each TP, the increase in the neutron abundance is evident between 0.61 and 0.63 $M_\odot$ as a result of the ^{22}Ne(α,n)^{25}Mg reaction being activated at the base of the PDCZ. During a TP neutron densities reach up to 10^{11} n cm^{-3} (see Figure 4.23). However, minimal *s*-process nucleosynthesis takes place. This is despite the higher neutron densities produced compared to the ^{13}C neutron source as the short timescale of the TP means that the neutron exposure remains low.

Figure 4.27 presents the composition profile of ^{208}Pb, a representative *s*-process element. The effect on ^{208}Pb, when changing the mass of the PMZ, is apparent where the larger ^{13}C pocket for the model with the more massive PMZ results in ^{208}Pb extending over a larger mass region but at a lower maximum abundance compared to the model with the standard PMZ mass. The ^{208}Pb is also produced sooner during the interpulse in the model with the larger PMZ. The net yield of ^{208}Pb of the model with the PMZ of 6×10^{-3} $M_\odot$ is 1.26×10^{-6} $M_\odot$. The model with the standard PMZ produces less ^{208}Pb with a net yield of 1.08×10^{-6} $M_\odot$.

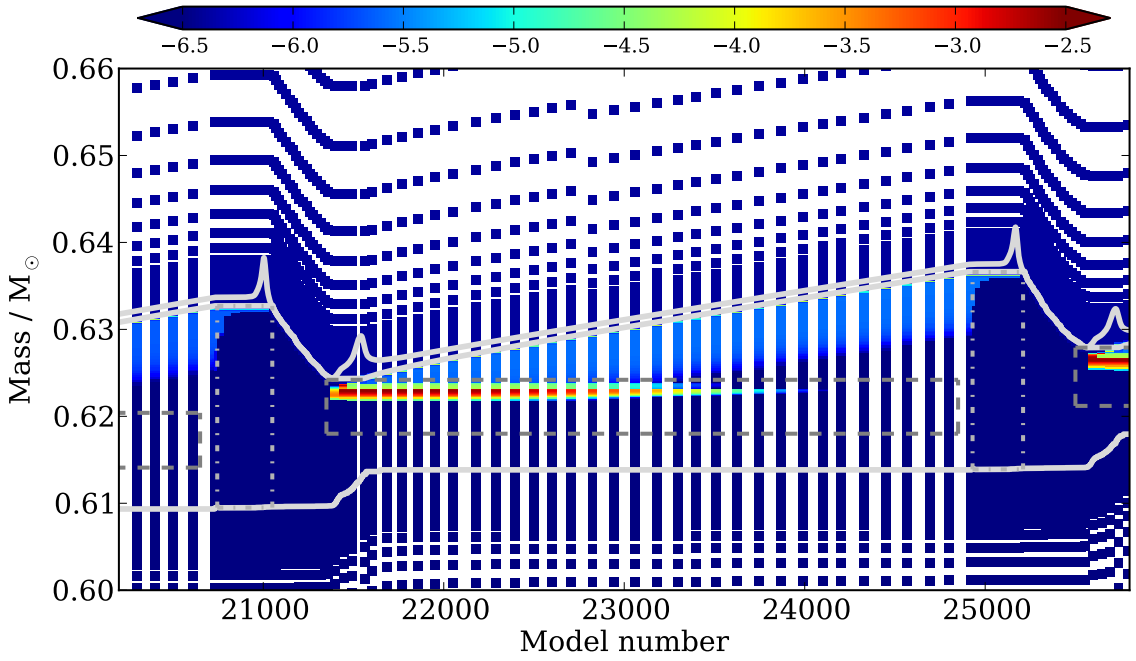

(a) 2 $M_\odot$ model with a PMZ mass of 2×10^{-3} $M_\odot$.

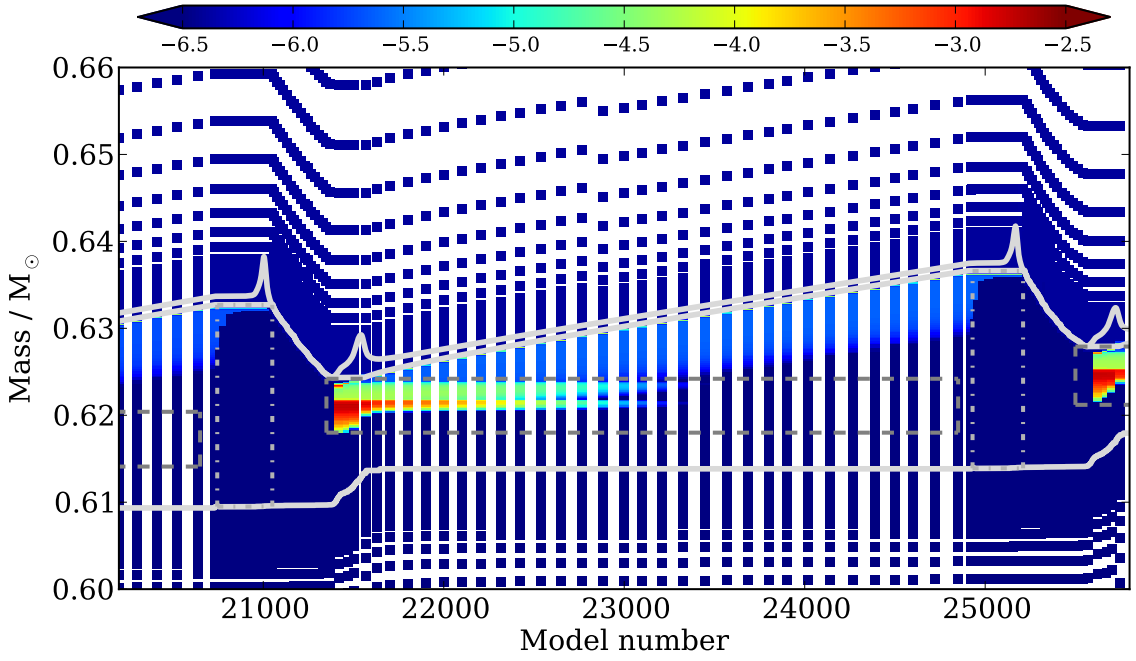

(b) 2 $M_\odot$ model with a PMZ mass of 6×10^{-3} $M_\odot$.

Figure 4.25 The composition profile of ^{13}C with model number for the 2 $M_\odot$ model with two different PMZ masses. The colour bar shows the abundance in log(Y) and the grey solid lines show the He-exhausted core, the H-exhausted core, and the inner edge of the convective envelope. The dashed line shows the region used to calculate the neutron exposure for the ^{13}C pocket whereas the dash-dotted line shows the region of the ^{22}Ne neutron source.

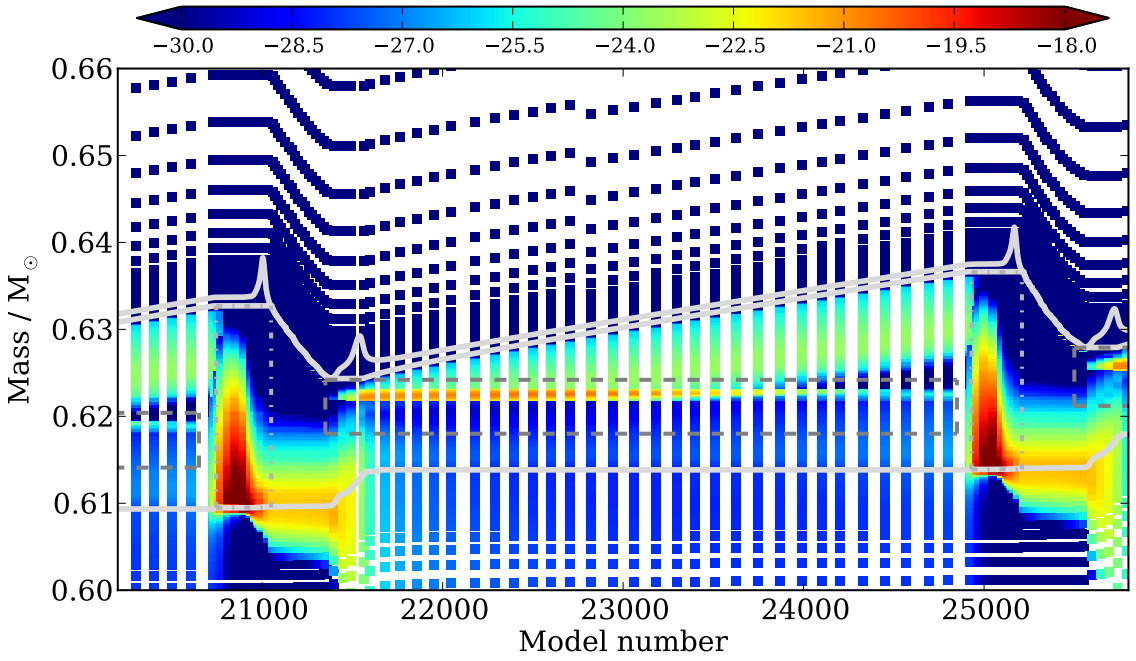

(a) 2 $M_\odot$ model with a PMZ mass of 2×10^{-3} $M_\odot$.

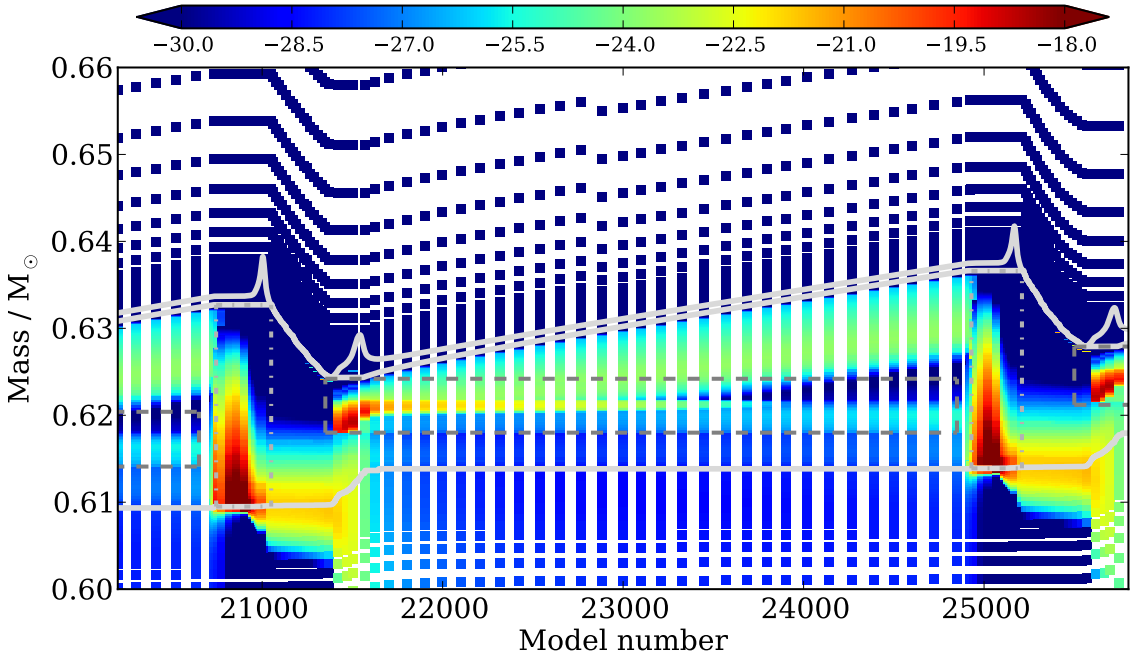

(b) 2 $M_\odot$ model with a PMZ mass of 6×10^{-3} $M_\odot$.

Figure 4.26 The composition profile of neutrons with model number for the 2 $M_\odot$ model with two different PMZ masses. The colour bar shows the abundance in log(Y) and the grey solid lines show the He-exhausted core, the H-exhausted core, and the inner edge of the convective envelope. The dashed line shows the region used to calculate the neutron exposure for the ^{13}C pocket whereas the dash-dotted line shows the region of the ^{22}Ne neutron source.

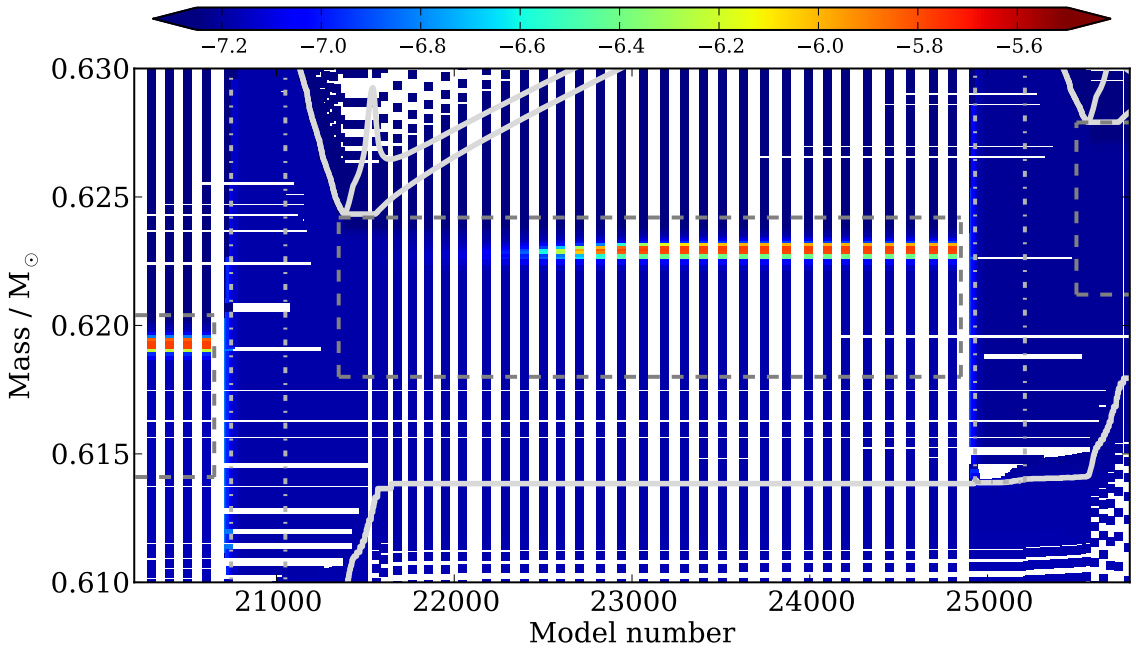

(a) 2 $M_\odot$ model with a PMZ mass of 2×10^{-3} $M_\odot$.

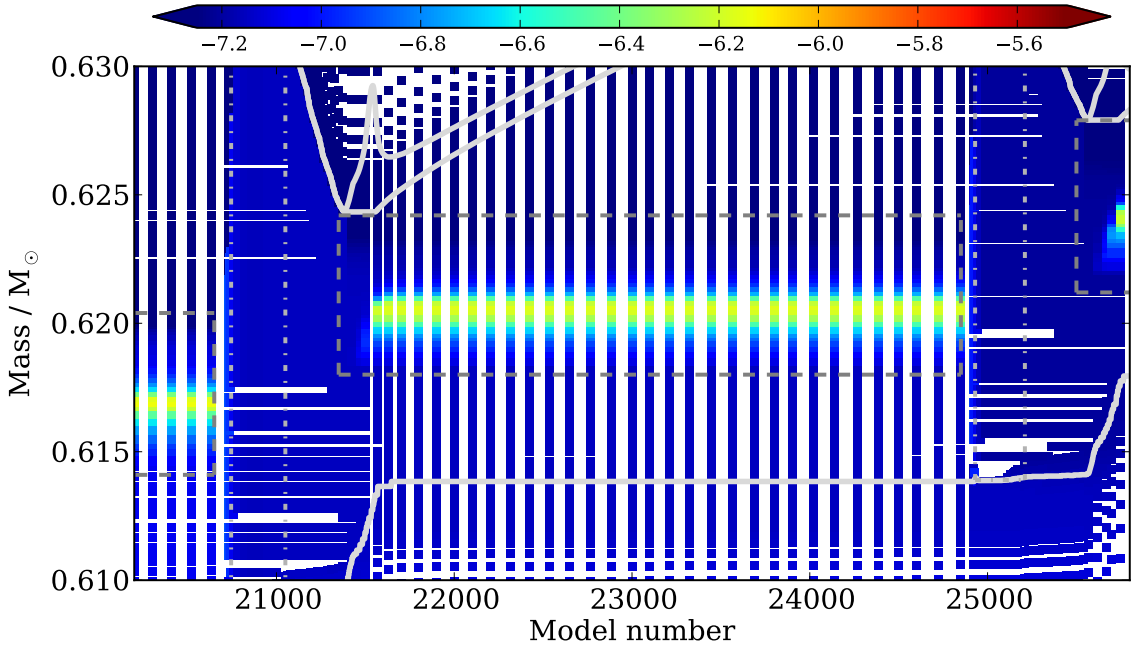

(b) 2 $M_\odot$ model with a PMZ mass of 6×10^{-3} $M_\odot$.

Figure 4.27 The composition profile of ^{208}Pb with model number for the 2 $M_\odot$ model with two different PMZ masses. The colour bar shows the abundance in log(Y) and the grey solid lines show the He-exhausted core, the H-exhausted core, and the inner edge of the convective envelope. The dashed line shows the region used to calculate the neutron exposure for the ^{13}C pocket whereas the dash-dotted line shows the region of the ^{22}Ne neutron source.

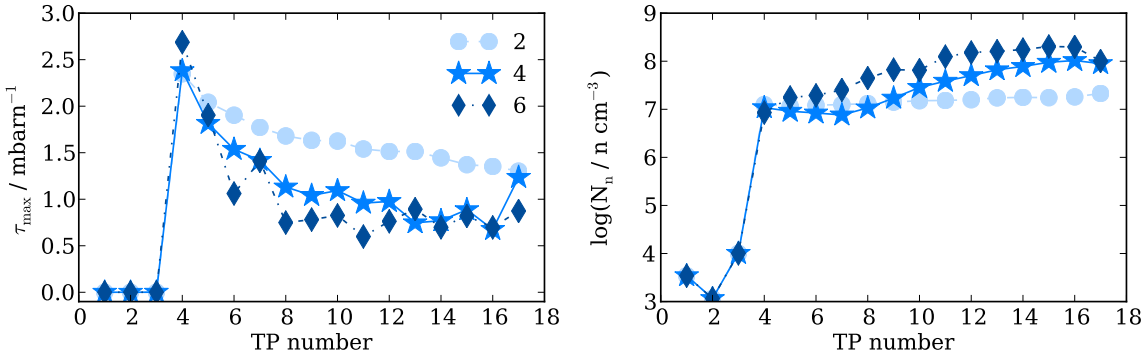

(a) Peak neutron exposure, τ_{max}.

(b) Peak neutron density, log(N_n).

Figure 4.28 Peak neutron exposures and densities as a function of TP number for three 2 $M_\odot$ models with a PMZ of (2, 4, 6) $\times$ 10^{-3} $M_\odot$.

The final abundances of the neutron-capture elements depend on the complex interplay between radiative ^{13}C burning, the dilution of the ^{13}C pocket with previously produced *s*-process material, the mixing of fresh Fe seeds and H-burning ashes, and the overlap between successive TPs (Gallino et al. 1998). In particular, it is these factors that affect the neutron exposure and density for each PMZ. In Figure 4.28 we present the evolution of the maximum local neutron exposure and maximum neutron density (at 8 keV, which is the typical temperature of ^{13}C burning) with PMZ number for the 2 $M_\odot$ models with three different PMZ masses.

The first three TPs are not followed by TDU and it is only after the fourth TP that a PMZ is added at the end of TDU. The neutron densities are below 10^4 n cm^{-3} during the first three interpulse periods and are too low to activate neutron-capture nucleosynthesis. It is only until a PMZ is added that the neutron exposure reaches around 2.5 mbarn^{-1} and the peak neutron density is 10^7 n cm^{-3}.

When looking at each individual model, the peak local neutron exposure, in general, decreases with each ^{13}C pocket. The lower neutron exposures result from the shorter duration of the ^{13}C pocket with PMZ number. This effect was also observed by Gallino et al. (1998). In contrast, the maximum neutron density increases with PMZ number due to fewer neutron seeds being available.

The different local neutron exposures ($\delta\tau$) experienced in the different mass layers of the intershell result in very different enhancement factors relative to the initial scaled-solar composition (Gallino et al. 1998). For neutron exposures above 1 mbarn^{-1}, the highest enhancement factor occurs for ^{208}Pb (see Fig. 15 of Gallino et al. 1998). As presented in Figure 4.28a, the peak neutron exposures for the model with the standard PMZ (2×10^{-3} $M_\odot$) stay above 1 mbarn^{-1} for each PMZ whereas the models with more massive PMZs have their peak neutron exposures after later TPs fall below 1 mbarn^{-1}.

CHAPTER 5

Neutron-capture and Sc abundances in low- and high-α Galactic halo stars

This chapter is currently in preparation to be submitted to the Monthly Notices of the Royal Astronomical Society.

We determine relative abundance ratios for the neutron-capture elements Zr, La, Ce, Nd, and Eu for a sample of 27 Galactic halo dwarf stars with $-1.5 <$ [Fe/H] < -0.8. We also measure the iron-peak element Sc. These stars separate into three populations (low-α, high-α, and thick-disc) based on the abundance of [α/Fe] and their kinematics as discovered by Nissen & Schuster. We find differences in the abundance ratios of [Sc/Fe], [Zr/Fe], and [La/Zr] between the low-α and high-α populations but not in [La/Fe], [Ce/Fe], [Nd/Fe], and [Eu/Fe]. Only [La/Zr] has a higher abundance in the low-α stars compared to the high-α stars while [Sc/Fe] and [Zr/Fe] have lower abundances. Using the measurements of Nissen & Schuster, we find that the low-α stars have a lower [Y/Eu] ratio than the high-α stars. We conclude that the low-α stars display the same abundance pattern of high [Ba/Y] and low [Y/Eu] as observed in present-day dwarf spheroidal galaxies, although with smaller abundance anomalies, when compared to the high-α stars. The chemical separations have resulted from differences in the star formation rate between the two populations which has allowed for the contribution of low-metallicity, low-mass asymptotic giant branch (AGB) stars in the low-α population. We consider the contribution of AGB stars to the low-α population by comparing observations to calculations of AGB stellar models.

5.1. Introduction

Understanding the earliest phases of the assembly of our Galaxy, the Milky Way, remains a key issue in modern astronomy. Cosmological simulations incorporating ΛCDM (e.g., Pillepich et al. 2014) predict that mergers and the accretion of satellite dwarf galaxies may

play an important role through the hierarchical structure formation. Our Galaxy is no exception. Observational support for the hierarchical nature of Galactic formation, and the role dwarf galaxies play in that process, come from the accretion of the Sagittarius dwarf galaxy (Ibata et al. 1994) and numerous tidal streams observed in the Galactic halo (e.g., Belokurov et al. 2006).

The chemical abundance and kinematics of Galactic halo stars hold valuable clues concerning Galactic formation at earliest times (e.g., Eggen et al. 1962; Searle & Zinn 1978). Due to their long lifetimes, FGK-type dwarf stars trace the entire Galactic history. Additionally, their atmospheres retain the chemical composition of the gas clouds from which they formed. Therefore, spectroscopic studies of these 'stellar fossils' enable us to probe the chemical and kinematic history of our Galaxy over cosmic time.

Comparison of the chemical abundances between the Galactic halo and dwarf galaxies reveals differences in their chemical composition, most notably in the [α/Fe] ratio (e.g., Venn et al. 2004). On average, dSphs stars with a [Fe/H] $\gtrsim -2$ have, on average, lower [α/Fe] than the Galaxy. The [α/Fe] ratio depends on the relative number of Type Ia to Type II supernovae, and this quantity is sensitive to the star formation rate (e.g., Tinsley 1979; Wheeler et al. 1989; Nomoto et al. 2013). The lower [α/Fe] observed in dSphs would therefore suggest a slower star formation rate relative to the Galaxy. Differences in the [α/Fe] ratio between the Galactic halo and present-day dwarf galaxies precludes the continuous merging of such systems although it may be that the mergers of massive dwarf galaxies occurred at very early times in the formation of the Galactic halo (Venn et al. 2004).

Although a handful of α-poor stars were known to exist in the Galactic halo (e.g., Ivans et al. 2003), the study by Nissen & Schuster (2010) (hereafter NS10) provided convincing evidence that the halo hosts two populations that are well separated in [α/Fe]. NS10 studied 94 halo dwarf stars using a careful differential analysis resulting in abundance errors for [α/Fe] of only 0.02 dex. They argued that the low-α stars have kinematics consistent with accretion from a satellite galaxy with a slower star formation rate than the high-α population which most likely formed in-situ in the Galaxy. Additionally, NS10 found that the low- and high-α populations also separate in [Na/Fe] and [Ni/Fe]. A separation was not seen for [Cr/Fe].

Before continuing, it is important to recognise that any attempts to infer the chemical enrichment history of any stellar population requires a detailed understanding of the nucleosynthetic origin of individual elements (Nissen 2011). Low- to intermediate-mass stars undergo rich nucleosynthesis once they reach the asymptotic giant branch (AGB) phase. It has been observationally confirmed that the *slow* neutron-capture process (the *s*-process) takes place in AGB stars (e.g., Abia et al. 2001). The *s*-process is responsible for the production of around half of the abundance of the heavy elements beyond iron. Through strong mass loss, AGB stars eject enriched material into the interstellar medium polluting the next generation of stars.

AGB stars may play an important role in the origin of chemical abundance differences observed between the Galaxy and nearby dwarf galaxies. In addition to the differences in [α/Fe], Venn et al. (2004), and more recently Venn et al. (2012), identified differences in the ratios of [Ba/Y] and [Y/Eu] in dwarf spheroidal galaxies (dSphs). The high [Ba/Y]

observed is attributed to low-mass AGB stars enriching the interstellar medium thanks to a slower chemical evolution. To explain the low [Y/Eu] observed, Venn et al. (2004) suggested that metal-poor AGB stars did not contribute as much Y (compared to more metal-rich AGB stars) because the production of second *s*-process elements such as Ba and La were favoured over first *s*-process peak elements such as Zr and Y.

Nissen & Schuster (2011) (hereafter NS11) determined abundances for two neutron-capture elements produced by the *s*-process in AGB stars, Ba and Y (along with the iron-peak elements Mn, Cu, and Zn). They discovered that the low- and high-α populations could be separated in [Cu/Fe] and [Zn/Fe]. More importantly, NS11 found that the [Ba/Y] ratio differs between the two populations with the low-α stars showing a higher [Ba/Y] value. Such a finding is similar to that found in the dSphs by Venn et al. (2004) and reinforces the hypothesis that the low-α stars are likely to have been accreted from dSphs.

The NS10 sample provides a unique opportunity to study additional neutron-capture elemental abundances in the low- and high-α populations. Such an analysis will enable us to examine the abundances for a larger range of neutron-capture elements, with high-precision, in stars likely to have been accreted from dwarf galaxies. Such studies of stars currently in dwarf galaxies cannot be conducted with existing facilities. The aim of this study is to investigate the role of AGB stars in the chemical enrichment of the Galactic halo and dSphs. Specifically, we build upon the work of NS10 and NS11 by studying additional *s*-process elements (Zr, Ce, and Nd). We also measure, for the first time with this unique sample, an *r*-process neutron-capture element (Eu). Finally, we measure Sc which has been observed to behave like an α element (e.g., Nissen et al. 2000).

5.2. Sample selection and observations

Our observational campaign focused on obtaining high quality blue spectra for stars in the NS10 sample. This is to extend the wavelength coverage as, in the analysis of NS11, only lines redder than 4700 Å were measured. Our targets were selected to include both low- and high-α stars across the metallicity range of $-1.5 <$ [Fe/H] < -0.8. The sample consists of 13 low-α stars, 6 high-α stars, and 8 thick-disc (TD) stars, including the two reference TD stars used in the studies by NS10 and NS11, HD 22879 and HD 76932.

Programme stars were observed using the Magellan Inamori Kyocera Echelle (MIKE) spectrograph (Bernstein et al. 2003) on the Magellan (Clay) telescope during February 2011 and June 2011. We used the 0.35" slit size which gives a resolving power of 83,000 in the blue. Typical exposure times ranged from 500 to 5000 seconds per target and the signal-to-noise ratio per pixel of the spectra was approximately 400 at 4500 Å. The wavelength coverage provided by MIKE is 3350 to 9000 Å. Data reduction was accomplished using IRAF[1] with the MIKE MTOOLS package. Continuum fitting was performed using the Spectroscopy Made Hard (SMH) package as used in Casey et al. (2014) and described in Casey (2014).

[1] http://iraf.noao.edu/

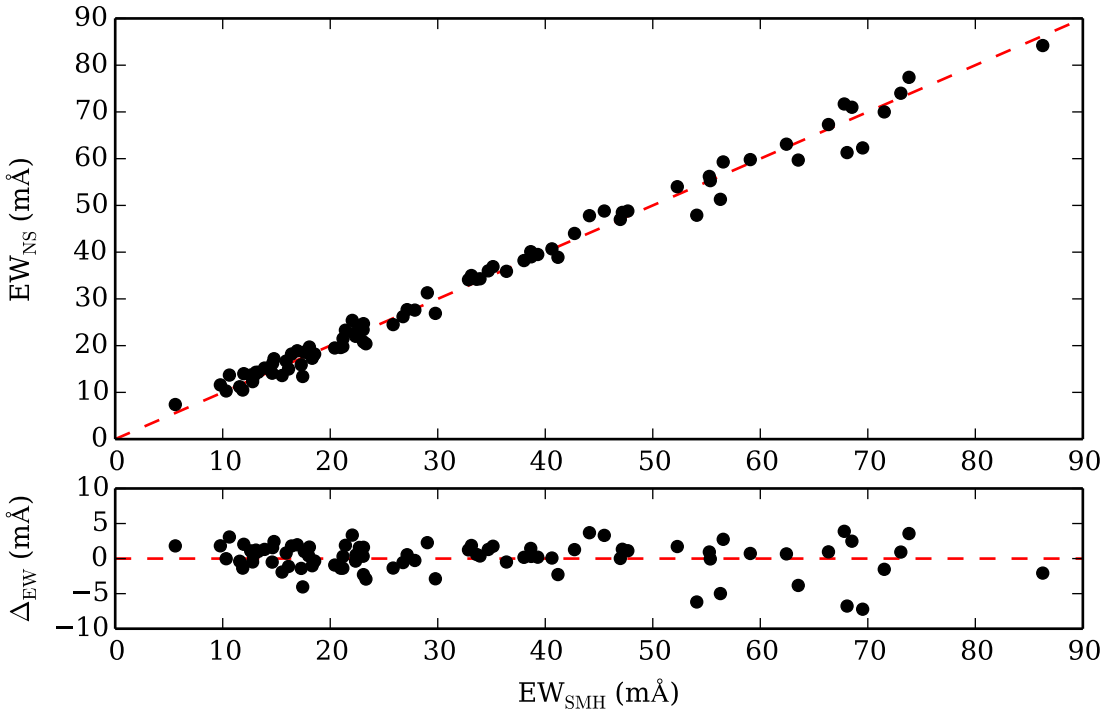

Figure 5.1 Comparison between EW measurements for HD 22879 from NS10 and NS11 (EW$_{NS}$) and by using SMH (EW$_{SMH}$). The dashed line shows the one-to-one correspondence line. The bottom panel shows the difference between the two analyses.

5.3. Abundances

Following NS10, we perform a differential line-by-line analysis relative to the TD star HD 22879. This approach enables us to obtain high-precision abundance ratios which are necessary in identifying possible separations between the low- and high-α populations. The model atmospheres used in the analysis were one-dimensional, plane parallel, LTE ATLAS9 models by Castelli & Kurucz (2003) interpolating between $T_{\rm eff}$, $\log g$, [Fe/H], and [α/Fe]. Interpolation was required to produce model atmospheres with a specific value for $T_{\rm eff}$, $\log g$, [Fe/H], and [α/Fe]. The stellar parameters, $T_{\rm eff}$, $\xi_{\rm turb}$, and $\log g$, as well as the abundance ratios of [Fe/H] and [α/Fe] are taken from NS10 and NS11 (see Table 5.1). For a complete discussion on the determination of these parameters see NS10 and NS11. We use stellar parameters from NS10 without the correction for effective temperature of $\sim$ 100 K from NS11. Given the differential nature of the abundance analysis and that most stars have fairly similar stellar parameters, a systematic shift of 100 K is likely to have a minimal effect on the final differential abundances.

Elemental abundances for Zr, Ce, and Nd are derived from the analysis of equivalent widths (EWs) using SMH. For lines with an EW < 60 mÅ, a Gaussian profile was fitted to the line. For lines with an EW larger than 60 mÅ, a Voigt profile was used providing a better fit to the line. Figure 5.1 presents a comparison of 85 EW measurements (excluding Fe I and Fe II) of NS10 and NS11 to the EWs measured using SMH with the same line list for HD 22879. The mean EW difference between the two methods is 0.16 ± 2.18 mÅ.

Table 5.1 Atmospheric parameters and abundance ratios for each of stars (taken from NS10 and NS11).

ID	$T_{\rm eff}$ (K)	$\log g$ (cgs)	$\xi_{\rm turb}$ (km s^{-1})	[Fe/H]	[α/Fe]	Class[a]
CD-45 3283	5597	4.55	1.0	−0.91	0.12	low-α
CD-61 0282	5759	4.31	1.3	−1.23	0.22	low-α
G 16-20	5625	3.64	1.5	−1.42	0.26	(low-α)
G 18-28	5372	4.41	1.0	−0.83	0.31	high-α
G 18-39	6040	4.21	1.5	−1.39	0.34	high-α
G 31-55	5638	4.30	1.4	−1.10	0.29	high-α
G 56-30	5830	4.26	1.3	−0.89	0.11	low-α
G 56-36	5933	4.28	1.4	−0.94	0.20	low-α
G 66-22	5236	4.41	0.9	−0.86	0.12	low-α
G 170-56	5994	4.12	1.5	−0.92	0.17	low-α
HD 3567	6051	4.02	1.5	−1.16	0.21	low-α
HD 22879	5759	4.25	1.3	−0.85	0.31	TD
HD 25704	5868	4.26	1.4	−0.85	0.24	TD
HD 76932	5877	4.13	1.4	−0.87	0.29	TD
HD 103723	5938	4.19	1.2	−0.80	0.14	low-α
HD 105004	5754	4.30	1.2	−0.82	0.14	low-α
HD 111980	5778	3.96	1.5	−1.08	0.34	high-α
HD 120559	5412	4.50	1.1	−0.89	0.30	TD
HD 126681	5507	4.45	1.2	−1.17	0.35	TD
HD 179626	5850	4.13	1.6	−1.00	0.32	high-α
HD 189558	5617	3.80	1.4	−1.12	0.35	TD
HD 193901	5650	4.36	1.2	−1.07	0.17	low-α
HD 194598	5942	4.33	1.4	−1.09	0.20	low-α
HD 199289	5810	4.28	1.3	−1.04	0.30	TD
HD 205650	5698	4.32	1.3	−1.17	0.30	TD
HD 219617	5862	4.28	1.5	−1.45	0.28	(low-α)
HD 230409	5318	4.54	1.1	−0.85	0.27	high-α

[a] For stars with [Fe/H] < -1.4, the classification is uncertain.

We use the atomic data compiled by Yong et al. (2005) for the measured absorption lines. The abundances of Zr is derived from the EW of the Zr II line at 4208.98 Å which is unblended with other lines allowing for a reliable measurement. The Zr II line is detected in all stars with all EW measurements being greater than 10 mÅ (see Table 5.2). Ce abundances have been determined using the EWs of two Ce II lines at 4562.36 Å and 4628.16 Å. Seven stars only have one Ce II line available for measurement: five stars do not have a measurable 4562.36 Å line whereas two stars do not have a measurable 4628.16 Å line (see Table 5.2). For all but three Ce lines, the EW is less than 10 mÅ. All EWs are above the minimum reliable EW measurement of 2 mÅ. The derived Nd abundances have been determined using the one Nd II line at 4706.54 Å. As with Ce, the EW measurements are less than 10 mÅ except in two stars (G 66-22 and HD 230409). We use a limit of 2 mÅ for reliable EW measurements

Table 5.2 EW measurements (in mÅ) of Zr II, Ce II, and Nd II for each of the stars.

ID	Zr II 4208.98 Å	Ce II 4562.36 Å	Ce II 4628.16 Å	Nd II 4706.54 Å
CD-45 3283	21.3	7.6	5.3	7.0
CD-61 0282	17.7	5.2	2.7	4.0
G 16-20	22.1	6.6	4.1	4.0
G 18-28	29.1	10.3	…	9.4
G 18-39	17.3	…	2.0	3.0
G 31-55	23.8	4.9	3.6	4.6
G 56-30	23.1	6.6	7.2	2.9
G 56-36	26.1	6.7	4.4	5.4
G 66-22	26.2	…	8.9	10.6
G 170-56	23.4	6.8	3.4	4.2
HD 3567	21.3	4.9	5.3	4.0
HD 22879	31.4	8.2	6.5	7.9
HD 25704	22.4	6.5	6.1	7.1
HD 76932	34.3	8.4	5.1	7.9
HD 103723	27.5	9.4	7.4	7.7
HD 105004	24.6	…	9.4	5.0
HD 111980	37.4	10.6	6.5	6.6
HD 120559	23.8	…	4.1	7.5
HD 126681	28.9	7.4	5.4	5.0
HD 179626	27.6	5.9	4.1	4.1
HD 189558	39.3	10.9	8.9	7.1
HD 193901	17.4	5.2	…	5.3
HD 194598	15.8	3.6	3.2	2.9
HD 199289	19.1	3.3	2.5	3.6
HD 205650	19.1	4.6	3.4	3.0
HD 219617	10.7	…	3.3	2.0[a]
HD 230409	26.2	8.2	5.8	10.5

[a] Upper limit

of Nd. One star, the most metal-poor in the sample (HD 219617), falls below this limit therefore we adopt an upper limit of 2 mÅ for the Nd EW.

For Sc, La, and Eu, we fit synthetic spectra generated by the spectrum synthesis program MOOG (Sneden 1973) to determine abundances. These elements require the consideration of hyperfine splitting (HFS) and/or isotopic shifts. Figure 5.2 illustrates the fit of the synthetic spectrum to the observed spectrum for the Sc and Eu lines of HD 22879. The best fitting synthetic spectrum was determined using χ^2 minimisation. For Sc, the log gf values of Prochaska et al. (2000) were utilised for the 5526.81 Å absorption line. La was determined using one La II line at 4086.71 Å with log gf values from Lawler et al. (2001a). For the Eu II spectral line at 4129.72 Å we use the log gf values from Lawler et al. (2001b) and

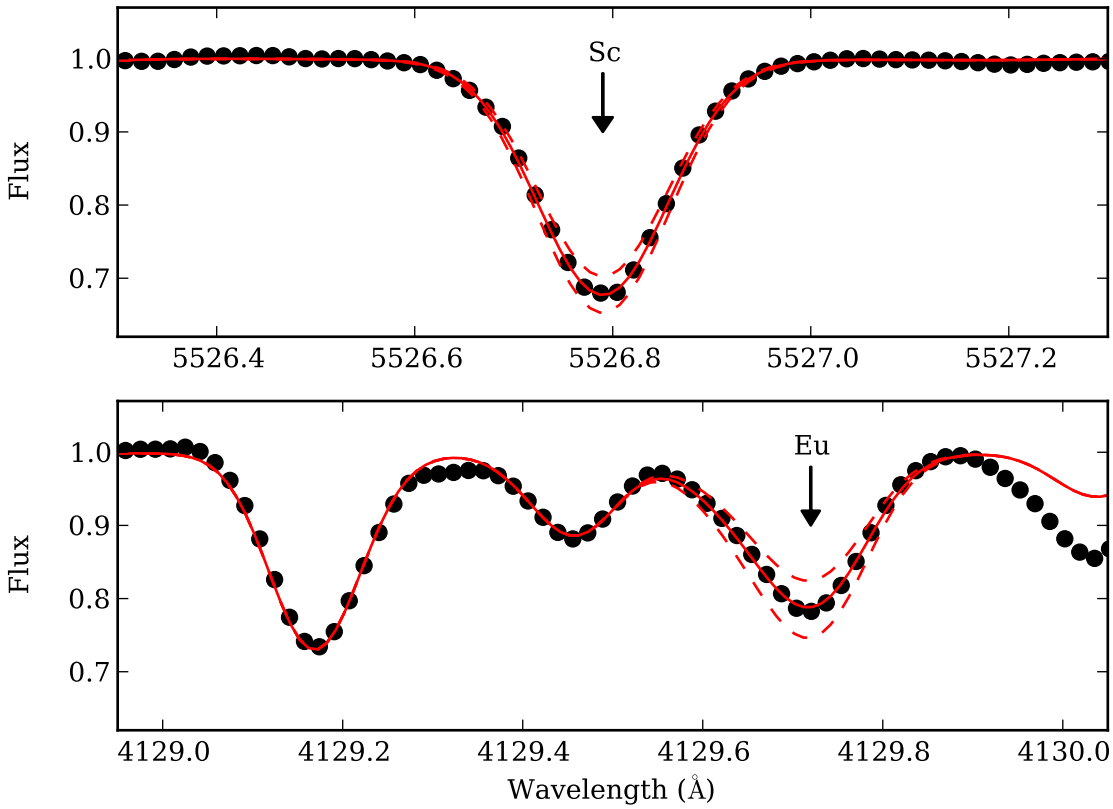

Figure 5.2 Synthetic spectrum fit (solid line) to the observations (black points) of the Sc line at 5526 Å (top) and the Eu line at 4129 Å (bottom) for HD 22879. The dashed lines show synthetic spectra with [Sc/Fe] and [Eu/Fe] of ±0.1.

solar isotope ratios from Lodders (2003). The Eu line at 4129.72 Å gives the most reliable abundance of Eu in a star.

We use solar elemental abundances from Asplund et al. (2009) as detailed in Table 5.3. As we perform a differential analysis to measure abundances, the choice of solar abundance only shifts the stellar abundances up or down and does not affect the relative abundances. To reiterate, we are primarily interested in relative abundances, and therefore abundance differences, between the low- and high-α populations. The determined abundances are given in Table 5.4.

We determine errors using the stellar parameter uncertainties as stated in NS10 where the differential errors for $\sigma(\log g)$ and $\sigma(T_{\rm eff})$ are ±0.05 and ±30 K, respectively. The 1-σ errors for [Fe/H] and [α/Fe] were determined by NS10 and are given as 0.04 and 0.02. We determine the 1-σ errors in [Zr/Fe], [Ce/Fe], [Nd/Fe] to be 0.04 and for [Sc/Fe], [La/Fe], and [Eu/Fe] to be 0.05. We also approximate the error in the EW measurement to be about 1 mÅ due to uncertainties in determining the continuum.

5.3.1. Zr

The neutron-capture element Zr is predominately produced by AGB stars and is an example of a first *s*-process peak element. By determining the abundance of Zr, we expand on the

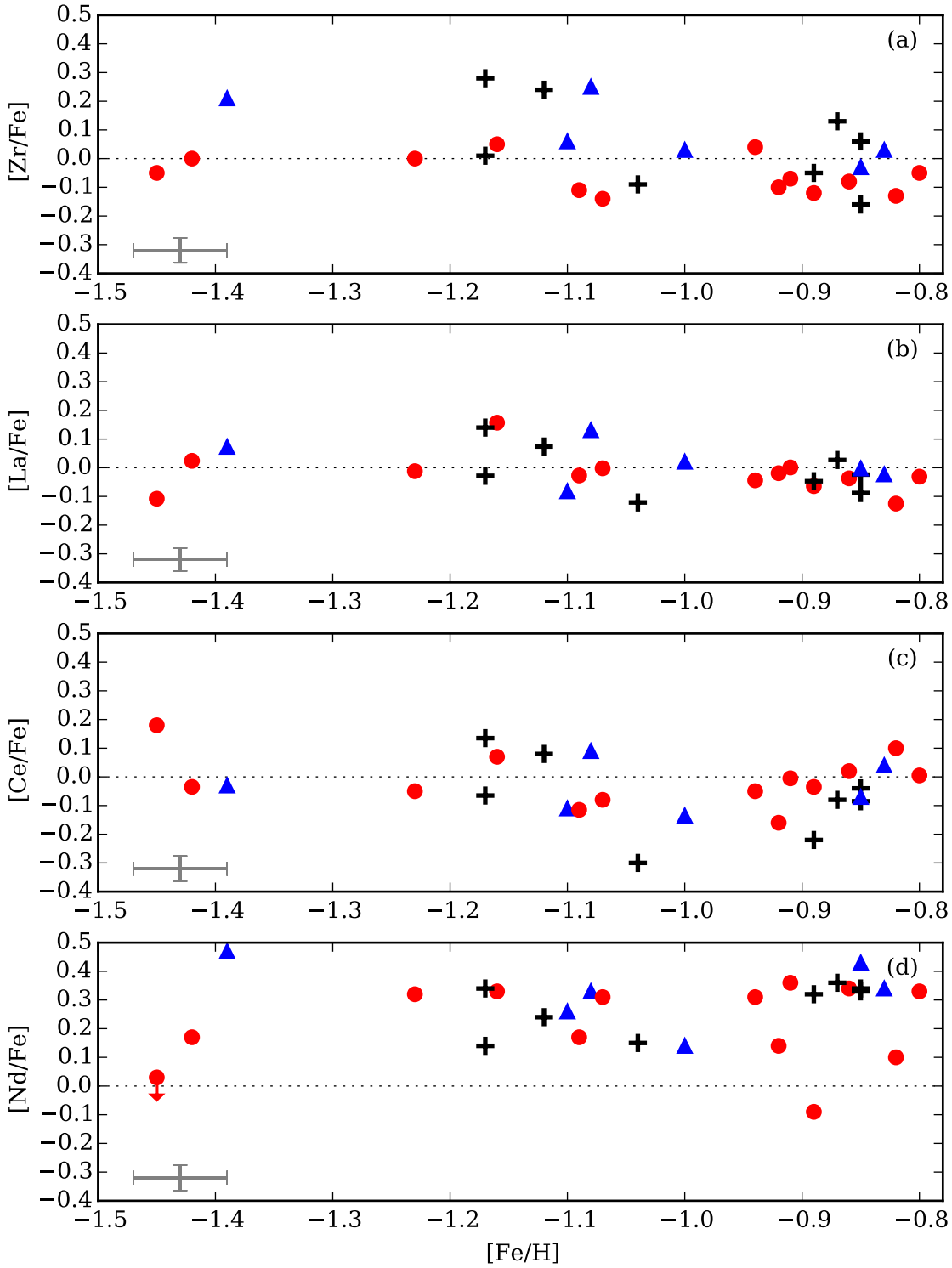

Figure 5.3 Four *s*-process elements (Zr, La, Ce, and Nd) versus [Fe/H]. The red circles indicate low-α stars, the blue triangles indicate high-α stars, and the plus signs indicate TD stars. The 1-σ error is shown in the bottom-left of each plot.

Table 5.3 Adopted solar elemental abundances from Asplund et al. (2009).

Element	Z	log(X/H) + 12
Sc[a]	21	3.05
Zr	40	2.58
La	57	1.10
Ce	58	1.58
Nd	60	1.42
Eu	63	0.52

[a] Meteoritic value.

measurements of Y, another first *s*-process peak element, by NS11.

Figure 5.3(a) shows [Zr/Fe] as a function of [Fe/H]. The dispersion in [Zr/Fe] is ~ 0.12 which is larger than the error of 0.04. When considering the two populations, the scatter in [Zr/Fe] is lower for the low-α stars with a dispersion of 0.06 compared to a dispersion of 0.13 for the high-α and TD stars. In addition to the difference in the dispersion of [Zr/Fe], the low-α stars have a systematically lower [Zr/Fe] abundance compared to the high-α and TD stars.

This possible separation in the high- and low-α populations is in agreement with the slight separation in abundance measurements of [Y/Fe] for the two populations seen in NS11. As Zr and Y are both first-peak *s*-process elements, they are expected to follow the same trend. Figure 5.4 demonstrates the difference in the Zr abundance for a low-α star (HD 194598) and a high-α star (HD 111980) at nearly the same metallicity (Table 5.1). The low-α star has a weaker Zr II line than the high-α star. While the effective temperature differs between these two stars by approximately 150 K, all other lines in this region exhibit very similar strengths.

A comparison between the [Y/Fe] as measured by NS11 and [Zr/Fe] is presented in Figure 5.5. The abundance of Zr follows the abundance of Y which is expected if Y and Zr have a common origin. The high-α stars have a tighter correlation between [Y/Fe] and [Zr/Fe] compared to the low-α stars.

5.3.2. La, Ce, and Nd

We extend upon the Ba measurements of NS11 by determining abundances for other elements belonging to the second *s*-process peak, namely La, Ce, and Nd.

There are a number of advantages with using La as an *s*-process indicator compared to Ba (Winckler et al. 2006). While Ba consists of five isotopes and requires the consideration of isotope shifts, 99.91 per cent of La consists of ^{139}La. Ba lines are also generally saturated making accurate abundance measurements difficult. Figure 5.3(b) presents [La/Fe] as a function of [Fe/H]. There is no clear difference in La abundance between the low-α, high-α and TD stars. The dispersion in the abundance of [La/Fe] is ~ 0.07, the lowest of all the

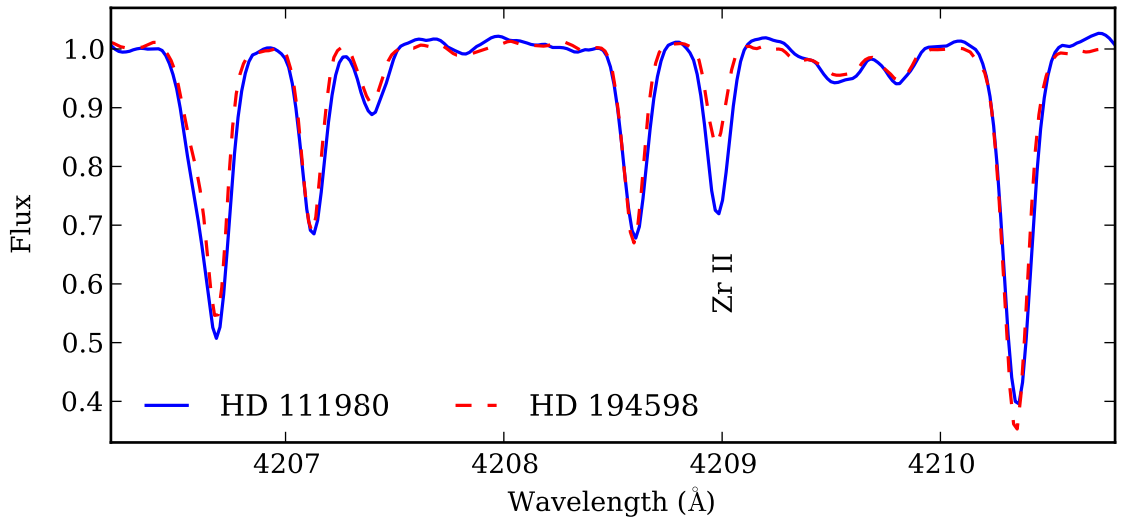

Figure 5.4 MIKE spectra around the Zr line at 4208.98 Å for a low-α star (HD 194598) and a high-α star (HD 111980).

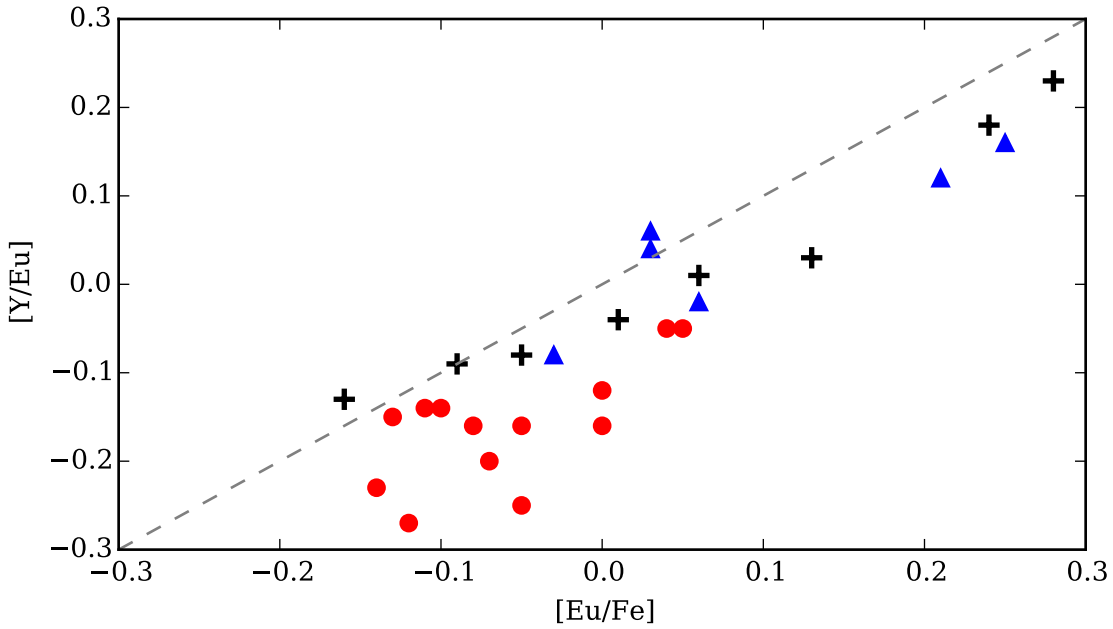

Figure 5.5 Comparison of [Y/Fe] (taken from NS11) and [Zr/Fe]. The red circles indicate low-α stars, the blue triangles indicate high-α stars, and the plus signs indicate TD stars. The dashed line shows the one-to-one correspondence line. The 1-σ error is shown in the top-left.

Table 5.4 Abundances for each of the measured elements. The values for [Fe/H] are taken from NS10.

Star	[Fe/H]	[Sc/Fe]	[Zr/Fe]	[La/Fe]	[Ce/Fe]	[Nd/Fe]	[Eu/Fe]
CD-45 3283	−0.91	−0.11	−0.07	0.00	−0.01	0.36	0.31
CD-61 0282	−1.23	−0.15	0.00	−0.01	−0.05	0.32	0.26
G 16-20	−1.42	−0.11	−0.00	0.02	−0.04	0.17	0.32
G 18-28	−0.83	0.11	0.03	−0.02	0.04	0.34	0.13
G 18-39	−1.39	−0.00	0.21	0.07	−0.03	0.47	0.26
G 31-55	−1.10	−0.03	0.06	−0.08	−0.11	0.26	0.05
G 56-30	−0.89	−0.22	−0.12	−0.06	−0.04	−0.09	0.09
G 56-36	−0.94	−0.02	0.04	−0.04	−0.05	0.31	0.13
G 66-22	−0.86	−0.16	−0.08	−0.04	0.02	0.34	0.30
G 170-56	−0.92	−0.14	−0.10	−0.02	−0.16	0.14	0.16
HD 3567	−1.16	−0.04	0.05	0.16	0.07	0.33	0.39
HD 22879	−0.85	0.12	0.06	−0.09	−0.04	0.34	0.16
HD 25704	−0.85	0.09	−0.16	−0.02	−0.09	0.33	0.15
HD 76932	−0.87	0.15	0.13	0.03	−0.08	0.36	0.21
HD 103723	−0.80	−0.03	−0.05	−0.03	0.01	0.33	0.17
HD 105004	−0.82	−0.04	−0.13	−0.12	0.10	0.10	0.04
HD 111980	−1.08	0.00	0.25	0.13	0.09	0.33	0.14
HD 120559	−0.89	0.17	−0.05	−0.05	−0.22	0.32	0.20
HD 126681	−1.17	0.00	0.28	0.14	0.13	0.34	0.20
HD 179626	−1.00	0.12	0.03	0.02	−0.14	0.14	0.03
HD 189558	−1.12	0.09	0.24	0.07	0.08	0.24	0.17
HD 193901	−1.07	−0.19	−0.14	−0.00	−0.08	0.31	0.24
HD 194598	−1.09	−0.07	−0.11	−0.03	−0.11	0.17	0.27
HD 199289	−1.04	0.08	−0.09	−0.12	−0.30	0.15	0.09
HD 205650	−1.17	−0.01	0.01	−0.03	−0.07	0.14	0.19
HD 219617	−1.45	−0.11	−0.05	−0.11	0.18	0.03[a]	0.21
HD 230409	−0.85	0.05	−0.03	−0.00	−0.07	0.43	0.27

[a] Upper limit

s-process abundances measured here. The [La/Fe] abundance is almost constant with [Fe/H] with a mean abundance close to the solar value.

The *s*-process contribution to Ce in the Solar System is 81 per cent where ^{140}Ce is the only stable isotope accessible by the *s*-process (Sneden et al. 2008). Figure 5.3(c) presents the results for [Ce/Fe]. Two-thirds of the stars show a subsolar [Ce/Fe] abundance and the dispersion in the abundance is approximately 0.1 with a mean of around −0.04. There is no apparent separation between the low- and high-α stars. However, the dispersion between the low-α stars and the high-α stars are essentially the same, 0.09 compared to 0.10 respectively).

Only 58 per cent of Nd in the Solar System is due to the *s*-process (Sneden et al. 2008). This is a result of its isotopes having higher neutron-capture cross sections compared to isotopes

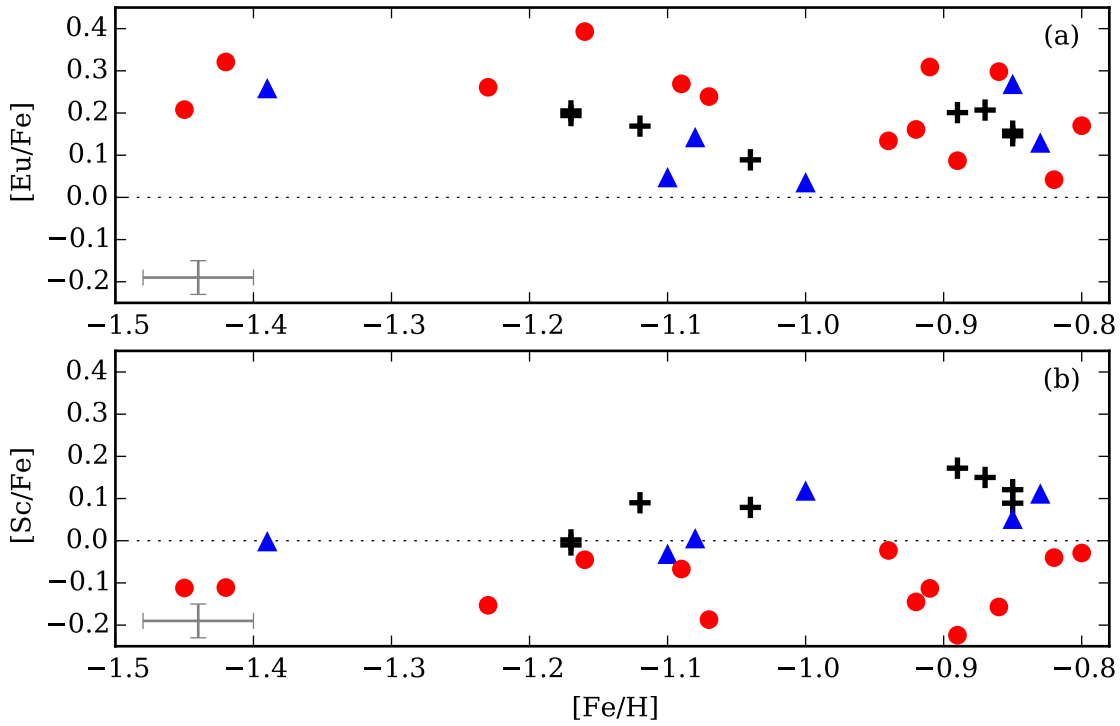

Figure 5.6 (*a*) [Sc/Fe] and (*b*) [Eu/Fe] versus [Fe/H]. The red circles indicate low-α stars, the blue triangles indicate high-α stars, and the plus signs indicate TD stars. The 1-σ error is shown in the bottom-left of each plot.

of Ba, La, and Ce (Dillmann et al. 2006). Figure 5.3(d) presents the abundance of [Nd/Fe] against [Fe/H]. Due to the weak Nd II line for HD 219617, we provide an upper limit of [Nd/Fe] = 0.03 for this object. There is no obvious difference in [Nd/Fe] between the two populations except for a few low-α stars having a lower Nd abundance. This causes the dispersion to be higher for the low-α stars than the high-α stars, 0.14 compared 0.10. The mean abundance of [Nd/Fe] is 0.26 and all but one star has a supersolar [Nd/Fe] abundance.

5.3.3. Eu

Eu is predominately an *r*-process element with less than 2 per cent of the Solar System abundance a result of *s*-process nucleosynthesis (Sneden et al. 2008). We have included Eu in this study to investigate the relative contribution of *r*-process nucleosynthesis to the low- and high-α stars.

Figure 5.6(a) presents the [Eu/Fe] abundances where there is a potential separation between the two populations: the low-α stars appear to show a higher [Eu/Fe] abundance compared to the high-α stars. However, due to the few stars at lower metallicities, the separation is not as clear as what is found for other elements such as Zr. The low-α group also shows a potential decrease in [Eu/Fe] with increasing metallicity. These results would need to be confirmed using a larger sample of stars.

5.3.4. Sc

There is only one stable isotope of Sc (^{45}Sc) and it is mainly synthesised during carbon and neon burning in massive stars (Woosley et al. 2002). It is also produced to a lesser extent in AGB stars (Fishlock et al. 2014a). We measure Sc to verify the conclusions of Nissen et al. (2000) where the low-α stars have a lower [Sc/Fe] abundance compared to the high-α stars.

Figure 5.6(b) shows that there is a clear separation in [Sc/Fe]. The low-α stars have a subsolar [Sc/Fe] abundance with a mean abundance of -0.11 whereas the high-α stars have a mostly supersolar abundance with a mean of 0.07. These results confirm the separation in [Sc/Fe] found in the earlier work by Nissen et al. (2000) between the low- and high-α populations.

5.4. Analysis

As with the NS10 and NS11 studies, we combine the high-α TD and high-α halo stars into one high-α group. Due to a smaller sample size compared to NS11, we do not remove the dependence of [Fe/H] on the abundance of the high-α stars as it cannot be definitively determined. Given that our sample size is smaller than in NS10, we now seek to quantify this potential limitation by introducing our methodology on how we determine whether a given abundance ratio exhibits a difference (i.e., separation) between the low- and high-α populations.

We first consider the NS10 measurements of Cr, a representative element for which NS10 found no significant separation between the low- and high-α groups. Using a two sample Kolmogorov-Smirnov (KS) test between the low- and high-α groups (without distinguishing TD stars), we find the [Cr/Fe] p-value for all stars in the NS10 sample with $-1.45 \leq$ [Fe/H] ≤ -0.8 to be 0.07.

In order to investigate the effect of our smaller sample size, we randomly select 13 low-α and 14 high-α stars from the full NS10 sample with $-1.45 \leq$ [Fe/H] ≤ -0.8, apply the KS test and check the p-value. We repeat this exercise 10,000 times and find that for approximately 25 per cent of the realisations, the p-value is below a significance level of 0.07. If we arbitrarily define the threshold to be a p-value of 0.03, roughly 10 per cent of the random realisations result in a p-value below 0.03.

We now examine [Ba/Y], an abundance ratio that was found to exhibit a significant separation between the low- and high-α populations. For the full NS10 sample with $-1.45 \leq$ [Fe/H] ≤ -0.8, we compute a p-value of 2.9×10^{-9}. We then seek to quantify the effect of having a smaller sample size. As above, we randomly select 13 low-α and 14 high-α stars from the full NS10 sample with $-1.45 \leq$ [Fe/H] ≤ -0.8, apply the KS test and check the p-value. We repeat the exercise 10,000 times. For a threshold p-value of 0.03, about 99.7 per cent of random realisations have a p-value below this level, indicating that we are able to pick the separation in [Ba/Y] in all but 0.3 per cent of cases.

Based on these tests, we choose a p-value of 0.03 which suggests that there is at least a 90 per cent chance that the abundance separation in the sample of 27 stars is genuine despite

Table 5.5 Mean value and standard deviation of each abundance ratio for the low-α group and the high-α group. The p-value between the two groups is also given.

	low-α		high-α		
	$\tilde{x}$	σ	$\tilde{x}$	σ	p-value
[Sc/Fe]	−0.107	0.062	0.067	0.063	0.000
[Zr/Fe]	−0.058	0.061	0.069	0.131	0.017
[La/Fe]	−0.022	0.065	0.004	0.076	0.589
[Ce/Fe]	−0.012	0.087	−0.058	0.114	0.340
[Nd/Fe]	0.217	0.137	0.299	0.098	0.614
[Eu/Fe]	0.222	0.097	0.161	0.068	0.173
[La/Zr]	0.037	0.061	−0.066	0.084	0.005
[*ls*/Fe]	−0.109	0.057	0.049	0.117	0.004
[*hs*/Fe]	0.005	0.056	0.038	0.084	0.303
[*hs*/*ls*]	0.114	0.046	−0.010	0.065	0.000
[Y/Eu]	−0.382	0.101	−0.133	0.122	0.000
[*ls*/Eu]	−0.332	0.092	−0.112	0.126	0.001
[Ba/Eu]	−0.387	0.122	−0.253	0.122	0.024
[La/Eu]	−0.244	0.064	−0.157	0.082	0.173
[*hs*/Eu]	−0.218	0.082	−0.122	0.081	0.022
[Y/Fe]	−0.160	0.064	0.028	0.107	0.000
[Ba/Fe]	−0.165	0.070	−0.092	0.115	0.303
[Ba/Y]	−0.005	0.055	−0.120	0.030	0.000

having a smaller sample of stars than NS10 and NS11. We also confirm using a KS test that the high-α population and TD stars have a significant probability of coming from the same population. In Table 5.5 we present the mean of each abundance ratio and its standard deviation for both low- and high-α groups. We also present the p-value of the two sample KS test between the low- and high-α groups. The analyses of [Y/Fe], [Ba/Fe], and [Ba/Y] are included in Table 5.5 for comparison using the abundances measured by NS11 for our sample of 27 stars.

For abundances relative to Fe (e.g., [Zr/Fe]), the only elements measured in this study that show a separation between the low- and high-α groups are Sc and Zr. The abundance ratio of [Sc/Fe] has a p-value of 4×10^{-6} which strongly suggests that the high-α group has a higher [Sc/Fe] ratio than the low-α group. To compare, the mean p-value calculated for [Mg/Fe] when randomly selecting 13 low-α and 14 high-α stars is 4.9×10^{-7}. As previously mentioned, this separation in [Sc/Fe] confirms the same conclusion made by Nissen et al. (2000).

We find that the separation between the low- and high-α groups is detected for [Y/Fe] despite having a smaller sample size than NS11. When using NS11 measurements of the 27 stars, the calculated p-value of 2.2×10^{-4} is well below the chosen significance level giving a high likelihood that the separation is real. The potential separation in [Zr/Fe] is evident

with a p-value of 0.017 and confirms the results of NS11 who found a slight separation in [Y/Fe], another first s-process peak element. In contrast to the first s-process peak elements Y and Zr, the abundance ratios for elements belonging to the second peak [La/Fe], [Ce/Fe], and [Nd/Fe] show no difference between the low- and high-α groups which is confirmed by the calculated p-values (see Table 5.5). The second s-process peak element, Ba, measured by NS11 also shows no separation in [Ba/Fe] between the two groups.

In NS11, a separation in [Ba/Y] was observed between the low- and high-α groups (see Figure 5.7(a)). We confirm this in our sample with a p-value of 4.7×10^{-6}. In Figure 5.7(b) we plot [La/Zr] and are able to reproduce the separation between a light-s (ls) element at the first s-process peak and a heavy-s (hs) element at the second peak. Despite the smaller sample size in this study, the separation is evident with a p-value of 0.005. This p-value is lower than the p-value of 0.017 for [Zr/Fe] or the p-value of 0.589 for [La/Fe] alone suggesting that lower p-values can be obtained for certain combinations of elements.

Assuming that the [La/Zr] ratio in the low-α stars is due to pollution from AGB stars, we can use the model predictions of [Fe/H] = −1.2 from Fishlock et al. (2014a) to estimate the mass range of those AGB stars. Starting at lower masses (1 to 3 $M_\odot$), calculations predict [La/Zr] ratios above solar; for example, the 3 $M_\odot$ model predicts a final [La/Zr] ratio of 0.32. Moving to the intermediate masses (3.25 to 7 $M_\odot$), calculations predict [La/Zr] ratios below solar; for example, the 6 $M_\odot$ model predicts a final [La/Zr] ratio of −0.68. Therefore, based on the [La/Zr] ratio, AGBs stars in the range 1 to 3 $M_\odot$ could be responsible for the abundance difference between the low- and high-α populations.

For stars in the range $-1.5 <$ [Fe/H] < -1, there is a possible separation in [Eu/Fe] where the low-α group has a higher [Eu/Fe] abundance compared to the high-α group. However, higher metallicity stars show no difference between the two groups and the hint of a separation is not statistically significant with a p-value of 0.173. We return to this possibility of a separation in the following section.

The s-process indicators are the average of the abundance of the elements at each of the two s-process peaks. We include the Y and Ba results of NS11 and define [ls/Fe] and [hs/Fe] to be:

$$[ls/\mathrm{Fe}] = ([\mathrm{Y/Fe}] + [\mathrm{Zr/Fe}])/2 \tag{5.1}$$

and

$$[hs/\mathrm{Fe}] = ([\mathrm{Ba/Fe}] + [\mathrm{La/Fe}] + [\mathrm{Ce/Fe}] + [\mathrm{Nd/Fe}])/4. \tag{5.2}$$

The [ls/Fe] and [hs/Fe] ratios against [Fe/H] are presented in Figure 5.7(c) and 5.7(d). The low-α stars have a lower [ls/Fe] ratio than the high-α stars with a p-value of 0.004. For [hs/Fe], there is no apparent difference between the two populations where the p-value is 0.303, well above the chosen significance level of 0.03.

Figure 5.7(e) shows there is a clear separation in the s-process indicator [hs/ls] between the low- and high-α groups with the low-α stars showing a higher [hs/ls] ratio. This separation

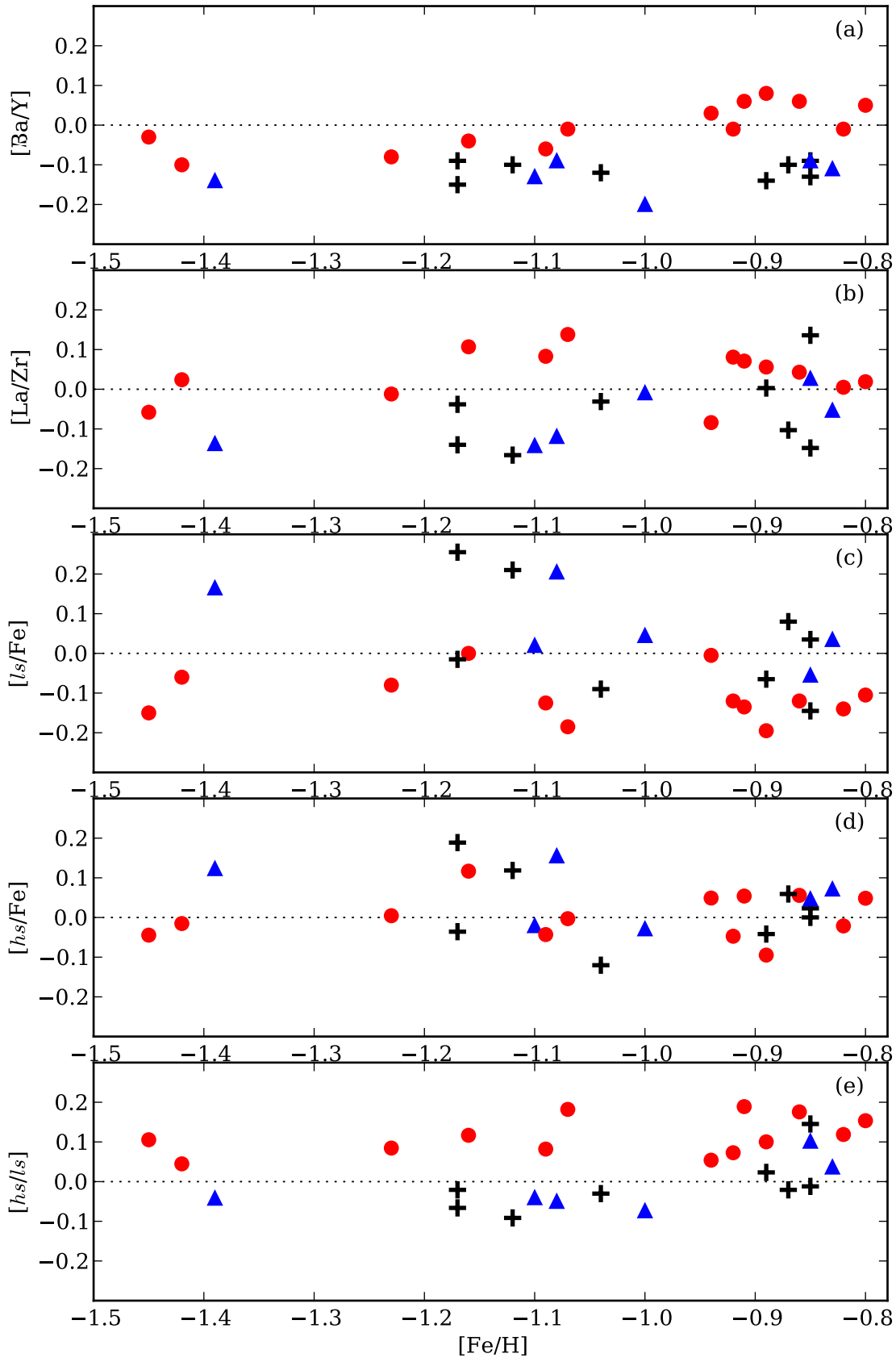

Figure 5.7 [Ba/Y] (from NS11), [La/Zr], [*ls*/Fe], [*hs*/Fe], and [*hs*/*ls*] versus [Fe/H] where *ls* is the average abundance of Y and Zr and *hs* is the average abundance of Ba, La, Nd, and Ce. The red circles indicate low-α stars, the blue triangles indicate high-α stars, and the plus signs indicate TD stars.

is confirmed with a calculated p-value of 3×10^{-5}. The low-α population has a higher [hs/ls] ratio than the high-α population with a mean [hs/ls] value of 0.11 compared to -0.01 for the high-α population. Additionally, all the low-α stars have a supersolar [hs/ls] ratio. This is predicted for stars enriched by previous generations of low-mass AGB stars. For example, the low-mass models of Fishlock et al. (2014a) end the AGB phase with [hs/ls] ratios of between 0.45 and 0.59, excluding the 1 $M_\odot$ model which experiences minimal third dredge-up. In contrast, the intermediate-mass models have final [hs/ls] ratios between -0.71 and -0.41. The differences between the low-mass and intermediate-mass models are a result of the different neutron sources that occur (Busso et al. 1999).

The abundance ratio of s-process elements to r-process elements offers a powerful diagnostic for Galactic chemical evolution (Wheeler et al. 1989; McWilliam 1997). In Figure 5.8 we present the abundance ratios of [ls/Eu], [Y/Eu], [hs/Eu], and [La/Eu] against [Fe/H]. There is a high likelihood that the separation in [ls/Eu] is genuine with a low p-value of 0.001. The low-α stars show a lower [ls/Eu] ratio compared to the high-α stars with the separation more evident at [Fe/H] $\lesssim -1$. There is also an apparent increase in [ls/Eu] with increasing [Fe/H] for the low-α group which is not seen in the high-α group.

Figure 5.8(b) presents the abundance ratios of the ls element, Y, relative to Eu. The low-α group has a lower abundance of [Y/Eu] compared to the high-α group with a p-value of 2.2×10^{-4}. This p-value is more significant than the [ls/Eu] separation. We also find that the [Y/Eu] abundance for the low-α stars with [Fe/H] less than -1 is almost constant at approximately -0.4 with minimal scatter. This behaviour is also seen for [ls/Fe].

The observed separation in [hs/Eu] is not as clear when compared to [ls/Eu] although it has a p-value of 0.022 which is just below the chosen significance level. The low-α group has a [hs/Eu] ratio that is closer to the r-process contribution of the hs elements and Eu in the Solar System than the high-α group. As with [ls/Fe], there is an apparent increase in [hs/Eu] with increasing [Fe/H] for the low-α stars.

Figure 5.8(d) presents the abundance ratios of the hs element, La, relative to Eu where all the stars have a subsolar [La/Eu] ratio. Unlike the separation found for [hs/Eu], we do not find a separation in [La/Eu] between the two groups. We also show the r-process contribution to the Solar System abundances of La and Eu (and its uncertainty) as determined by Winckler et al. (2006). The theoretical prediction of an AGB stellar model with an initial mass of 3.25 $M_\odot$ at a metallicity of [Fe/H] = -1.2, from Fishlock et al. (2014a) is also presented in Figure 5.8. Of all the models calculated by Fishlock et al. (2014a), the lowest [La/Eu] ratio of 0.08 occurs for the 3.25 $M_\odot$ model.

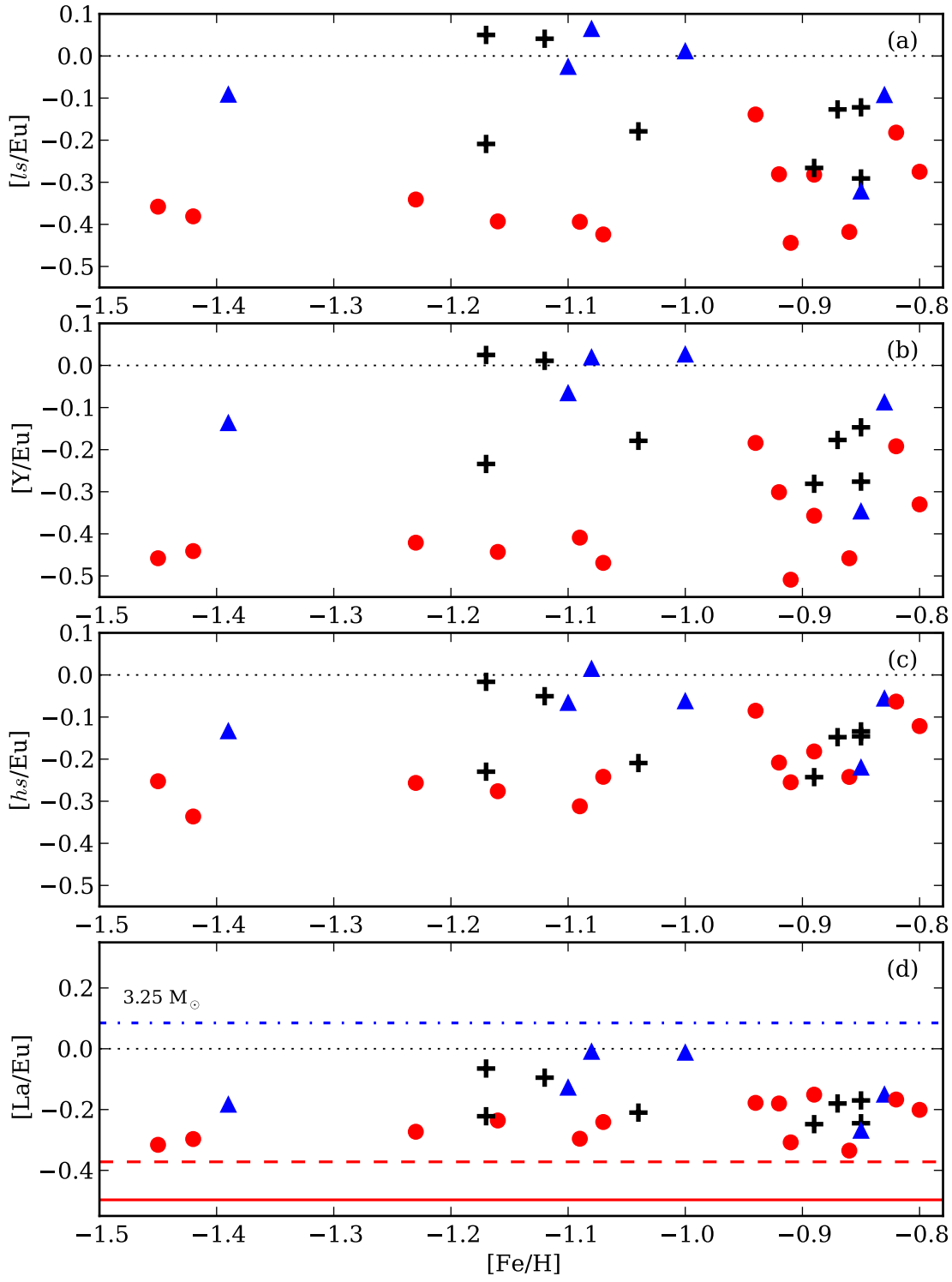

Figure 5.8 [*ls*/Eu], [Y/Eu], [*hs*/Eu], and [La/Eu] versus [Fe/H] where *ls* is the average abundance of Y and Zr and *hs* is the average abundance of Ba, La, Nd, and Ce. The red circles indicate low-α stars, the blue triangles indicate high-α stars, and the plus signs indicate TD stars. The red solid line represents the *r*-process ratio for [La/Eu] and the red dashed line its upper uncertainty (Winckler et al. 2006). The final surface abundance of [La/Eu] for the 3.25 $M_{\odot}$, Z = 0.001 AGB model from Fishlock et al. (2014a) is also indicated (dash-dotted line).

5.5. Discussion

As previously mentioned, the chemical abundance ratios as measured from FGK-type dwarf stars can reveal important details of the formation and evolution of a stellar population. This paper focuses on examining a subsample of low- and high-α stars compiled by NS10. Further, kinematics indicate that the low-α stars were likely accreted from a dwarf galaxy whereas the high-α stars are representative of Galactic halo objects.

Over the common metallicity range spanned by the surviving local group dSphs and the Galactic halo, the [α/Fe] ratio differs between these objects. However, the [α/Fe] ratio alone cannot provide an unambiguous separation between the two. For example, Venn et al. (2004) confirmed that there is some overlap in [α/Fe] ratios between dSph stars and Galactic halo stars with extreme retrograde orbits (Fulbright 2002; Stephens & Boesgaard 2002). Additionally, the most metal-poor stars in dSphs appear to have halo-like [α/Fe] ratios (Frebel et al. 2010; Venn et al. 2012). Gilmore & Wyse (1998) conclude that the differences in [α/Fe] for stars in the halo could be due to variations in the duration of star formation in regions of the proto-halo.

As noted in the introduction, there is another chemical signature that distinguishes halo stars from their dSph counterparts, namely, the [Ba/Y] and [Y/Eu] ratios. In dSphs, roughly two-thirds of the stars show a higher [Ba/Y] ratio and a lower [Y/Eu] ratio compared to Galactic halo stars (Venn et al. 2004; Tolstoy et al. 2009). They concluded that the dSphs of today are chemically different to the higher mass galaxies that merged early during the formation of the Galaxy.

The findings presented here, together with the results of NS11, reveal that the low-α population also displays this chemical signature when compared to the high-α group. The NS11 study found that the low-α stars, likely accreted from dSphs, show a higher [Ba/Y] ratio than the high-α stars which are believed to have formed in-situ in the Milky Way. The abundance anomaly is not as large as observed in Fornax (Letarte et al. 2010) however Schuster et al. (2012) demonstrated that the low-α stars have ages of around 10 Gyr, older than the stars of Fornax. This age difference was also noted in NS11.

Using the [Y/Fe] abundances determined by NS11, we find that the low-α population has a lower [Y/Eu] ratio than the high-α group. This evidence suggests that present-day dSphs share a similar chemical enrichment history to the dwarf galaxies that were hosts to the low-α stars and merged later during the formation of the Galactic halo. The abundance of [Y/Eu] increases with increasing [Fe/H] indicating that the accreted dwarf galaxies had sufficient time to form stars enriched with the ejecta of AGB stars before merging.

Having confirmed and extended the chemical abundance differences between the low- and high-α populations , and the connection with dSphs, we now turn our attention to the possible sources that could have produced such abundance differences. Intermediate-mass AGB stars (> 3 M$_\odot$) produce [Ba/Y] ratios less than solar (cf. Karakas & Lattanzio 2014). In low-metallicity, low-mass AGB stars ($\lesssim 3$ M$_\odot$), the [Ba/Y] ratio is above solar (e.g., Cristallo et al. 2011; Fishlock et al. 2014a). As the low-α stars formed in a system with a slower star

formation rate than the high-α population, it is reasonable to also expect lower mass stars to contribute to the chemical enrichment. NS11 concluded that the high [Ba/Y] trend observed in the low-α group can be explained by the enrichment of low-metallicity, low-mass AGB stars as a result of the slower rate of chemical evolution. In this study, we find high [La/Zr] and [*hs*/*ls*] ratios for the low-α population confirming this conclusion. Model predictions from Fishlock et al. (2014a) find that low-metallicity, low-mass stars have lifetimes between 0.29×10^9 yr to 6.8×10^9 yr. These results give constraints on the enrichment timescales involved in the earliest dwarf galaxies.

The study by McWilliam et al. (2013) of the Sagittarius dSph provides additional observational support for these conclusions. They analysed three Sagittarius dSph stars and found that the stars have, relative to Galactic stars, low [α/Fe], [Na/Fe], [Al/Fe], and [Cu/Fe] ratios along with a high [La/Y] ratio. These observations match the abundance patterns of the low-α stars when compared to the high-α group.

Recently, considerable effort has been devoted to the nucleosynthesis of fast-rotating massive stars. Frischknecht et al. (2012) calculated *s*-process production factors for low-metallicity massive rotating stars of 25 $M_\odot$. It was shown that these stars produce more Y than Ba resulting in [Ba/Y] less than solar. Rotation in AGB stars can also affect neutron-capture nucleosynthesis where an increased rotation velocity decreases the [*hs*/*ls*] ratio however it never falls below solar for low-mass stars (Piersanti et al. 2013).

When considering the *r*-process element Eu we find that the [Y/Eu] ratio differs between the low- and high-α populations with the low-α populations having a lower [Y/Eu] ratio. The *r*-process is responsible for producing the majority of Eu in the Solar System (Sneden et al. 2008). In the absence of grids of theoretical yields for the production of neutron-capture elements via the *r*-process, it is difficult to trace the enrichment of the heavy elements using chemical evolution models. Here we use observations to guide our interpretations.

Tolstoy et al. (2009) confirmed that the evolution of [Eu/Fe] for both Galactic stars and dSph stars generally follows that of [α/Fe] indicating a common origin, most likely to be massive stars. With this in mind, we would expect the low-α stars to have a lower [Eu/Fe] abundance than the high-α stars at a given metallicity. Lanfranchi et al. (2008) also predicted that strong galactic winds and a decreased star formation rate further decrease the [Eu/Fe] abundance in dSphs. However, we have found that there is the slight possibility that the low-α stars have a higher [Eu/Fe] ratio than the high-α stars, in contrast to our expectations. This separation is only observed at [Fe/H] less than -1 and includes half the sample. When using the whole metallicity range, the KS test does not find a statistically significant separation between the two populations (see Table 5.5). Additionally, the study by McWilliam et al. (2013) found that a number of stars in the Sagittarius dSph have a slightly higher [Eu/Fe] (and [La/Y] abundances than Galactic TD stars.

If the low-α stars do have a higher Eu abundance than the high-α stars at lower metallicities, it would suggest that the *r*-process contributed more to the chemical evolution of the low-α stars at a given metallicity. This is difficult to reconcile with chemical evolution models which support the idea that intense galactic winds remove Eu from a system. To determine

if there is the possibility of a statistically significant separation, additional observations of Eu for the NS10 sample are required, particularly for stars with [Fe/H] lower than −1.

We observe lower [Y/Eu] ratios in the low-α stars compared to the high-α stars with the separation becoming more noticeable at lower metallicities. The study of the Carina dSph by Venn et al. (2012) also found that the low-metallicity stars have slightly lower [Y/Eu] ratios (and slightly higher [Ba/Y] ratios) when compared to Galactic stars. Venn et al. (2012) concluded that these differences are a result of metal-poor AGB stars contributing to the chemical enrichment of Carina. In contrast, Venn et al. (2004) inferred that the low [Y/Eu] ratio (along with low [α/Fe]) occurring in dSphs is a result of the lack of the α-process which contributes to the production of α elements and light *r*-process elements.

We observe constant [Y/Eu] abundances (~ -0.4) in the lower metallicity low-α stars ($-1.5 \leq$ [Fe/H] ≤ -1) suggesting that Y and Eu have a common origin or timescale for enrichment, most likely to be the *r*-process, at these metallicities. The dSph chemical evolution models of Lanfranchi et al. (2008) show constant [Y/Eu] ratios up to a [Fe/H] ratio of approximately −1.5. The ratio of [Y/Eu] then increases at higher metallicities due to the production of Y by AGB stars.

5.6. Conclusions

We found that the low-α and high-α populations of NS10 separate when using the abundance ratios of [Sc/Fe], [Zr/Fe], [La/Zr], [*ls*/Fe], [*hs*/*ls*], [Y/Eu], [*ls*/Eu], and [*hs*/Eu]. The observed separations have only been detected using a differential analysis relative to a reference star with comparable stellar parameters to reduce the error in abundance measurements. The separation observed using [La/Zr] confirms the results of NS11 who find a separation in [Ba/Y], where Zr and Y are first *s*-process peak elements and La and Ba are second *s*-process peak elements.

The low abundance of [Y/Eu] found in the low-α population compared to the high-α population matches one of the chemical signature of present-day dSphs discovered by Venn et al. (2004). Venn et al. (2004) discards the possibility that the Galactic halo could consist of low-mass dwarf galaxies that have continuous merged with the Galaxy as a high [Ba/Y] and low [Y/Eu] is not observed in Galactic halo stars. In conjunction with the NS11 measurements, the results suggests the possibility of mergers with more massive dSphs as a smaller offset in [Ba/Y] and [Y/Eu] is observed compared to the offset found by Venn et al. (2004) using present-day dSphs. The idea of more massive mergers with the Galaxy was not ruled out by Venn et al. (2004). In addition, models of AGB stars are unable explain the lower [*hs*/Eu] ratios observed in the low-α stars compared to the high-α stars.

The results presented here offer new and important observational evidence regarding the nature of the Galactic halo. It is apparent from the study of NS10 and NS11 that there are at least two populations in the Galactic halo, one that formed in-situ as well as one accreted from dwarf galaxies. The low [Y/Eu] abundances in dSphs have been attributed to the contribution of metal-poor AGB stars (Venn et al. 2004). Low-metallicity AGB stars are also

responsible for the high [Ba/Y] abundances. Only with detailed chemical evolution models, along with measurements of additional *r*-process elements beyond Eu, will there be a better understanding of the chemical enrichment of the earliest dwarf galaxies that merged with the Galactic halo. In particular, through a better understanding of the *s*-process, we will be able to provide constraints on the formation site(s) of the *r*-process.

CHAPTER 6

Conclusions

One of the key questions in astronomy is understanding the formation and evolution of our Galaxy, the Milky Way. In particular, observations of chemical abundances and kinematics of stars provide a powerful diagnostic tool in revealing clues about the formation and evolution of the Galactic halo. It is possible to chemically disentangle the stars that have been accreted by the halo from those that were formed in-situ in the Galaxy as the chemical abundance patterns observed in stars can uncover information about their origin and how they were enriched by previous generations of stars. Further information can be obtained from theoretical stellar models where they play a key role in furthering our understanding of the origin of the elements. This is because stars of different mass, and less so metallicity, undergo different nucleosynthesis on different timescales.

This thesis has strived to further understand the accretion history of the Galactic halo. In particular, we aim to understand the role of asymptotic giant branch (AGB) stars in the enrichment of the Galactic halo and the dwarf galaxies that were accreted long ago. The study by Nissen & Schuster (2010) uncovered a population of stars that exhibit chemical similarities to present-day dwarf spheroidal galaxies (dSphs). They suggested that the stars, which have a low [α/Fe] abundance, formed in massive dwarf galaxies before being accreted during the formation of the Galactic halo. Nissen & Schuster (2010) also discovered a population of high-α stars that formed in-situ in the Galaxy. The dSph galaxies that have survived today have a larger offset in [α/Fe] to Galactic halo stars as they experienced an even slower star formation rate compared to the low-α population. Therefore, it is theorised that as a result of the slower star formation rate, AGB stars in the progenitor galaxies of the low-α population had less time to contribute to its chemical enrichment than observed in present-day dSphs. By measuring abundances of neutron-capture elements predominantly produced in AGB stars in the low- and high-α populations, it will be possible to quantify the differences between the two populations and the contribution of AGB stars to the chemical enrichment of these stars.

In order to understand the influence of AGB stars on the chemical enrichment of the low-α stars, we calculated detailed theoretical models of AGB stars at the mean metallicity of the

low- and high-α population. Stellar models are subject to uncertainties and we analyse the uncertainty related to the treatment of low-temperature molecular opacities in intermediate-mass AGB stellar models. Previous detailed intermediate-mass AGB models calculated with the Mt Stromlo evolutionary code used a molecular opacity treatment which did not consider the depletion of C and O due to hot bottom burning (HBB). Therefore, we improved the stellar evolution code by updating the low-temperature opacity treatment to account for the destruction of C and O.

In Chapter 2 we found that correctly accounting for the composition of the envelope of intermediate-mass stars experiencing HBB leads to a reduction in the uncertainty of the stellar yields. This is because intermediate-mass stars with HBB can become carbon rich, owing to efficient third dredge-up (TDU). The complex interplay of HBB and TDU means that the evolution of the C/O ratio at the surface varies with time from below solar to above solar. The C/O ratio starts below solar as a result of second dredge-up and the initial effects of HBB are to destroy C at the expense of N, leading to C/O ratios of ≈ 0.1 or lower. As the star evolves, the envelope C/O ratio fluctuates changing the calculated molecular opacity.

Results showed that the lower metallicity models are more affected by the improved low-temperature opacity treatment. When comparing the updated opacity treatment to the previously used treatment, the yield predictions are affected by up to 60 per cent for most isotopes in the $Z = 0.001$ models of 5 and 6 $M_\odot$. This is because the effective temperature decreases and the mass-loss rate increases as a result of an increase in the molecular opacity. Therefore, the duration of the AGB phase is shorter resulting in fewer TDU episodes. In the $Z = 0.02$ models, most isotopes experience changes up to 20 per cent.

In Chapter 3 we presented stellar evolutionary tracks and nucleosynthetic predictions for a grid of stellar models of low- and intermediate-mass AGB stars at $Z = 0.001$ ([Fe/H] $= -1.2$). The models cover an initial mass range from 1 $M_\odot$ to 7 $M_\odot$. Final surface abundances and stellar yields are calculated for all elements from hydrogen to bismuth as well as isotopes up to the iron group. The first study of neutron-capture nucleosynthesis in intermediate-mass AGB models of $Z = 0.001$ is presented. Neutron-capture elemental predictions for a super-AGB model are presented for the first time in literature at any metallicity. All models experience TDU which brings up the products of neutron-capture nucleosynthesis to the surface and HBB is activated in models with $M \geq 3$ $M_\odot$. With the 3 $M_\odot$ model we investigate the effect of varying the extent in mass of the region where protons are mixed from the envelope into the intershell at the deepest extent of each TDU. The 3 $M_\odot$ model is in the transition zone between the lower mass models and the more massive models. Increases in the mass of the PMZ result in larger enhancements in the abundances of neutron-capture elements and a number of light elements (O, F, Ne, Na, Mg, Al, and P).

We compare the results of the low-mass models to three post-AGB stars with a metallicity of [Fe/H] $\simeq -1.2$ using the abundances measured by van Aarle et al. (2013) and De Smedt et al. (2014). The composition is a good match to the predicted neutron-capture abundances except for Pb and we confirm that the observed Pb abundances are lower than what is calculated by AGB models.

In Chapter 4 we presented further structural properties relevant for nucleosynthesis during

the pre-AGB and AGB phases. The minimum core mass required for TDU agrees extremely well with the $Z = 0.001$ models of Cristallo et al. (2011). This is despite the different treatment of convection which affects the occurrence of TDU. We also examine the role of the PMZ in a low-mass AGB model of 2 $M_\odot$. We find that a more massive PMZ produces higher neutron densities but lower neutron exposures as a result of the ^{13}C neutron source. This affects the neutron-capture nucleosynthesis that takes place in the intershell. The 2 $M_\odot$ model with a PMZ of 6×10^{-3} $M_\odot$ produces nearly four times more Rb than the model with the standard PMZ as a result of reaching higher neutron densities.

Chapter 5 investigates the abundances of the neutron-capture elements Zr, La, Ba, Ce, Nd, and Eu in a subsample of stars from Nissen & Schuster (2010). We are able to separate the populations using the abundances of [Zr/Fe], [La/Zr], [*ls*/Fe], [*hs*/*ls*], [Y/Eu], [*ls*/Eu], and [*hs*/Eu]. We also measure the iron-group element Sc where the low-α population is observed to have a lower [Sc/Fe] abundance than the high-α population. These separations were only detected using a differential analysis relative to a reference star with comparable stellar parameters to reduce the error in abundance measurements.

The low [Y/Eu] observed in the low-α population, along with the high [Ba/Y] observed by Nissen & Schuster (2011), suggests that present-day dSphs share a similar chemical enrichment history to the dwarf galaxies that were hosts to the low-α stars and merged during the formation of the Galactic halo. These observations match the chemical abundance pattern observed in dSphs by Venn et al. (2004). This confirms that low-metallicity AGB stars of low mass were able to contribute more to the chemical enrichment of the low-α population compared to the high-α population. Further evidence showing that accreted dwarf galaxies had sufficient time to form stars enriched with the ejecta of AGB stars before merging is seen in the abundance of [Y/Eu] which increases with increasing [Fe/H]. Stellar models show that AGB stars contribute more Y than Eu resulting in an increase of [Y/Eu] with time (and metallicity).

With these results we confirm that the level of enrichment from AGB stars in the low-α population is not as high as observed in present-day dSph galaxies. This suggests that AGB stars did not have as much time to have an appreciable contribution to the chemical evolution before the dwarf galaxies were accreted despite having a slower star formation rate than the Galactic halo (as evidenced by the lower [α/Fe] abundance). Additionally, the models cannot explain the lower [*hs*/Eu] ratios observed in the low-α stars compared to the high-α stars.

6.1. Future directions

6.1.1. Extending the metallicity grid

The calculation of detailed AGB models is limited by computational time and predictions of neutron-capture elemental yields of low- and intermediate-mass AGB models were only presented for a single metallicity. In order to develop a chemical evolution model to follow the enrichment of neutron-capture elements in dwarf galaxies as a function of time, further

metallicities will need to be calculated. A homogeneous grid of models will be invaluable for the study of neutron-capture elements in the Galactic halo, dwarf galaxies, and globular clusters.

One highly uncertain parameter in the modelling of neutron-capture nucleosynthesis in low-mass AGB stars is the treatment of the ^{13}C pocket (Straniero et al. 2009). The study by Lugaro et al. (2012) found that a number of regimes of neutron capture can occur in low-mass AGB models. Different ratios of [Ba/Y] can be produced depending on whether the ^{13}C neutron source operates in radiative or convective conditions and which of these conditions is more dominant. This warrants further investigation.

6.1.2. Harnessing high-quality spectra

The nature of the hierarchical formation of the Galactic halo is still being disputed with the fraction of accreted stars in the halo under debate (e.g., Bell et al. 2008). The identification of more stars, both kinematically and chemically, that have been accreted from low-mass dwarf galaxies will provide further evidence for the formation and evolution of the Galaxy. Therefore, the sample of Nissen & Schuster (2010, 2011) can be expanded upon, providing better statistics on the number of stars possibly accreted from dwarf galaxies. There is also the potential to extend the low-α study to lower, as well as higher, metallicities than the Nissen & Schuster (2011) study where the separation in the neutron-capture elemental abundances can be explored further. Expanding the observations to include the full Nissen & Schuster (2010) sample will also increase the probability that the observed separations are real. The full sample would also help verify if there is indeed a difference in [Eu/Fe] between the low- and high-α populations.

The faintness of dSph stars restricts the quality of the spectra that can be obtained to measure abundances. The low-α population provides an ideal opportunity to measure the abundances of additional neutron-capture elements, particularly *r*-process elements (such as Te and Os), in stars that formed in dwarf galaxies. By further exploiting the high resolution, high signal-to-noise spectra and going beyond Eu, abundance measurements of *r*-process elements would reveal more about the level of *r*-process nucleosynthesis that took place during the enrichment of these dwarf galaxies.

Bibliography

Abia, C., Busso, M., Gallino, R., Domínguez, I., Straniero, O., & Isern, J. 2001, The Astrophysical Journal, 559, 1117

Abia, C., Cunha, K., Cristallo, S., de Laverny, P., Domínguez, I., Recio-Blanco, A., Smith, V. V., & Straniero, O. 2011, The Astrophysical Journal Letters, 737, L8

Abia, C., Recio-Blanco, A., de Laverny, P., Cristallo, S., Domínguez, I., & Straniero, O. 2009, The Astrophysical Journal, 694, 971

Abia, C., et al. 2002, The Astrophysical Journal, 579, 817

—. 2010, The Astrophysical Journal Letters, 715, L94

Alexander, D. R., & Ferguson, J. W. 1994, The Astronomical Journal, 437, 879

Alongi, M., Bertelli, G., Bressan, A., & Chiosi, C. 1991, Astronomy and Astrophysics, 244, 95

Angulo, C., et al. 1999, Nuclear Physics A, 656, 3

Arnould, M., Goriely, S., & Jorissen, A. 1999, Astronomy and Astrophysics, 347, 572

Arnould, M., Goriely, S., & Takahashi, K. 2007, Physics Reports, 450, 97

Asplund, M., Grevesse, N., Sauval, A. J., & Scott, P. 2009, Annual Review of Astronomy and Astrophysics, 47, 481

Bao, Z. Y., Beer, H., Käppeler, F., Voss, F., Wisshak, K., & Rauscher, T. 2000, Atomic Data and Nuclear Data Tables, 76, 70

Beer, H., Corvi, F., & Mutti, P. 1997, The Astrophysical Journal, 474, 843

Beer, H., & Macklin, R. L. 1989, The Astrophysical Journal, 339, 962

Bell, E. F., et al. 2008, The Astrophysical Journal, 680, 295

Belokurov, V., et al. 2006, The Astrophysical Journal, 642, L137

—. 2007, The Astrophysical Journal, 658, 337

Bernstein, R., Shectman, S. A., Gunnels, S. M., Mochnacki, S., & Athey, A. E. 2003, Instrument Design and Performance for Optical/Infrared Ground-based Telescopes: Proceedings of the SPIE, 4841, 1694

Bisterzo, S., Gallino, R., Straniero, O., Cristallo, S., & Käppeler, F. 2010, Monthly Notices of the Royal Astronomical Society, 404, 1529

Bisterzo, S., Travaglio, C., Gallino, R., Wiescher, M., & Käppeler, F. 2014, The Astrophysical Journal, 787, 10

Blöcker, T. 1995, Astronomy and Astrophysics, 297, 727

—. 2001, Astrophysics and Space Science, 275, 1

Blöcker, T., & Schoenberner, D. 1991, Astronomy and Astrophysics, 244, L43

Böhm-Vitense, E. 1958, Zeitschrift für Astrophysik, 46, 108

Bonaparte, I., Matteucci, F., Recchi, S., Spitoni, E., Pipino, A., & Grieco, V. 2013, Monthly Notices of the Royal Astronomical Society, 435, 2460

Boothroyd, A. I., & Sackmann, I.-J. 1988, The Astrophysical Journal, 328, 671

—. 1999, The Astrophysical Journal, 510, 232

Bullock, J. S., & Johnston, K. V. 2005, The Astrophysical Journal, 635, 931

Burbidge, E. M., Burbidge, G. R., Fowler, W. A., & Hoyle, F. 1957, Reviews of Modern Physics, 29, 547

Busso, M., Gallino, R., Lambert, D. L., Travaglio, C., & Smith, V. V. 2001, The Astrophysical Journal, 557, 802

Busso, M., Gallino, R., & Wasserburg, G. J. 1999, Annual Review of Astronomy and Astrophysics, 37, 239

Cameron, A. G. W. 1957, Publications of the Astronomical Society of the Pacific, 69, 201

—. 1960, Astronomical Journal, 65, 485

Cameron, A. G. W., & Fowler, W. A. 1971, The Astrophysical Journal, 164, 111

Cannon, R. C. 1993, Monthly Notices of the Royal Astronomical Society, 263, 817

Canuto, V. M., & Mazzitelli, I. 1991, The Astrophysical Journal, 370, 295

Casagrande, L., Flynn, C., Portinari, L., Girardi, L., & Jimenez, R. 2007, Monthly Notices of the Royal Astronomical Society, 382, 1516

Casey, A. R. 2014, arXiv:1405.5968v1

Casey, A. R., et al. 2014, Monthly Notices of the Royal Astronomical Society, 443, 828

Cassisi, S., Salaris, M., & Bono, G. 2002, The Astrophysical Journal, 565, 1231

Castelli, F., & Kurucz, R. L. 2003, arXiv:astro-ph/0405087v1

Caughlan, G. R., & Fowler, W. A. 1988, Atomic Data and Nuclear Data Tables, 40, 283

Cescutti, G., Matteucci, F., Caffau, E., & Francois, P. 2012, Astronomy and Astrophysics, 540, 33

Charbonnel, C. 1995, Astrophysical Journal Letters, 453, L41

Constantino, T., Campbell, S., Gil-Pons, P., & Lattanzio, J. 2014, The Astrophysical Journal, 784, 56

Cristallo, S., Straniero, O., Gallino, R., Piersanti, L., Domínguez, I., & Lederer, M. T. 2009, The Astrophysical Journal, 696, 797

Cristallo, S., et al. 2011, The Astrophysical Journal Supplement, 197, 17

Cyburt, R. H. 2004, Physical Review D, 70, 023505

Cyburt, R. H., et al. 2010, The Astrophysical Journal Supplement, 189, 240

de Boer, T. J. L., Belokurov, V., Beers, T. C., & Lee, Y. S. 2014, Monthly Notices of the Royal Astronomical Society, 443, 658

De Smedt, K., Van Winckel, H., Kamath, D., Karakas, A. I., Siess, L., Goriely, S., & Wood, P. 2014, Astronomy and Astrophysics, 563, L5

Dillmann, I., Heil, M., Käppeler, F., Plag, R., Rauscher, T., & Thielemann, F. K. 2006, in CAPTURE GAMMA-RAY SPECTROSCOPY AND RELATED TOPICS: 12th International Symposium. AIP Conference Proceedings, 123–127

Dinerstein, H. L., & Geballe, T. R. 2001, The Astrophysical Journal, 562, 515

Doherty, C. L., Gil-Pons, P., Lau, H. H. B., Lattanzio, J. C., & Siess, L. 2014a, Monthly Notices of the Royal Astronomical Society, 437, 195

Doherty, C. L., Gil-Pons, P., Lau, H. H. B., Lattanzio, J. C., Siess, L., & Campbell, S. W. 2014b, Monthly Notices of the Royal Astronomical Society, 441, 582

Doherty, C. L., Gil-Pons, P., Siess, L., Lattanzio, J. C., & Lau, H. H. B. 2015, Monthly Notices of the Royal Astronomical Society, 446, 2599

Eggen, O. J., Lynden-Bell, D., & Sandage, A. R. 1962, The Astrophysical Journal, 136, 748

Ferguson, J. W., Alexander, D. R., Allard, F., Barman, T., Bodnarik, J. G., Hauschildt, P. H., Heffner-Wong, A., & Tamanai, A. 2005, The Astrophysical Journal, 623, 585

Fishlock, C. K., Karakas, A. I., Lugaro, M., & Yong, D. 2014a, The Astrophysical Journal, 797, 44

Fishlock, C. K., Karakas, A. I., & Stancliffe, R. J. 2014b, Monthly Notices of the Royal Astronomical Society, 438, 1741

Forestini, M., Goriely, S., Jorissen, A., & Arnould, M. 1992, Astronomy and Astrophysics, 261, 157

Francois, P., Matteucci, F., Cayrel, R., Spite, M., Spite, F., & Chiappini, C. 2004, Astronomy and Astrophysics, 421, 613

Frebel, A., Simon, J. D., Geha, M., & Willman, B. 2010, The Astrophysical Journal, 708, 560

Freeman, K., & Bland-Hawthorn, J. 2002, Annual Review of Astronomy and Astrophysics, 40, 487

Frischknecht, U., Hirschi, R., & Thielemann, F. K. 2012, Astronomy and Astrophysics, 538, L2

Frost, C. A., Cannon, R. C., Lattanzio, J. C., Wood, P. R., & Forestini, M. 1998, Astronomy and Astrophysics, 332, L17

Frost, C. A., & Lattanzio, J. C. 1996, The Astrophysical Journal, 473, 383

Fulbright, J. P. 2002, The Astronomical Journal, 123, 404

Gallino, R., Arlandini, C., Busso, M., Lugaro, M., Travaglio, C., Straniero, O., Chieffi, A., & Limongi, M. 1998, The Astrophysical Journal, 497, 388

Garcia-Hernandez, D. A., Zamora, O., Yagüe, A., Uttenthaler, S., Karakas, A. I., Lugaro, M., Ventura, P., & Lambert, D. L. 2013, Astronomy and Astrophysics, 555, L3

Garcia-Hernandez, D. A., et al. 2009, The Astrophysical Journal Letters, 705, L31

Geisler, D., Smith, V. V., Wallerstein, G., Gonzalez, G., & Charbonnel, C. 2005, The Astronomical Journal, 129, 1428

Gilmore, G., & Wyse, R. F. G. 1998, The Astronomical Journal, 116, 748

Goriely, S., & Siess, L. 2004, Astronomy and Astrophysics, 421, L25

Gratton, R., Sneden, C., & Carretta, E. 2004, Annual Review of Astronomy and Astrophysics, 42, 385

Guo, B., et al. 2012, The Astrophysical Journal, 756, 193

Haselgrove, C. B., & Hoyle, F. 1956, Monthly Notices of the Royal Astronomical Society, 116, 515

Heil, M., Käppeler, F., Uberseder, E., Gallino, R., Bisterzo, S., & Pignatari, M. 2008a, Physical Review C, 78, 25802

Heil, M., et al. 2008b, Physical Review C, 78, 25803

Helmi, A., White, S. D. M., de Zeeuw, P. T., & Zhao, H. 1999, Nature, 402, 53

Hendricks, B., Koch, A., Lanfranchi, G. A., Boeche, C., Walker, M., Johnson, C. I., Peñarrubia, J., & Gilmore, G. 2014, The Astrophysical Journal, 785, 102

Herwig, F. 2004a, The Astrophysical Journal, 605, 425

—. 2004b, The Astrophysical Journal Supplement Series, 155, 651

—. 2005, Annual Review of Astronomy and Astrophysics, 43, 435

Herwig, F., Austin, S. M., & Lattanzio, J. C. 2006, Physical Review C, 73, 25802

Herwig, F., Langer, N., & Lugaro, M. 2003, The Astrophysical Journal, 593, 1056

Ibata, R. A., Gilmore, G., & Irwin, M. J. 1994, Nature, 370, 194

Iben, I. J. 2013a, Stellar Evolution Physics, 1

—. 2013b, Stellar Evolution Physics, 2

Iglesias, C. A., & Rogers, F. J. 1996, The Astrophysical Journal, 464, 943

Iliadis, C., Longland, R., Champagne, A. E., Coc, A., & Fitzgerald, R. 2010, Nuclear Physics A, 841, 31

Ivans, I. I., Sneden, C., James, C. R., Preston, G. W., Fulbright, J. P., Höflich, P. A., Carney, B. W., & Wheeler, J. C. 2003, The Astrophysical Journal, 592, 906

Izzard, R. G., Glebbeek, E., Stancliffe, R. J., & Pols, O. R. 2009, Astronomy and Astrophysics, 508, 1359

Izzard, R. G., Lugaro, M., Karakas, A. I., Iliadis, C., & van Raai, M. 2007, Astronomy and Astrophysics, 466, 641

Izzard, R. G., Tout, C. A., Karakas, A. I., & Pols, O. R. 2004, Monthly Notices of the Royal Astronomical Society, 350, 407

Jaeger, M., Kunz, R., Mayer, A., Hammer, J. W., Staudt, G., Kratz, K.-L., & Pfeiffer, B. 2001, Physical Review Letters, 87, 202501

Johnson, J. A., Herwig, F., Beers, T. C., & Christlieb, N. 2007, The Astrophysical Journal, 658, 1203

Jorissen, A., Smith, V. V., & Lambert, D. L. 1992, Astronomy and Astrophysics, 261, 164

Kalirai, J. S. 2012, Nature, 486, 90

Kalirai, J. S., Marigo, P., & Tremblay, P.-E. 2014, The Astrophysical Journal, 782, 17

Kamath, D., Karakas, A. I., & Wood, P. R. 2012, The Astrophysical Journal, 746, 20

Karakas, A., & Lattanzio, J. C. 2007, Publications of the Astronomical Society of Australia, 24, 103

Karakas, A. I. 2010, Monthly Notices of the Royal Astronomical Society, 403, 1413

—. 2014, Monthly Notices of the Royal Astronomical Society, 445, 347

Karakas, A. I., Campbell, S. W., & Stancliffe, R. J. 2010, The Astrophysical Journal, 713, 374

Karakas, A. I., Garcia-Hernandez, D. A., & Lugaro, M. 2012, The Astrophysical Journal, 751, 8

Karakas, A. I., & Lattanzio, J. C. 2003, Publications of the Astronomical Society of Australia, 20, 279

—. 2014, Publications of the Astronomical Society of Australia, 31, e030

Karakas, A. I., Lattanzio, J. C., & Pols, O. R. 2002, Publications of the Astronomical Society of Australia, 19, 515

Karakas, A. I., & Lugaro, M. 2010, Publications of the Astronomical Society of Australia, 27, 227

Karakas, A. I., Lugaro, M. A., Wiescher, M., Görres, J., & Ugalde, C. 2006, The Astrophysical Journal, 643, 471

Karakas, A. I., Marino, A. F., & Nataf, D. M. 2014, The Astrophysical Journal, 784, 32

Klement, R. J. 2010, The Astronomy and Astrophysics Review, 18, 567

Kobayashi, C., Izutani, N., Karakas, A. I., Yoshida, T., Yong, D., & Umeda, H. 2011a, The Astrophysical Journal Letters, 739, L57

Kobayashi, C., Karakas, A. I., & Umeda, H. 2011b, Monthly Notices of the Royal Astronomical Society, 414, 3231

Kratz, K.-L., Farouqi, K., Pfeiffer, B., Truran, J. W., Sneden, C., & Cowan, J. J. 2007, The Astrophysical Journal, 662, 39

Lanfranchi, G. A., Matteucci, F., & Cescutti, G. 2008, Astronomy and Astrophysics, 481, 635

Lattanzio, J. C. 1986, The Astrophysical Journal, 311, 708

—. 1992, Proceedings of the Astronomical Society of Australia, 10, 120

Lau, H. H. B., Gil-Pons, P., Doherty, C., & Lattanzio, J. 2012, Astronomy and Astrophysics, 542, 1

Lawler, J. E., Bonvallet, G., & Sneden, C. 2001a, The Astrophysical Journal, 556, 452

Lawler, J. E., Wickliffe, M. E., Den Hartog, E. A., & Sneden, C. 2001b, The Astrophysical Journal, 563, 1075

Lederer, M. T., & Aringer, B. 2009, Astronomy and Astrophysics, 494, 403

Lee, M. G., Freedman, W. L., & Madore, B. F. 1993, The Astrophysical Journal, 417, 553

Letarte, B., et al. 2010, Astronomy and Astrophysics, 523, 17

Liu, S., Nissen, P. E., Schuster, W. J., Zhao, G., Chen, Y. Q., & Liang, Y. C. 2012, Astronomy and Astrophysics, 541, 48

Lodders, K. 2003, The Astrophysical Journal, 591, 1220

Lugaro, M., Herwig, F., Lattanzio, J. C., Gallino, R., & Straniero, O. 2003, The Astrophysical Journal, 586, 1305

Lugaro, M., Karakas, A. I., Stancliffe, R. J., & Rijs, C. 2012, The Astrophysical Journal, 747, 2

Lugaro, M., Tagliente, G., Karakas, A. I., Milazzo, P. M., Käppeler, F., Davis, A. M., & Savina, M. R. 2014, The Astrophysical Journal, 780, 95

Lugaro, M., Ugalde, C., Karakas, A. I., Görres, J., Wiescher, M., Lattanzio, J. C., & Cannon, R. C. 2004, The Astrophysical Journal, 615, 934

Marigo, P. 2002, Astronomy and Astrophysics, 387, 507

—. 2007, Astronomy and Astrophysics, 467, 1139

Marigo, P., & Aringer, B. 2009, Astronomy and Astrophysics, 508, 1539

Marigo, P., Bressan, A., Nanni, A., Girardi, L., & Pumo, M. L. 2013, Monthly Notices of the Royal Astronomical Society, 434, 488

Marino, A. F., et al. 2011, Astronomy and Astrophysics, 532, 8

Mattsson, L., Wahlin, R., Höfner, S., & Eriksson, K. 2008, Astronomy and Astrophysics, 484, L5

McWilliam, A. 1997, Annual Review of Astronomy and Astrophysics, 35, 503

McWilliam, A., Wallerstein, G., & Mottini, M. 2013, The Astrophysical Journal, 778, 149

Meléndez, J., & Cohen, J. G. 2007, The Astrophysical Journal, 659, L25

—. 2009, The Astrophysical Journal, 699, 2017

Merrill, P. W. 1952, The Astrophysical Journal, 116, 21

Mowlavi, N. 1999, Astronomy and Astrophysics, 350, 73

Mowlavi, N., Jorissen, A., & Arnould, M. 1996, Astronomy and Astrophysics, 311, 803

Mowlavi, N., & Meynet, G. 2000, Astronomy and Astrophysics, 361, 959

Nataf, D. M., Gould, A. P., Pinsonneault, M. H., & Udalski, A. 2013, The Astrophysical Journal, 766, 77

Nissen, P. E. 2011, arXiv:1109.4010v1

Nissen, P. E., Chen, Y. Q., Schuster, W. J., & Zhao, G. 2000, Astronomy and Astrophysics, 353, 722

Nissen, P. E., & Schuster, W. J. 2010, Astronomy and Astrophysics, 511, L10

—. 2011, Astronomy and Astrophysics, 530, A15

Nomoto, K., Kobayashi, C., & Tominaga, N. 2013, Annual Review of Astronomy and Astrophysics, 51, 457

Piersanti, L., Cristallo, S., & Straniero, O. 2013, The Astrophysical Journal, 774, 98

Pignatari, M., et al. 2013, arXiv:1307.6961v1

Pillepich, A., et al. 2014, Monthly Notices of the Royal Astronomical Society, 444, 237

Plez, B., Smith, V. V., & Lambert, D. L. 1993, The Astrophysical Journal, 418, 812

Pols, O. R., Izzard, R. G., Stancliffe, R. J., & Glebbeek, E. 2012, Astronomy and Astrophysics, 547, 76

Prochaska, J. X., Naumov, S. O., Carney, B. W., McWilliam, A., & Wolfe, A. M. 2000, The Astronomical Journal, 120, 2513

Raut, R., et al. 2013, Physical Review Letters, 111, 112501

Recio-Blanco, A., de Laverny, P., Worley, C., Santos, N. C., Melo, C., & Israelian, G. 2012, Astronomy and Astrophysics, 538, 117

Reimers, D. 1975, Mémoires of the Société Royale des Sciences de Liège, 8, 369

Renzini, A., & Voli, M. 1981, Astronomy and Astrophysics, 94, 175

Romano, D., Karakas, A. I., Tosi, M., & Matteucci, F. 2010, Astronomy and Astrophysics, 522, 32

Ryan, S. G., & Norton, A. J. 2010, Stellar Evolution and Nucleosynthesis, Cambridge University Press

Sackmann, I. J., & Boothroyd, A. I. 1992, The Astrophysical Journal, 392, L71

Salaris, M., & Cassisi, S. 2006, Wiley

Schuster, W. J., Moreno, E., Nissen, P. E., & Pichardo, B. 2012, Astronomy and Astrophysics, 538, 21

Searle, L., & Zinn, R. 1978, The Astrophysical Journal, 225, 357

Sheffer, Y., Rogers, M., Federman, S. R., Lambert, D. L., & Gredel, R. 2007, The Astrophysical Journal, 667, 1002

Shetrone, M. D. 2003, The Astrophysical Journal, 585, L45

Shingles, L. J., & Karakas, A. I. 2013, Monthly Notices of the Royal Astronomical Society, 431, 2861

Shingles, L. J., Karakas, A. I., Hirschi, R., Fishlock, C. K., Yong, D., Da Costa, G. S., & Marino, A. F. 2014, The Astrophysical Journal, 795, 34

Siess, L. 2007, Astronomy and Astrophysics, 476, 893

Siess, L., Goriely, S., & Langer, N. 2004, Astronomy and Astrophysics, 415, 1089

Simmerer, J., Sneden, C., Cowan, J. J., Collier, J., Woolf, V. M., & Lawler, J. E. 2004, The Astrophysical Journal, 617, 1091

Smith, C. L., Zijlstra, A. A., & Dinerstein, H. L. 2014, Monthly Notices of the Royal Astronomical Society, 441, 3161

Smith, V. V., & Lambert, D. L. 1989, The Astrophysical Journal, 345, L75

—. 1990, The Astrophysical Journal, 361, L69

Sneden, C. 1973, The Astrophysical Journal, 184, 839

Sneden, C., Cowan, J. J., & Gallino, R. 2008, Annual Review of Astronomy and Astrophysics, 46, 241

Stancliffe, R. J., Izzard, R. G., & Tout, C. A. 2005, Monthly Notices of the Royal Astronomical Society: Letters, 356, L1

Stancliffe, R. J., & Jeffery, C. S. 2007, Monthly Notices of the Royal Astronomical Society, 375, 1280

Stancliffe, R. J., Tout, C. A., & Pols, O. R. 2004, Monthly Notices of the Royal Astronomical Society, 352, 984

Starkenburg, E., et al. 2013, Astronomy and Astrophysics, 549, 88

Stephens, A., & Boesgaard, A. M. 2002, The Astronomical Journal, 123, 1647

Straniero, O., Cristallo, S., & Gallino, R. 2009, Publications of the Astronomical Society of Australia, 26, 133

Straniero, O., Cristallo, S., & Piersanti, L. 2014, The Astrophysical Journal, 785, 77

Straniero, O., Gallino, R., Busso, M., Chiefei, A., Raiteri, C. M., Limongi, M., & Salaris, M. 1995, The Astrophysical Journal, 440, L85

Straniero, O., Gallino, R., & Cristallo, S. 2006, Nuclear Physics A, 777, 311

Suda, T., Hirschi, R., & Fujimoto, M. Y. 2011, The Astrophysical Journal, 741, 61

Tinsley, B. M. 1979, The Astrophysical Journal, 229, 1046

Tolstoy, E., Hill, V., & Tosi, M. 2009, Annual Review of Astronomy and Astrophysics, 47, 371

Trippella, O., Busso, M., Maiorca, E., Käppeler, F., & Palmerini, S. 2014, The Astrophysical Journal, 787, 41

Truran, J. W., & Iben, I. J. 1977, The Astrophysical Journal, 216, 797

Ugalde, C., et al. 2008, Physical Review C, 77, 35801

van Aarle, E., Van Winckel, H., De Smedt, K., Kamath, D., & Wood, P. R. 2013, Astronomy and Astrophysics, 554, 106

van Loon, J. T., et al. 1998, Astronomy and Astrophysics, 329, 169

van Raai, M. A., Lugaro, M., Karakas, A. I., Garcia-Hernandez, D. A., & Yong, D. 2012, Astronomy and Astrophysics, 540, 44

Van Winckel, H. 2003, Annual Review of Astronomy and Astrophysics, 41, 391

VandenBerg, D. A., Bergbusch, P. A., Dotter, A., Ferguson, J. W., Michaud, G., Richer, J., & Proffitt, C. R. 2012, The Astrophysical Journal, 755, 15

Vassiliadis, E., & Wood, P. R. 1993, The Astrophysical Journal, 413, 641

Venn, K. A., Irwin, M., Shetrone, M. D., Tout, C. A., Hill, V., & Tolstoy, E. 2004, The Astronomical Journal, 128, 1177

Venn, K. A., et al. 2012, The Astrophysical Journal, 751, 102

Ventura, P., Carini, R., & D'Antona, F. 2011, Monthly Notices of the Royal Astronomical Society, 415, 3865

Ventura, P., & D'Antona, F. 2005a, Astronomy and Astrophysics, 431, 279

—. 2005b, Astronomy and Astrophysics, 439, 1075

—. 2008, Astronomy and Astrophysics, 479, 805

—. 2010, Monthly Notices of the Royal Astronomical Society: Letters, 402, L72

Ventura, P., D'Antona, F., Di Criscienzo, M., Carini, R., D'Ercole, A., & Vesperini, E. 2012, The Astrophysical Journal Letters, 761, L30

Ventura, P., & Marigo, P. 2009, Monthly Notices of the Royal Astronomical Society: Letters, 399, L54

—. 2010, Monthly Notices of the Royal Astronomical Society, 408, 2476

Wallerstein, G., & Knapp, G. R. 1998, Annual Review of Astronomy and Astrophysics, 36, 369

Wallerstein, G., et al. 1997, Reviews of Modern Physics, 69, 995

Weiss, A., & Ferguson, J. W. 2009, Astronomy and Astrophysics, 508, 1343

Wheeler, J. C., Sneden, C., & Truran, J. W. J. 1989, Annual Review of Astronomy and Astrophysics, 27, 279

White, S. D. M., & Rees, M. J. 1978, Monthly Notices of the Royal Astronomical Society, 183, 341

Winckler, N., Dababneh, S., Heil, M., Käppeler, F., Gallino, R., & Pignatari, M. 2006, The Astrophysical Journal, 647, 685

Wood, P. R., Bessell, M. S., & Fox, M. W. 1983, The Astrophysical Journal, 272, 99

Woosley, S. E., Heger, A., & Weaver, T. A. 2002, Reviews of Modern Physics, 74, 1015

Woosley, S. E., & Weaver, T. A. 1995, The Astrophysical Journal Supplement, 101, 181

Yong, D., Grundahl, F., Nissen, P. E., Jensen, H. R., & Lambert, D. L. 2005, Astronomy and Astrophysics, 438, 875

Yong, D., et al. 2014a, Monthly Notices of the Royal Astronomical Society, 439, 2638

—. 2014b, Monthly Notices of the Royal Astronomical Society, 441, 3396